



DISSERTATION

THE VARIABILITY IN KERMA OUTPUT AND RADIATION QUALITY OF MEDICAL DIAGNOSTIC X-RAY UNITS

ausgeführt zum Zwecke der Erlangung des akademischen Grades eines
Doktors der Technischen Wissenschaften unter der Betreuung von

Univ. Prof. D.I. Dr. Hannes Aiginger
TU-WIEN, Atominstitut der Österreichischen Universitäten

Und

Ao. Univ. Prof. Dr. Robert Nowotny
Medizinische Universität WIEN,
Institut für Biomedizinische Technik und Physik

eingereicht an der Technischen Universität Wien
Technisch Naturwissenschaftliche Fakultät

von
Khadoudja Meghzifene
(Matr.Nr. 9827283)
Friedlgasse 52/4, 1190 Wien

A handwritten signature in black ink, which appears to read 'Meghzifene', is written over the printed name.

Wien, am October 2004

KURZFASSUNG

Die Strahlenbelastung des Patienten in medizinischen Röntgenuntersuchungen hängt neben anderen Parametern von der Strahlenqualität der Röntgenstrahlung ab, die in der Regel durch die Halbwertsschichtdicke (HWS) angegeben wird. Mit dem Gebrauch der Röntgenröhre nimmt die Rauigkeit der Anodenoberfläche wegen der hohen Leistungsdichte im Brennfleck zu. Dieser Effekt der Röhrenalterung erhöht die inhärente Filtration der Röntgenröhre, die eine Reduktion der Strahlenausbeute und eine Erhöhung der Durchdringungsfähigkeit zur Folge haben. Dieser Effekt, der Einfluss auf Strahlenbelastung und Bildqualität hat, wurde an Hand von Drehanoden von außer Betrieb genommenen Röntgenröhren untersucht. Die Anodenrauigkeit wurde durch eine Messung von Oberflächenprofilen an 8 Brennfleckbahnen ermittelt. Die Rauigkeit wurde als das arithmetische Mittel R_a der Abweichungen von der Mittellinie für Profillängen von 200 μm bestimmt. Es ergaben sich Werte für R_a von 1.32 μm (sandgestrahlte Oberfläche im ursprünglichen Zustand) bis 5.22 μm (kleiner Fokus mit starker Belastung). Die Oberflächenprofile wurden dann für eine Simulation von Röntgenspektren benutzt [No85]. Für jedes Profil wurden etwa 40000 Spektren berechnet und gemittelt, wobei die Elektronen auf der Anode an randomisierten Stellen auftreffen. Die Ergebnisse zeigen, dass eine erhöhte Rauigkeit zu einer zusätzlichen Schwächung der Röntgenstrahlung in Wolfram führt. Die Anode mit der grössten Rauigkeit ($R_a=5.22 \mu\text{m}$) ergab eine mittlere zusätzliche Schichtdicke in Strahlrichtung von etwa 18 μm und einen Verlust in der Strahlungsausbeute von $\sim 30\%$ bei 70 kV Röhrenspannung. Die Auswirkungen auf mittlere Photonenergie und HWS sind insgesamt geringer, aber am deutlichsten um etwa 70 kV und am geringsten bei 140 kV. Dies ist auf die K-Kante im Schwächungskoeffizient von Wolfram bei 69.5 keV zurückzuführen.

Um den Einfluß der Röhrenalterung auf Strahlungsausbeute, HWS und gesamte Filtration bei klinischen Röntgengeräten zu untersuchen, wurden in 19 Fällen Schwächungskurven mit Aluminiumfiltern mittels der Messung der Luftkerma aufgenommen. Zunächst wurde die Gesamtfilterung wie in der gültigen Norm [ISO97] vorgesehen nach der HWS-Methode ermittelt. Diese und andere indirekte Methoden zeigen manche auf die unbekannte spektrale Verteilung der Röntgenstrahlung zurückzuführenden Unzulänglichkeiten. Deshalb wurde eine neue Methode zur

Bestimmung der gesamten Filterwirkung entwickelt, welche die Veränderungen der Anodenoberfläche berücksichtigt. Der grundlegende Ansatz liegt hierfür in einer Anpassung von berechneten Schwächungskurven, die aus einem Modell für die Produktion von Röntgenstrahlung gewonnen werden, an die gemessenen Werte, wobei nur die Dicke eines zusätzlichen Filters und ein allgemeiner Normierungsfaktor variiert werden. Die Dicke der derart ermittelten Wolframschichten variiert von 2.43 μm bis 11.89 μm , das einer Rauigkeit R_a von 1.5 bis 4.5 μm entspricht. Diese Rauigkeit liegt in guter Übereinstimmung in dem Bereich, der aus den Messungen an den Anoden ermittelt wurde. Eine ähnliche Ermittlung der zusätzlichen Filtration durch ein äquivalentes Aluminiumfilter ergab Dicken von 0.34 bis 1.72 mm Al.

Das Anpassungsverfahren ergab im Vergleich mit der HWS-Methode stets größere Filterdicken. Aus der Simulation des Einflusses der Anodenrauigkeit auf die Strahlungsqualität ergab sich die größte Variation der HWS bei etwa 80 kV Röhrenspannung. Die HWS-Methode verwendet aber nur eine bei 60 kV gemessenen Schwächungskurve während das hier beschriebene Verfahren mehrere Schwächungskurven aus dem Bereich der Röhrenspannung verwendet. Dies könnte die Ursache für diese Abweichung sein. Die Anpassungsmethode liefert jedenfalls die bessere Übereinstimmung von gemessenen und berechneten Kerma-Werten als die HWS-Methode. Das hier konzipierte Anpassungsverfahren beruht nicht auf festgelegten Voraussetzungen, wie Messung bei festen Röhreneinstellungen, sondern benötigt nur einen Satz von Schwächungskurven, die mit beliebigen Röhrenspannungen und Filterdicken aufgenommen werden können.

ABSTRACT

Radiation dose to the patient in medical x-ray examinations depends amongst other parameters on the radiation quality of the x-rays often described by the Half-Value Layer (HVL). In the course of the usage of a diagnostic x-ray unit the roughness of the anode surface increases due to tube loading. This effect of tube ageing increases the inherent filtration of the x-ray tube with the consequence of reduced radiation output and increased radiation hardness, HVL. As this effect is of importance to both radiation dose and image quality, it was studied with rotating anodes collected from decommissioned clinical x-ray tubes. The roughening of anodes was measured by a determination of surface profiles for 8 focal tracks. Surface roughness was determined as the arithmetic mean R_a of the deviation from the centre line for profile lengths of 200 μm . R_a was ranging from 1.32 μm (sandblasted finish without surface degradation) to 5.22 μm (a track for a small focus with heavy usage). The surface profiles were then used to calculate x-ray spectra using a computer code [No85]. For each surface profile about 40000 spectra were thus calculated and averaged with the electrons entering the anode at random position. The results indicate that an increased roughness induces an additional filtration in tungsten. The roughest surface ($R_a=5.22 \mu\text{m}$) yields a mean additional absorber thickness in direction of the x-ray beam of about 18 μm with a corresponding loss in kerma output of about 30% at 70 kV. The effects on mean photon energy and HVL are rather small but highest around 70 kV and lowest at 140 kV. This is due to the K-edge in the attenuation coefficients of tungsten at 69.5 keV.

To study the influence of tube ageing on kerma output, HVL and total filtration with clinical x-ray units kerma measurements were made for 19 samples as to determine attenuation curves with aluminium filters. Total filtration was first determined using the HVL method as recommended by the current standard [ISO97]. This and all other indirect methods show some deficiencies mostly due to the unknown spectral distribution of the x-rays. Therefore another method for the determination of total filtration was devised including the effects of anode surface deterioration. The basic idea is to fit calculated attenuation curves obtained by a model to the measured data by only varying the thickness of an additional filter and a general normalization factor. The thicknesses of the tungsten layers obtained using the fit method vary from 2.43 μm to 11.89 μm with an associated surface roughness R_a from 1.5 to 4.5 μm corresponding

very well to the thicknesses of the additional absorbing layers determined for rough anodes. A determination of additional filtration in terms of an equivalent aluminium filter gave thicknesses from 0.34 to 1.72 mm aluminium.

The total filtration determined by the fit method consistently gave larger filter thicknesses than with the HVL method. From the simulation of the effect of surface roughness on beam quality, it was concluded that the variation of HVL with tube voltage for varying roughness is not constant but has its maximum variation at 80 kV. The HVL-method uses an attenuation curve determined at a tube voltage of 60 kV while the fit method comprises measurements for a larger range of tube voltages. This could explain the larger values for the added filtration as determined by the fit method. Comparing experimental and calculated kerma data the fit method gives better results than the HVL method. The fit method does not rely on any prerequisites as specific parameter settings but only requires the measurement of a set of kerma yields for some tube voltages and filter thicknesses.

ACKNOWLEDGEMENTS

I would like to thank Univ. Prof. D.I. Dr. Hannes Aiginger from the Atominstitut of the Austrian Universities, TU Vienna, who gave me the opportunity to carry out the doctoral thesis under his auspices. I am also indebted for his continuous support and interest, and for his lectures and seminars that have inspired me.

Most of the work was made at the Institute for Biomedical Engineering and Physics at the former University of Vienna, now the Vienna Medical University, and I want to thank my supervisor there, Univ. Prof. Dr. Robert Nowotny, for his support and encouragement in the course of this work. His capacity to combine comments on critical issues and commitment have always inspired me.

I would also like to thank Univ. Prof. Dr. Helmar Bergmann for making available the facilities and the infrastructure of IBMTP. Many thanks go also to Ing. Angela Taubek and Ing. Peter Stadlmaier for their help in the course of my experimental work.

Abbreviations

This is a list of common abbreviations used in this thesis.

BMTP	Biomedizinische Technik und Physik
DIN	Deutsches Institut für Normung
DN	Diagnose Nach
DV	Diagnose Vor
ESAK	Entrance Surface Air Kerma
ESD	Entrance Surface Dose
EU	European Union
HVL	Half Value Layer
IAEA	International atomic Energy Agency
ICRP	International Commission on Radiation
ICRU	International Commission on Radiation Units and Measurements
IEC	International Electrotechnical Commission
ISO	International Organisation for Standardisation
NMi	Netherlands Meetinstituut
NPL	National Physical Laboratory
PSDL	Primary Standards Dosimetry Laboratory
PTB	Physikalisch-Technischen Bundesanstalt
PTW	Physikalisch-Technische Werkstätten
RQA	Radiation Qualities based on a phantom made up of an aluminium Added filter
RQR	Radiation Qualities in Radiation beams emerging from the x-ray source assembly

Contents

1. INTRODUCTION	1
2. THE PRODUCTION OF X-RAYS	4
2.1. INTRODUCTION	4
2.2. INTERACTIONS PRODUCING X-RAYS	5
2.2.1. The continuous spectrum	7
2.2.2. Characteristic x-rays	9
2.3. ATTENUATION OF X-RAYS	12
2.4. INTERACTION ABSORBING X-RAYS	13
2.4.1. Rayleigh (coherent) scattering	13
2.4.2. Photoelectric effect	14
2.4.3. Compton effect (incoherent scattering)	16
2.4.4. Total attenuation coefficient	18
2.4.5. Summary of photon interactions	22
2.5. MODELS FOR THE GENERATION OF X-RAYS	23
2.5.1. Ideal spectrum (Kramers)	24
2.5.2. Birch and Marshall model	26
2.5.3. XCOMP5R model	27
2.5.4. Monte Carlo calculation	38
2.6. THE X-RAY TUBE	39
2.6.1. Components of the x-ray tube	40
2.7. FACTORS AFFECTING THE X-RAY SPECTRUM.	46
2.7.1. Tube current	46
2.7.2. Time of exposure	47
2.7.3. Tube voltage	47
2.7.4. Waveform of tube voltage	47
2.8. FILTRATION OF X-RAYS	49
2.8.1. Effect of filtration on spectral output	50
2.8.2. Sources of filtration	51
2.8.3. Legal requirements	53

3. SIMULATION OF THE EFFECT OF ANODE SURFACE ROUGHNESS ON DIAGNOSTIC X-RAY SPECTRA	57
3.1. INTRODUCTION	57
3.2. MEASUREMENT OF SURFACE PROFILES FOR ANODE SAMPLES	58
3.3. ANODE SURFACE PROFILE	61
3.4. DETERMINATION OF SURFACE ROUGHNESS	67
3.5. X-RAY PRODUCTION IN ROUGH ANODES	68
3.6. SIMULATION OF X-RAY SPECTRA	69
3.7. ADDITIONAL TUNGSTEN ABSORBER	74
3.8. SIMULATED X-RAY SPECTRA	74
3.9. KERMA YIELD	76
3.10. EFFECT OF SURFACE ROUGHNESS ON THE FIRST HALF-VALUE- LAYER	77
3.11. VARIATION OF THE MEAN PHOTON ENERGY	78
3.12. DISCUSSION	80
 4. DETERMINATION OF TOTAL FILTRATION USING A SPECTRAL MODEL AND ATTENUATION CURVES.....	 83
4.1. INHERENT FILTRATION AS A PARAMETER FOR THE CHARACTERISATION OF X-RAY UNITS	83
4.2. EXISTING METHODS FOR THE DETERMINATION OF TOTAL FILTRATION	84
4.2.1. X-ray spectrometry	84
4.2.2. The extrapolation method	85
4.2.3. The comparison method	86
4.2.4. The dual detector method	87
4.2.5. The K-edge filter method	87
4.2.6. The homogeneity coefficient method	88
4.2.7. The HVL method	89

4.3. A FIT METHOD FOR THE DETERMINATION OF TOTAL FILTRATION USING A SPECTRAL MODEL	91
4.3.1. Measurement of attenuation curves	93
4.3.2. Measurement of tube voltage	102
4.3.3. Fitting process	105
4.4. EXPERIMENTAL RESULTS	116
4.4.1. Determination of total filtration using the HVL method	117
4.4.2. Determination of total filtration using the fit method.	120
4.5. SENSITIVITY OF FIT RESULTS WITH INPUT PARAMETERS	127
4.7.1. Influence of anode angle.	127
4.7.2. Influence of kVp	128
4.7.3. Influence of voltage ripple	130
4.6. CALCULATION OF ENTRANCE SURFACE DOSE FROM THE FIT PARAMETERS.	131
4.7. DISCUSSION	134
 5. CONCLUSION	 144
 REFERENCES	 149
 ANNEX	 A-1

1. INTRODUCTION

The widespread use of x-rays for medical diagnosis ensures that diagnostic medical radiology represents by far the most significant man-made source of exposure to ionising radiation for the populations. In view of the significant benefits to patients from properly conducted medical exposures, the principal concern in radiological protection is the reduction of unnecessary exposures. Guidance levels or reference doses have been recommended by various organizations as a means of patient dose reduction as the European Union [EU97] and in the Basic Safety Standards issued by the International Atomic Energy Agency [IAEA96]. These are regarded as a tool for optimisation and dose minimisation, and are based on the results of patient dose surveys. Various dosimetric quantities have been specified for that purpose. Regular patient dose surveys in hospitals are an integral part in this process of dose minimisation.

Optimisation also involves patient dosimetry measurements. To achieve optimum radiation conditions for the examinations the x-ray output should be determined on installations followed by tests at intervals thereafter. The most complete specification of an x-ray field is given by the spectral distribution of the photon fluence. Since the spectrometry of x-ray spectra is a demanding task, radiation qualities are often expressed in terms of the x-ray the first and the second Half-Value Layer (HVL) for a given tube voltage. However, due to differences in the design and the age of x-ray tubes in terms of anode angle, anode roughening and inherent filtration, two radiation qualities produced at a given x-ray tube voltage and having the same first half value layer can still have quite different spectral distributions.

In diagnostic units some minimum photon attenuation by the absorbing materials between the anode and beam exit is mandatory to reduce radiation dose to the patient from the low energy x-rays in the spectrum. Some additional filters are introduced to achieve a total filtration of an equivalent in aluminium of typically

2.5 mm. This minimum filtration is required by international recommendations [ICRP82]. Besides, the attenuation of the x-rays in the anode material itself also contributes to filtration. The x-rays produced by electrons slowed down in the anode encounter some attenuation in the anode material depending on the anode angle and the beam direction. Hence, the total filtration includes both the attenuation of the x-rays in the anode and in all other materials being passed until exiting at the tube diaphragm.

The condition of the anode surface and the deposition of sputtered tungsten in the tube envelope have also been made responsible for an increased effective inherent filtration (see e.g. Ardran and Crooks [Ar72]). Tungsten deposits on the inner side of the tube are found to be much less than 1 μm in thickness [St86, Na88] and consequently should give little contribution to attenuation. Less data are available on the influence of anode roughness on spectra and spectral parameters. Nagel [Na88] has determined experimentally variations in the HVL of up to 0.5 mm Al at 80 kV and 2.5 mm Al filtration due to anode roughness. However, a larger range of roughness, due to tube ageing, can be encountered in x-ray tubes. The purpose of this work was therefore first to simulate x-ray spectra obtained with anodes of varying degree of surface roughness to obtain better data on the influence of anode surface roughness on the spectral outcome of clinical x-ray tubes and the variation of spectral parameters as HVL or mean photon energy. The bases for this simulation are anode surface profiles and data for surface roughness obtained by measurement for anode samples from decommissioned clinical x-ray tubes.

Total filtration initially is specified and tested by the manufacturer but is variable depending on the state of the anode surface. Since in general the anode surface deteriorates with tube usage the total filtration will increase. From this point of view it is also interesting to obtain information on the actual total filtration of an x-ray tube assembly. Nagel [Na88] showed that the HVL method, which is the most commonly used for the determination of the filtration, and recommended by the currently applicable standard [ISO97], allows only a rough estimation of the filtration and could lead typically to errors that can reach $\pm 30\%$ mostly due to the unknown spectral distribution of the x-rays and the variability of radiation quality with the continuing use of the x-ray tubes. Since HVL is the most widely used spectral parameter describing radiation quality it was the second objective in this work to study the implications of a varying total inherent filtration on HVL and the methods for its determination. It was an incentive to devise and evaluate a new method for the determination of total filtration

exploiting the effects of anode surface deterioration. This method is based on the use of a spectral model and attenuation curves.

A further benefit in carrying out the method described in this work will deal with results through which patient doses can be assessed in hospitals. The determination of the total filtration from accurate measurements of kerma output and kilovoltage, and using the code XCOMPW [No97] would facilitate an assessment of patient doses in radiological x-ray examinations.

2. *THE PRODUCTION OF X-RAYS*

2.1. INTRODUCTION

X-rays are produced whenever electrons interact with matter, with the conversion of some of their kinetic energy into electromagnetic radiation. The use of x-rays has developed mainly in two fields. In medicine, x-rays have either been applied in diagnostic imaging using the transmitted x-rays or in radiotherapy transferring energy to the human tissues by the absorption of x-rays. In contrast, x-ray diffraction, based on the scattering of x-rays, is a method of choice for studying atomic and molecular structure of matter.

The present work is restricted to diagnostic radiology where x-rays with photon energies of up to 150 keV are used. Essential components of any x-ray system are an electron source, an evacuated path for electron acceleration, a target electrode, and an external voltage source to accelerate the electrons. The x-ray tube contains the electron source and a target within an evacuated glass or ceramic-metal envelope; the tube housing provides shielding and cooling by a surrounding oil-bath for the tube. The tube housing further provides for adequate electric isolation and mechanical protection. The radiation is passing the exit window and is finally collimated by an external variable beam restriction device.

The generator supplies all voltages required for the operation of the x-ray tube. These are in particular the heating current for the cathode filament controlling the tube current and the high voltage source for the acceleration of the electrons. In this way the generator permits the control of the x-ray output through the selection of tube voltage,

tube current and exposure time. These components work together to create a beam of known intensity, penetrability and spatial distribution of x-ray photons necessary for medical imaging.

In this section, the important aspects of processes producing x-rays, absorption of x-rays, the characteristics of the x-ray beam, x-ray spectra and the influence of the various components in an x-ray unit are described.

2.2. INTERACTIONS PRODUCING X-RAYS

Electrons as all charged particles interact with matter and lose their energy via excitation, ionisation and/or radiative losses. These types of interactions become dominant depending on the impact parameter b versus the atomic radius a , as shown in figure 2.1. [At86].

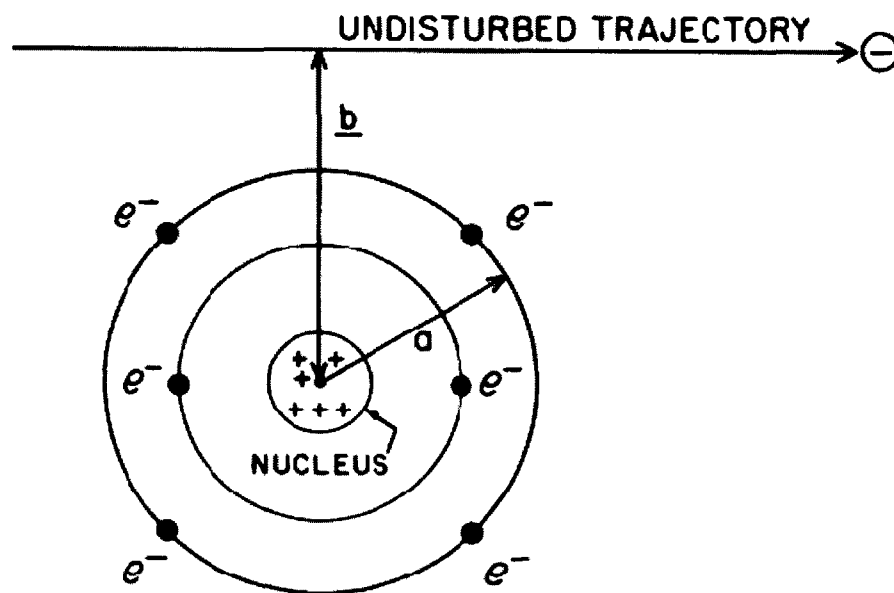


Figure 2.1. Important parameters in charged particle collisions with atoms: a is the atomic radius, b is the impact parameter.

- **Soft collisions ($b \gg a$)**

When a charged particle passes an atom at a considerable distance, the influence of the particle's Coulomb force field affects the atom as a whole, thereby distorting it,

exciting it to a higher energy level, and sometimes ionising it by ejecting a valence-shell electron. The net effect is the transfer of a very small amount of energy (a few eV) to an atom of the absorbing medium. Because large values of b are clearly more probable than are near hits on individual atoms, soft collisions are by far the most numerous type of charged particle interaction, and they account for roughly half of the energy transferred to the absorbing medium.

- **Hard (or “knock-on”) collisions ($b \sim a$)**

When the impact parameter b is of the order of the atomic dimensions, it becomes more likely that the incident particle will interact primarily with a single atomic electron, which is then ejected from the atom with considerable kinetic energy. Such electrons are called delta (δ) rays. In the theoretical treatment of the knock-on process, atomic binding energies are neglected and the atomic electrons are treated as free. δ -rays are energetic enough to undergo additional Coulomb-force interactions on their own. Thus a δ -ray dissipates its kinetic energy along a separate track (called a “spur”) from that of the primary charged particle. Although hard collisions are few in number compared to soft collisions, the fractions of the primary particle’s energy that are spent by these two processes are generally comparable [At86].

Whenever an inner-shell electron is ejected from an atom by hard collision, characteristic x-ray and/or Auger electrons will be emitted. Thus some of the energy transferred to the medium may be transported some distance away from the primary particle track by these carriers as well as by the δ -rays.

- **Coulomb-force interactions with the external nuclear field ($b \ll a$)**

When the impact parameter of a charged particle is much smaller than the atomic radius, the Coulomb-force interaction takes place mainly with the nucleus. In all but 2-3% of such encounters, the electron is scattered elastically and does not emit an x-ray photon or excite the nucleus. It loses just the significant amount of kinetic energy necessary to satisfy conservation of momentum for the collision. Hence this is not a mechanism for the transfer of energy to the absorbing medium, but it is an important means of deflecting electrons. It is the principal reason why electrons follow very

tortuous paths, especially in high Z media, and why electron backscattering increases with Z . The differential elastic-scattering cross section per atom is proportional to Z^2 [At86].

In the other 2-3% of the cases in which an electron passes near the nucleus, an inelastic radiative interaction occurs in which an x-ray photon is emitted. The electron is not only deflected in this process, but also transfers a significant fraction (up to 100%) of its kinetic energy to the photon, slowing down in the process. Such x-rays are referred to as Bremsstrahlung. This interaction has also a differential atomic cross section proportional to Z^2 , as is the case for nuclear elastic scattering.

2.2.1 The continuous spectrum

A detailed theoretical description of the bremsstrahlung production is given in paragraph 2.5.1, but the following comment is helpful to describe the shape of the continuous spectrum.

When electrons hit a thick target (anode) they will be slowed down gradually losing their energy mostly by soft and hard collisions. The amount of energy lost by each electron during the bremsstrahlung process and thus, the energy of the x-ray that is produced, is determined by the impact parameter, i.e. the distance between the electron and the nucleus, as the Coulomb force of attraction varies strongly with distance. At very large distances from the nucleus, the coulombic force is weak, resulting in little acceleration of the electron and consequently, the creation of low-energy x-rays. There is a high probability of such an interaction because the cross-sectional area of the annulus defining a coulomb field increases with increased radial distance. If, however, an electron passes in closer distance to the nucleus, the energy of the x-rays increases, resulting also in a higher energy loss of the electron. There is a lower probability of high-energy x-ray emission due to the smaller cross sectional area presented to the impinging electrons. The highest x-ray energy will be obtained when all of the kinetic energy of the electron is converted to a bremsstrahlung photon. The probability for this process is extremely low, because of the very small cross-sectional area around the nucleus where such interactions will happen [Ev55]. Figure 2.2 illustrates the concept of

impact distance and the forces exerted upon the electron by the positive charge of the nucleus.

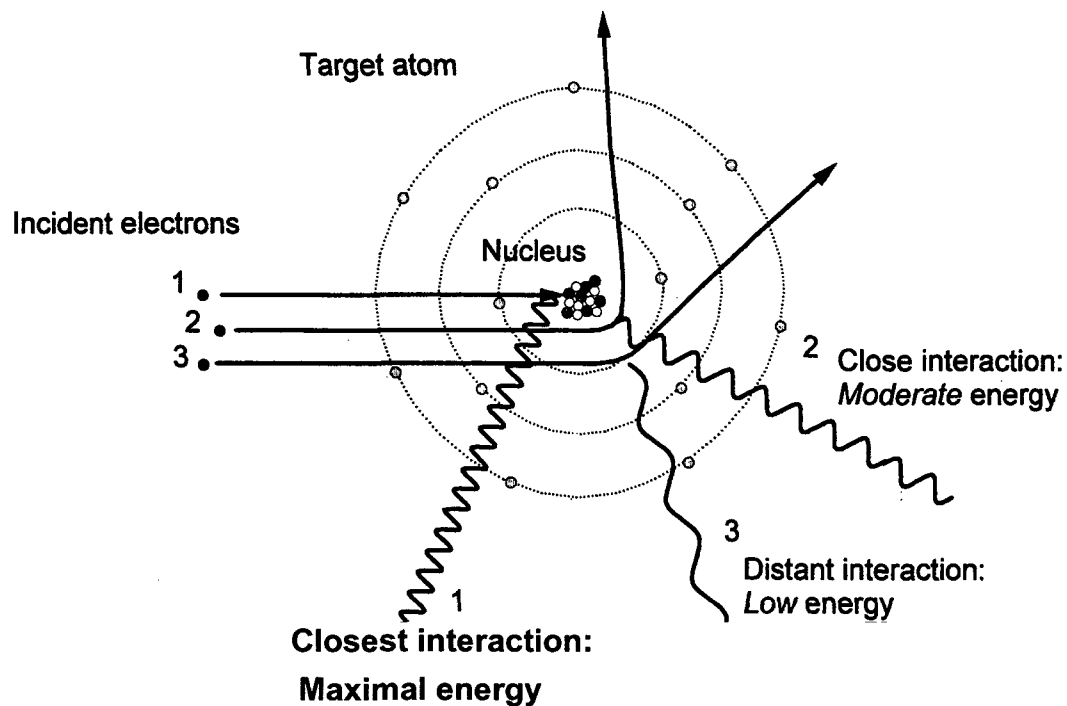


Figure 2.2. Creation of bremsstrahlung distribution. Electrons interact with an atomic nucleus of the target atom via coulombic attraction, causing a conversion of kinetic energy to electromagnetic (x-ray) energy.

A bremsstrahlung spectrum depicts the number of x-ray photons as a function of their energy. The unfiltered bremsstrahlung spectrum, illustrated in figure 2.3(a), demonstrates a wedge shaped relationship between the number of photons and the x-ray energy. The highest x-ray energy obtained is determined by the potential applied between the electrodes in the x-ray tube. However, before the x-rays emerge from the x-ray tube, the intensity distribution will be modified in two ways. First, x-rays produced deep in the anode will be attenuated before reaching the surface of the anode and secondly x-rays will be attenuated while penetrating the window of the x-ray tube and any added filter. Both processes will reduce the intensity of the low energy radiation more than that of the higher energies, yielding the result of the filtered bremsstrahlung spectrum shown in figure 2.3 (b).

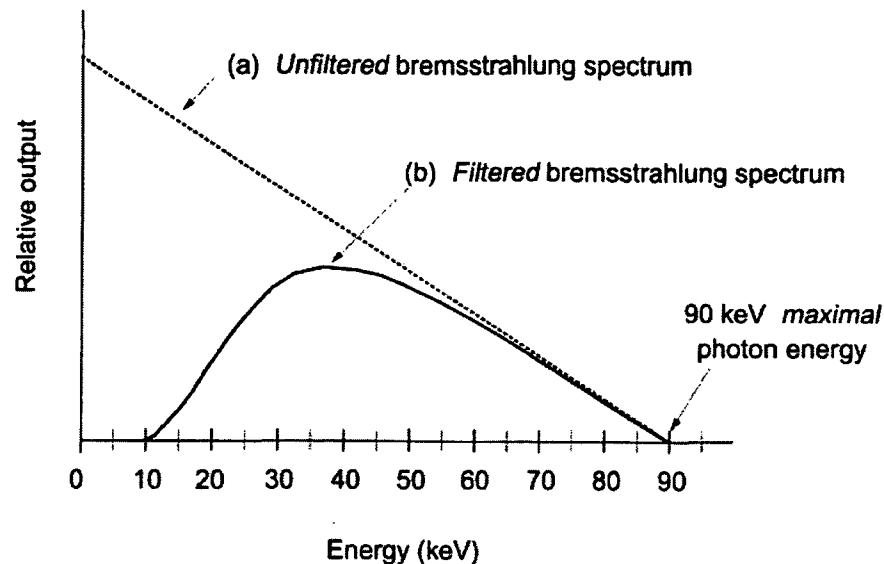


Figure 2.3. The distribution of energies in a bremsstrahlung x-ray spectrum produced by the interaction of 90 keV electrons.

2.2.2 Characteristic x-rays

Superimposed on the continuous spectrum, there may be a set of line spectra that result from electron transitions in the atomic shell. Vacancies in the inner shells of an atom are produced by two mechanisms in an anode. First, an incoming electron colliding with a bound orbital electron can ionise the atom, and secondly the bremsstrahlung produced could be absorbed in the anode material by a photoelectric interaction thus also producing a vacancy in the shell.

A requirement for ionisation by a collision interaction of an electron is a sufficient kinetic energy to overcome the binding energy of the shell electron. Also the photon energy has to exceed the binding energy of the electron when the atom is ionised by a photoelectric interaction. The probability of this happening is greatest for the innermost shells.

An electron from the higher energy level falling into an inner shell then fills this vacant energy level and the excess energy is emitted as an x-ray photon. Thus, if for example the vacancy is created in the K shell, an electron falling from the L shell, the M shell or outer shell may fill it. Even a free electron may fill the vacancy but the most likely transition is from the L shell (figure 2.4).

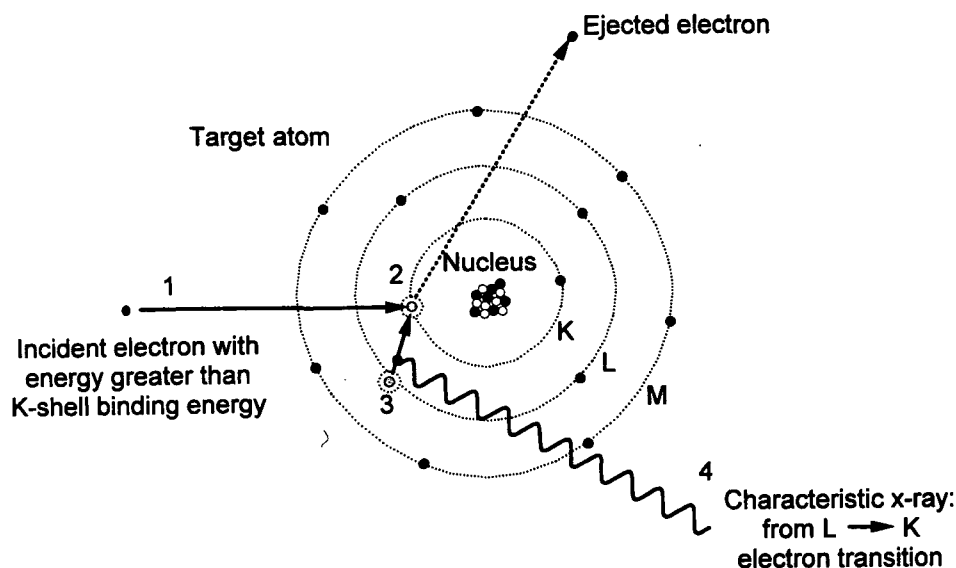


Figure 2.4. Generation of characteristic x-rays in a target occurs in the following sequence:

1. incident electron impacts on K-shell orbital electron,
2. orbital electron is ejected with energy equal to the difference of the incident electron energy from the binding energy of the K-shell electron,
3. cascading L shell electron fills vacancy, and
4. emission of a characteristic K_{α} x-ray photon.

As orbital electrons must occupy well-defined energy levels and these energy levels are different for different elements, the x-ray photon emitted when an electron moves from one energy level to another has an energy equal to the difference between the two energy levels in that atom and hence is characteristic for that element. In the case of tungsten, an L shell electron filling the K shell vacancy results in a characteristic x-ray energy of:

$$E_{\text{K-shell}} - E_{\text{L-shell}} = 69.5 \text{ keV} - 10.2 \text{ keV} = 59.3 \text{ keV}$$

A variety of energy transitions occurs from adjacent and nonadjacent shells in the atom, giving rise to several discrete energy peaks superimposed on the continuous bremsstrahlung spectrum. The designation of characteristic x-rays first gives the shell capturing the electron followed by a subscript as α , β , etc., e.g. K_{α} . A subscript α refers to a transition from an adjacent shell (e.g., $L \rightarrow K$ or $M \rightarrow L$), the subscript β to transitions from the first non-adjacent shell (e.g., $M \rightarrow K$ or $N \rightarrow L$), etc. A K_{α} x-ray is therefore less energetic than a K_{β} x-ray. Also, within electron shells discrete energy

states are designated with subscripts 1, 2, and 3, indicating the fine energy splitting that could be seen in the total x-ray spectrum.

In the case of tungsten, the prominent lines in the total spectrum arise from the $K_{\alpha 1}$, $K_{\alpha 2}$, $K_{\beta 1}$ and the $K_{\beta 2}$ transitions as shown in figure 2.5. Characteristic x-rays other than K x-rays are not relevant in diagnostic imaging because they are almost entirely attenuated by the tube window and added filtration. The important target materials used for production of x-rays in medicine are tungsten, molybdenum and rhodium. Tables 2.1a and 2.1b list their electron shell binding energies and K shell characteristic x-ray energies.

Table 2. 1. a. Electron binding energies in keV of common x-ray tube target materials [Jo84].

Electron shell	Tungsten	Molybdenum	Rhodium
K	69.5	20.0	23.2
L	12.1; 11.5; 10.2	2.8; 2.6; 2.5	3.4; 3.1; 3.0
M	2.8; 1.9	0.5; 0.4	0.6; 0.2

Table 2. 1. b. K-shell characteristic X-ray energies (keV) [Jo84].

Shell transition	Molybdenum	Tungsten	Rhodium
$K_{\alpha 1}$	59.32	17.48	20.22
$K_{\alpha 2}$	57.98	17.37	20.07
$K_{\beta 1}$	67.2	19.61	22.72
$K_{\beta 2}$	69.09	19.96	23.17

Characteristic K x-rays will only appear in the spectrum when the energy of the electrons impinging on the target exceeds the binding energy of the K shell electrons. With tungsten anodes the acceleration potentials must therefore be greater than 69.5 kVp to produce K shell x-rays. Figure 2.5 shows an example for a total x-ray spectrum, bremsstrahlung plus characteristic radiation for a tungsten target.

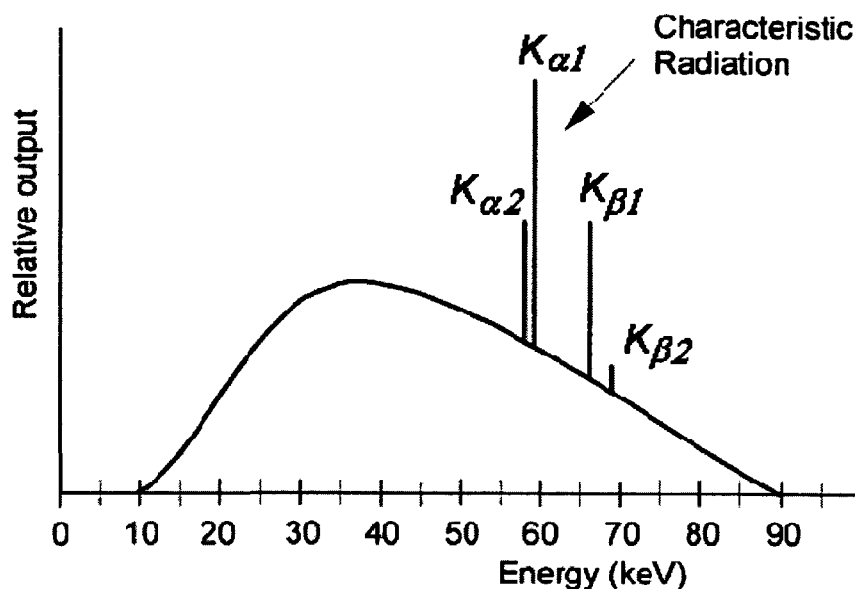


Figure 2.5. Total spectrum of x-ray tube with tungsten target, (at a potential of 90 kVp bremsstrahlung plus characteristic radiation).

2.3. ATTENUATION OF X-RAYS

An attenuation of x-rays occurs at any position within the x-ray beam in a radiodiagnostic procedure. X-rays produced in the slowing down process of the electrons in the target material will undergo attenuation before reaching the surface of the anode. X-rays emerging from the target surface will first be filtered by tube envelope and other materials contained in the tube housing. Then additional aluminium or copper absorbers are applied to adapt and optimise the radiation quality before entering the patient. The patient also must be regarded as a filter changing the x-ray spectrum. Continuing in beam direction the patient table, the grid and the ionisation chambers for the automatic exposure control reduce x-ray intensities by photon attenuation. Finally, the detection of x-rays in an imaging detector is based on the attenuating properties of the detector. Hence, the characteristics of x-ray attenuation in a photon range typical for diagnostic examinations are summarized here.

The intensity $I(x)$ of a narrow beam of photons with energy $h\nu$, attenuated by an attenuator of thickness x , is given as:

$$I(x) = I(0) \cdot e^{-\mu(h\nu, Z)x}$$

where $I(0)$ is the original intensity of the unattenuated beam and $\mu(h\nu, Z)$ is the linear attenuation coefficient that depends on photon energy $h\nu$ and attenuator atomic number Z . A common unit for the linear attenuation coefficient is cm^{-1} with x then taken correspondingly in units of cm . The linear attenuation coefficient depends also on the density ρ of the attenuating medium. To obtain a quantity not depending on density the mass attenuation coefficient μ/ρ is defined.

The mass attenuation coefficient μ/ρ relates to the atomic attenuation cross-section ${}_a\sigma$, and electronic attenuation cross-section ${}_e\sigma$ through the following relationships [Ev55],

$$\frac{\mu}{\rho} = \frac{N_A \cdot {}_a\sigma}{A} = \frac{N_A Z \cdot {}_e\sigma}{A}$$

where Z and A are the atomic number and atomic mass number of the attenuator, respectively. Typical units for the mass attenuation coefficient and the atomic and electronic cross sections are: cm^2/g , cm^2/atom , and $\text{cm}^2/\text{electron}$, respectively.

2.4. INTERACTIONS ABSORBING X-RAYS

For diagnostic x-rays with photon energies of up to 150 keV the three most relevant types of photon interactions are: 1) Rayleigh scattering, 2) photoelectric absorption and 3) Compton scattering.

2.4.1 Rayleigh (coherent) scattering

In Rayleigh scattering (also referred to as elastic scattering), the photon is absorbed by the atom as an atomic oscillator and reemitted instantaneously. The event is elastic in the sense that the photon loses essentially none of its energy with the atomic

mass taking up the recoil energy for the conservation of momentum. The scattered photon is usually emitted in a small angle in forward direction. The scattering attenuation coefficient σ_R is proportional to $Z/(h\nu)^2$. Hence at diagnostic photon energies this interaction contributes little to the total attenuation in human tissues, typically accounting for less than 5% of interactions. Since the attenuation at low photon energies for high Z material is dominated by the photoelectric effect the contribution of Rayleigh scattering there is even less.

2.4.2 Photoelectric effect

Photoelectric absorption is the process in which a photon impinging on an atom transfers its entire energy to an inner (e.g. K or L) shell electron of the atom. This electron (photoelectron) is ejected from the atom. The kinetic energy of the ejected photoelectron KE is given as:

$$KE = h\nu - BE,$$

where $h\nu$ is the incident photon energy and BE is the binding energy of the electron.

The resulting vacancy in the shell is filled by an electron from an outer orbit (with lower binding energies), leaving a vacancy in this outer orbit, which in turn is filled by another electron from an orbit even further away from the nucleus. The difference in binding energy set free in the transition of the electron from an outer shell to a shell closer to the nucleus results in the emission of characteristic radiation and/or Auger electrons as discussed in 2.2.2.

The atomic cross section for the photoelectric effect is approximately proportional to $Z^4/(h\nu)^3$, while the mass attenuation coefficient τ/ρ is proportional to $Z^3/(h\nu)^3$.

In addition to a steady decrease of τ/ρ with increasing photon energy, τ/ρ also shows sharp discontinuities when $h\nu$ equals BE for a particular electronic shell of the attenuator. These discontinuities, called absorption edges reflect the fact that for $h\nu < BE$

photons cannot undergo a photoelectric effect with electrons in that particular shell, while for $h\nu \geq BE$ this process is possible. The contribution to the attenuation of x-rays due to the photoelectric effect depends significantly on the atomic composition of the absorber resulting in rather little effect in soft tissues but dominating the attenuation for higher Z-materials. The K-electron binding energy for tungsten is 69.5 keV.

The increase in attenuation at the K-absorption edge plays an important role in the selection of imaging detectors as the average photon energies in typical x-ray spectra used in imaging are in the same energy range as the binding energies of elements as caesium (Cs), iodine (I), gadolinium (Gd) and barium (Ba), which are used for the detection of x-rays in screen phosphors, scintillators and storage phosphors. It can then happen that an absorber containing elements with high Z shows less absorption than phosphors with a K-edge below the most frequent x-ray energies in the spectrum. The K-edge of iodine is also considered in the optimisation of imaging parameters, as iodine is frequently used in contrast agents (figure 2.6). Also the K-edge of the anode material will show up in the x-ray spectrum due to the attenuation of the bremsstrahlung continuum in the anode itself.

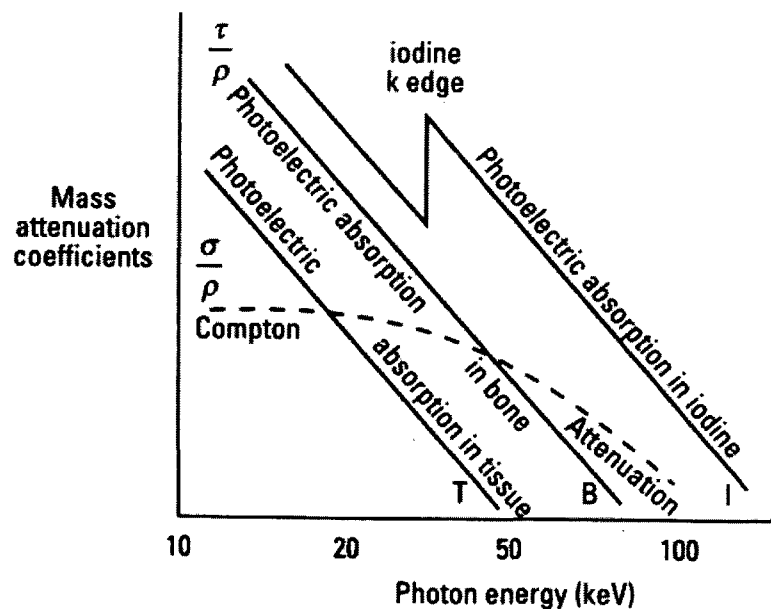


Figure 2.6. Photoelectric (τ/ρ) and Compton (σ/ρ) mass attenuation coefficients of materials of different atomic numbers at different photon energies. K-edge for iodine is 33keV [Fa97].

2.4.3 Compton effect (incoherent scattering)

The Compton effect (also called inelastic scattering or incoherent scattering) represents a photon interaction with a free and stationary orbital electron, i.e. $h\nu \gg BE$. The electron is ejected from the atom and an x-ray photon of lower energy is scattered from the atom. Compton scattering results in the ionisation of the atom and a division of the incident photon energy between the scattered photon and ejected electron. σ_C denotes the Compton linear attenuation coefficient, which is proportional to the number of electrons per unit volume. The number of electrons per mass unit depends on Z/A . Z/A , at least for elements present in human tissues, is fairly constant except for Hydrogen. In a first approximation the number of electrons per unit volume is therefore proportional to the physical density (mass per unit volume) of the material and nearly independent of the atomic composition of the material. σ_C decreases only slightly over the range of photon energies encountered in diagnostic radiology, and may be thought of as being very approximately proportional to $1/h\nu$.

The incident photon with energy $h\nu$ loses part of its energy to the recoil (Compton) electron and is scattered as a photon with energy $h\nu'$ through a scattering angle θ as shown schematically in figure 2.7. Angle ϕ represents the angle between the incident photon direction and the direction of the recoil electron.

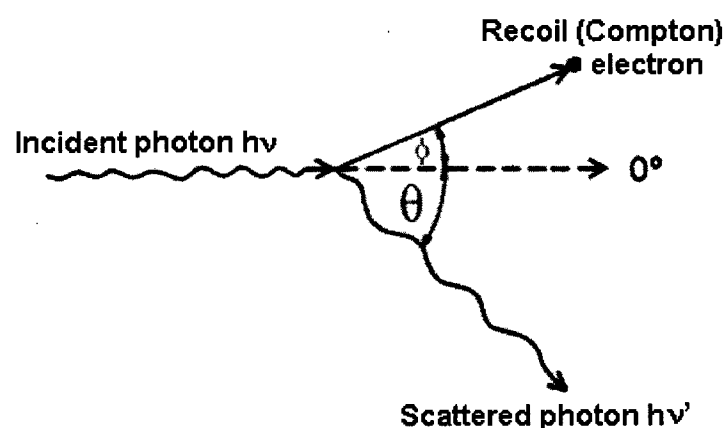


Figure 2.7. Schematic diagram for Compton scattering. Incident photon with energy $h\nu$ interacts with a loosely bound (essentially free) atomic electron. The electron is ejected from the atom as a recoil (Compton) electron with kinetic energy KE and a scattered photon with energy $h\nu' = h\nu - KE$ is produced.

From conservation of energy and momentum in the Compton process, the energy of the scattered photon $h\nu'$ can be derived:

$$h\nu' = h\nu \cdot \frac{1}{1 + \varepsilon \cdot (1 - \cos \theta)}$$

where ε is the normalised incident photon energy, i.e. $\varepsilon = h\nu/(m_e c^2)$.

It is important to note that for photon energies used in diagnostic radiology the energy loss of the scattered photon is rather small. The photon energies of the secondary radiation field produced by Compton scatter therefore are very similar to the primary x-ray energies (figure 2.8) [At86]. The scattered radiation is an important factor in imaging as the image quality depends on the amount of scattered radiation received by the image detector and furthermore, is the main source of radiation exposure to the medical staff in radiological examinations.

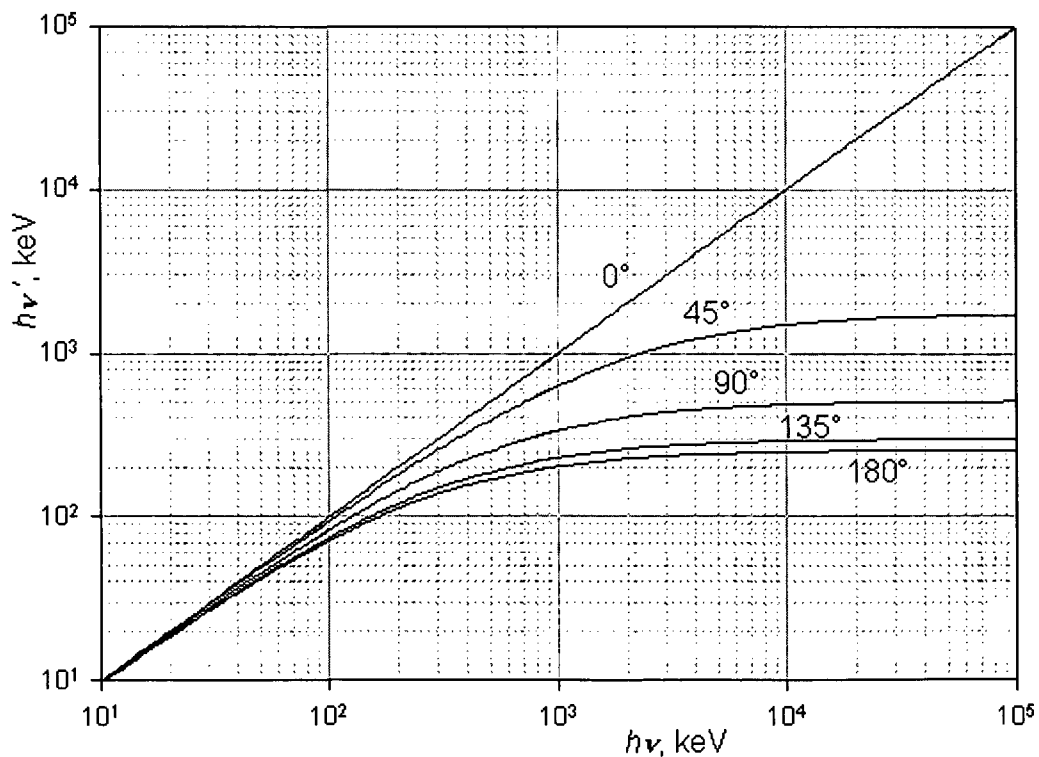


Figure 2.8. Energy $h\nu'$ of inelastically scattered photon vs. initial energy $h\nu$ for various scattering angles. Note that diagnostic x-rays have photon energies below 150 keV.

2.4.4 Total attenuation coefficient

For a given photon energy and atomic number Z of the absorber, the linear attenuation coefficient μ is given as the sum of coefficients for the individual photon interactions,

$$\mu = \tau + \sigma_R + \sigma_C$$

where τ , σ_R and σ_C denote the linear attenuation coefficients for photoelectric effect, Rayleigh- and Compton scattering, respectively. Similarly, the individual components of the mass attenuation coefficients, when summed up, result in the total mass attenuation coefficient as:

$$\mu/\rho = \tau/\rho + \sigma_R/\rho + \sigma_C/\rho$$

To compare and stress the attenuation characteristics of diagnostic x-rays the attenuation coefficients in the photon energy range from 10 keV to 150 keV for three materials typical for the use of x-rays in diagnostic radiology, i.e. soft tissue, aluminium and tungsten, are discussed below. Only the photoelectric effect and the Compton effect as the two dominant interactions are considered.

First, the attenuation of soft tissue is considered. Figure 2.9 shows the mass attenuation coefficient of soft tissue together with two typical x-ray spectra. Because the photoelectric coefficient is decreasing with photon energy and the Compton coefficient is fairly constant, one could find the photon energy where the attenuation coefficients of both interactions are equal. This energy is at about 30 keV for soft tissue (see figure 2.9a). It is evident that for the mammographic spectrum the photoelectric attenuation contributes more than Compton scattering to total absorption. Hence atomic composition of soft tissue has more influence on image contrast here. For most of the other radiological imaging procedures including computed tomography, x-ray spectra for which Compton scattering dominates photon absorption are used (see fig. 2.9b). At these photon energies image contrast will be relatively insensitive to differences in atomic composition but rather reflect tissue density. Bone tissue always gives some

contrast produced by photoelectric absorption due to the higher atomic numbers of calcium and phosphorus.

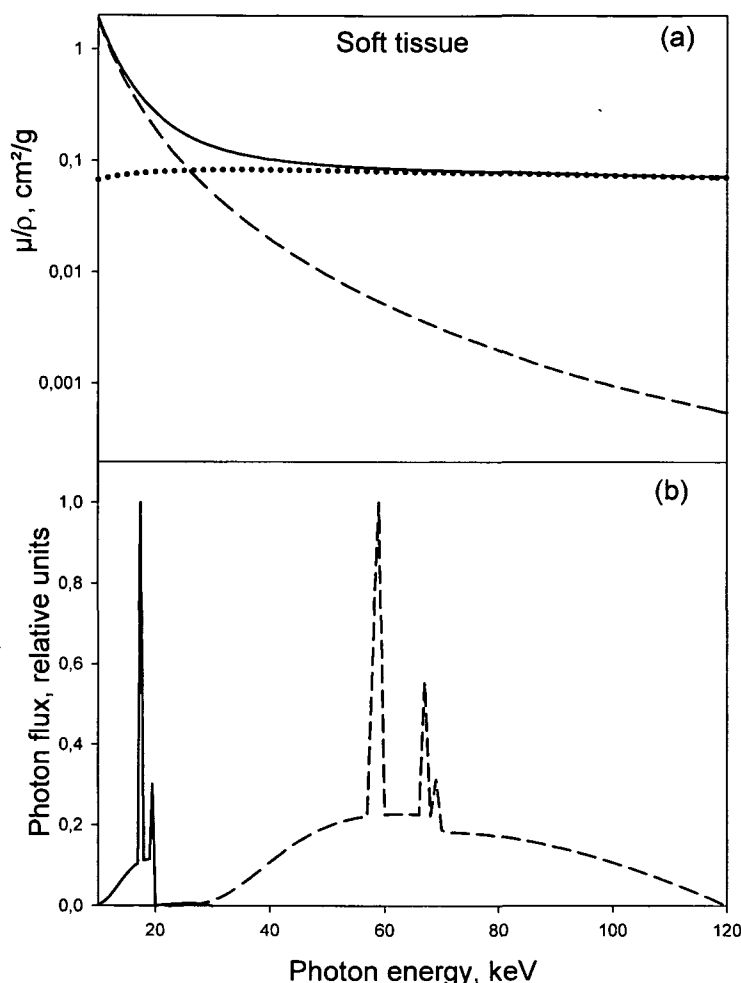


Figure 2.9. (a): Total mass attenuation coefficient μ/ρ (solid line) for soft tissue together with the photoelectric (dashed line) and the Compton effect (dotted line) [Be99]; (b): Spectra emerging from an x-ray tube with Mo-anode (30 μm Mo-filter, 30 kV) (solid line) and a W-anode (2.5 mm Al equiv. filtration, 120 kV) having passed through 20 cm of soft tissue (dashed line) [Bi79a].

With aluminium the photoelectric interactions predominate for energies up to 50 keV (see figure 2.10a). If used as filter, material aluminium will therefore preferentially remove lower energy photons. The spectrum is then shifted to higher photon energies giving higher half value layers and increased mean photon energies. This is demonstrated in fig. 2.10b for an x-ray spectrum obtained for 120 kV and standard conditions (2.5 mm inherent filtration) and an additional filtration giving a total of 4 mm Al. The mean photon energy then rises from 47.8 keV to 52 keV.

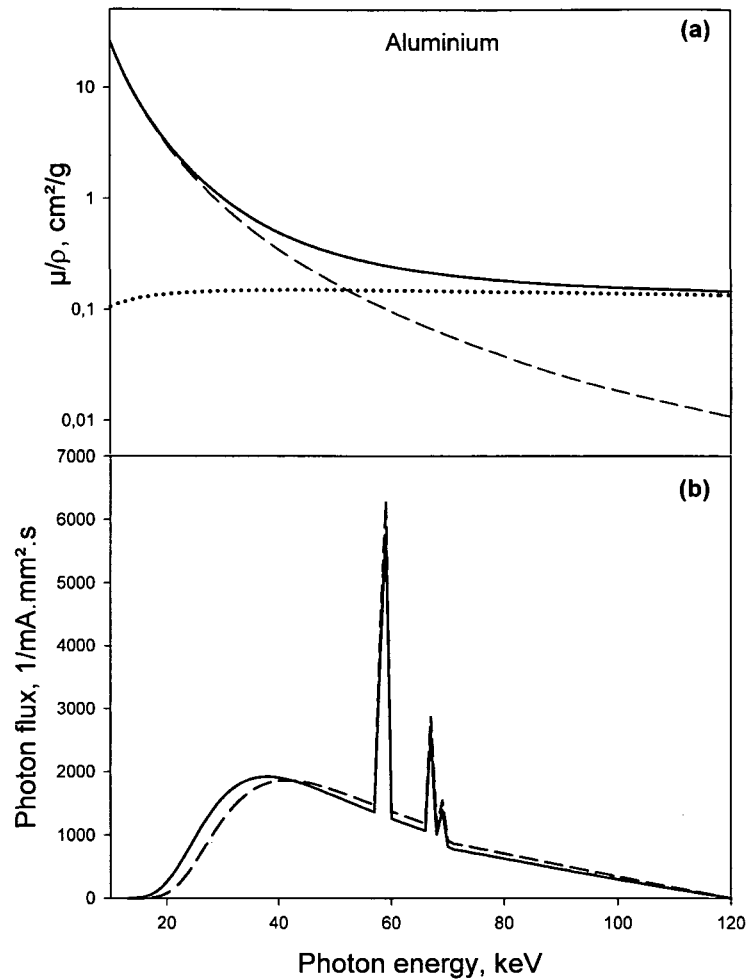


Figure 2.10. (a): Total mass attenuation coefficient μ/ρ for aluminium (solid line). The dashed line indicates the contribution of the photoelectric effect, the dotted line that of the Compton effect [Be99]. (b): Spectra emerging from an x-ray tube with 120 kV at 75 cm distance from the focus and 2.5 mm Al filtration (solid line) and 4 mm Al (dashed line) [Bi79a] .

The last example reflects the situation with high-Z absorbers, e.g. the anode material. Photons produced in a tungsten target and then traversing it are subjected to photon attenuation in the anode material. Attenuation in tungsten is dominant in the range of diagnostic energies (see fig. 2.11a). A typical property of the attenuation coefficient for tungsten is the K-edge at 69.5 keV, which is equal to the binding energy of the K-shell electrons in tungsten. Characteristic x-rays are produced as a secondary radiation enhancing those produced after ionisation of the atom by incident electrons. This characteristic radiation shows up in the spectral distribution (fig. 2.11b). The increased attenuation for photon energies above the K-edge can also be seen in the

spectral distribution as a marked decrease in x-ray intensities for photon energies above the K-edge.

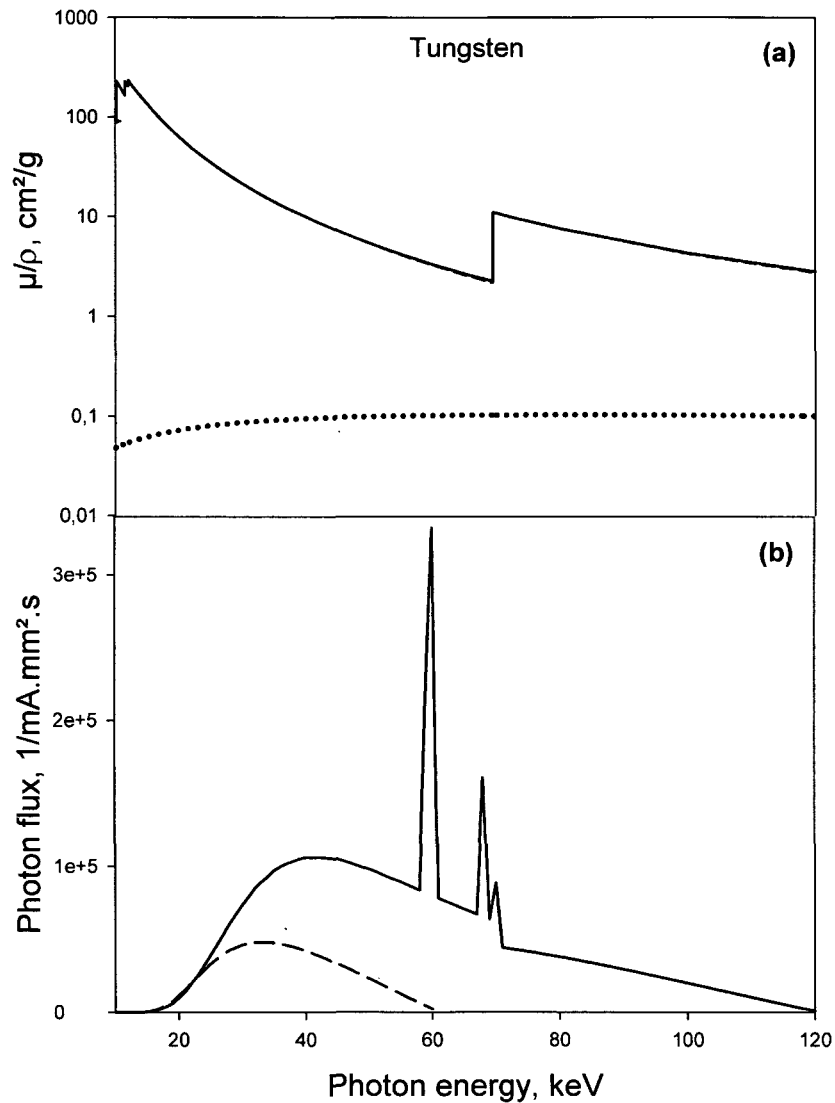


Figure 2.11. (a): Total mass attenuation coefficients μ/ρ for tungsten (solid line) with the contribution by the Compton effect (dotted line). The total coefficient practically resembles the coefficient for photoelectric absorption [Be99]. (b): X-ray spectra for 60 kV (dashed line) and 120 kV (solid line) at 75 cm distance and 2.5 mm Al filtration [Bi79a].

Finally, in figure 2.12 [Ev55] the predominance of photoelectric absorption and Compton scattering depending on photon energy and atomic number is shown (pair production is not relevant in this energy range).

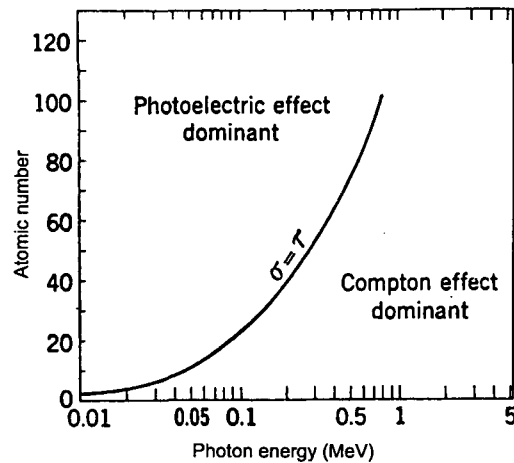


Figure 2.12. Regions of relative predominance of the two main forms of photon interaction with matter.

2.4.5 Summary of photon interactions

Table 2. 2. Main characteristics of photoelectric effect, Rayleigh scattering and Compton effect

	Photoelectric effect	Rayleigh Scattering	Compton effect
Photon interaction	with whole atom (bound electrons)	with bound electrons	with free electrons
Mode of photon interaction	Photon disappears	Photon scattered	Photon scattered
Energy dependence	$1/(h\nu)^3$	$1/(h\nu)^2$	decreases with energy
Attenuation Coefficient	τ	σ_R	σ_C
Particles Released	Photoelectron	None	Compton (recoil) Electron
Atomic coefficient dependence on Z	${}_a\tau \propto Z^4$	${}_a\sigma_R \propto Z^2$	${}_a\sigma_C \propto Z$
Mass coefficient dependence on Z	$(\tau/\rho) \propto Z^3$	$(\sigma_R/\rho) \propto Z^2$	independent
Subsequent effect	characteristic x-ray, Auger effect	none	characteristic x-ray, Auger effect
Significant energy Region	0 to 0.5 MeV	< 1 MeV	around 1 MeV

2.5. MODELS FOR THE GENERATION OF X-RAYS

Since the determination of the spectral distribution of x-rays particularly in the diagnostic energy range is difficult and cumbersome, global spectral parameters have been in use for a long time to characterise the properties of the x-ray field with respect to imaging and patient dosimetry. Such spectral parameters describing the radiation quality of the x-rays, as mean photon energy, first or second half-value layers, are well-established quantities for the characterisation of the x-ray tube radiation output. While these parameters are useful in many situations in dosimetry and radiation metrology, data on x-ray spectra are of interest in a more detailed evaluation of radiation detectors and in patient dosimetry.

As an example, dose requirements can be studied when using a new kind of intensifying screens [Ha84], or the absorption of screens and also the signals in x-ray detectors can be calculated [Br82; No84]. The influence of the various parameters as anode angle, voltage ripple and transmission for various kinds of tissues on the image formation can be evaluated. The whole imaging process from absorption in the patient to absorption in the image detectors might be simulated and evaluated. X-ray spectra are also useful as an input in dosimetric calculations [De02, Me00a, Ca98].

Parameters as x-ray tube voltage and radiation beam quality are not necessarily satisfactory for a characterization with regard to imaging or dosimetry. Due to differences in the design and the age of x-ray tubes in terms of anode angle, anode roughening and inherent filtration, two x-ray beams produced with the same tube voltage and the same first half value layer still could have quite different spectral distributions [Se79].

The measurement of spectra in diagnostic radiology is made difficult by the high photon fluxes and the associated high-count rates in an energy-dispersive spectrometer. Further corrections have to be applied to the measured pulse height distributions according to the response of the detector. This is less demanding for monoenergetic spectra but for the unfolding of continuous x-ray spectra a precise measurement or a Monte-Carlo simulation of the energy response of the detector is required.

Therefore, the ability to simulate spectra with adequate accuracy can in many circumstances, help to minimise time, efforts and expenditures involved. The availability of desktop computing has created the opportunity for using this essential data in routine applications. Different authors have carried out simulations of x-ray spectra used in diagnostic radiology using analytical or Monte Carlo codes. This paragraph deals with some of them. A detailed description to one of them developed by Nowotny et al. [No85] is given as it was used in this work.

2.5.1 Ideal spectrum (Kramers)

The interaction of x-rays in a target would have to take into account (a) the paths of the electron into the target, (b) the change in direction at each interaction, (c) the chance of an energy loss by ionisations or excitations, and the chance of a radiation loss in each increment of path, (d) the direction of emission of the bremsstrahlung, and (e) its attenuation and scattering in emerging from the target. This is so complex that an analytical solution to the problem cannot be achieved. A first simplified model of these processes was given by Kramers [Kr23].

- **Thin target radiation:**

If one restricts the problem of bremsstrahlung production to a thin target with no electron suffering more than one collision on the average in passing through the target, then the problem can be solved. Simplified theory indicates that when a beam of electrons of kinetic energy E_1 strikes a thin target, the intensity of radiation in terms of energy fluence emitted in each energy interval from 0 to E_1 is constant giving a rectangular distribution (see figure 2.13).

- **Thick target radiation:**

A thick target may be considered as a number of thin targets superimposed. Thus, electrons with initial energy E_1 will, after passing through a thin layer of target, have energy E_2 and will then produce the spectrum corresponding to E_2 represented by insert b (figure 2.13). After passing through the next layer the electron will have energy

E_3 and produce spectrum c, etc. The total spectrum is then obtained by superposition of all the rectangular distributions (thin target spectra) for energies E_1, E_2, E_3, E_4, E_5 , etc. This total distribution is indicated by the dotted straight line XY (figure 2.13) and is given by Kramers [Kr23] as:

$$I(E) = CZ (E_{\max} - E) \quad \text{Kramers' formula}$$

where $I(E)$ is the energy fluence at energy E . In this equation E_{\max} is the maximum energy of the photons emitted and is also equal to the energy of the bombarding electron as it enters the target. C is a constant (2.76×10^{-6} per keV energy interval) and Z the atomic number of the target. The energy fluence has its maximum value of $C.Z.E_{\max}$ at $E=0$ and drops linearly to zero as E is approaching E_{\max} . Since the base OX and the altitude OY are both proportional to E_{\max} , the area under the dotted line, which represents the energy radiated as x-rays, is proportional to E_{\max}^2 . This triangular distribution is also called the *ideal spectrum*, as it does not consider any absorption within the target. The dashed lines A and B (figure 2.13) show such ideal spectra produced by the bombardment of a target with 60 and 100 keV electrons.

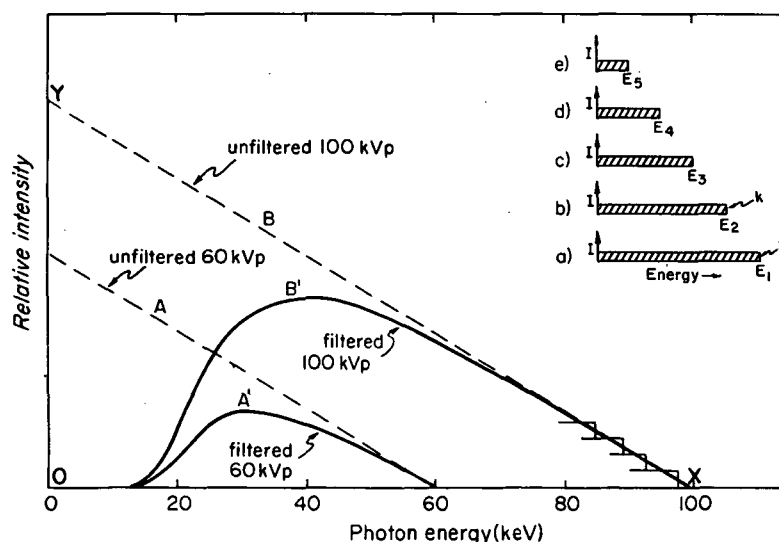


Figure 2.13. Relative energy (energy fluence) I , in each photon energy interval produced when a beam of monoenergetic electrons of energy E_1 bombards a thin target. Curves b, c, d and e are thin target intensity spectra similar to a , but for electron energies of E_2, E_3, E_4 and E_5 . The main diagram shows thick target spectra (dashed lines A and B) produced by the superposition of many thin target spectra when the target is bombarded with 60 and 100 keV electrons. The solid curves A' and B' are obtained taking into account the attenuation of 2 mm Al [Kr23].

Actual x-ray spectra do not perfectly resemble to the ideal spectrum, as one should take into account the effects of filtration of the beam by the inherent filtration of the tube and any added filter. Filtration removes x-ray photons particularly at lower photon energies. Typical spectra obtained considering photon absorption within the target are given by the solid curves (figure 2.13).

The ideal spectra suggest that the thick target x-ray intensity depends upon $(\text{kVp})^2$ and this can be taken as a first approximation when estimating exposures in radiology. As filtering preferentially removes the low energy photons, its effect on the 60 kVp radiation will be proportionally greater than on the 100 kVp curve so the intensity will depend on a higher power than 2.0 of tube voltage. For example, increasing the kilovoltage on a typical diagnostic machine from 100 kVp to 105 kVp (i.e. 5%) keeping the tube current constant will increase the x-ray intensity by some 15%, showing that the yield depends on the third power of E. This emphasizes the importance of accurate control of kV in attempting to make a series of identical x-ray exposures.

2.5.2 Birch and Marshall model

Kramers' theoretical spectra incorporated many simplifying assumptions. For example, the backscattering of electrons in the target was neglected, the bremsstrahlung cross sections were assumed to be independent of electron energy, and the absorption of photons in the target was ignored. Because the factors for x-ray absorption and electron backscattering are now better known, a more accurate simulation of the x-ray continuum from the target is possible.

Birch and Marshall developed a model [Bi79] giving spectra that agree with measured spectra obtained with constant potential for a range of voltages, filtrations and target angles. A programme named "XCOMP5R" developed by Nowotny et al. [No85] follows, in essence, the concept by Birch and Marshall [Bi79], to predict bremsstrahlung x-ray spectra. The improvement by Nowotny et al. lies in the use of new data on mass attenuation coefficients for photons and on stopping power data for electrons and also for the production of characteristic x-rays. For this reason, and to

avoid redundancy, the formulation by Birch and Marshall will not be considered further. However, a detailed description of the methodology by Nowotny et al. to derive theoretical x-ray spectra will be given below.

2.5.3 XCOMP5R model

Most published x-ray spectra have been determined for specific experimental conditions. An application of such data to a particular problem can rarely be achieved due to an inevitable variation in the experimental parameters. Helpful data, for the diagnostic energy range, have been given in the catalogue of spectra by Birch, Marshall and Ardran [Bi79], by Cranley et al. [Cr97] and also for dosimetry in a publication by Seelentag et al [Se79]. These data compilations are sufficient in many cases but nevertheless they do not cover all the possible setups and device parameters, in particular tube voltage, voltage ripple, anode angle and additional absorption.

For this reason, Nowotny et al. [No85] introduced a computer code called “XCOMP5R”, which proposed a formulation for the calculation of the spectra emitted by an x-ray tube. This formulation takes into account the continuous (Bremsstrahlung) spectra and the emission of characteristic K- and L-radiation. The XCOMP5R model calculates diagnostic x-ray spectra over a range of tube voltages from 20 to 150 kVp. Running on a desktop microcomputer, the code calculates also data for the spectral distribution, the mean photon energy, kerma in air, mean energy for the kerma distribution and the first and second half value layers in aluminium and copper.

2.5.3.1. Bremsstrahlung distribution

In diagnostic radiology the tube voltages are usually limited to 150 kV giving electron energies in the x-ray tube of at most 150 keV. The slowing down and the scattering of the electrons in the anode material give rise to a series of tracks with tortuous paths. Neither for the electron tracks nor for the energy distribution of the electrons exist formal descriptions. The actual path length of the electrons amounts to a

multiple of the extrapolated range of the electrons, which have been determined by transmission measurements on thin metal sheets.

A simplifying approach for estimating the penetration depth x of electrons slowed down to an electron energy T can be given for initial energies T_0 below 100 keV by the Thomson-Whiddington [Wh12] relationship as:

$$x = (T_0^2 - T^2)/\rho C \quad (2.1)$$

where T_0 denotes the initial electron energy, ρ the density of the anode material and C a specific constant. This specific constant is called Thomson-Whiddington constant, which also depends on T_0 , because the energy loss by ionisation is not exactly proportional to $1/T$ [So72]. The range R is accordingly obtained as $R = T_0^2/\rho C$. The x-rays produced at penetration depth p will be absorbed according to path $a = x \cdot \cot(\theta)$, (figure 2.14). θ denotes the anode angle, i.e. the angle between the anode-cathode axis and the perpendicular to the anode surface under the condition that the x-ray beam used is emitted perpendicular to the tube axis.

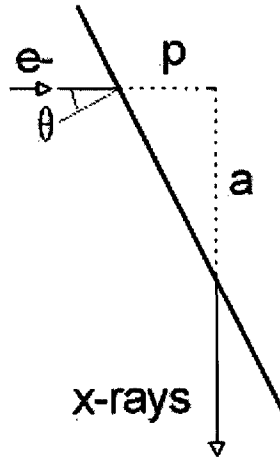


Figure 2.14. X-rays produced at penetration depth p travel the distance a in the anode in direction of the axis of the x-ray beam.

The calculation of bremsstrahlung on thin metal sheets is described in [Ev55]. Basically, a tungsten target is divided into a set of thin target layers. While the electron is penetrating the target layers, the bremsstrahlung yield in each of the target layers is computed from a generalized yield function. For an electron of energy T , the x-ray energy, which will be emitted in x-ray energy range of zero to T ($0 \leq E_v \leq T$), will be

described by the differential energy intensity function B . B depends very weakly on T and the atomic number Z of the anode material.

To simplify the calculation it is assumed that the kinetic electron energy decreases with depth according to equation 2.1 not taking into account the distribution of electron energy in each layer. The electron flux density will be constant up to the range R .

If one can also find a parameterised representation for the differential energy intensity function in the diagnostic energy range of up to a photon energy of 150 keV, then the integration of the bremsstrahlung intensity along the path length of the electrons can be simply performed. The differential energy intensity function B can be given as a function of the photon energy E_ν and the kinetic energy of the electron T , as $B = B(E_\nu/T)$, with $0 \leq E_\nu/T \leq 1$.

The photon flux density ϕ_ν for photons in an energy interval ΔE_ν including the absorption of x-rays in the anode is given in equation 2.2:

$$\phi_\nu = \sigma_0 \cdot \frac{L}{A} \cdot \rho \cdot \Delta E_\nu \cdot Z^2 \int_T^{T_0} \frac{B}{T} \cdot \left(1 + \frac{T}{m_0 c^2}\right) \cdot \exp\left[-\frac{\mu(E_\nu)}{\rho} \cdot \frac{\cot \theta}{C} \cdot (T_0^2 - T^2)\right] \cdot \frac{dT}{(dT/dx)} \quad (2.2)$$

where $\sigma_0 = \frac{r_0^2}{137} = \left(\frac{e^2}{m_0 c^2}\right)^2 = 5.80 \cdot 10^{-32} \text{ m}^2 / \text{nucleus}$ and r_0 is the classical electron radius.

L is Avogadro's number (same as Loschmidt's number), A the atomic weight, ρ the density, dT/dx the stopping power for electrons in the anode material, $m_0 c^2$ the energy equivalent of the electron at rest, mass and μ the linear attenuation coefficient.

Due to the assumptions made, the Thomson-Whiddington constant and the intensity function B are independent from each other. Consistent data, obtained from measured spectra, have been given by Birch et al. [Bi79a]. The data for C can be

obtained in the range from 20 to 150 keV with deviations of less than 2% by the following equation:

$$C=10360 \cdot T_0^{0.4173} \text{ keV}^2 \cdot \text{m}^2 \cdot \text{kg}^{-1} \quad (2.3)$$

The term $\sigma_0 B$ from the equation (2.2) can be given as the energy flux density P at 75 cm distance. Since values for P are required fairly often by the programme, it is advantageous to write the polynom $P(E_0/T)$ according to [Bi79a] in the form

$$P(u) = 0.503 + u(-0.94597 + u(0.1553 + u(1.1632 - 0.6818 u))) \cdot 10^{-18} \quad (2.4)$$

where $u = E_0/T$ is the ratio of photon energy to electron energy. P is given in units energy flux density (keV/mm^2) per energy interval (keV) and tube current (mA), and atomic density (atoms/m^2).

2.5.3.2. Characteristic x-rays

In the range of tube voltages used in diagnostic radiology, the characteristic K-Fluorescence is only relevant for voltages larger than the K absorption edge of tungsten (69.52 keV). The L-fluorescence of tungsten (10.2 to 12.1 keV) should only be considered for low filtrations of effectively less than 1.2 mm Al. Such low filtrations are not used in common practice with patients and are in conflict with legal requirements due to radiation protection regulations [ICRP60].

Emission of characteristic x-rays can happen directly after ionisation of the atom by incident electrons or indirectly by absorption of bremsstrahlung photons by the photoelectric effect. The ratio of direct to indirect production yield depends very much on Z and also on the penetration depth of the electron. For K radiation of tungsten, the yield for indirectly produced K-fluorescence amounts to about 76% of the total K-fluorescence yield [Gr64], but for L radiation, this amount is only 11.9 to 15.4% [Bi82].

The type of production also determines the mean production depth of fluorescence radiation. The direct production takes place during the slowing down process of the electrons until the kinetic energy of the electron drops below the absorption edge, and for this reason the direct production will take place relatively close to the surface of the anode. Bremsstrahlung is emitted in all directions resulting in a centre of gravity for bremsstrahlung absorption much deeper within the anode than for the direct production [Bi82].

The total intensity of the K-fluorescence according to [Gr68] is proportional to $(T_0/E_K-1)^{1.63}$, where $T_0 \leq E_K$. Total intensity is given by a normalisation factor $K_K=1.301 \cdot 10^6$ photons/(mm².mA.s) at 75 cm distance including also the mean absorption that is calculated for the mean production depth. The photon yield for K line i is then obtained using the relative intensity p_i . Data for p_i and photon energy E_i for the K fluorescence lines are given in table 2.3.

Attenuation of K-fluorescence depends on the production depth. For the mean production depth of K-fluorescence of tungsten no data have been found and for this reason the data from [Se79, Bi79] have been analysed. It was found that the mean production depth can be given for K-fluorescence in terms of the fraction r of the electron range R with $r = 0.98$. Due to the large contribution of the indirect production, the mean production depth for the K-fluorescence is larger than for the L-fluorescence. Using $R = T_0^2 / (\rho \cdot C)$ for the electron range and considering the anode angle θ (see figure 2.14), the photon flux density φ_i for K line i is finally given as

$$\varphi_i = K_K \cdot p_i \cdot (T_0/E_K - 1)^{1.63} \cdot \exp\left(-\frac{\mu(E_i)}{\rho} \cdot \frac{\cot \theta}{C} \cdot T_0^2 \cdot 0.98\right) \quad (2.5)$$

Table 2. 3. Energy E_i and relative intensity p_i of the characteristic K-lines from tungsten determined from [St70; Sa74].

Line	p_i , %	E_i , keV
K _{α1}	59.32	100
K _{α2}	57.99	57.6
K _{β1,3,5}	67.15	33.3
K _{β2,4}	69.13	8.9

Table 2. 4.Normalisation factor $K_{L\alpha}$, $K_{L\beta}$ and $K_{L\gamma}$ for the calculation of photon flux density of L-lines in unit photons/ (mm². mA. s) at 75 cm distance depending on the tube voltage [No85].

kVp	$K_{L\alpha}$	$K_{L\beta}$	$K_{L\gamma}$
20	$8.50 \cdot 10^5$	$5.23 \cdot 10^5$	$0.74 \cdot 10^5$
30	$24.75 \cdot 10^5$	$16.63 \cdot 10^5$	$2.53 \cdot 10^5$
40	$43.48 \cdot 10^5$	$29.87 \cdot 10^5$	$4.39 \cdot 10^5$
50	$67.13 \cdot 10^5$	$45.19 \cdot 10^5$	$7.11 \cdot 10^5$

L-fluorescence can be dealt with in a similar manner except the yield of the L lines as a function of tube voltage cannot be expressed in a simple way. For that reason the data from Birch and al. [Bi82] for the relative intensities of L_{α} -, L_{β} - und L_{γ} -lines referred to the mean production depth as well as the contribution of the L-lines to the total spectrum, have been used. For the calculated bremsstrahlung spectra, normalisation factors K_l for a single L-line l are determined by linear interpolation of the values given in table 2.4.

For L-fluorescence it has been shown [Bi82] that the weighted mean \bar{z} of the depth for direct and for indirect production varies relatively little with respect to the electron range R in the voltage range from 20 to 50 kV. It can be expressed in terms of the fraction r of the electron range R as $\bar{z} = r \cdot R$, where r varies from 0.52 to 0.56 with a mean of 0.53. The corresponding contribution of an L-line to the spectrum is therefore given by equation 2.6

$$\varphi_l = K_l \cdot \exp\left(-\frac{\mu(E_l)}{\rho} \cdot \frac{\cot \theta}{C} \cdot T_o^2 \cdot 0.53\right) \quad (2.6)$$

where E_l is the weighted mean energy for the L_{α} -, L_{β} - or L_{γ} -lines which have been obtained from [St70] as 8.39, 9.71 and 11.47 keV, respectively.

2.5.3.3. Calculation of x-ray spectra

The bremsstrahlung spectrum is calculated according to equation 2.2 by calculating the intensities in energy intervals of either 0.5 or 1 keV in the energy range given by the tube voltage and then summing them up to give the total bremsstrahlung distribution. The intensities of the K- and L-lines are calculated according to equations 1.5 and 1.6 and added to the corresponding energy channels. The x-ray spectrum is then filtered by attenuating materials in the beam. The attenuation of tube envelope, coolant oil, tube exit window, etc. is commonly represented by an equivalent in filtration of an aluminium absorber but absorber materials can be included deliberately as a beryllium tube window, air, etc. The photon flux is finally adjusted according to the distance chosen.

Besides the spectral distribution other characteristic data are calculated as the mean photon flux density, the mean photon energy, the kerma and the mean energy of the kerma distribution in air. The kerma in air is obtained by integration over the spectrum up to the maximum photon energy equal to T_0 [Te90] according to

$$K_{air} = \int_0^{T_0} \varphi_v \cdot \left(\frac{\mu}{\rho} \right)_{tr,air,E_v} \cdot E_v \cdot dE_v , \quad (2.7)$$

First and second half value layers in aluminium and copper are calculated using a successive binary approximation. The data required for the mass attenuation coefficients of tungsten, aluminium, beryllium and air as well as the mass energy absorption coefficient for air are obtained by log-log interpolation of the tabulated values by Hubbell [Hu82]. The relative ratio of the coefficients at the absorption edges has been taken from [Mc69]. The data for the stopping power of electrons in tungsten have been calculated according to [Se82; Se82a]. All data were obtained for 0.5 keV intervals and stored in files.

The first version of the computer code was programmed in BASIC for a Hewlett-Packard HP85 table desk computer. Later versions were written in Borland Turbo Pascal 4 to be used with IBM personal computers. The computation time for the calculation of bremsstrahlung spectra and the aluminium half-value layers take most of

the time and is approximately proportional to the square of the tube voltage. Using a 1 keV energy interval the computation time amounts to a few seconds only on PCs currently in use (Intel Pentium 4; 2 GHz).

Table 2. 5. Comparison of calculated and experimental data [HPA77] for air kerma K and first Al half value layer HVL at 75 cm distance together with the corresponding ratio R_K und R_{HVL} for various x-ray tube voltages kVp and aluminum filter thicknesses d (inherent filter of 3 mm Be and 4.7 mm plexiglas).

kVp (kV)	d (mm)	K (μ Gy/mAs)		R_K	HVL (mm Al)		R_{HVL}
		Cal.	Exp.		Cal.	Exp.	
50	1.0	197.7	140	1.412	1.14	1.14	1,00
60		267.7	180	1.487	1.34	1.31	1,02
80		409.9	278	1.474	1.74	1.75	0,99
100		558.7	410	1.363	2.22	2.21	1,01
50	2.0	106.0	273	1.455	1.61	1.62	0,99
60		155.1	100	1.551	1.89	1.87	1,01
80		262.7	170	1.545	2.44	2.48	0,98
100		386.2	268	1.441	3.07	3.11	0,99
100	4.0	236.1	160	1.476	4.38	4.47	0,98
120		341.8	240	1.424	5.18	5.2	1,00
140		461.1	320	1.441	5.96	5.95	1,00

To obtain absolute spectral data, the calculated dose values have been compared with experimental data [HPA77]. This comparison is shown in table 2.5. The average ratio of calculated to experimental dose output R_K amounts to 1.461 (3.6% relative standard deviation). In comparison to reference [Bi79a], this normalisation factor is by 11% larger, which is due to the application of new data sets. The ratio of calculated to experimental first HVLs amounts to 0.998 (1.2% s. d.), which means that the agreement is excellent. The same is true for the spectral distributions, which agree very well with experimental and calculated data from [Bi79] and [Bi79a] (see fig.2.15).

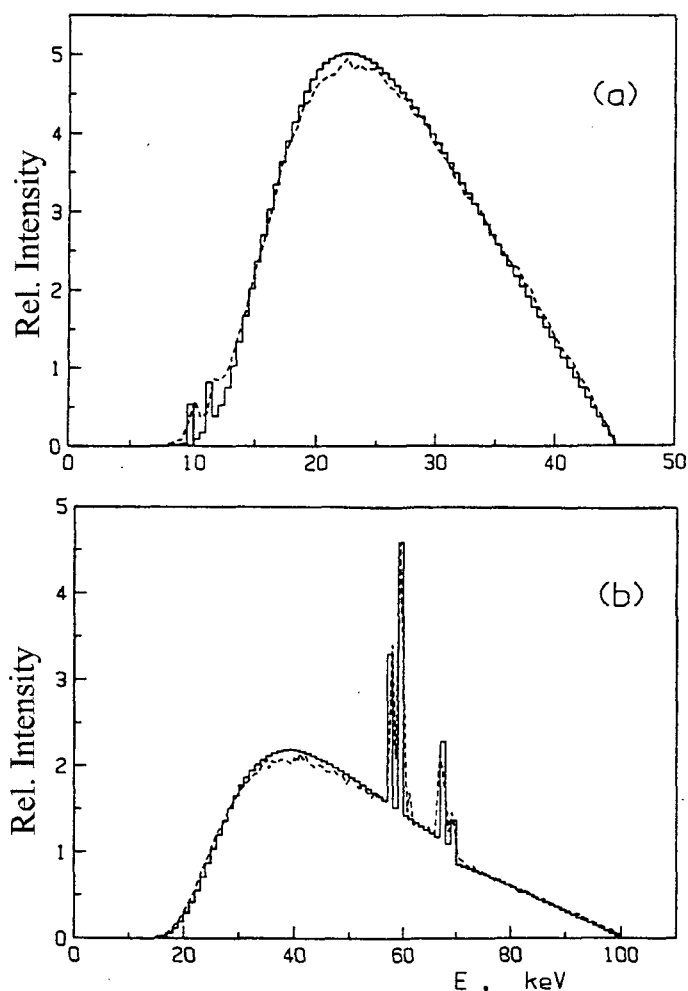


Figure 2.15. Comparison of experimental data (---) from Birch et al. [Bi79a] with calculated x-ray spectra (—) for (a) 45 kV tube voltage; 17° anode angle; 0.62 mm Al-filter and 2 m air and (b) 100 kV; 10°; 2.5 mm Al; 2 m air.

Seelentag et al. have measured spectra for therapeutic x-ray units with an anode angle of 40° [Se79], some of them in the diagnostic energy range. The agreement of these spectra with calculated spectra is less satisfactory (see fig. 2.16a and 2.16b). In general the calculated spectra are too soft. It could be that the differential energy intensity function and the Thomson-Whiddington constants, which depend on each other due to the simplifications made, give only good results for anode angles less than 30°, and for larger anode angles the calculated penetration depth is too small, or the differential energy intensity is too soft. But one can also show that only small amounts of additional absorption layers of tungsten that could be produced by the roughening of the anode surface caused by electrons bombarding the tungsten anode but also a possible tungsten deposit on the inner side of the glass envelope could contribute to produce beam hardening of such amounts.

In figures 2.16b and 2.17b the calculated spectra with 2 or 3 μm additional tungsten filter are shown. Since in [Se79] no absolute dose data have been given, it is difficult to make assumptions on the state of the anode surface and one cannot make statements on the deviation of the calculation to the experimental data for larger anode angles.

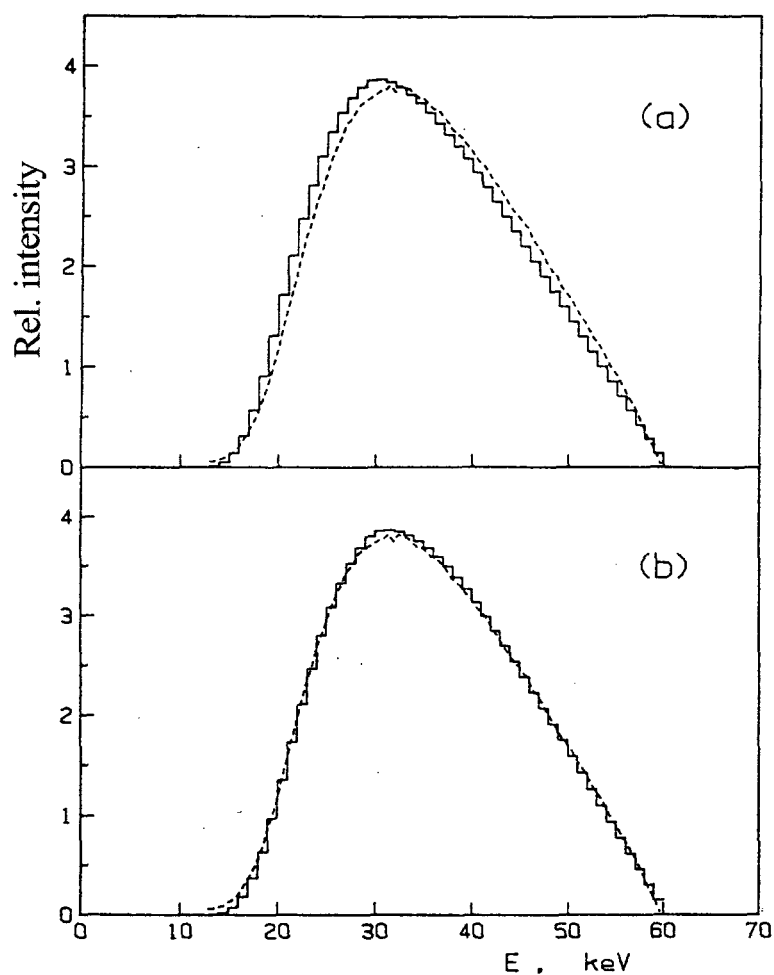


Figure 2.16. Comparison of an x-ray spectrum Nr. C50 from [Se79] (---) with the calculated spectra (—) for (a) tube voltage 60 kV; filtration 3.6 mm Be, 2.5 mm Al and 75 cm air; anode angle 40° and (b) as in (a) but using an additional 2 μm tungsten filtration for the calculated spectrum (see. text).

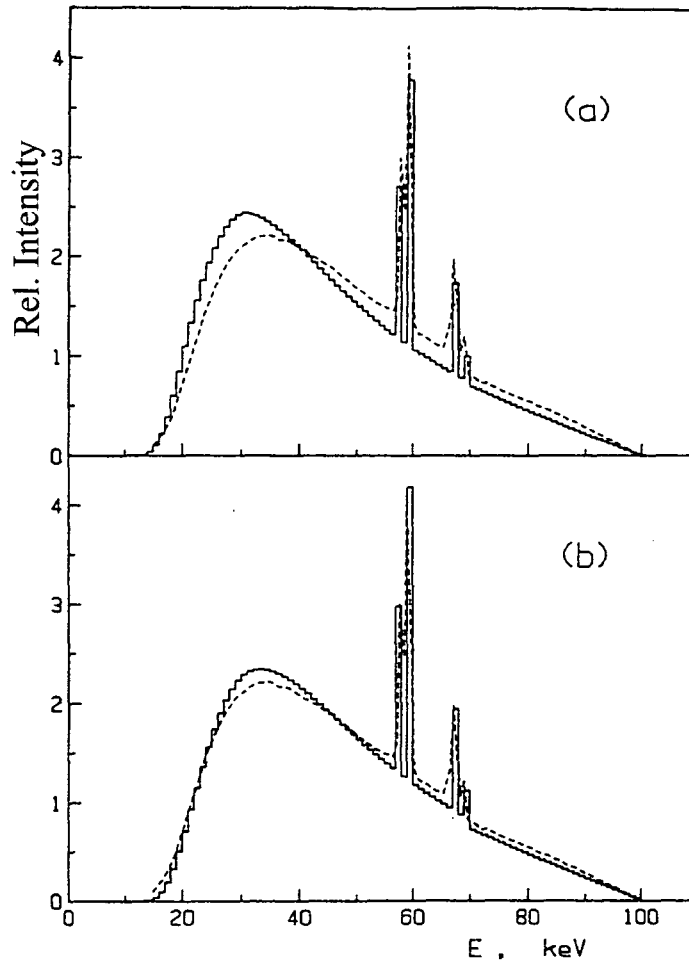


Figure 2.17. Comparison of an x-ray spectrum Nr. C68 from [Se79] (---) with the calculated spectra (—) for (a) tube voltage 100 kV; filtration 3.6 mm Be, 2.03 mm Al, 75 cm air; anode angle 40° and (b) as in (a) but with additional 3 μ m tungsten-filtration for the calculated spectrum (see. text).

It should be noted that any change of the anode surface would also have an impact on the radiation quality leading to a change of kerma output and HVLs. This effect should be taken into account and will be discussed in more detail in this thesis. One should keep in mind that the mean roughness of rotating anodes of new diagnostic x-ray tubes will be in the range 0.3 to 0.8 μ m depending on the kind of surface treatment.

The agreement of calculated and measured intensities of the fluorescent lines is good if one takes into account the limited energy resolution of the experimental spectra. The XCOMP5R code can calculate spectra for tungsten anodes in the range of 20 to 150 kV. For the calculation of spectra with various voltage ripple, one first makes

files for spectra obtained for constant voltages and then adds these spectra for a given voltage ripple according to the weight for these spectra. Other authors have also derived semi-empirical codes for the calculation of x-ray spectra. Caon et al. [Ca98] have compared some of these methods including XCOMP5R for calculating x-ray spectra used in a calculation of radiation dose in computed tomography phantoms.

2.5.4 Monte Carlo calculation

Different authors have carried out simulation of x-ray spectra generated by keV electrons using Monte Carlo codes, for example [Ve99, Ac98, Ll03]. The recent codes based on the Monte Carlo method allow simulating the transport of photons and electrons in matter, i.e. simulating the trajectories of the particles and their individual interactions from the source until the end of their path. The Monte Carlo method consists in building up "individual histories" of a very large number of particles, by taking into account the probability of occurrence of all events that constitute the histories. Monte Carlo simulation has proven to be a suitable theoretical tool for the computation of x-ray spectra as it can incorporate realistic interaction cross-sections and can be applied to complex geometry [Ac98, Ll03].

The probability of an interaction, its differential cross-section, the production of secondary photons and particles, the distance covered by the particles and the energy after an interaction are obtained by random sampling.

For a large number of histories the sum of all individual histories can give statistically representative results for macroscopic quantities. In dosimetry such quantities could be kerma, depth dose data, dose distributions, in metrology detection efficiencies of radiation detectors are of interest, while with x-ray production the resulting x-ray spectrum can be obtained.

Several software packages have been developed in the past for the treatment of radiation transport problems [Ne85, Br97, Sa01]. In the majority of cases, only the electron transport is directly simulated and the photon generation and transport is described by other means. Most programs used in medical physics are directed to

applications in the field of radiation therapy involving mostly high energy photons or electrons. A calculation of diagnostic x-rays requires a full treatment of the absorption of low energy electrons and photons including x-ray fluorescence and production of Auger-electrons. Therefore not many such calculations have been undertaken [Ac98, L103].

The main limitation of the Monte Carlo method arises from its random nature. Moreover, a comparison of simulated or calculated results with experimental spectra is usually made in relative terms, e.g., by normalizing the measured x-ray spectrum to the same area as the Monte Carlo result, due to the fact that the conversion of measured spectra to absolute units requires knowledge of various instrumental parameters that are usually affected by large uncertainties. On the other hand, computation times up to several days might be required for simulations of a complete set-up depending on the complexity of the problem.

2.6. THE X-RAY TUBE

The essential elements of a simple x-ray tube are shown in figure 2.18 and comprise:

- 1) a cathode assembly consisting of a filament of tungsten to provide an abundant supply of electrons by thermionic emission;
- 2) an evacuated tube to avoid interactions of the electrons with a gas and to prevent electric discharges of the high voltage applied;
- 3) a metal anode (the target) suitable to withstand high temperatures; and
- 4) a thin window in the tube envelope that will exhibit little attenuation to the x-rays.

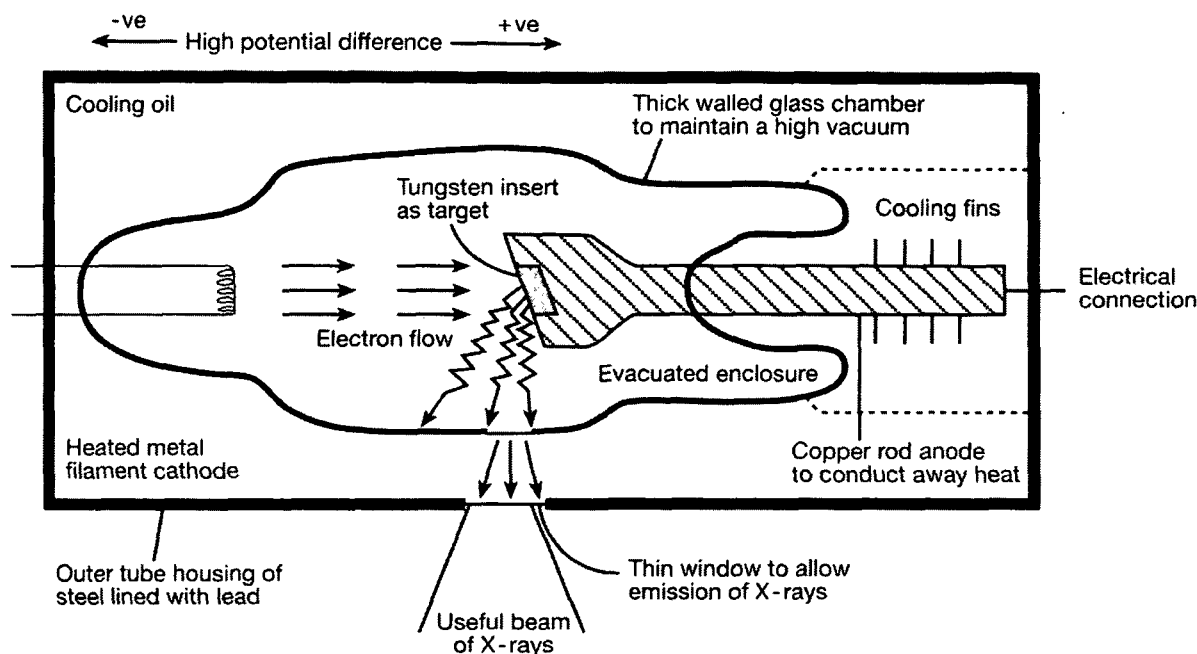


Figure 2.18. Essential features of a simple, stationary anode x-ray tube [De99].

2.6.1 Components of the x-ray tube

Electrons released from the source (cathode) are accelerated toward the target (anode) in a vacuum by a voltage supplied by the x-ray generator. For typical diagnostic imaging applications, the potential difference, given as the peak tube voltage, ranges from 20 to 150 kVp. Tube current, measured in milliamperes (mA), is the rate of electron flow from the source to the target in the x-ray tube, where $1\text{mA} = 1.602 \times 10^{16}$ electrons/sec. The tube voltage, tube current, and exposure time are the three major selectable parameters that determine the x-ray beam characteristics and are set using the x-ray generator control panel.

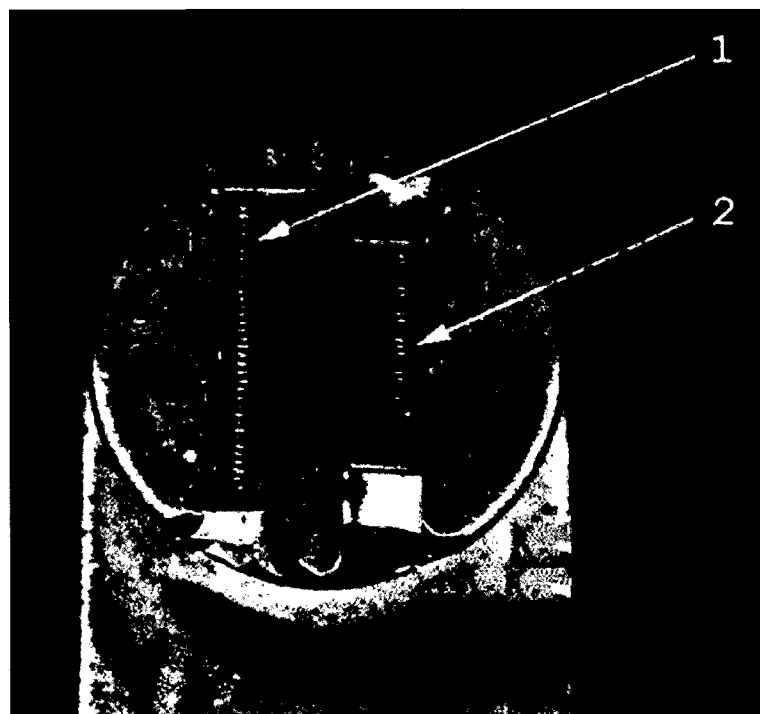
2.6.1.1. The cathode

The source of electrons in an x-ray tube is the cathode constructed as a helical filament made of tungsten wire that has a melting point of 3370°C . Due to the elevated temperatures electrons can overcome the binding energy of electrons to the metal forming a space charge in the vicinity of the filament. The number of electrons in the

space charge tends to be self-limiting depending on the filament temperature due to the repulsive action of the space charge to electrons leaving the metallic surface.

Ideally, the area emitting x-rays on the anode (focal spot) should be as small as possible to avoid any geometrical unsharpness in the image. The size of the focal spot is controlled by the geometrical arrangement of the tungsten filament, a focusing electrode, the potential applied between filament and focusing electrode and the tube voltage. The essential element is the focusing cup shaping the electrical field to give a focusing action on the electrons. Besides the electric field also the mutual repulsion of the electrons within the electronic beam is responsible for the focal spot size. This beam widening is also taken care of by the focusing electrode.

Most diagnostic x-ray tubes have a dual filament assembly (figure 2.19), each filament having its own focusing cup, as to produce two spots of different sizes. The effective or apparent size of the focal spot on the anode is smaller than the actual focal spot because of the anode angle. The smaller the anode angle is the smaller the apparent focal spot size would be (figure 2.22).

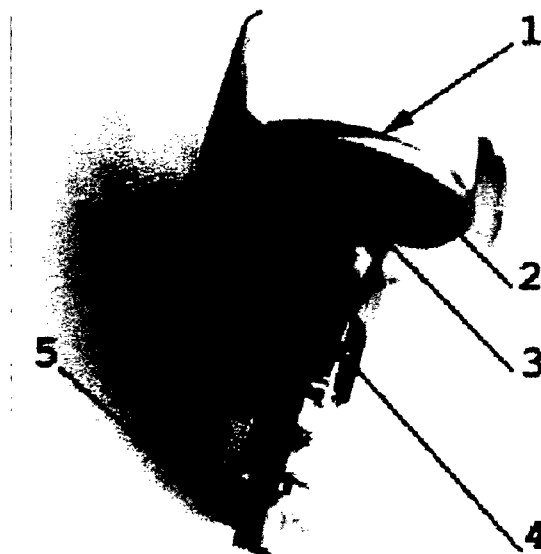


1- Filament of the large Focus (in its focusing cup)
2- Filament of the small Focus (in its focusing cup)

Figure 2.19. Enlarged cathode of the x-ray tube with a dual filament assembly

2.6.1.2. The anode

The anode (figure 2.20) is the target electrode maintained at a positive potential with respect to the cathode. Electrons released from the cathode are accelerated toward the anode. Upon impact, most of the kinetic energy of the electrons is transferred by excitations and collisions to the anode producing heat. Only a small fraction of the energy dissipated in the tube is converted by radiative interactions of the electrons to electromagnetic radiation as x-rays. On the average about 0.5% of the energy carried by the electrons to the anode is emitted as x-rays at the x-ray tube voltages used for diagnostic imaging. Consequently, the production of x-rays in quantities needed for acceptable image quality generates a large amount of heat in the anode. The technical problems related to the dissipation of heat at the focal spot and the cooling of the anode limits the rate of x-ray production that can be achieved without damage to the anode. Part of the problem can be overcome by using rotating anodes where the heat is distributed along a circular focal track instead of a single focal spot.



- 1- Tungsten/rhenium (W-Re) coating (anode material)
- 2- Molybdenum body of the anode
- 3- Anode stem
- 4- Anode rotor (with bearings)
- 5- Anode support

Figure 2.20. Overview of a typical rotating anode

2.6.1.3. The anode material

The material chosen for the anode should satisfy a number of requirements:

- 1) a high conversion efficiency for electrons into x-rays. High atomic numbers are favourable since the x-rays intensity is proportional to Z^2 ,
- 2) a high melting point so that a large amount of heat dissipated causes minimal damage to the anode,
- 3) a high thermal conductivity so that the heat can be removed rapidly,
- 4) a low vapour pressure, even at high temperatures, so that atoms are not sputtered or 'boiled off' from the anode surface, and
- 5) suitable metallurgic and mechanical properties.

In stationary anodes the target area is usually made of pure tungsten ($Z = 74$, melting point 3370°C) soldered to a metal of higher thermal conductivity, such as copper. Originally, rotating anodes were made of pure tungsten. However, at the high temperatures generated in the rotating anode, deep cracks can develop at the track of electron impact. The addition of 5-10% rhenium (Rh) ($Z = 75$, melting point 3170°C) greatly reduces the cracking by increasing the ductility of tungsten at high temperatures. The wear resistant rhenium alloy in the focal spot path ensures less aging, thus high and constant exposure values for a long life. However, pure W/Rh anodes would be extremely expensive so molybdenum is now chosen as the base metal. The specific heat of molybdenum ($Z = 42$, melting point 2620°C) is about twice that of tungsten. Further thermal conductivity of molybdenum is also higher resulting in a faster heat transfer and cooling of the anode. As shown in figure 2.21(a) only a thin layer of W/Rh is used, to prevent distortion that might arise from differences in thermal expansion of the different metals.

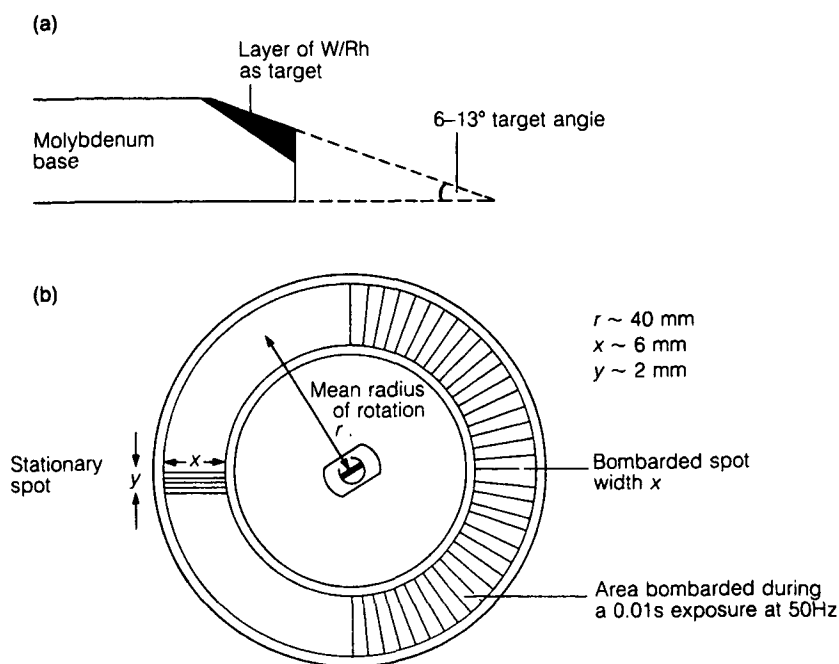


Figure 2.21. (a) Detail of the target area on a rotating anode
(b) Rotating anode showing bombarded the area

2.6.1.4. Anode angle and focal spot size

Diagnostic x-ray tubes are designed to produce a sharp picture of a patient. According to the principles of a central projection x-rays must be emitted from a point source to keep geometric unsharpness low. Otherwise, movement of the patient will result in unsharpness as well. Even if the patient is completely immobilized and keeps his breath, some physiological motion is always present due to heart motion and peristaltic movements of guts and bowels. Hence the exposure times must be as short as possible. A small point source and short exposure times are however incompatible since they imply high electron fluxes concentrated on small focal areas resulting in very high energy densities eventually destroying the anode. A geometrical solution exists to spread the electrons over a larger area of the target and yet make the x-rays appear to come from a much smaller one.

The anode angle is defined as the angle of the perpendicular to the target surface to the central axis of the x-ray tube, usually parallel to the electron beam as shown in figure 2.22. Typically anode angles in diagnostic x-ray tubes range from 7° to 20° . The

electronic focal spot size is equal to the area on the anode struck by the electrons. The length of the electronic focus is mainly determined by the length of the cathode filament. As the centre of the x-ray beam is usually perpendicular to the tube axis, the effective focal spot size in direction of the x-ray beam will appear smaller as for anode angles of less than 45° the projected effective focal spot length is less than the electronic focal spot length. The effective and electronic focal spot lengths are related as:

$$\text{Effective focal length} = \text{Electronic focal length} \cdot \sin \theta$$

where θ is the anode angle. The width of the electronic focus is determined by the focusing of the electron beam in transverse direction to the tube axis. The width of the effective focus is essentially equal to the width of the electronic focus. It should be noted that for other positions in the x-ray beam not coinciding with the central beam the focus size changes accordingly. Typical dimensions of focal spots used in diagnostic radiology range from 0.2 mm to 2 mm.

Many x-ray tubes have two focal spot sizes that can be selected by the operator. The main advantage of a larger focal spot is increased loading capacity. The choice of the focal spot size largely depends on the imaging requirements of the radiological examination. If sharp images are required as in the examination of bone structures the use of the small focal spot is mandatory but implies prolonged exposure times. Whenever possible the large focal spot is used to ensure short exposures and avoid the risk of unsharpness due to patient movement.

The optimal choice of anode angle depends on the clinical application. A small anode angle is recommended for cine-angiographic equipment, in which x-ray field coverage is limited by the image intensifier diameter. Larger anode angles are necessary for general radiographic work to achieve large field area coverage at short focal spot to image distances (figure 2.22).

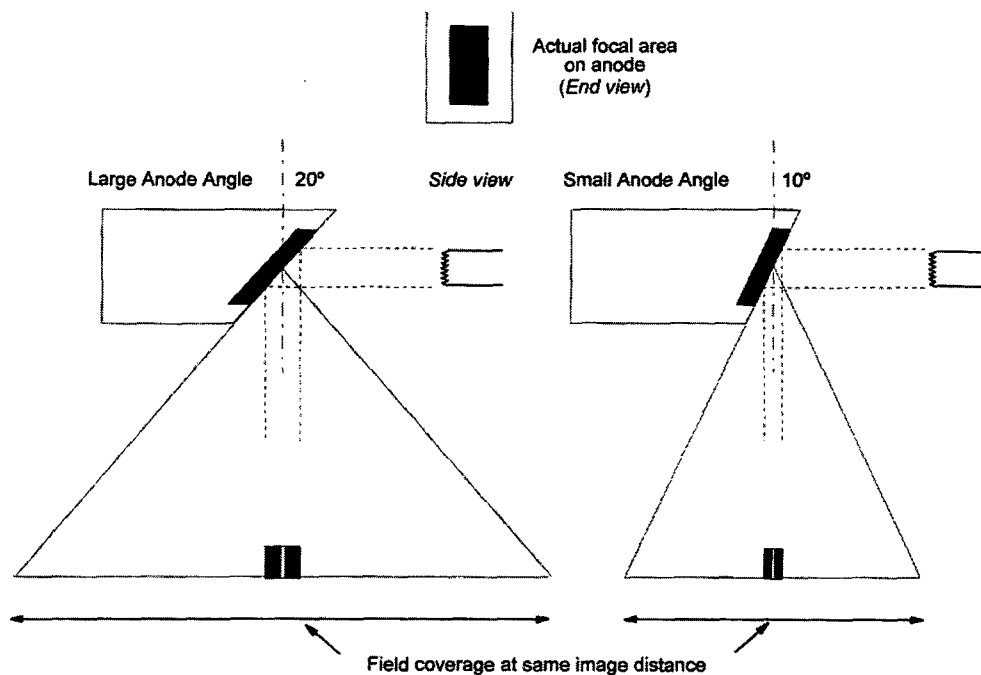


Figure 2.22. The effective focal spot size varies with anode angle. For the same actual size, the projected effective size is smaller for the smaller anode angle.

2.7. FACTORS AFFECTING THE X-RAY SPECTRUM

If the spectrum changes in such a manner that its shape remains unaltered, i.e. the intensity or number of photons at every photon energy changes by the same factor, there has been a change in radiation **quantity**. If on the other hand, the intensities vary such that the shape of the spectrum also changes, there has been a change in radiation **quality** (the penetrating power of the x-ray beam). Some of the factors that affect the x-ray spectrum and intensity are considered below.

2.7.1 Tube current

Tube current I_t determines the number of electrons striking the anode. Thus only the number of photons produced change accordingly leaving the distribution of photon energies the same. The radiation quality of the x-ray beam is not affected; the kerma K obtained will be proportional to tube current ($K \propto I_t$).

2.7.2 Time of exposure

Time of exposure again determines the total number of electrons striking the anode so kerma output for a given tube current depends on exposure time but radiation quality of the x-ray beam is not affected.

2.7.3 Tube voltage

If other tube operating conditions are kept constant, x-ray intensity increases approximately with the square of tube voltage ($I \propto (kVp)^2$) [Cu90]. Two factors contribute to this increase. First the electrons have more energy to lose when they hit the target. Secondly, the efficiency of conversion of electrons into x-rays rather than into heat also increases with tube kilovoltage by a small amount over the range of diagnostic kilovoltage. Thus, both the flux of x-ray photons and their mean energy, increase. Consequently increasing the tube voltage alters the radiation quality giving higher HVLs. The position of any characteristic lines will not change.

2.7.4 Waveform of tube voltage

Ideally, the tube voltage should be constant which is technically difficult to achieve. The tube voltage is usually given as the peak voltage in the voltage waveform applied to the tube (kVp). The fluctuation of the tube voltage is expressed as voltage ripple defined as the amount of variation in the applied x-ray tube voltage waveform relative to the peak voltage of the voltage waveform:

$$\text{Voltage ripple (\%)} = [(V_{\max} - V_{\min})/V_{\max}] \times 100$$

Several solutions for the generation of high voltages have been used with x-ray units differing in stability and voltage ripple according to the electrical circuitry used. Older units operate directly from mains supply using alternating current. The simplest method for a rectification of alternating high voltages employs the rectifying properties of the x-ray tube. Since one end of the x-ray tube must act as a cathode and the other

end as an anode, no current flows when an alternating potential is applied during the half cycle when the cathode is positive with respect to the anode (figure 2.23). Improved half wave rectification may be achieved by inserting a rectifier in the anode circuit. Since x-rays are only emitted for half the cycle, exposure times are long and the output is poor. Improved output can be achieved by full wave rectification using a simple bridge circuit. However, at times of low voltage within the cycle the tube is still emitting very little x-rays. Furthermore, the average tube voltage is much lower than the peak value (kVp). This method could be improved somewhat by full-wave rectification of the single phase (2-pulse generator). Still, all single-phase generator systems give 100% voltage ripple.

A more constant voltage will improve the quality of the radiation and this can be achieved by using a three-phase supply. The three phases are 120° out of phase. By full-wave rectification 6 pulses are obtained per cycle giving finally a resultant voltage profile as shown in figure 2.23 with a voltage ripple of about 15%. Three-phase alternating current could be transformed in Y- and Δ -connection. Full wave rectification of the high voltages obtained in both ways finally will give 12 pulses per cycle with a voltage ripple of less than 5% [Cu90].

A DC-voltage (0% ripple) would be ideal, giving a constant voltage and constant radiation properties throughout the exposure. Constant potential generators have ripple less than 2% and hence deliver the highest x-ray output for a given kV and mAs but are rarely used in medicine.

The technical standards of today are medium/high frequency inverter generators having a voltage ripple similar to 12-pulse generators.

Inverter generators produce a stabilized tube voltage and current using a feedback loop. Figure 2.23 shows the voltage ripple for each of the x-ray generator types.

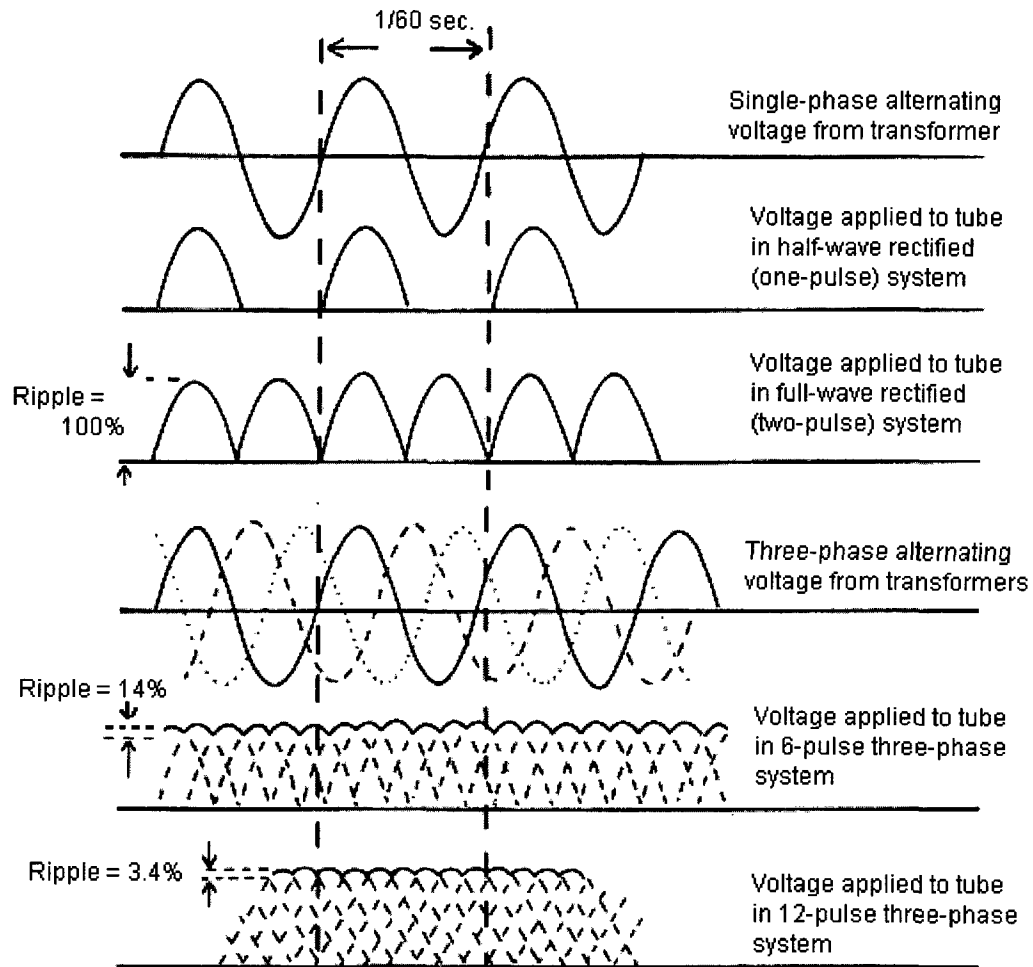


Figure 2.23. Examples of different voltage waveforms with voltage ripple for various x-ray generators used in diagnostic radiology varying from 100% voltage ripple for a single phase generator to nearly 0% ripple for a constant potential generator [Sp87].

2.8. FILTRATION OF X-RAYS

Filtration has a marked effect on both quantity and quality of the x-ray beam, not only reducing the overall output but also reducing the fraction of low energy photons in the spectrum. Because the attenuation coefficient decreases with increasing photon energy, low energy photons are preferentially removed from an inhomogeneous or polychromatic beam, a phenomenon referred to as beam hardening. The main purpose of filtration is to remove soft x-rays that would increase the patient dose without contributing to the x-ray image.

2.8.1 Effect of filtration on spectral output

X-ray machines produce a continuous spectrum of x-rays with energies ranging from near zero up to some maximum value, determined by the selected tube potential (figure 2.24). The average energy in a Bremsstrahlung spectrum appears at energies much lower than the maximum. An estimate for the average energy of an x-ray beam is approximately one third of the maximum energy.

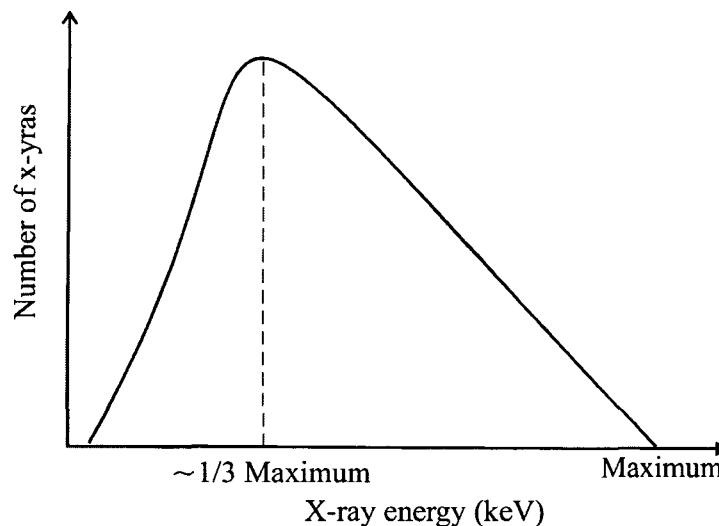


Figure 2.24. X-ray spectrum.

This spectral distribution is not ideal for diagnostic radiology for two reasons. First, the lower energy x-rays are heavily absorbed by the body tissues and can therefore not contribute to any diagnostic information on the film or image receptor, but do result in unnecessary skin exposure. Second, latitude of radiation dose and image contrast is determined by the spectral distribution. The latitude is given by the ratio of the largest x-ray dose to the smallest x-ray dose appearing in the image and carrying true image information, i.e. excluding the collimation area and directly exposed image receptor area. Latitude decreases with increasing tube voltage or increasing half-value layer due to the decrease in attenuation of tissues with photon energy. If an image receptor has a limited dynamic range of recording the signal (e.g. x-ray films) the latitude in dose could be adjusted according to the receptors properties by increasing the tube voltage. This is done in chest x-rays where the high differences in absorption from lung tissue to

bony structures are made visible on film by using high-voltage techniques (tube voltages between 125 to 150 kV).

From a radiologist point of view maximum image contrast is desirable. The image contrast is also determined by the differences in attenuation by the various tissue components in the object imaged as with latitude. Generally, increasing the tube voltage or increasing the half-value layer with filters yields a decreasing image contrast. Hence selecting tube voltage and filtration is always a compromise between patient dose and radiological requirements.

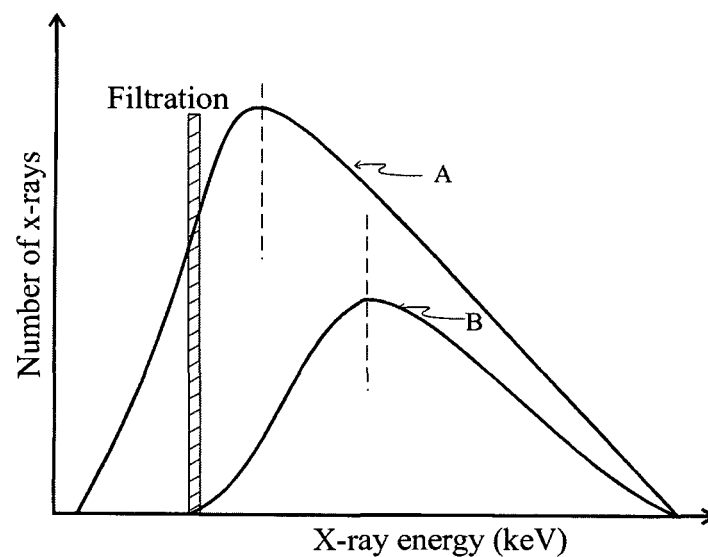


Figure 2.25. X-ray spectrum: A, without additional filtration and B, with additional filtration

In figure 2.25, curve A is an x-ray spectrum without added filtration, and curve B is the same spectrum with the beam filtered. The filtration has cut out a significant percentage of low energy x-rays and the lowest energy has increased substantially. The spectral peak has been shifted towards the higher energies also giving a higher effective energy than before. By continuing to add more filtration, the effective energy could theoretically be made to approach the maximum kVp with elimination of all but the most energetic x-rays. However, as can be seen in the figure, the filtration reduces the total number of x-rays and continuing to add filtration will finally result in too few to produce a useful image. Therefore, the amount of filtration placed in the beam is a compromise among the three effects (i.e., low energy x-ray elimination and increased

effective energy, reduction in number of x-rays and increased tube loading for a compensation of filter attenuation).

2.8.2 Sources of filtration

Filtration of the emitted x-ray spectrum is caused in an x-ray device by inherent and added attenuators in the path of the x-ray beam.

Inherent filtration results from the x-ray tube target itself and from the thickness and elemental composition of x-ray tube envelope usually made of glass or metal-ceramic composites, the cooling oil surrounding the tube, the radiation exit window in the tube housing and the various structures in the beam restrictor (e.g. the light-beam diaphragm mirror). The inherent filtration is approximately equivalent to the filtration of 0.5–1 mm of aluminium at 80 kV tube voltage. With tube aging, the surface of the anode becomes roughened and pitted, and the distances within the anode material x-rays will have to penetrate get larger. Inherent filtration will thus depend on tube age. A detailed treatise of this effect will be given below.

Added filtration refers to any additional attenuator in the beam to further alter the radiation quality. The use of added filters is again to increase x-ray hardness with the benefits of either reducing patient entrance dose or reducing latitude of image dose. The classical example of this is again imaging of the chest, where the contrast from ribs, shoulder blades, spine and heart relative to lung tissue must be reduced. In some diagnostic examinations, but more important in many fluoroscopic procedures, such added filtration could save radiation dose to the patient but still giving an acceptable image contrast.

Total filtration of the x-ray beam gives the sum of all filters in the x-ray beam before it reaches the patient. All filters are usually referred to their equivalent in aluminium giving the same filtration for an 80 kV x-ray spectrum.

2.8.3 Legal requirements

In view of the above, international recommendations [ICRP34] and national legislation requires provisions for keeping radiation dose to the patient as low as achievable but compatible with the required image quality. A characterization of these conditions can be achieved in two ways: using the concept of "beam quality" in terms of half-value layer or defining a minimum filtration in terms of an aluminium absorber equivalent to total filtration.

2.8.3.1. Requirements for beam quality

As the effective energy of an x-ray beam is increased (i.e., reducing the number of low energy x-rays by adding filtration), the penetrability is also increased. Penetrability refers to the range of x-ray beams in matter; higher energy x-ray beams are able to penetrate matter farther than low energy beams. The penetrability, or penetrating power, of an x-ray beam is called the "x-ray quality". X-ray beams with high penetrability are termed high quality, or "hard" beams, while those with low penetrability are of low quality and are called "soft" beams. In radiology, the quality of x-rays is characterised numerically by half-value layer (HVL). The HVL of an x-ray beam is the thickness of absorbing material necessary to reduce the x-ray intensity to one-half its original value. The advantage of using HVL is that it is a performance characteristic of the x-ray machine and allows the manufacturer freedom of design for any type of filtration as long as the x-ray beam quality is of the specified HVL. One additional advantage is that the HVL can be measured quickly using non-invasive techniques. The filtration of an x-ray tube can then be obtained from published HVL-total filtration data.

Although any material may be used for filtration, aluminum is the most common because it is lightweight, inexpensive, easy to machine, and has desirable absorption properties for diagnostic x-ray energies. Thus the HVL requirement is specified in terms of millimeters of aluminum equivalence. Furthermore, since the attenuation of an aluminum filter depends on its impurities, performance standards define the purity (type of aluminum alloy) the requirements are based upon.

The half-value layer of the useful beam for a given x-ray tube potential shall not be less than the values shown in table 2.6 [ICRP34]. For kVp values not found in the table, simple linear interpolation or extrapolation can be used to compute the required HVL.

The values in table 2.6 were determined empirically and, are fairly linear within each kVp operating range with respect to kVp. For example, at 90 kVp the required HVL is 2.5 mm Al. The filtration in a machine meeting this requirement will have an HVL of 2.5 mm Al at 90 kVp and (with the same total filtration) an HVL of 3.5 mm Al at 130 kVp.

Table 2. 6. Half-Value Layer as a function of tube potential.

TABLE OF ACCEPTABLE HALF-VALUE LAYER (HVL)		
Design operating range (kVp)	Measured potential (kVp)	Half-value layer (mm Al)
< 50	30	0.3
	40	0.4
	49	0.5
50 to 70	50	1.2
	60	1.3
	70	1.5
> 70	71	2.1
	80	2.3
	90	2.5
	100	2.7
	110	3.0
	120	3.2
	130	3.5
	140	3.8
	150	4.1

Testing for HVL is performed by making successive exposures with increasing thicknesses of aluminum sheets interposed in the beam. A plot is made with the exposure reading on the y-axis versus the aluminum thickness on the x-axis (see figure 2.26). The HVL can be determined by finding the 50% value of the initial output (for example, air kerma) on the y-axis and then across to the curve and down to the x-axis for the equivalent aluminum thickness.

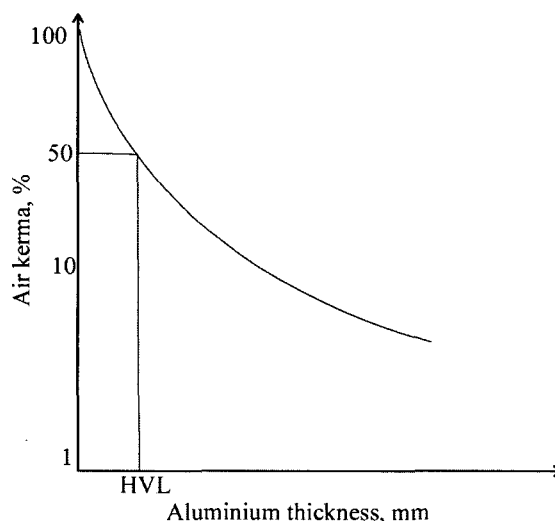


Figure 2.26. Example of attenuation curve obtained with aluminium absorbers

Due to the spectral nature of x-rays, the half-value layer is not constant. When measuring multiple half-value layers, the second HVL is greater than the first. This is due to the fact that the mean energy of the x-ray spectrum is increased following passage of the first HVL, which results in x-rays becoming more penetrating.

2.8.3.2. Requirements for total filtration

The above HVL criteria is considered to have been met if it can be demonstrated that the aluminium equivalent of the total filtration in the primary beam is not less than that shown in table 2.7 [ICRP34].

The International Commission on Radiological Protection [ICRP82] has recommended that the total filtration in the useful beam for normal diagnostic work should be equivalent to not less than 2.5 mm Al, with exceptions for mammography units and for conventional dental units not exceeding an operating voltage of 70 kV.

Measurements must be made to determine the total filtration as accurately as possible, since although minimum values are specified by the regulations, it can be undesirable to have too much filtration fitted. This can give rise to a shortening of the life of the x-ray tube due to increased tube loading. The International Electrotechnical Commission [IEC76] has recommended to manufacturers that the actual inherent filtration should not exceed the nominal inherent filtration by more than 15%.

Table 2. 7. Filtration as a function of tube voltage.

TABLE OF FILTRATION REQUIRED VS. OPERATING VOLTAGE	
Operating Voltage (kVp)	Total Filtration (inherent + added) (mm Al equivalent)
< 50	0.5
50 - 70	1.5
> 70	2.5

The fourth section will deal with the development of a semi-empirical approach for the determination of the inherent filtration in x-ray units.

3. SIMULATION OF THE EFFECT OF ANODE SURFACE ROUGHNESS ON DIAGNOSTIC X-RAY SPECTRA

3.1. INTRODUCTION

As seen in section 2 some minimum filtration is mandatory with diagnostic x-ray units to reduce radiation dose to the patient from the low energy x-rays in the spectrum. As inherent filtration usually gives insufficient attenuation some additional filters are introduced to achieve the legally required filtration of an equivalent in aluminium of 2.5 mm. In other applications of x-rays, as in radiation and metrology various filter combinations are used to achieve the radiation qualities required in these fields. Total inherent filtration also includes the attenuation of the x-rays in the anode material itself. The x-rays, produced by electrons slowed down in the anode, encounter some attenuation in the anode material, depending on the anode angle and the beam direction. The contribution to attenuation within the anode to inherent filtration is generally not known.

The condition of the anode surface and the deposition of sputtered tungsten on the inner side of tube envelope have also been made responsible for an increased inherent filtration (see e.g. [Ar72]). Tungsten deposits on the inner side of the tube are found to be much less than 1 μm in thickness ([St86], [Na88]) and consequently should give little contribution to attenuation. Less data are available on the influence of anode roughness on spectra and spectral parameters [Na88].

From the second section, it appeared that target roughening is likely to have a significant effect on the spectrum and may explain some differences between the experimental x-ray spectra data from Seelentag [Se79] and those calculated using the code XCOMP5R. Indeed, it was observed that only small amounts of additional absorption layers of tungsten would be sufficient to produce beam hardening that yields simulated x-ray spectra similar to those from [Se79]. The roughening of the anode surface developing by the bombardment of the tungsten anode with electrons could induce some amounts of additional absorption layers of tungsten (see paragraph 2.5.3.3).

Target pitting induced by tube loading will affect the range distribution of the electrons as well as the attenuation of photons within the target. Hence the combined effect on the emitted x-ray spectrum will be complex. To quantify this effect, geometrical irregularities of pitted surfaces should be assessed. This section will be dealing with this topic in more details. For this, used rotating anodes were collected; the surface profiles and surface roughness of 8 focal tracks were determined. The surface profiles were then used to simulate x-ray spectra using the computer code XCOMP5R obtained with anodes of a varying degree of surface roughness. The bases for this simulation were anode surface profiles and data for surface roughness obtained by measurement for anode samples from x-ray tubes made available in the course of tube replacements in clinical x-ray units.

3.2. MEASUREMENT OF SURFACE PROFILES FOR ANODE SAMPLES

Tungsten anodes from x-ray tubes replaced in clinical x-ray units for various reasons, for example, broken tube, cracks in the anode or wear of the rotor bearings were collected. Examples of such samples are shown in figures 3.1 to 3.4. Total workload and age of the tubes were unknown. All anodes were plain rotating tungsten disks without other features, as compound anode, radial slits or graphite heat sink.

After inspection with a microscope five anodes either intact or fragmented were chosen for further measurements. These anodes appeared to cover the range of surface

deterioration present amongst the samples. With all anodes the focal tracks were clearly discernible from the original surface (figure 3.1, right), three of them showed two separate tracks for a large and a small focal spot, respectively.



Figure 3.1. Typical dismantled rotating tungsten anode (left). The two focal tracks are clearly seen (right: enlargement of roughened focal tracks) as their appearance is different due to the roughened surfaces (inner track: small focus; outer track: large focus)

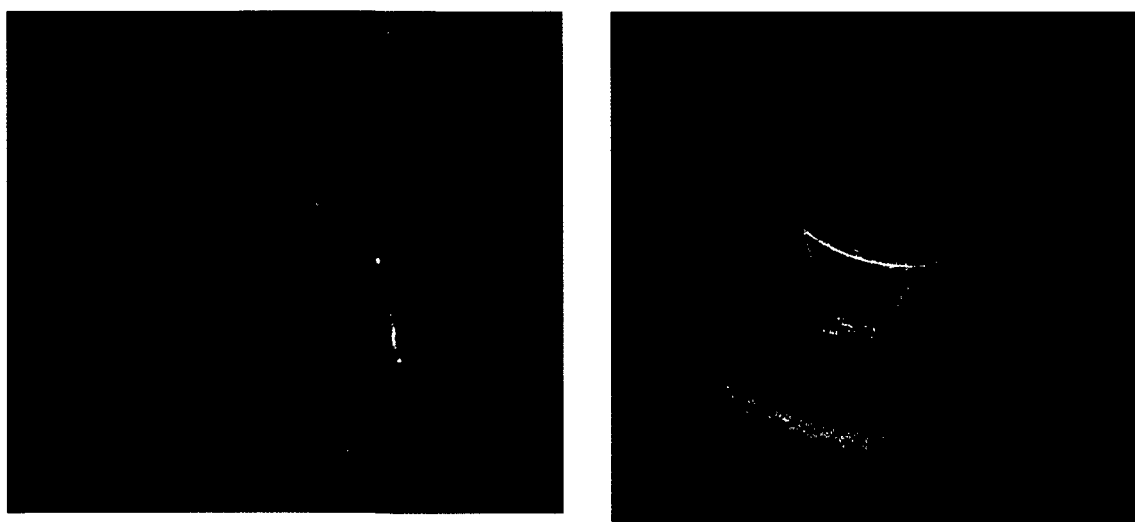


Figure 3.2. Anode fragments from dismantled tubes



Figure 3.3. A crack in one of the anodes



Figure 3.4. Example of heavy surface deterioration in a focal track

3.3. ANODE SURFACE PROFILES

The surfaces of the anodes were investigated with a surface profile recorder (Perthograph, Mahr-Perthen, Göttingen, Germany) using a diamond tipped stylus with a 90° tip of $1\text{ }\mu\text{m}$ radius. In each measurement a track of about 2 mm length was scanned across the focal track in the radial direction near the centre line of the focal track (figure 3.5 left). Taking into account the nature of rotative anode, the probability of roughness is assumed to be uniformly distributed over all of the focal track area. Therefore, the position of the scanning line has been arbitrary chosen. This line is considered as being representative of the roughness for the other parts of the focal track (figure 3.5 right). On two anodes an unaffected surface still showing the initial surface finish was scanned in a similar manner with scan lengths of 1 mm.

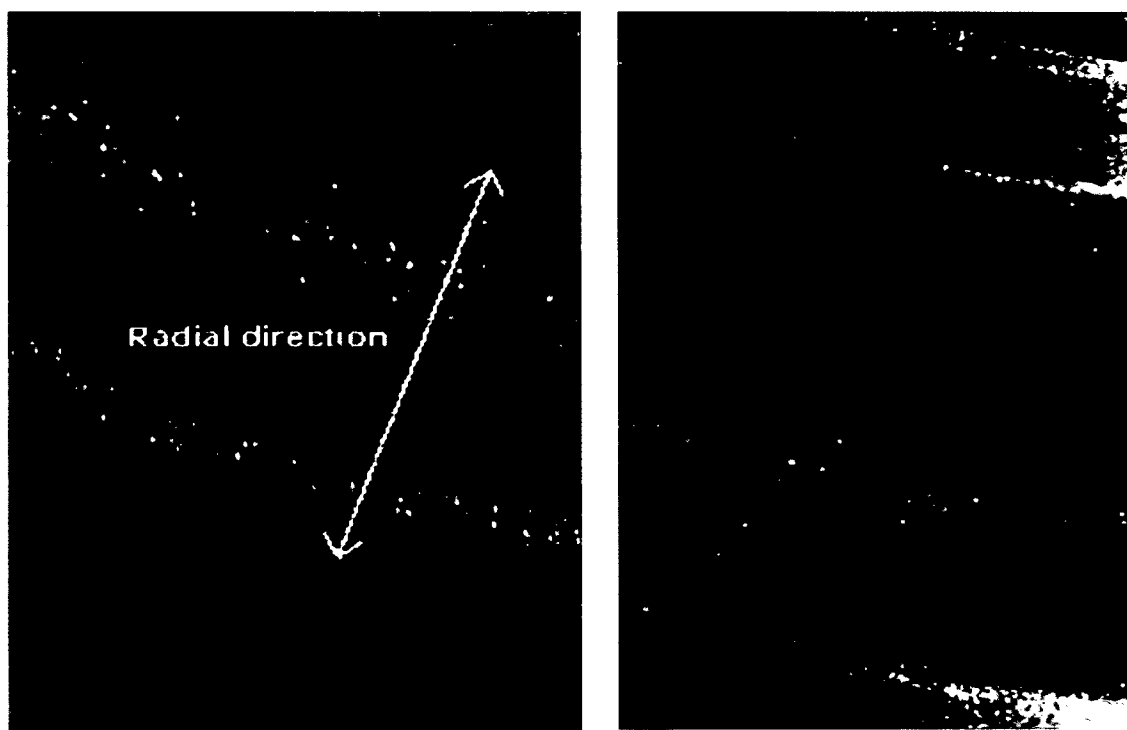


Figure 3.5. Direction for scanning the surface profile (left). The length of each scan was 2 mm. The marks on the right figure indicate the position of the scanning line

The surface profiles were recorded, excursion and position of the stylus digitised. Using linear regression a straight line was fitted to the data to obtain a centre

line of the surface profile. This centre line was assumed to be in plane with the original anode surface inclined to the incoming electron beam at the anode angle. The actual anode angles of the anode disks were determined with a goniometer.

Figures 3.6 to 3.10 give the results for such measurements. In viewing the graphs one should note the different scales for track distance x and excursion from the centre line.

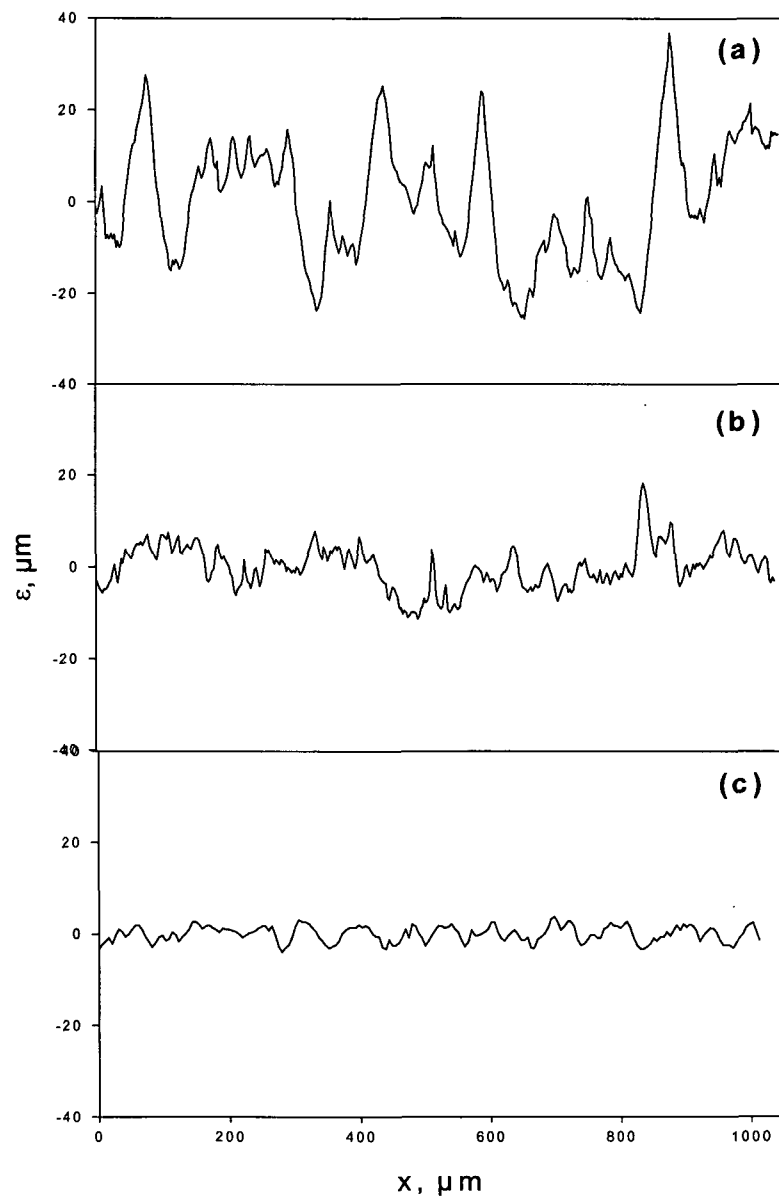


Figure 3.6. Surface profile for the anode no.3 in table 3.1. Data show the deviation from a centre line versus position for (a): the surface of the small focal track, (b): the surface of the large focal track and (c): the original anode surface ground surface finish.

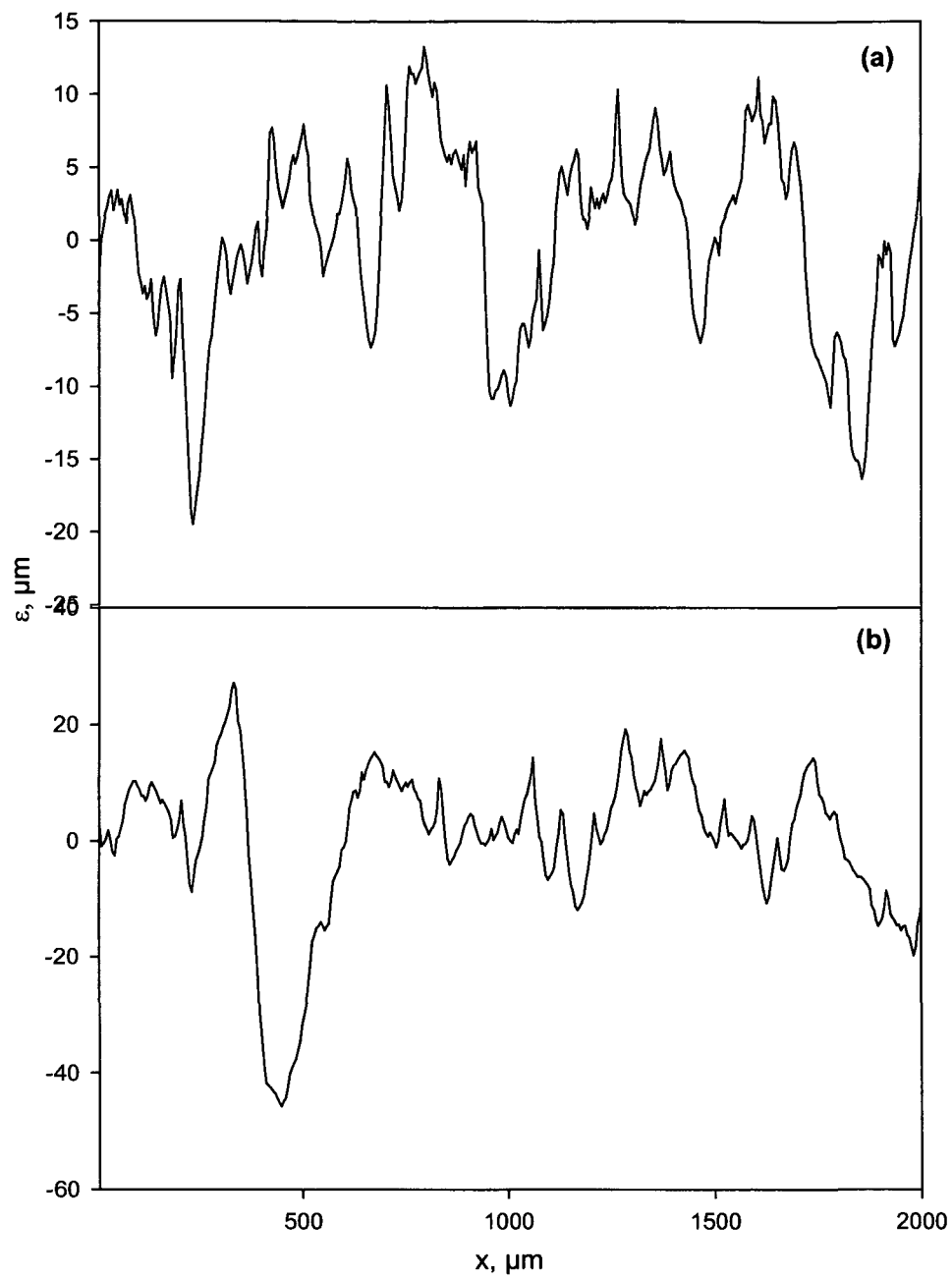


Figure 3.7. Surface profiles for the anode no.4 in table 3.1. Data show the deviation from a centre line versus position for (a): the surface of the large focal track and (b): the surface of the small focal track

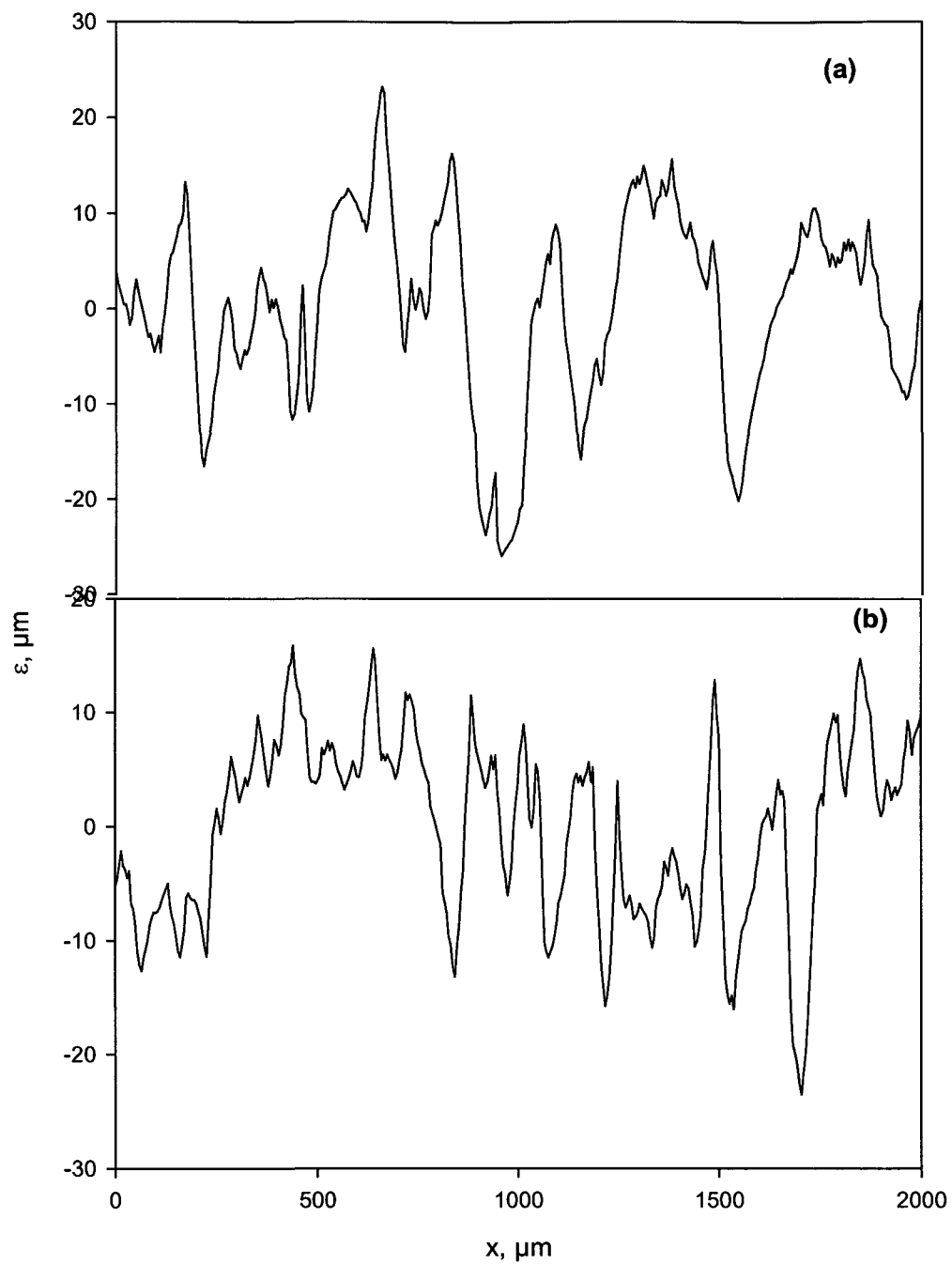


Figure 3.8. Surface profiles for the anode no.5 in table 3.1. Data show the deviation from a centre line versus position for (a): the surface of the small focal track and (b): the surface of the large focal track

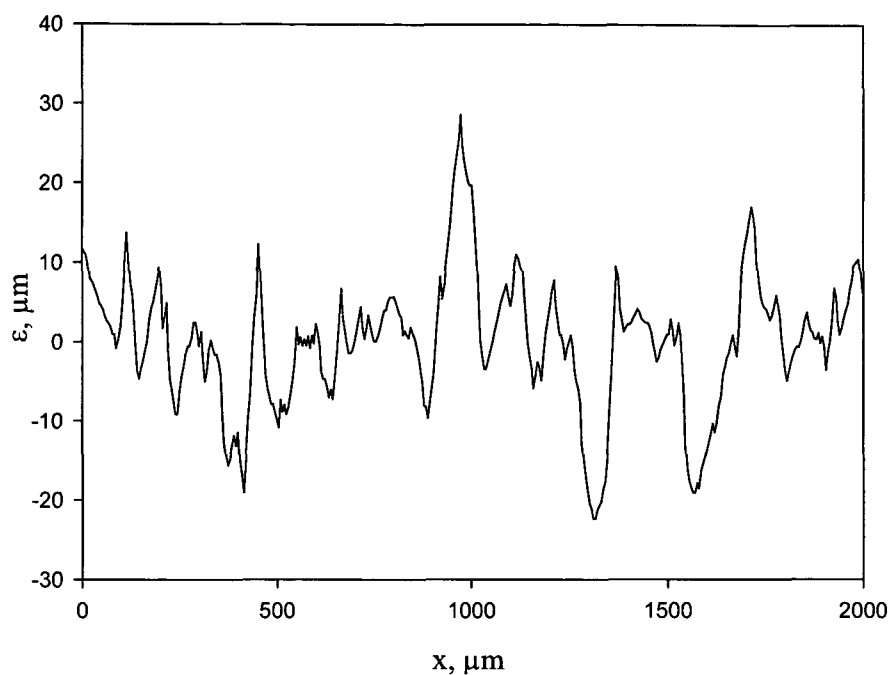


Figure 3.9. Surface profiles for the anode no.6 in table 3.1. Data show the deviation from a centre line versus position for the surface of the focal track.

In the course of our investigation also the surface profile of a stationary anode was analysed. The scan direction was transverse to the tube axis covering the full focal spot width (see figure 3.10). It showed an inversed bimodal distribution.

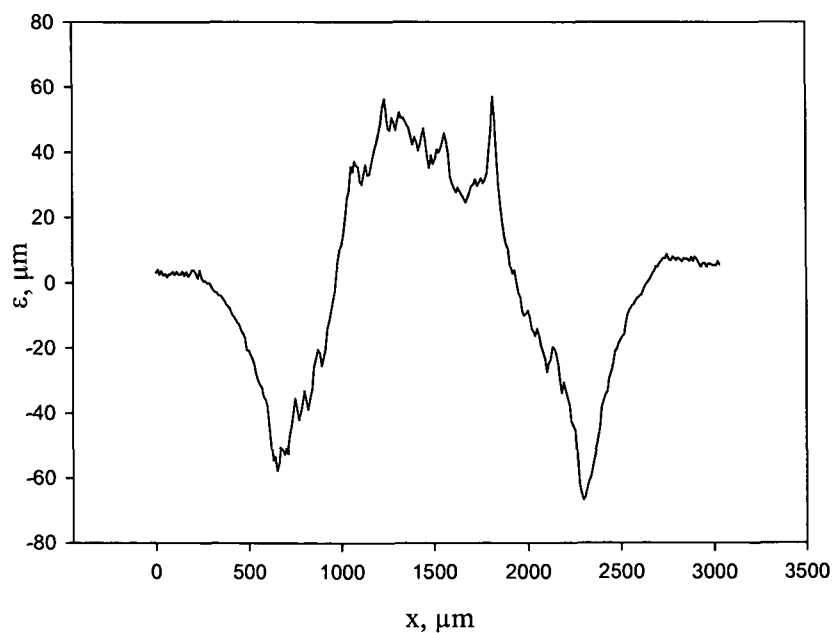


Figure 3.10. Surface profiles for the stationary anode. Data show the deviation from a centre line versus position for the surface of the focal track

This can be explained if we consider the current distribution coming from the cathode filament and hitting the anode. The electronic focal spot (the spot on the anode onto which the electrons accelerated from the cathode filament are focused) looked upon along the central line of x-ray beam in the field, is commonly shaped as a square. This would be the situation if a uniform flux density of electrons impinged all over the focal spot, the electron flux dropping to zero at the periphery of the square area. In an actual situation, the spot is shaped more like a “double banana” as shown in figure 3.11, which shows a pinhole recording of a focal spot.

As a result of the higher current densities at the edges of the focal spot current distribution creates lateral hot spots causing melting of the anode material from the sides sputtering it at the centre of the focus in the course of the tube usage. This is clearly reflected in figure 3.10.

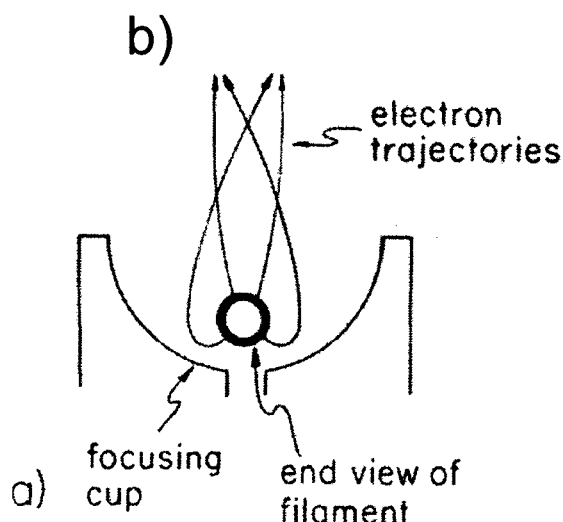


Figure 3.11. (a) Schematic diagram of filament in its focusing cup showing the electron trajectories and the way there are focused into two lines on the target. (b) Pinhole picture of the focal spot of the tube.

The data for the stationary anode were not used and analysed any further but demonstrate the degree of surface roughness or rather deformation, which could be obtained with x-ray tubes after high and prolonged tube loading. The maximum tube deviations from the original anode surface exceed 50 μm in both directions.

3.4. DETERMINATION OF SURFACE ROUGHNESS

Roughness of surfaces on a similar scale is mainly a subject in mechanical engineering. A consequence of roughness is friction and the quantities describing roughness there are defined for that purpose. Two quantities were adopted here for a description of roughness, an arithmetic average and a root-mean-square average of the profile deviation from the centre line, R_a and R_g , respectively,

$$R_a = \frac{1}{\ell} \int_{\ell} |\varepsilon| dx \quad \text{and} \quad R_g = \left(\frac{1}{\ell} \int_{\ell} \varepsilon^2 dx \right)^{1/2},$$

where ε denotes the distance of the surface from centre line and ℓ gives a reference length interval for the determination of the average along the scan path in direction x [Sc58].

The size of the reference length used here should be related to the geometry involved in the production of x-rays with such anodes (figure 3.12(a)). If one chooses the full 2 mm scan length as the reference length interval then any long-range deviation from centre line would be included in the roughness data. Such a variation could appear if the original anode surface was not plain but was slightly curved. With diagnostic x-ray facilities tube voltages of up to 150 kV are applied. Thus electrons with a maximum energy of 150 keV will penetrate the tungsten target up to a maximum range of about 30 μm . In a simple model x-rays can be thought being generated along the electron path and those emitted in the direction of the central x-ray beam, i.e. at 90° to the tube axis, will pass the anode surface at a length given by the projection of the electron range onto the anode surface. For an anode angle of 10° this gives about a maximum interval of 86 μm at the anode surface. For a rough surface that interval should be increased somewhat to include all patterns of electron penetration and x-ray absorption. Hence a reference length ℓ of 200 μm was thought to be appropriate to cover the effects of roughness for a range of typical anode angles ($\geq 10^\circ$) in diagnostic x-ray tubes. Greater reference lengths would include long-range surface deformations and increase the numerical values for R_a and R_g without being of consequence for the x-ray production geometry as opposed to mechanical friction where longer averaging intervals are

appropriate.

R_a and R_g were determined for consecutive intervals of 200 μm lengths along the profile and then averaged. The results are given in table 3.1. A mean ratio for R_g/R_a of 1.35 was determined which is quite close to a ratio of 1.25 expected for a gaussian distribution of the deviations ε from the centre line. Consequently for a characterisation of the surface roughness only the arithmetic average R_a was chosen. For most anodes roughness, the track for the small focus was larger than for the large focus due to the increase power densities applied. Anode #5 was obviously used with a much higher workload for the large focus. According to a manufacturer of tungsten anodes the finishes of anode surfaces are either obtained by sand blasting or grinding. The roughness of sand blasted surfaces is usually less than for ground surfaces. Roughness for the ground original surface of anode # 3 is well in the range for a roughness obtained with this surface finishing method.

Table 3.1. Arithmetic average R_a and root-mean-square average R_g of surface roughness obtained with a reference length of 200 μm and anode angle θ .

Anode #.	θ	Surface type	$R_a, \mu\text{m}$	$R_g, \mu\text{m}$
3	-	Initial finish (ground surface)	1.32	1.58
3	16°	large focus	2.05	2.69
3	16°	small focus	5.22	7.22
4	16.5°	large focus	2.70	3.51
4	16.5°	small focus	4.08	5.94
5	16°	large focus	4.09	5.35
5	16°	small focus	3.81	5.10
6	18°	large focus	4.89	6.19

3.5. X-RAY PRODUCTION IN ROUGH ANODES

Absorption of x-rays in the anode is determined by the penetration depth p of the electrons and the anode angle θ (figure 3.12a). When hitting the target of a plain anode, electrons having penetrated a distance p produce x-rays that travel an absorption length of

$$a = p \cdot \cot(\theta), \quad (3.1)$$

where θ is the anode angle. In this case, the absorption length is independent of the impact point of the electrons on the anode (figure 3.12a). For a rough surface, electrons enter the anode at arbitrary points with varying distances from the centre line. X-rays produced at a given depth will travel an absorption length that depends on the surface profile (figure 3.12b). For an increased roughness there is even a chance for the x-rays of re-entering the anode material a second or third time. Finally, the path length for a photon travelling in the anode bulk material will therefore depend on the position of the electron hitting the anode surface and the surface profile.

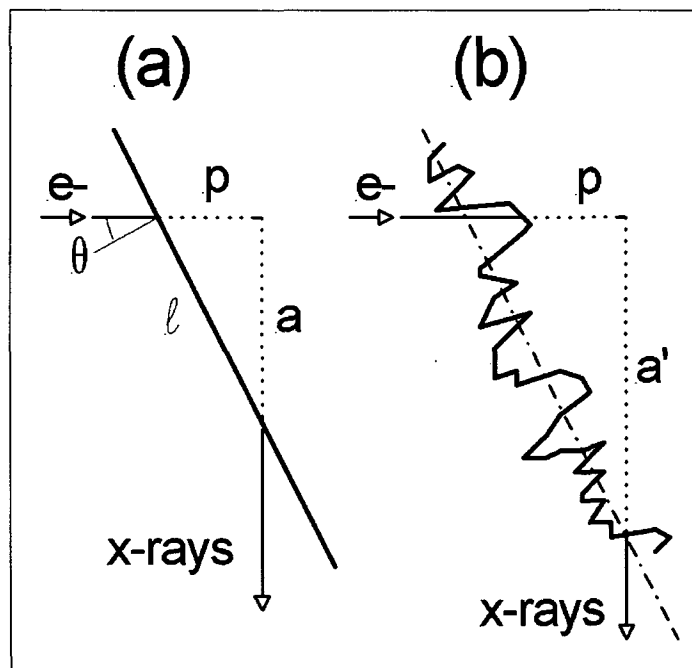


Figure 3.12. Schematic representation of x-ray production in anodes. Electrons hit the anode from the left (θ anode angle). With (a) plain surfaces x-rays produced at a depth p travel a distance a before leaving the target in beam axis, while (b) for a rough surface the distance a' depends on the position of the electron entering the anode and the position of x-rays escaping the target.

3.6. SIMULATION OF X-RAY SPECTRA

X-ray spectra were calculated using the same principles as in the computer code XCOMP5R from [No85] described in section 2. To include the effect of surface roughness on the total x-ray output individual x-ray spectra were generated for electrons entering the anode at random position along the surface profile. For each step in the

slowing down process of the electrons the absorption lengths in tungsten were calculated using the measured surface profiles. For each single electron the path was divided into 1 keV slowing down intervals. In each interval the x-rays generated were calculated, from the current penetration depth of the electron and the surface profile data the net x-ray path length in the anode bulk material was determined, and finally, the energy dependant absorption for the x-ray spectrum was applied. All spectra generated for the slowing down intervals were summed up and normalized to give the total spectrum for that surface profile. The number of electrons hitting the surface at random positions and consequently the number of calculated spectra ranged from 10000 to 40000 to obtain results for the absorption lengths with a stability of better than 0.5%.

As an illustration, two examples are presented in figures 3.13 and 3.14 to show the distribution of absorption lengths depending on slowing down of the electrons i.e. their penetration depth, and on surface profile. Figure 3.13 shows the results for the large focus of anode #4, which has the lowest roughness ($R_a = 2.70 \mu\text{m}$) and figure 3.14 gives the distributions for the small focus of anode #3 exhibiting the highest roughness amongst all samples investigated ($R_a = 5.22 \mu\text{m}$).

The distribution of absorption lengths were calculated for 90 kV tube voltage and three penetration depths of the electrons: first position is the electron entering the anode surface, i.e. the electron still carrying the full kinetic energy, the second distribution is calculated for an intermediate position with the electron slowed down to 50 keV, and finally the last distribution was obtained for the electrons coming to rest, i.e. 1 keV remaining kinetic energy.

For the electrons entering the anode (figures 3.13(a) and 3.14(a)) the distribution of absorption lengths is quite narrow coming close to the value for a plain anode obtained by calculating the absorption length using equation 3.1 and the Thomson-Whiddington relationship (equation 2.1) for the penetration depth p . Larger absorption lengths are not very frequent but could occur when the electron hits the anode in pitches of the surface. For larger penetration depths the distributions become much broader extending too much greater absorption lengths for the rougher anode with the average absorption lengths increasing with penetration depths.

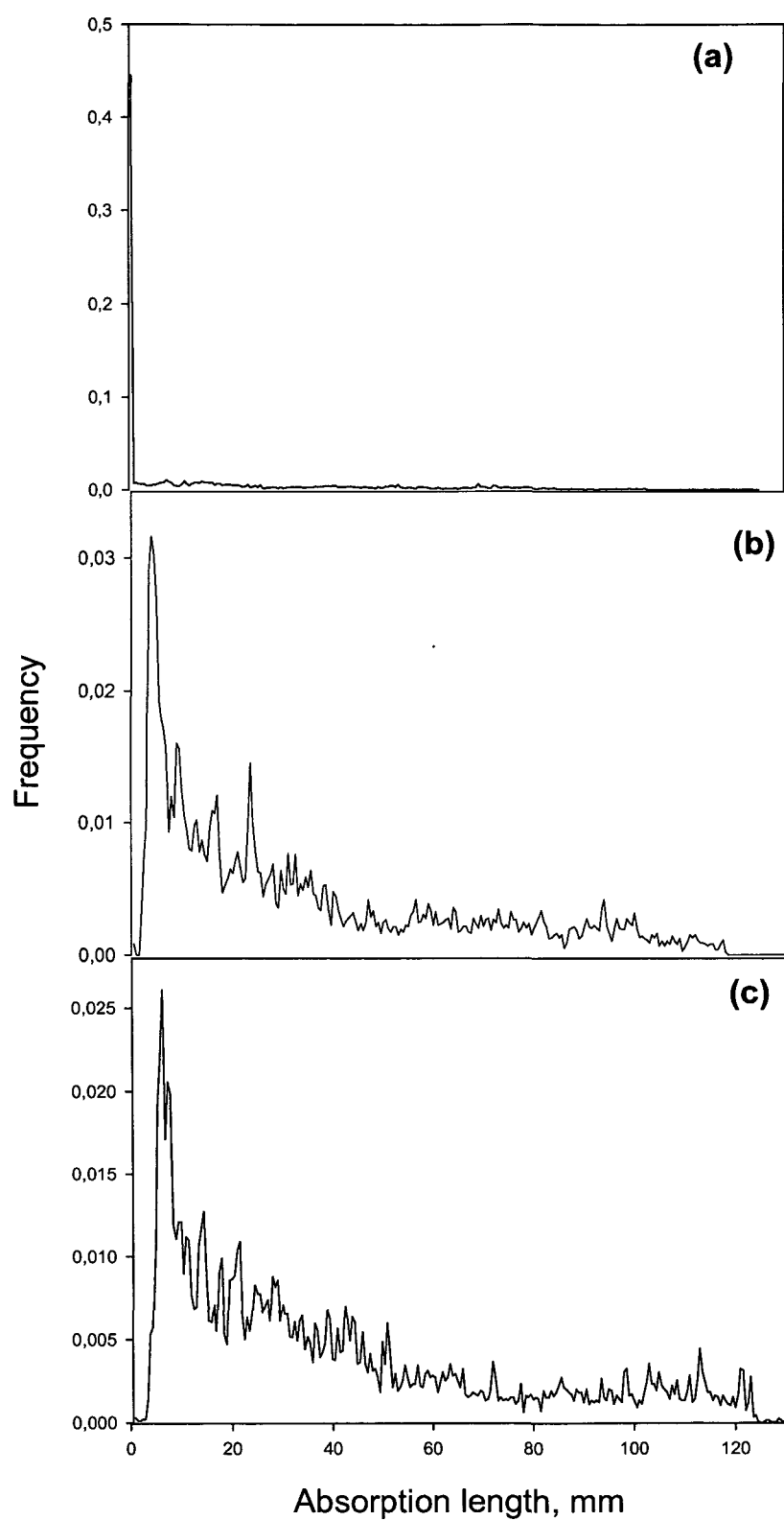


Figure 3.13. Frequency distribution of absorption lengths for anode # 4 (large focus) and for 16° anode angle, 100 cm distance, 90 kVp tube voltage, 2.5 mm Al filtration and 10000 electron events. The distributions are for electrons slowed down to (a) 1 keV, (b) 50 keV and (c) 90 keV

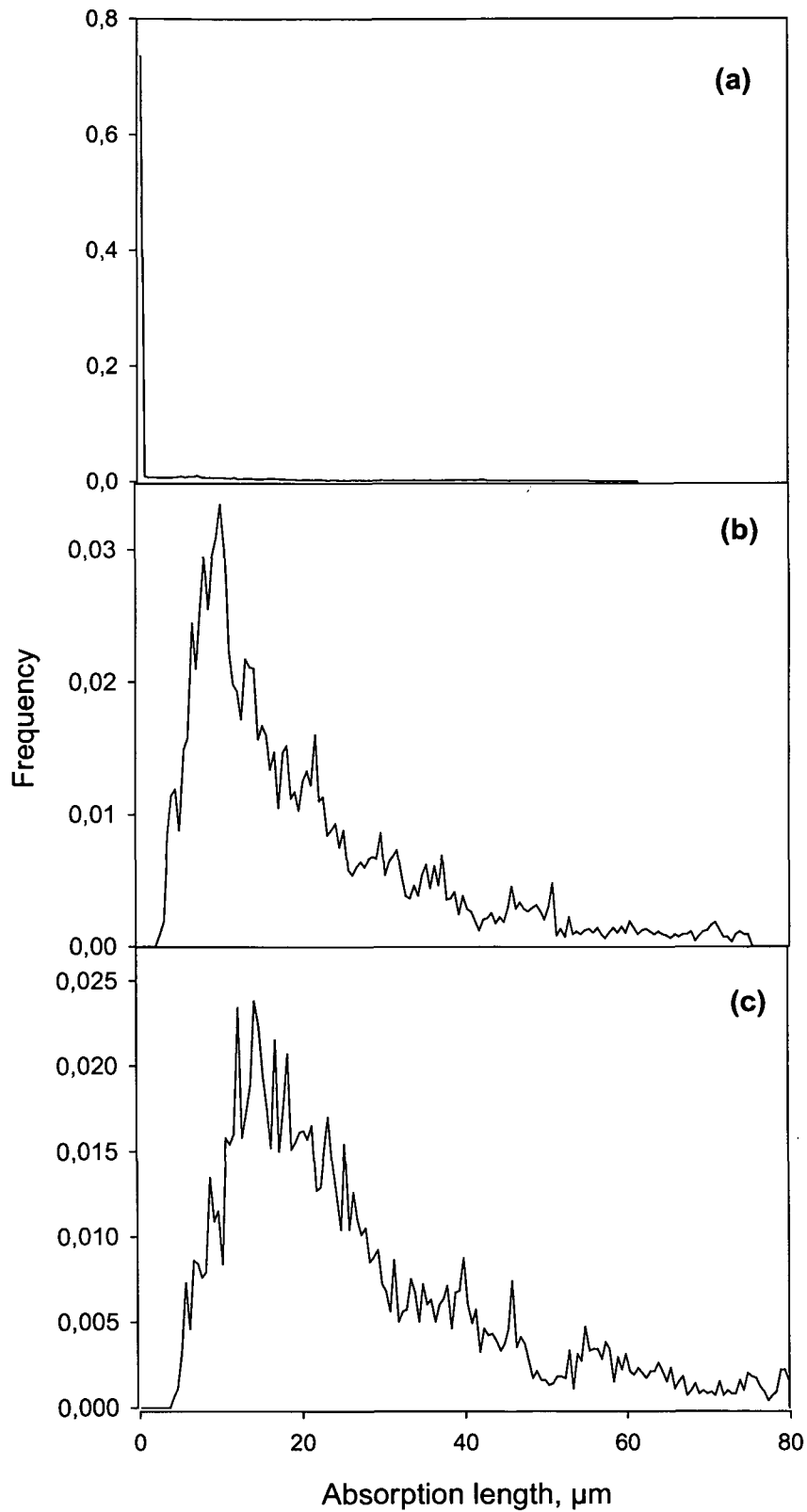


Figure 3.14. Frequency distribution of absorption lengths for anode # 3 (small focus) and for 16° anode angle, 100 cm distance, 90 kVp tube voltage, 2.5 mm Al filtration and 10000 electron events. The distributions are for electrons slowed down to (a) 1 keV, (b) 50 keV and (c) 90 keV

To illustrate the changes in absorption lengths introduced by rough anodes in comparison to plain anodes some results are shown for a 90 kVp tube voltage and electrons slowed down to 90, 50 and 1 keV. Tables 3.2 and 3.3 give the mean absorption length (AL_m) in the anode material obtained by the simulation using the measured surface profile, the Thomson-Whiddington absorption length (AL_{TW}) which is the absorption length for a plain anode, and the mean difference ($AL_{diff} = AL_m - AL_{TW}$). All these data are given for two different values of anode roughness and three different penetration depths of the electrons as given by figures 3.13 and 3.14.

Table 3.2. Calculated absorption lengths for plain anode (AL_{TW}) and roughened anode (AL_m) and the difference (AL_{diff}) corresponding to the additional absorbing length for the anode # 4 (large focus) with an anode roughness of $R_a = 2.70 \mu m$.

Calculated data	Electron energy, keV		
	90	50	1
$AL_m, \mu m$	4.00	20.48	27.01
$AL_{TW}, \mu m$	0.00	14.94	21.60
$AL_{diff}, \mu m$	4.00	5.54	5.41

Table 3.3. Calculated absorption lengths for plain anode (AL_{TW}) and roughened anode (AL_m) and the difference (AL_{diff}) corresponding to the additional absorbing length for the anode # 3 (small focus) with anode roughness of $R_a = 5.22 \mu m$.

Calculated data	Electron energy, keV		
	90	50	1
$AL_m, \mu m$	17.99	33.81	39.43
$AL_{TW}, \mu m$	0.00	14.94	21.60
$AL_{diff}, \mu m$	17.99	18.87	17.83

A comparison of results shows that the mean absorption lengths calculated for rough anodes is always larger than the absorption lengths calculated according to the Thomson-Widdington relationship for a plain anode (see equations 2.1 and 2.2). This increase in absorption length for rough anode surfaces can be thought of as an additional absorbing tungsten layer in x-ray beam direction. To obtain data for this additional absorption layer the differences AL_{diff} of absorption lengths for all the individual spectra calculated for the various electron paths were averaged to give a mean additional absorption length L_r for the rough anode (see figure 3.15).

3.7. ADDITIONAL TUNGSTEN ABSORBER

The dependence of the mean additional absorption length L_r in the anode on surface roughness is shown in figure 3.15. There is a clear increase of L_r with roughness with rather little dependence on tube voltage. The relationship of roughness R_a and additional absorption length L_r is not linear showing a steeper gradient for a larger roughness. The anode with the roughest focal track (5.22 μm with anode #3, small focus) yields a mean additional absorber thickness in direction of the x-ray beam of about 18 μm . L_r is consistently lower for the higher tube voltages over the whole range of R_a under investigation.

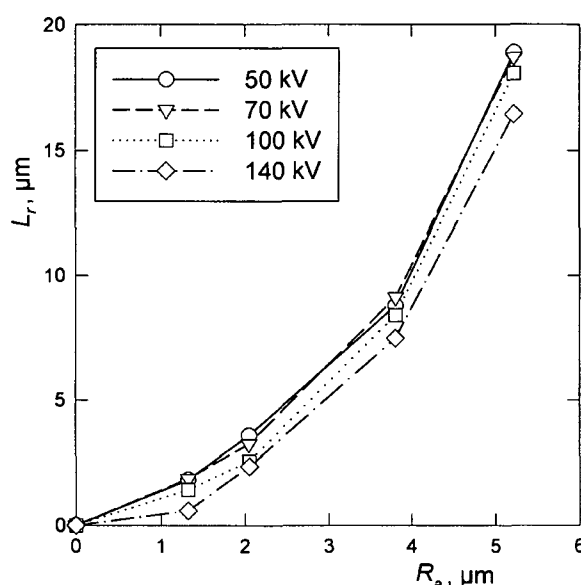


Figure 3.15. Thickness L_r of the additional tungsten absorber versus surface roughness R_a derived from simulated x-ray spectra calculated for tungsten anodes (anode angle 16°) and various tube voltages.

3.8. SIMULATED X-RAY SPECTRA

Spectra were calculated for an anode angle of 16° and tube voltages from 50 to 150 kV (no ripple) in steps of 10 kV for plain anodes and 4 selected surface profiles thus covering a roughness range of R_a from 0 to 5.22 μm . Finally, an additional filtration with aluminium was applied to the spectral data for filter thicknesses of 1 to 4 mm Al.

The calculated spectral distributions for the various anode surfaces are shown in figure 3.16. As can be expected from the increased filtration by the tungsten layer the x-ray output is reduced with increasing roughness of the anode surface. The reduction in intensity is largest at low tube voltages. The increasing absorption in the tungsten anode also gives a more pronounced appearance of the tungsten K-edge in the bremsstrahlung spectrum at 69.5 keV with increasing anode roughness (figure 3.16 b and c).

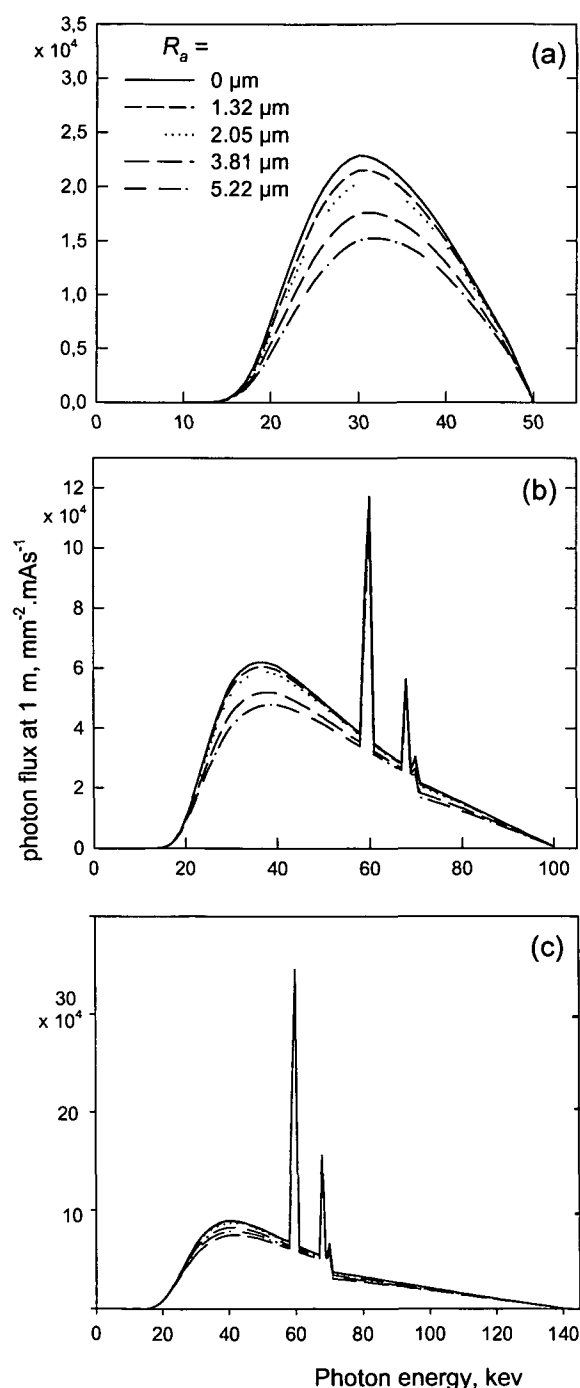


Figure 3.16. Calculated x-ray spectra for tungsten anodes with various degrees of surface roughness R_a for (a) 50 kV, (b) 100 kV and (c) 140 kV tube voltage (no voltage ripple, anode angle 16° , total filtration 2.5 mm Al, distance 1 m).

3.9. KERMA YIELD

Figure 3.17 shows the relative air kerma versus surface roughness. For all voltages the kerma output is clearly reduced for increasing roughness. This occurs most notably with low tube voltages as absorption for lower energy photons increases at lower photon energies due to the photoelectric effect. For a roughness of 5 μm the air kerma is reduced to about 67% of the output for a plain anode for 50 kV tube voltage, and to 88% for 140 kV, respectively.

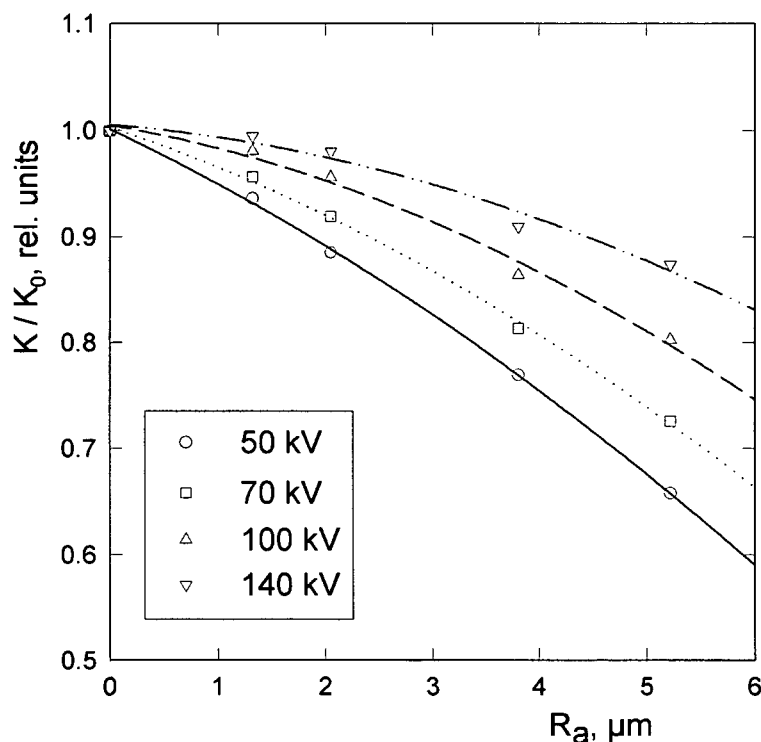


Figure 3.17. Air kerma K for tungsten anodes versus surface roughness R_a normalized to the air kerma, K_0 , for a plain surface calculated for tube voltages of 50, 70, 100 and 140 kV (no voltage ripple, anode angle 16° , total filtration 2.5 mm Al, distance 1 m).

If the data for the air kerma are normalized to the kerma at 70 kV tube voltage a comparison with measured data is feasible (figure 3.18). The kerma for a clinical x-ray device (BI150/12/59R-100 tube assembly and Polydoros 50S generator, Siemens, Erlangen, Germany) was determined with an ionisation chamber (DALi Dosimeter, PTW, Freiburg, Germany) in a low-scatter setup. The measured data fit well into the range of the simulated data.

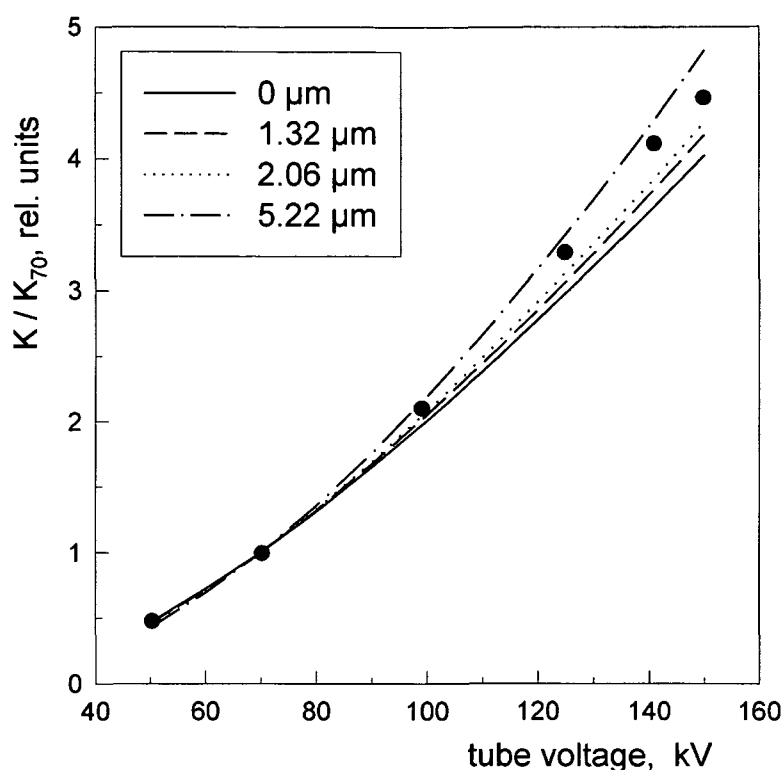


Figure 3.18. Air kerma K for tungsten anodes with various degrees of surface roughness normalised to the air kerma at 70 kV, K_{70} , versus tube. Dots (●) indicate measured data for a clinical x-ray unit (voltage ripple $\sim 3.4\%$, anode angle 16° , inherent filtration 2.7 mm Al).

3.10. EFFECT OF SURFACE ROUGHNESS ON THE FIRST HALF-VALUE LAYER

The effect of surface roughness, on the first half-value layer for aluminium (1. HVL), is shown in figure 3.19. Here, the HVL is plotted versus the total filtration (in mm Al) for various R_a and tube voltages. The pattern changes from low to high tube voltages: for low tube voltages an increased roughness gives increased beam hardening. At 150 kV and higher filtration the influence of roughness on HVL is cancelled while at lower filtration the trend is even reversed and rougher anodes produce a less hard spectrum.

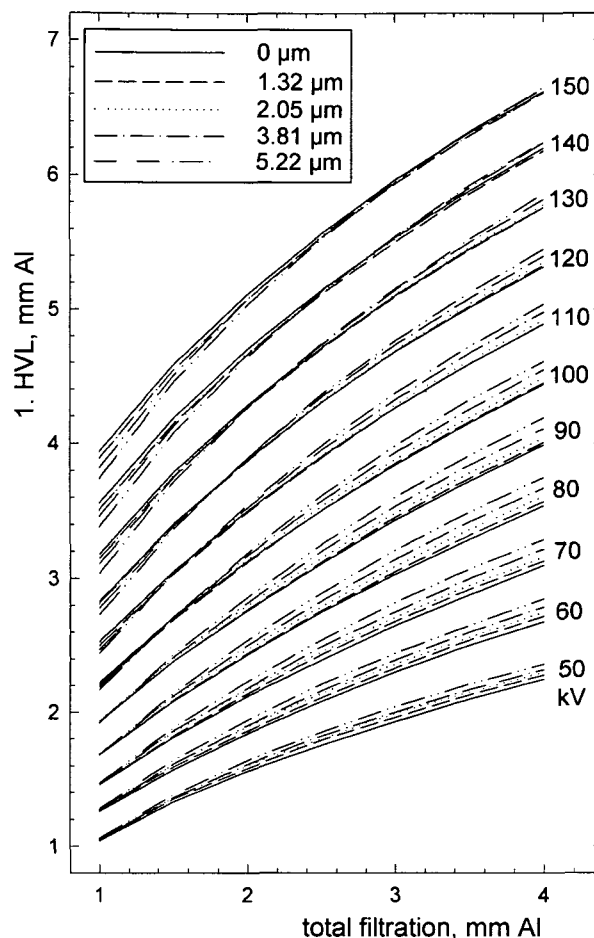


Figure 3.19. First half value layer for aluminium (1. HVL) versus total filtration for tungsten anodes with various degrees of surface roughness calculated from x-ray spectra for tube voltages of 50 to 150 kV (anode angle 16° , distance 1 m).

3.11. VARIATION OF THE MEAN PHOTON ENERGY

The variation of the mean photon energy in the x-ray spectrum is given in figure 3.20(a) showing the largest variation for 70 kV tube voltage. The maximum photon energy is then close to the K-edge of tungsten (69.5 keV). Still, the maximum shift in mean photon energy amounts to only about 1 keV for the roughest anode. For higher voltages the increased photon attenuation above the K-edge balances the increased attenuation at lower energies giving practically no variation with roughness of mean photon energy at a tube voltage of 140 kV. The pattern for HVL is very similar (figure 3.20(b)). A maximum increase in HVL of 0.2 mm Al was found at 80 kV tube voltage.

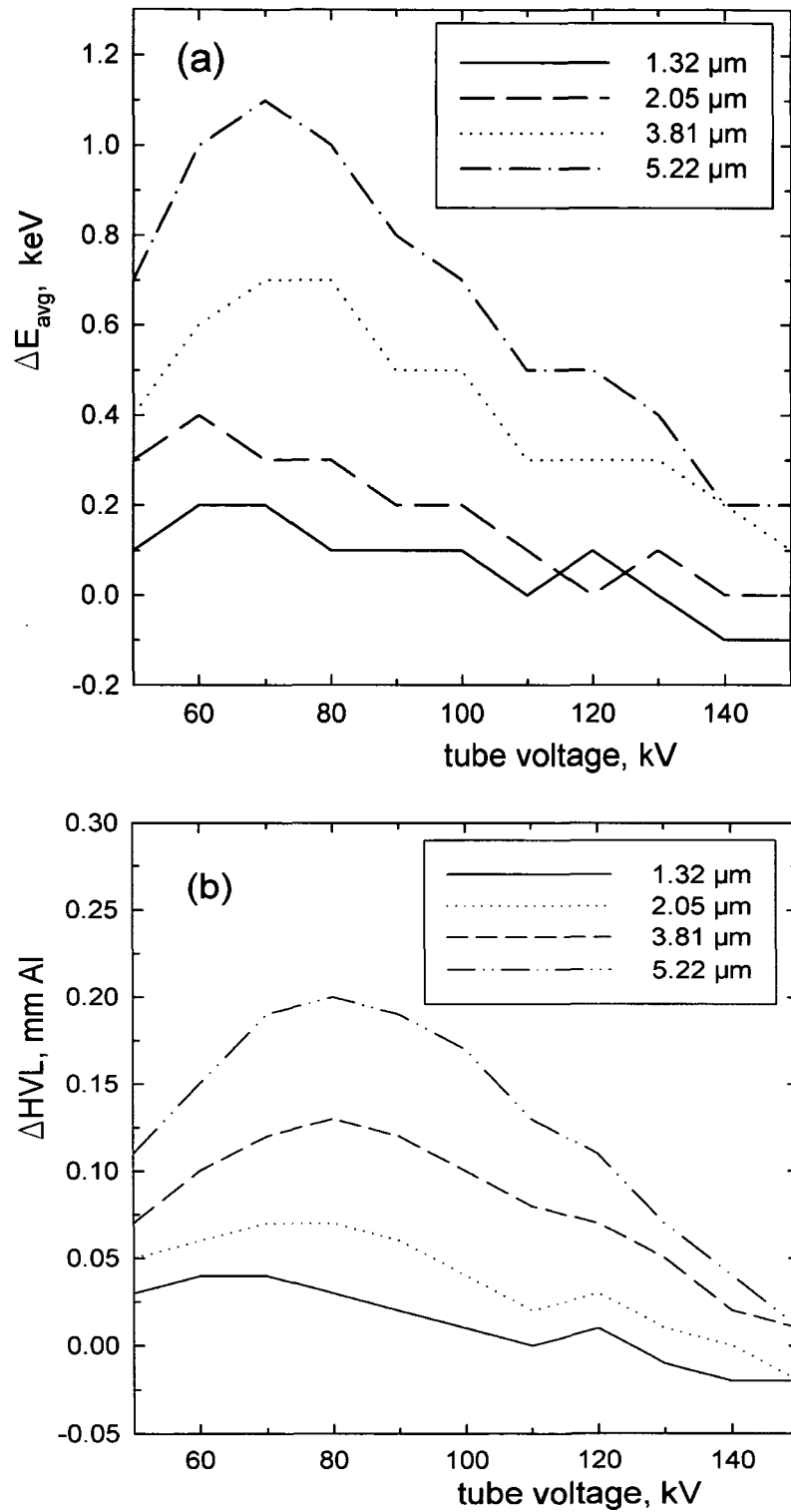


Figure 3.20. Difference in (a) mean photon energy ΔE_{avg} and (b) ΔHVL , for x-ray spectra calculated with roughness R_a and a plain anode vs. tube voltage (anode angle 16° , 2.5 mm Al, distance 1 m).

3.12. DISCUSSION

Investigating the effect of anode surface roughness on x-ray tube output with common clinical x-ray facilities without knowledge of the anode condition would be a difficult task. To better understand the potential effects, a simulation study based on measured anode surface data was performed. For the anode samples available, the surface roughness given as the arithmetic mean of the measured deviations from a centre plane in the surface profiles ranged from about 1.32 to 5.22 μm . While an initial finish of the surface roughness of around 1 μm is prepared by the manufacturers on purpose to avoid a rapid initial dose loss after installation of a tube, it is difficult to estimate the full range of roughness occurring with clinical units from the anode samples available in this study.

Taking into account the geometry of the anode surface and the x-ray beam, this roughness results in a mean additional filtration in tungsten of up to 18 μm thicknesses for anodes with an anode angle of 16° . The correlation of surface roughness and thickness of the additional tungsten filter showed little variation with the tube voltage. Tungsten deposits on the glass envelope of the x-ray tube have sometimes been taken as the source of additional filtration but the thickness of such layers were estimated to be less than 0.01 μm [St86] or much less than 1 μm [Na88]. A tungsten deposit of such a thickness is much less than the additional filtration due to roughness obtained from this simulation and certainly not sufficient to account for the attenuation of x-ray output.

X-ray spectral parameters were all obtained from spectra calculated for the anode surface profiles determined experimentally. For a comparison the roughness R_a of the anode was used as a parameter to characterize the effects on radiation output. All effects appearing in the simulated spectra follow from the increase in attenuation of the x-rays in the additional tungsten absorber. Both calculated x-ray spectra (figure 3.16) and air kerma (figure 3.17) reflect the increasing attenuation with surface roughness. The decrease in kerma with roughness depends on tube voltage and conforms to dose losses encountered with clinical x-ray tubes [El62], an effect also seen particularly with high workload devices as computer tomographs.

Changes in spectral shape are less pronounced than the reduction of kerma output. Taking the mean photon energy as an indicator, beam hardening increases with surface roughness in the lower tube voltage range. A maximum shift of about 1 keV is obtained for a tube voltage of 70 kV and 5 μm of roughness (figure 3.20). For higher tube voltages the increased absorption of photons with energies above the tungsten K-edge (69.5 keV) compensates somewhat the higher attenuation in the lower photon energy range giving less variation of mean photon energy with anode roughness. Further the mean production depths of low energy x-rays increase with tube voltage as the electrons penetrate farther into the anode. This reduces also the contributions to the spectrum at low energies adding further to a balance with high energy x-rays.

At 140 kV tube voltage the mean photon energy is practically independent of roughness due to this effect. Figure 3.21 gives a better illustration of the minute spectral changes obtained in this simulation showing spectra normalized to the maximum of the bremsstrahlung distribution. These variations due to anode roughness are small but give an indication of the uncertainty in spectral distributions encountered when measuring or comparing x-ray spectra for anodes of unknown condition. Differences in spectral shape on a similar scale as found in this simulation for variations of anode roughness are often discussed when comparing various measured or calculated x-ray spectra [Ca98], [Me00].

HVL is more sensitive to anode roughness than mean photon energy. As with mean photon energy the HVL shows its largest variation with tube roughness at tube voltages around 70 kV (figure 3.19). HVL increases with roughness by about 0.2 mm Al for x-ray assemblies with an inherent filtration of 2.5 mm Al and for an anode roughness of up to 5 μm . Increasing HVL has often been attributed to tube ageing [Na88] but Stears *et al.* [St86] do not come to such a conclusion from their measurements. There, an error in the determination of HVL of ± 0.1 mm Al is given. Hence a possible change in HVL due to roughness is in the range of the measurement error.

Conversely a determination of the inherent filtration with a variation in HVL of 0.2 mm Al would give an additional equivalent inherent filtration of about 0.3 mm Al due to roughness. Nagel [Na88] has determined experimentally the influence of tube

roughness on the relationship of HVL and total filtration giving similar results. At higher voltages the influence of roughness on HVL diminishes for the same reasons as with the variation of mean photon energy.

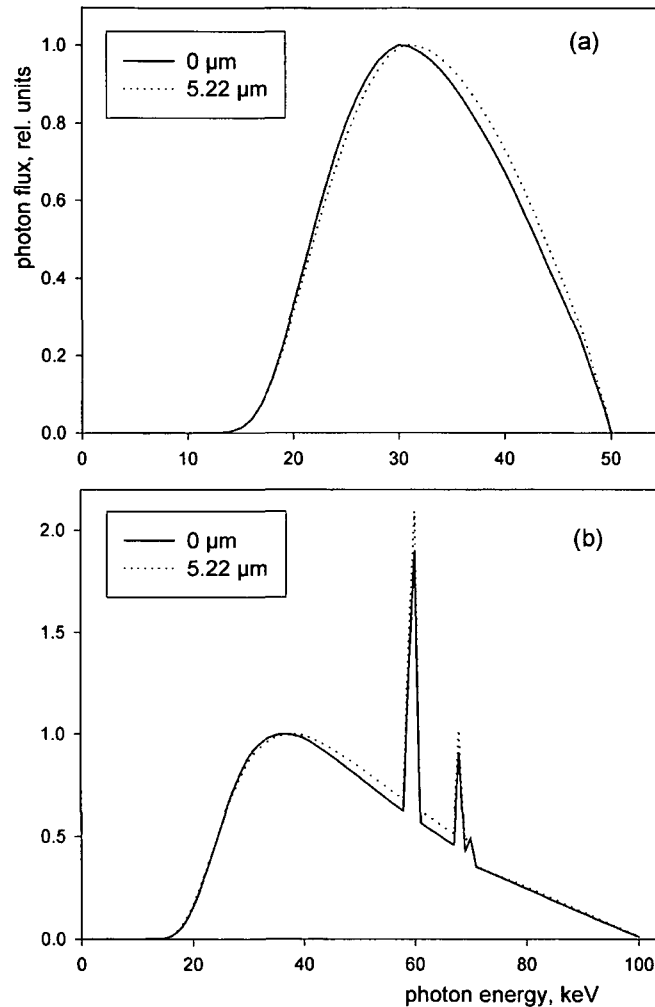


Figure 3.21. X-ray spectra for a plain anode (roughness 0 μm) and an anode with a roughness of 5.22 μm normalized to the maximum of the bremsstrahlung distribution calculated for tube voltages of (a) 50 kV and (b) 100 kV.

The data obtained for x-ray spectra and spectral parameters from this simulation should rather be taken as an indication of possible effects of anode surface deterioration due to tube ageing than final data. The number of measured surface profiles is limited and does not necessarily cover the range of roughness encountered with x-ray tubes. Unfortunately, in nearly all publications on x-ray spectra or spectral parameters for obvious reasons no indication is given on the tube workload or the condition of the x-ray tube. A further validation of the results is therefore hardly feasible.

4. DETERMINATION OF TOTAL FILTRATION USING A SPECTRAL MODEL AND ATTENUATION CURVES

4.1. INHERENT FILTRATION AS A PARAMETER FOR THE CHARACTERIZATION OF X-RAY UNITS

As already seen in the previous sections, attenuation by the absorbing material between the anode and beam exit is necessary to reduce radiation dose to the patient from the low energy x-rays in the spectrum. This is a basic concept used by many regulations, international standards and recommendations [IEC73, IEC84; ICRP34]. A measurement of the total filtration to ensure compliance with this concept is then recommended [ISO97]. As discussed in section 3 total filtration is variable depending on the state of the anode surface. In general total filtration will increase with tube usage. From this point of view it is also interesting to obtain information on the actual total filtration of an x-ray tube assembly.

Manufacturers have to guarantee the minimum values for the total filtration specified by the regulations but on the other hand exceeding the minimum filtration also means shortening of the life of the x-ray tube. Accurate methods for a measurement of the total filtration should therefore be available. The International Electrotechnical Commission [IEC76] has recommended a limit of +15% of the specified value of the inherent filtration.

As a direct measurement of the total filtration of the x-ray tube assemblies is not feasible, various indirect methods for its determination have been proposed [Ru49, Ar72, B 77, Th40, Su83, Po73]. All of these methods show some deficiencies mostly due to the unknown spectral distribution of x-rays and the variability of radiation quality with the continuing use of the x-ray tubes. This was the incentive to evaluate a new method for the determination of total filtration including the effects of anode surface deterioration. First, the methods used for the determination of total filtration will be presented.

This work will then focus on the development of a method for the determination of the total filtration that exploits the effect of anode surface roughness of x-ray tubes using a semi empirical approach. This method is based on the concept of an additional absorbing tungsten or aluminium layer to compensate for the effect of a rough anode surface from diagnostic x-ray units as explained in section 3.

4.2. EXISTING METHODS FOR THE DETERMINATION OF TOTAL FILTRATION

Almost all of the existing methods depend on an integral measurement of physical quantities related to the x-ray spectrum instead of an analysis of the emitted and filtered x-ray spectra. Some of these methods are described in detail by Rump [Ru49] and reviewed by Ardran and Crooks [Ar72].

4.2.1 X-ray spectrometry

X-ray spectrometry is usually regarded as the most accurate method for an indirect determination of total filtration (see e.g. [B 77]) comparing the spectra with reference spectra of known filtration. High-resolution photon spectrometry is a laborious method requiring special equipment. The instruments required are expensive and hardly mobile. Spectrometric methods are also time consuming and require a precise evaluation of the detector system's properties, in particular the photon detection

efficiency and the characteristic shapes of the pulse-height distributions versus photon energy. Further the applicability is restricted to kerma rates in the range of at most fluoroscopy conditions. At dose rates customary used in radiography the count rates obtained in a detector system exceed by far the capabilities of the most advanced pulse height analysis systems. Therefore energy dispersive x-ray spectrometry is generally not applicable, particularly in clinical environments, and restricted to specialized laboratories or manufacturers.

4.2.2 The extrapolation method

The concept of the extrapolation method [Ru49] is that the inverse value of x-ray kerma approaches zero for vanishing filtration. For a limited number of aluminium filters of increasing thickness t , the resulting kerma K is measured and then its reciprocal $1/K$ is plotted against the added filter thickness. The total filtration of the tube assembly under investigation, is obtained by extrapolating the graph towards zero of $1/K$ and taking its intersection with the abscissa (see figure 4.1)

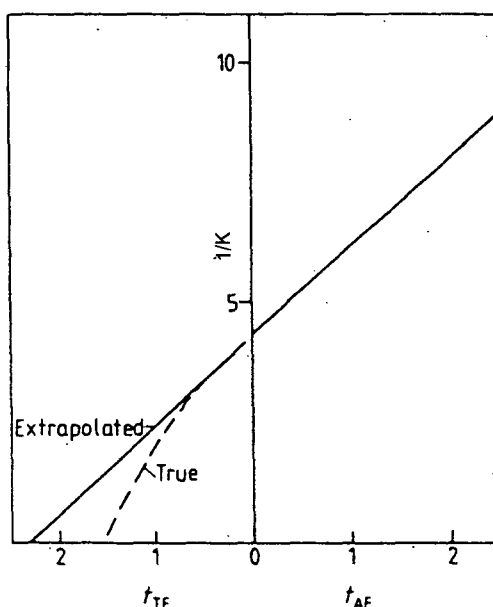


Figure 4. 1. Inverse of kerma plotted versus thickness of added filters

In contrast to all other indirect methods, no reference curves are needed to determine the filter thickness. Unfortunately, the plot of the inverse kerma does not show the expected linear relationship but rather attains zero value for a smaller

thickness of the added filter (see figure 4.1). This pattern is due to the absorption of the x-rays in the anode material, in particular a consequence of the L-absorption edge discontinuities between 10 and 13 keV. The extrapolation method provides an acceptable accuracy only for the determination of a filtration of up to 0.5 mm Al [Na88].

4.2.3 The comparison method

This method [Th40] stands for the comparison of attenuation curves with a so-called "standard-attenuation curve" which was obtained from an x-ray tube with known or negligible inherent filtration. The x-ray tube under investigation must be operated under identical conditions; the measured attenuation curve (which must be plotted on the same semi-logarithmic scale) is then shifted parallel to the axes of the reference curve until a reasonable fit is achieved. The difference on the abscissa between the origins of both curves, corrected for the inherent filtration of the reference x-ray tube, yields the total filtration t_{TF} (figure 4.2).

Most of the results and restrictions concerning the HVL method (see paragraph 4.2.7) also apply to this method.

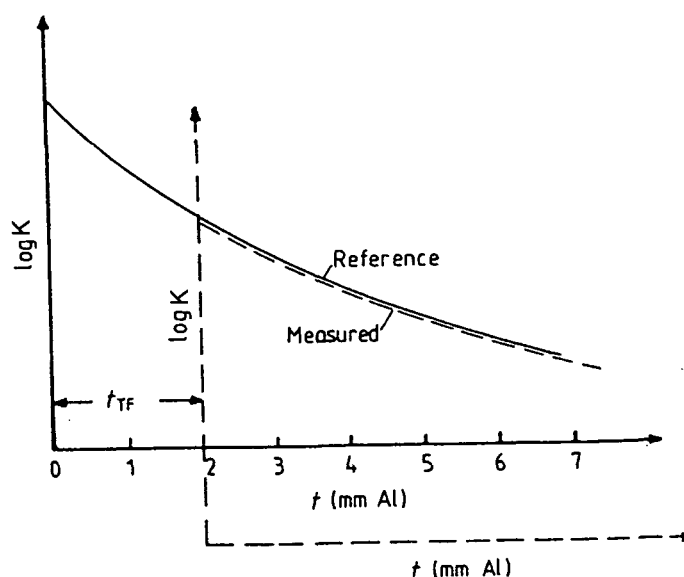


Figure 4. 2. Determination of total filtration by comparison with a standard attenuation curve, (the comparison method [Th40]). The filter thickness is obtained from the difference on the abscissa between the origins of the measured and the reference attenuation curves.

4.2.4 The dual detector method

In order to use this method described by Sutcliffe [Su83], a device is needed consisting of an ionisation chamber and a sodium iodine crystal scintillator which is optically coupled to a photodiode. If the crystal is sufficiently thick practically absorbing all photons, the second detector measures the energy fluence ψ , whereas the first detector monitors the kerma K . The signal ratio R represents a weighted average value of the mass-energy conversion coefficient η'/ρ of air which is depending on beam quality.

$$R = K / \psi = \frac{\int (\eta' / \rho)_{air} \psi_e dE}{\int \psi_e dE} = (\eta' / \rho) \quad (4.1)$$

Filtration is then deduced from a calibration curve for the tube voltage applied which could be determined with the same device. Like most other methods, the entire spectrum is used for the analysis. Thus, the dual-detector method is influenced by the same parameters as those that affect the accuracy of the HVL method described below in paragraph 4.2.7.

4.2.5 The K-edge filter method

This method, proposed by Bäuml [Bä79], requires the measurement of the signals S related to dose using three different test filters, two of them being so-called “K-edge filters” with a K-edge in the range from 20 to 30 keV. Test-filter thicknesses are matched for equal transmission of the spectral portions above the K-absorption edge of the filter with the highest Z . For a filter test consisting of tin (1), silver (2) and copper (3), the ratio of signal differences

$$Q = (S_1 - S_2) / (S_2 - S_3) \quad (4.2)$$

is largely determined by the low energy portion of the spectrum (see figure 4.3). Q can be related to the total filtration using a calibration curve.

The K-edge filter method, which appears to be very promising due to its energy selectivity, is extremely sensitive to measurement errors and filter mismatch. This becomes evident from equation 4.2, as the signal differences are much smaller than the signals themselves [Na88].

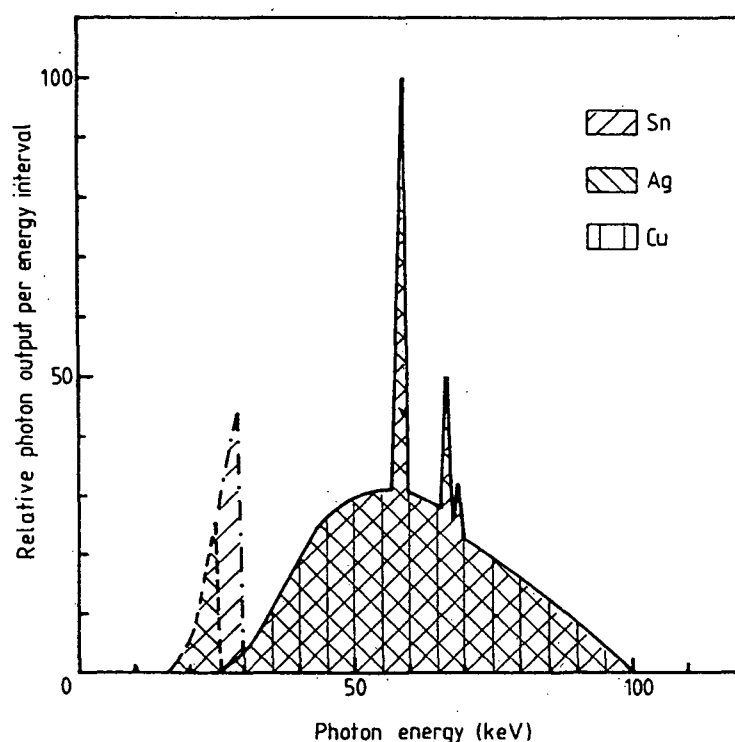


Figure 4. 3. Transmission spectra applying three different filters (tin, silver and copper) matched for equal transmission for the spectral portions above the higher K-edge; the difference in area between spectra 1 and 2, related to the difference in area between spectra 2 and 3, provides a measure for the total filtration (K-edge filter method [Bä79])

4.2.6 The homogeneity coefficient method

Procter [Po73] has proposed a method using the ratio of the first HVL to the first quarter-value layer (QVL) as a measure of the total filtration. This is closely related to the homogeneity coefficient, which is the ratio of the first to the second HVL. The presumption here is that the homogeneity coefficient is more dependent on filtration than on tube voltage, thus making this method more suitable than using HVL alone.

The experience of Nagel [Na88] has shown that the dependence on tube voltage is similar for both methods. In contrast to Procter, however, he found that the homogeneity coefficient varies only slowly with the total filtration, especially in the region of interest between 1.5 and 3 mm Al. This circumstance makes the accuracy of this method extremely dependent on even small measurement errors involved in the determination of HVL and QVL.

4.2.7 The HVL method

The “HVL method” is the most commonly used protocol for a determination of total filtration [ISO97, Ru49, Re60, Ar72]. It uses a so-called “quality diagram”, i.e. the relationship of HVL versus total filtration data as a reference curve (see figure 4.4). It is essential that the tube assembly under investigation is almost identical to and operated under the same conditions as the reference tube from which the quality diagram is obtained.

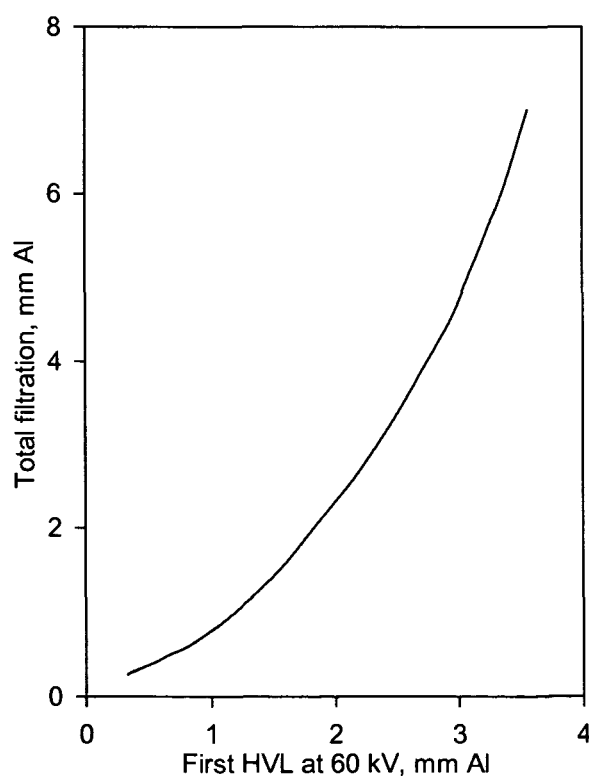


Figure 4.4. “Quality diagram”, i.e. the graph showing the relationship between filtration and HVL, which is used to deduce the total filtration from the HVL measured at 60 kV (HVL method [ISO97]). This curve taken by ISO comes from [Ta59].

The procedure uses quality diagrams; it is described in an ISO Standard [ISO97]. The attenuation curve is first measured using aluminium absorbers of high purity at a tube voltage of 60 kV. A purity of 99.9% is regarded as sufficient [ISO 2092]. Aluminium absorbers should be made of sheets from alloys 1100 or Al99.9. The first HVL is then determined from the attenuation curve. Finally, the corresponding total filtration for that HVL is retrieved from the quality diagram. For that purpose the ISO Standard [ISO97] recommends a quality diagram (figure 4.4).

The accuracy of this method depends on the availability of accurate quality diagrams appropriate to the conditions of measurement, i.e. target angle and voltage ripple of the x-ray set. The HPA [HPA77] has published quality diagrams for 22° tungsten targets for constant potential. Another set of data has been provided by Pasternack and Blatz [Pa65] covering x-ray units with full-wave rectification generators. However, the target angle has not been specified. Birch et al. [Bi79] have provided data for diagnostic x-ray sets with 17° tungsten targets at constant potential in a tube voltage range from 30 to 140 kV. However, a major limitation is that such data are not available for the full range of diagnostic target angles (6-22°) and the type of voltage waveform ripple encountered in practice.

In addition, Nagel [Na88] showed that the HVL method allows only for a rough estimation of the filtration and could typically give errors of up to $\pm 30\%$. Various relevant parameters such as tube voltage, tube voltage waveform, anode material, anode angle, anode roughening, composition of filtration, measurement geometry and methodology of dosimetry can contribute to the large discrepancies encountered in the results of the determination of total filtration.

While most of these influencing parameters can be controlled by measurement and proper maintenance, the assessment of anode surface roughness due to tube ageing having a significant effect on the inherent filtration of an x-ray tube (see section 3) would at best be feasible on experimental facilities but not with routine x-ray units. To the best of our knowledge, this has not been considered thoroughly in the literature. Nagel [Na88] has determined experimentally variations in HVL of up to 0.5 mm Al at 80 kV and 2.5 mm Al filtration due to anode roughness. However, a larger range of roughness, due to tube ageing, can be encountered in x-ray tubes.

A comparison of some of the many quality diagrams published shows large discrepancies, as demonstrated in figure 4.5. To give an indication of the variability in the total filtration deduced, a determination of filtration from a first HVL of 2.0 mm Al results in a total filtration between 1.7 and 3.0 mm Al, depending on the diagram used. Hence, filter thicknesses obtained from a measured HVL of 2 mm Al can differ by up to 60%.

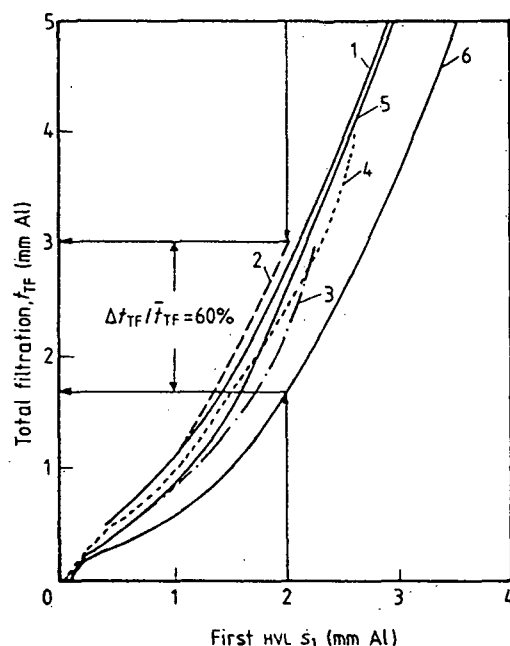


Figure 4. 5. Quality diagrams produced at 60 kVp from: (1) Rump [Ru49]; (2) Trout et al. [Tr56]; (3) Shaal [Sh74]; (4) Wachsmann and Drexler [Wa76].

4.3. A FIT METHOD FOR THE DETERMINATION OF TOTAL FILTRATION USING A SPECTRAL MODEL

Except for a direct comparison of x-ray spectra all methods for a determination of total filtration rely on global measured quantities as HVL. As experience has shown total filtration is not necessarily constant but increasing to some degree with the lifetime on an x-ray tube. The most important factor contributing to this is anode surface roughening as described in section 3. The state of the anode surface cannot be judged upon by any kind of inspection except by an evaluation of the tube output. Using the concept described in section 3 of an additional layer of tungsten taking care of the additional filtration due to surface roughness a method for the determination of total filtration was devised where first the spectral output is calculated using an algorithm as

described in paragraph 4.3.3, and then the output is attenuated by the inherent filtration and a variable additional layer of tungsten. The thickness of the additional filter is then optimised as to give a best fit to attenuation curves measured for that x-ray unit. Since the total filtration is usually given in terms of an equivalent thickness of an aluminium absorber, the same fitting process was also performed using aluminium instead of tungsten as the filter material for the additional filtration.

The calculated tube output considers all the specific parameters of the x-ray unit as anode angle, tube voltage, voltage ripple, nominal filtration and source to detector distance. The algorithm used for the calculation of the spectral tube output and its derived parameters (HVL, kerma, etc.), is the same as used in XCOMP5R [No85] but has been extended to include voltage ripple in the calculations. To obtain that functionality the tube voltage trace was divided into time segments of typically 1 kV step width in voltage (see figure 4.6). For the tube voltage in each of the time segments the x-ray spectrum is calculated. Finally, a weighed average of all spectra is obtained using the lengths of the time segments as the appropriate weights.

Several types of voltage waveforms are available in the program as DC, 1-, 2-, 6-, 12-pulse voltages and converter generator waveforms. The high-voltage generator type used in all x-ray units under investigation was a converter generator. This type of generator produces similar voltage ripples as 12-pulse generators, i.e. typically 3.4%. This ripple in essence should be constant but for technical reasons could vary somewhat with tube loading (tube voltage and current). Overall computing time is substantially increased when taking into account voltage ripple as compared to DC-voltage.

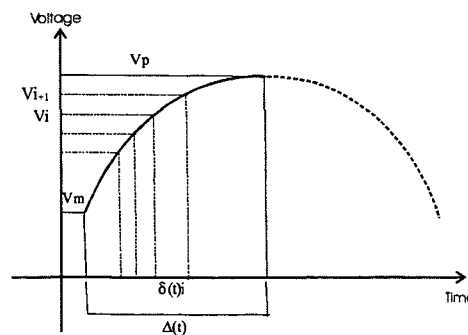


Figure 4. 6. Schematic diagram of the trace of a voltage waveform. The tube voltage rises from the minimum voltage V_m to the peak x-ray tube voltage V_p . V_i denotes the voltage and $\delta(t)_i$ the time interval of the i^{th} segment. $\Delta(t)$ is the total time interval considered as the following part of the waveform is symmetrical to the first half.

4.3.1 Measurement of attenuation curves

An establishment of an attenuation curve involves the measurement of air kerma with a suitable dose detector. In diagnostic radiology kerma measured free in air is still the quantity measured as the energy dependence of such detectors is known and suitable ionisation chambers are available. In contrast to some solid-state detectors, drift with time does not occur. For this measurements a 1cm³-flat ionisation chamber type M77334 with a UNIDOS Electrometer from PTW (Freiburg, Germany) were used. Calibration factors and correction factors for the energy dependence of the ionisation chamber traceable to PTB, Braunschweig, Germany, were used as given in the calibration certificate by the manufacturer for some radiation qualities from the DV- and DN-series (see table 4.1) [DIN01]. These series reflect tube exit spectra and x-ray spectra filtered by a patient and correspond to the RQR- and RQA-series defined by IEC [IEC94]. For intermediate voltage settings appropriate correction factors were obtained by interpolation according to HVL. For that purpose the correction factors k_C are plotted versus HVL in figure 4.7 together with a polynomial regression of order 4 ($k_C = 1.26 - 1.46 \cdot \text{HVL} + 3.11 \cdot \text{HVL}^2 - 3.5 \cdot \text{HVL}^3 + 1.45 \cdot \text{HVL}^4$). To account for the energy dependence of the ionisation chamber in the measurements, corrections according to the actual HVL were applied to all kerma readings.

Further, ionisation chamber readings were corrected for temperature and air pressure according to $k_{TP} = \frac{p_0(273.2 + t)}{p(273.2 + t_0)}$ where $p_0 = 1013$ hPa and $t_0 = 20^\circ\text{C}$ are the reference values of air pressure and temperature, respectively, given in the calibration certificate.

Table 4. 1. Characterisation of standard radiation qualities RQR and RQA [IEC94].

Radiation quality	KVp, kV	Filter, mm Al	HVL, mm Al
DV50	50	2.5	1.6
DV70	70	2.5	2.2
DV90	90	2.5	3.0
DV120	120	2.5	3.6
DV150	150	2.5	4.6
DN50	50	12.5	3.70
DN70	70	23.5	6.70
DN90	90	32.5	9.14
DN120	120	42.5	11.55
DN150	150	50.0	13.34

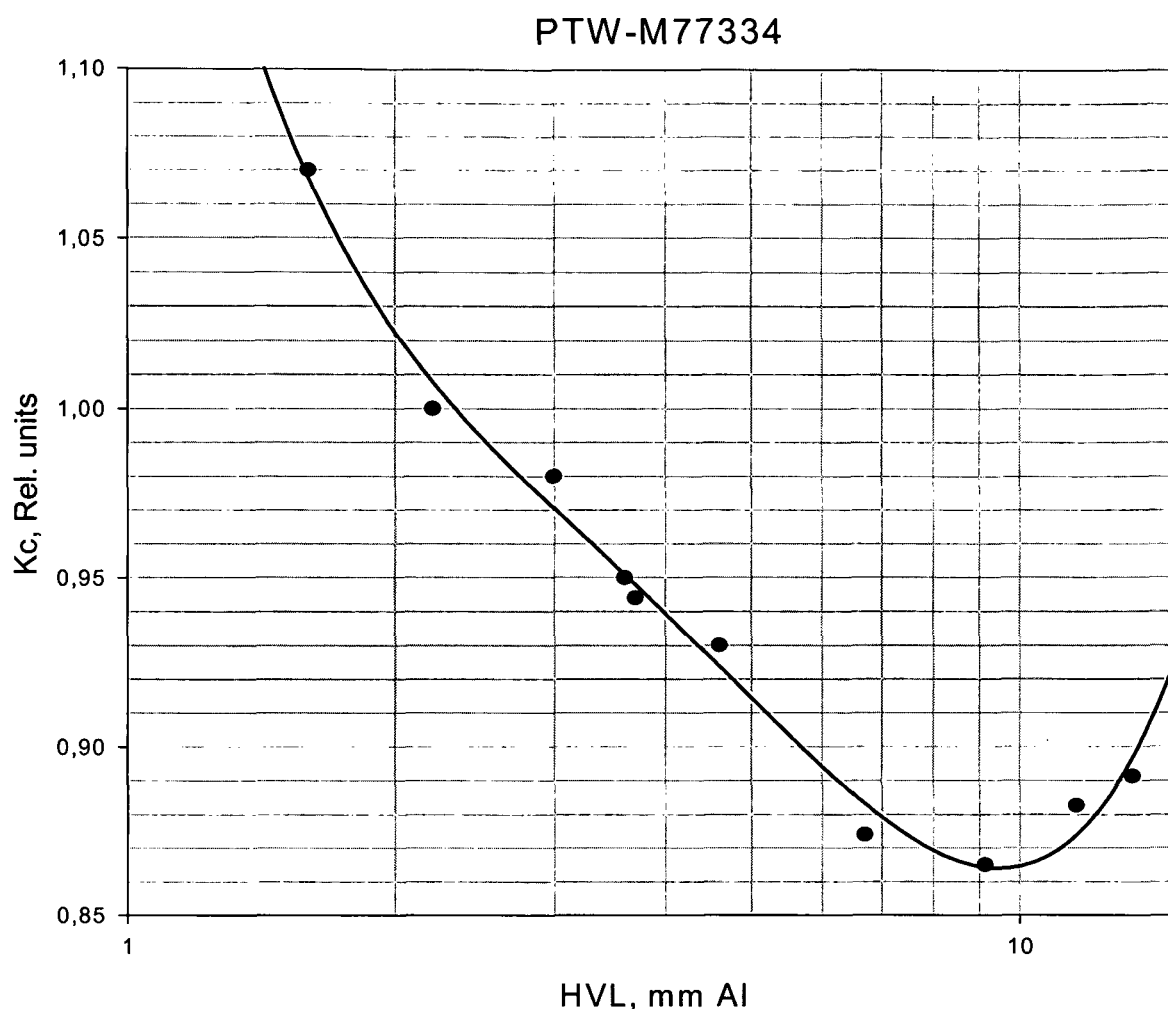


Figure 4. 7. Correction factors k_C vs. HVL giving the energy dependence of the ionisation chamber type M77334 according to the manufacturer (PTW, Freiburg). k_C is given relative to the sensitivity of the ionisation chamber at 70 kV and DV-radiation quality.

The attenuation measurements were performed in a low radiation scatter setup as recommended by [IEC94] (see figure 4.8). Indeed, consideration was given to the conditions required to minimize the influence of the scattered radiation emitted by the attenuator, which would otherwise increase the HVL. In order to minimize the influence of scattered photons, the following conditions have been observed: limiting the field size to reduce the amount of scattered radiation that would reach the ionisation chamber, but the field being large enough so that the x-ray beam covers entirely the chamber. A circular lead diaphragm of 5 mm thickness was used for beam limitation and definition of the primary beam.

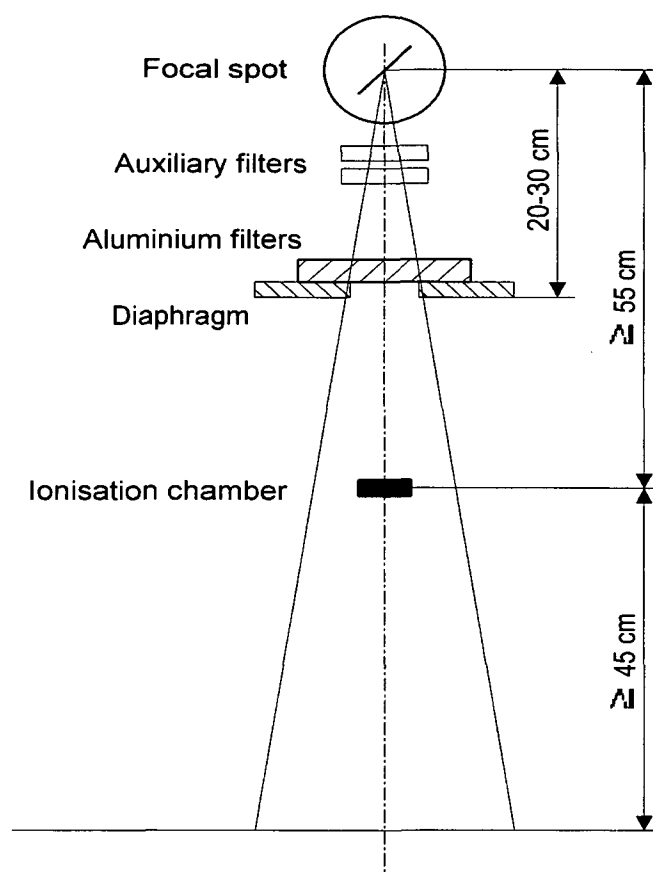


Figure 4. 8. Set-up for the measurement of attenuation curves. Standard radiation qualities are achieved with aluminium filters (see text). Distances as given in the figure were adhered to in all the measurements made.

Aluminium absorbers of variable thickness were placed on top of the diaphragm. The distance from the aluminium absorbers to the ionisation chamber was at least five times the diameter of the beam at the measurement point. Aluminium absorbers were of high purity (99.999%).

For each x-ray unit a series of measurements were made to determine attenuation curves for a number of tube voltages and filter thicknesses. To obtain an appropriate correction factor for each measurement one has to keep in mind that HVL changes with aluminium filter thickness. Accordingly the correction factors had to be determined for each single measurement. This was achieved by a method of successive approximation. An attenuation curve was first obtained in terms of the observed readings without correction. Then a first correction was applied according to the apparent HVLs for each measurement in the curve using interpolated data from figure 4.7. This process could be repeated, approaching final attenuation curves after some

iterations. In practice, a single approximation gave sufficiently accurate results in most cases. Figure 4.9 shows a typical example for an attenuation curve obtained.

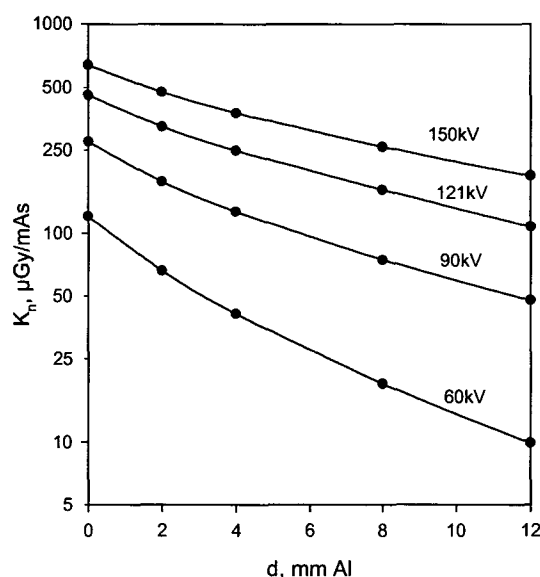


Figure 4. 9. Typical attenuation curves obtained for unit #1 (BMTP28). Normalized air kerma K_n ($\mu\text{Gy/mAs}$) is plotted versus added filter thickness d (mm Al) for a selection of tube voltages.

X-ray output measurements are subject to errors that need to be evaluated in order to estimate the quality of a result of a measurement. The achievable accuracy in attenuation curve measurement depends on the instruments used and the experimental technique applied. Consideration must be given to all sources of errors in interpreting whether the determined attenuation curve is acceptable.

The overall uncertainty related to attenuation curve determination includes uncertainties in the consistency of the kerma output, the accuracy of tube voltage applied to the tube, the linearity of kerma output with tube current or mAs, the thickness of the aluminium filters, the energy response and accuracy of the instrument used for kerma measurements and finally the experimental setup, i.e. the contribution to kerma by scattered radiation, which can be minimised by an appropriate technique.

The following factors contribute to the accuracy of the output measurements:

- Distance: due to the inverse relationship of kerma with squared distance a determination of the absolute kerma yield of an x-ray unit depends on the

accuracy of a determination of distance. The main problem is in this case to determine the location of the tube focus. Further the reference point of the ionization chamber has to be known. Since attenuation curves are obtained by relative measurements, i.e. kerma referred to the kerma with the unfiltered radiation, an accurate knowledge of distance within limits is not required as the solid angle for all measurements made is the same. Attenuation in air needs not be considered here for the photon energies involved and small variations in distance.

- Thickness and purity of aluminium filters: aluminium filters with a nominal thickness of 1 mm and 99.999% purity were used (Goodfellow Cambridge Ltd., England). The thickness of the filters was determined by a measurement of surface area for each filter along with its mass. The thickness was then calculated using the density of pure aluminium (2.699 g/cm³). For all single sheets the thickness agreed within 0.3% of the nominal thickness. A stack of 12 sheets gave a difference in thickness of less than 0.1%. A maximum variation in kerma output calculated using the code XCOMPW was found to be less than 0.08% in all cases when applying 0.3% of variation in aluminium filter thickness. A pile of 12 sheets with a maximum variation of 0.1% in thickness gave negligible variation in kerma output.
- Calibration accuracy: the accuracy of the calibration factor for the ionisation chamber together with the electrometer including the variation with photon energy was given in the calibration certificate by the manufacturer as $\pm 5\%$. The indicated uncertainty corresponds to the double standard deviation ($k=2$). For a coverage factor $k=1$ the uncertainty will be $\pm 2.5\%$.

Air density correction for the ionisation chamber: the mass of the air in the cavity of a vented ionisation chamber is subject to variations in temperature and air pressure. This is accounted for by applying a correction factor k_{TP} , which converts the cavity air mass to the mass under reference conditions (usually 20°C and 1013.25 hPa). Air pressure was measured using an electronic barometer type DIGITRON 2025P (SIFAM Ltd., Torquay, England) and temperature was determined with an electronic

thermometer type 175 (PTW, Freiburg, Germany). The accuracy of the correction factor k_{TP} was estimated as less than 0.2%.

- Reproducibility of radiation output: since no reference monitor was used in the measurements, a satisfactory stability of the radiation output is essential. Due to possible thermal drifts or instabilities in the electronic circuits, changes in the kerma output could appear. The consistency of the x-ray beam output was therefore determined by taking 10 measurements of air kerma per mAs at 1 m distance for selected tube current-time-products and voltages resembling the actual measurements. Typical results obtained with an x-ray unit are shown in table 4.2

Table 4. 2. Reproducibility of radiation output given as the average for normalized air kerma at 1 m distance together with standard deviation and relative variation for 10 measurements each.

Tube voltage kV	Current-time- product, mAs	Normalized air kerma, $\mu\text{Gy/mAs}$	Standard deviation, $\mu\text{Gy/mAs}$	Rel.variation, %
60	5	36.80	0.670	1.82
	50	38.40	0.520	1.35
	100	38.74	0.135	0.35
90	5	90.40	1.240	1.37
	50	92.90	0.094	0.10
	100	92.97	0.067	0.07
125	5	173.00	1.054	0.61
	50	172.72	0.107	0.06
	100	172.94	0.092	0.05

As it can be seen from this table the results show a range of standard deviations in the measurements changing with tube current-time-products. For low current-time-products the inaccuracies in the short exposure times for the falling load mode gives a larger variation of tube output than for larger mAs values. This mode provides the highest available tube current allowed by the x-ray tube, with an automatic continuous decrease in current during the exposure to avoid overheating the tube leading to very short exposure times for low mAs values. Fluctuations from switching short exposure times will then mainly affect the accuracy of the x-ray output. It is

thus advisable to make measurements of radiation output using higher mAs values, respecting however the limits of the maximum permissible tube loading for the tube voltage used. This has been taken into account in the course of our measurements by using exposure parameters that give less than 0.5% variation in tube output.

- Linearity of tube current: measurements were carried out to verify if the kerma output varies linearly with the tube current-time product (mAs). Typical results achieved for an x-ray unit are shown in figure 4.10. As it can be seen linearity of air kerma yield with tube current-time-product is well achieved above 10 mAs (figure 4.10.a). It is therefore advisable to use tube current-time-products with values above 10 mAs respecting again the limits of the maximum permissible tube loading for the tube voltage used.

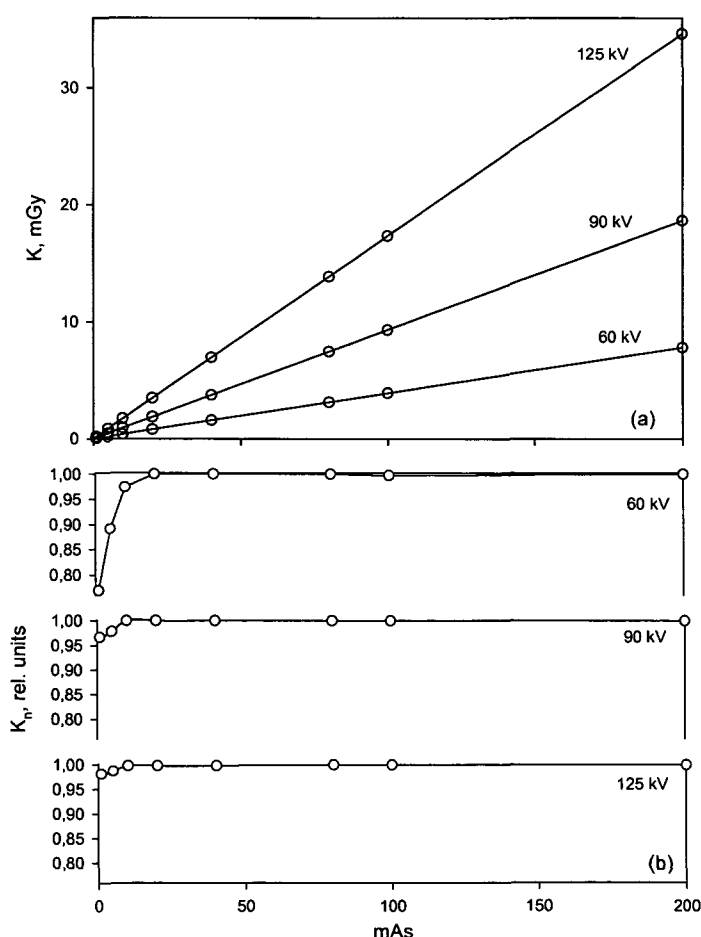


Figure 4. 10. Typical linearity of radiation yield with current-time-product for a selection of tube voltages given as (a) air kerma K , and (b) normalized air kerma K_n versus current-time-product (#1-BMTP28, see table 4.5).

The reduction in output observed at lower mAs values could be explained by the fact that when switching short high voltage pulses, the rise and fall times of the tube voltage are of a similar magnitude than the actual pulse width at nominal voltage. In particular the fall time is determined by the capacitances at the high voltage terminal of the generator. During the rise and fall of the tube voltage softer x-rays with less radiation yield will be produced contributing to the total output (see figure 4.11). This is probably responsible for the drop of the integral output related to mAs. The error is estimated to be less than 0.2% in the range used.

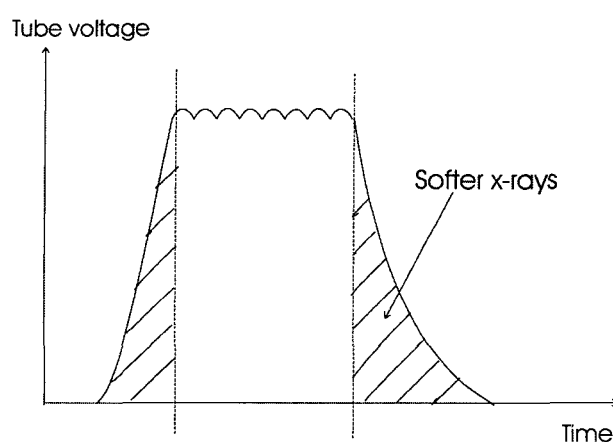


Figure 4. 11. Schematic diagram of a short pulse signal showing a gradual rise of tube voltage to the maximum value and its decrease back to zero.

Considering all the error sources investigated here a calculation of the error propagation will be dominated by the calibration factor accuracy (2.5%) and the reproducibility of radiation output (0.5%) giving an estimate of 2.6% for the global uncertainty for the kerma output determination ($k=1$).

For each x-ray unit, attenuation curves were plotted for a selection of three tube voltages ranging from 60 kVp to 125 kVp. The lowest energy for the tube voltage of an x-ray unit i.e. 40 kVp was not used to avoid longer time of exposure and the highest energy i.e., 150 kVp was also not used to avoid excessive tube loading. In the course of the measurements it was found that it was sufficient to have available attenuation curves measured for three different tube voltages. A larger number of curves resulted in only little improvement in the agreement of the data fit and it was therefore considered sufficient for the purpose of this work. A larger number of measurements for more

attenuation curves would result in excessive tube loading and measurement time with a clinically used x-ray unit.

Added filtration was achieved with aluminium sheets of 99.999% purity in the range from 2 to 12 mm in order to cover the set of DN-radiation qualities (table 4.1).

An important factor in the course of the measurements is the tube loading resulting from the exposures. Since for exposures with high filtration the mAs-values required could become quite large. Hence, one has to take care that a series of exposures will not result in an overloading of the tube with possible adverse effects and damage to the anode or tube. It was therefore always taken care not to exceed the limits specified for the tube assembly in the x-ray units under investigation. The tube rating charts given by the manufacturers were used to determine the appropriate cooling times according to tube voltage and mAs-value chosen. In case the generator did not indicate any cooling time at all the cooling times determined from the tube-rating chart were still observed to avoid any chance of impairing the condition of the tube. The limits for tube current and voltage in a given exposure are usually taken care of by the generator not accepting parameter settings on the console, which would lead to an excess tube loading within one exposure.

Manufacturers also recommend a warming up sequence of exposures particularly after a long idle time to prevent the electric surges and breakdown of the tube. When measurements were started with an x-ray unit with a 'cold' tube a series of low-kVp and low-mAs exposures were made first before any exposures with high load and high tube voltage were made.

The electrometer together with the ionisation chamber was warmed up for 5 minutes as specified by the manufacturer before making any measurements of kerma. Zeroing the electrometer was also performed according to the manufacturer's recommendations. Considering all of the above constraints, total duration for a set of measurements was about one hour for each x-ray unit.

4.3.2 Measurement of tube voltage

In the course of the experimental work it turned out that tube voltage is an essential parameter for the accuracy of the data interpretation. Tube voltage was therefore verified for the x-ray units involved.

Measurement of tube voltages was made using the NERO™ mAx Model 8000 x-ray multimeter (Cardinal Health, formerly Victoreen, Ohio, USA). The instrument determines tube voltage using the two-filter method in a voltage range from 30 to 160 kV. Further a hard copy of the recorded voltage trace is possible. The NERO™ mAx calculates kVp from the ratio between two differentially filtered detector channels. When an x-ray exposure is made, the NERO™ mAx samples the two detector channels simultaneously and calculates the actual tube voltage according to stored calibration data. These calibration data are given as function of the ration of the two signals. The signal traces is then stored for further analysis.

After the exposure is completed, the NERO™ mAx uses the stored signal traces for the determination of characteristic voltage data:

- kV Peak (kVp): highest tube voltage appearing during exposure
- kVp Average (kVp_{avg}): average peak voltage (average of the peak voltages of all voltage ripples in the pulse)
- kV Effective (kVp_{eff}): tube voltage calculated from the ratio of both integrated signal waveforms.

By definition the tube voltage is given by the maximum voltage appearing in the pulse. For technical reasons the peak voltages for each of the voltage ripples in the pulse could vary. Reasons are initial transient conditions in the voltage production originating from the feedback loops of the converter generator or also operation with falling load, i.e. with a tube current decreasing from an initial maximum in the course of the exposure according to the currently possible maximum tube loading. A difference between kVp and kVp_{avg} is an indicator for the variation of kVp within the exposure, which ideally should be constant. The difference of kVp_{eff} to kVp is an indicator for the amount of voltage ripple present in the voltage trace.

A time delay of up to 999 milliseconds may be used to delay the start of kV data acquisition because of possible initial transient conditions (see figure 4.12). This delay may be used to skip events that occur at the beginning of an exposure, such as an overshoot or undershoot. When the delay is used, only the kV data acquired after the delay are used for determination of kV data (see figure 4.13).

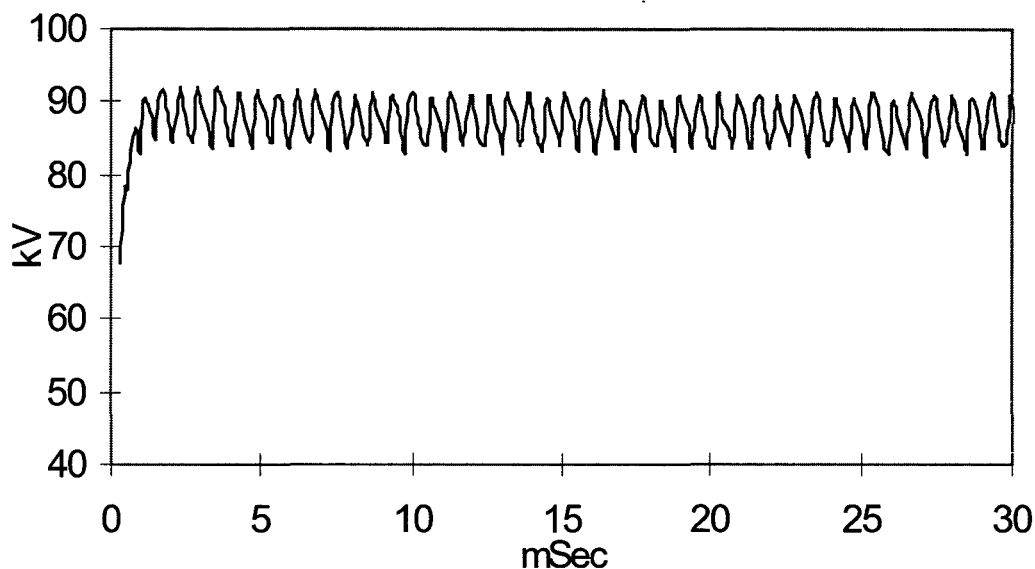


Figure 4.12. Typical diagram showing measured tube voltage (90 kV nominal tube voltage) together with voltage waveform. The initial transient can be seen here as no time delay is used.

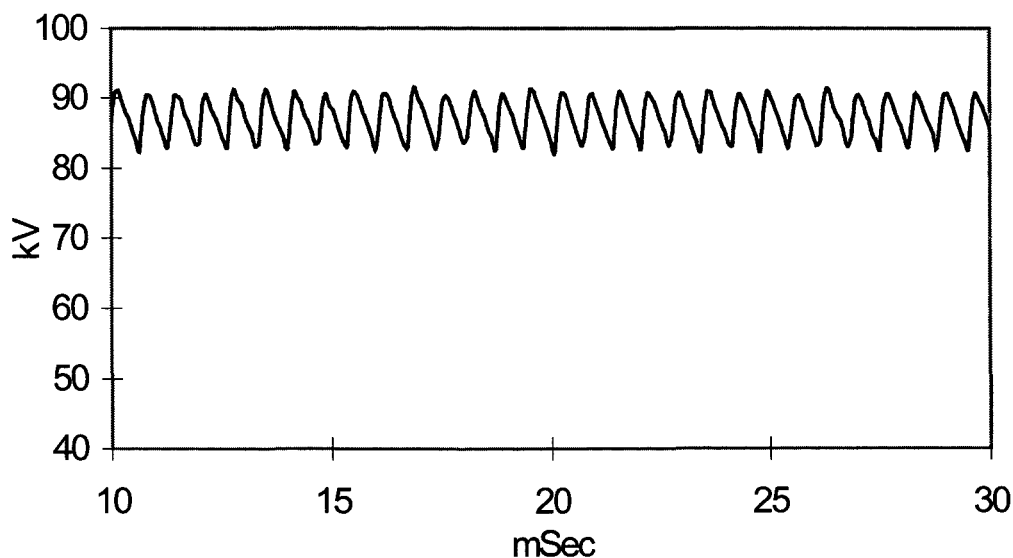


Figure 4.13. Same x-ray unit as in figure 3.12 but using a time delay of 10 msec.

The kVp instrument is placed centrally in the x-ray beam with its long axis perpendicular to the anode-cathode axis in order to reduce the influence of the heel effect. The unit was positioned within 80 cm from the x-ray source and the appropriate filter pack for the kV being anticipated. Measurement of peak voltage with an accuracy ± 1 kV is achievable with this instrument.

Typical results of tube voltages measurements are shown in tables 4.3. This table is a sample report generated by the instrument.

Table 4. 3. Sample report for tube voltage measurement with x-ray unit #3

Facility: Skelett3				
Location: F6				
Room: 0				
Machine: Philips				
Machine Settings				
kV	mA	FS	mSec	SDD
125	100		100	66.6 cm
90				
60				

Measurements				
kVp avg	kV eff	kV peak	mSec	μ Gy
125,2	120,1	126,2	100,8	1515,5
125,1	120	126,6	100,8	1512,2
125,2	120,1	126,4	101,1	1517,7
90,4	87,7	91,6	100,7	1600,1
90,4	87,7	91,6	100,7	1599
60,3	56,7	60,9	99,4	671,9
60,3	56,7	60,9	99,5	673,1
60,3	56,8	60,9	99,4	689,7

As can be seen from these results the agreement of nominal tube voltage with measured tube voltages (kVp and kVp avg.) in the case of unit #3 is within 0.5%.

4.3.3 Fitting process

The air kerma K depends on the spectral distribution for which a model has been described in section 2, paragraph 2.5.3.3. Using the x-ray spectrum K can then be obtained as given in relation 2.7. The kerma depends on many parameters as tube voltage kVp , voltage ripple p , inherent and additional filtration f and a , respectively, tube current I , exposure time t and distance d ,

$$K = K(kVp, p, f, a, I, t, d).$$

In the measurement of attenuation curves a series of measurements for air kerma normalized to the tube current-exposure time product, K_n , is made. Choosing a tube voltage kVp_i and an additional aluminium filter of thickness a_i , the measured normalized kerma $K_{m,i}$ for the i^{th} measurement is given by:

$$K_{m,i} = K_n(kVp_i, a_i; f; p, d),$$

where kVp_i and a_i constitute the independent variables of the function $K_{m,i}$. The total inherent filtration f could be split up into the nominal inherent filtration fn , usually given in terms of the equivalent in aluminium, and an additional inherent filtration fa which is then a parameter to be determined by the fit process with $f = fn + fa$. Nominal inherent filtration fn , voltage ripple p and distance d are constant for all measurements.

Using a model for the production of x-rays (see paragraph 2.5) one can calculate the normalized kerma K_c for the parameter set of the i^{th} measurement giving $K_{c,i}$

$$K_{c,i} = K_c(kVp_i, a_i; fa; p, d, fn),$$

with variables and constants as used in the measurement, the additional inherent additional filtration fa to be a fit parameter. Tube current I and exposure time t , or the current-time product $I.t$, resp., is usually taken as indicated on the console and used to obtain the normalized kerma. The deviation of true tube current or current-time product from the indicated values is usually small with modern converter generators but still

introduces a systematic deviation in all measured data. Comparing results from several x-ray units requires therefore a general factor c common to all measurements in a series to compensate for such deviations. This factor is also subject to the fitting process as a fit parameter,

$$K_{c,i} = c \cdot K_c(kVp_i, a_i; fa; p, d, fn).$$

K_c is the normalized kerma calculated using a model for the calculation of x-ray spectra (2.5.3). The given parameter set, kVp_i and a_i constitute the independent variables, the total inherent filtration f and the normalization factor c , are then the fit parameters.

To find a best fit for the parameters fa and c a least squares data fit was performed. The *figure-of-merit* or cost function S used is then given as

$$S = \sum_i \left[\frac{K_{m,i} - c \cdot K_c(kVp_i, a_i; fa; p, d, fn)}{K_{m,i}} \right]^2.$$

S gives the sum for all measurements of the squared differences of the experimental and the calculated normalized kerma data. As kerma values cover numerically a large range from low to high tube voltages and little to high filtration the differences are weighed by the experimental kerma to obtain the same relative accuracy for all experimental data in a series when S is minimized.

Many methods exist for fitting experimental data to a theoretical model. An approach of fitting the calculated attenuation curves to measured data would be facilitated if the air kerma for filtered x-ray spectra could be calculated using an analytical expression. If the cost function S could be given as an analytical expression with its derivatives in all the independent variables an iterative algorithm for a minimization could be applied using e.g. the Newton-Raphson type of algorithms. This and other similar numerical methods are described in a collection of numerical methods [Pr88].

Since already the calculation of x-ray spectra is not feasible using an analytical expression the same will be true for a calculation of air kerma. Hence, it is necessary to use a method for a minimization of the sum of the squared residuals not depending on a functional description of air kerma or its derivatives. A widely used algorithm not dependent on derivatives is the 'Downhill Simplex Method' first introduced by Nelder and Mead [Ne65], which will be described briefly below.

4.3.3.1 Downhill Simplex Method

The simplex method considers multidimensional minimisation, i.e. finding the minimum of a function of more than one independent variable. The method requires only function evaluations, not derivatives. Consequently the computational time required depends to a large degree on the number of function evaluations. The Simplex algorithm is not the most efficient type of algorithms as it needs rather more function evaluations than other more efficient codes like Direction Set Methods [Pr88] but for the type of minimization used here the Simplex algorithm is easier to implement than other algorithms as no special assumptions on the function have to be made.

A simplex is the most elementary geometrical figure that can be formed in dimension n and has $n + 1$ sides (e.g., a triangle in two-dimensional space, a tetrahedron in three-dimensional space). Dimension n is equal to the number of fit parameters. The vertices of the simplex are the result of the fit function for different sets of the fit parameters. The beginning is to give the algorithm a guess for a starting vertex, that is, an n -dimensional vector of parameters as the first point to try. The other vertices of the simplex are then obtained by the program by scaling the initial guess by a given scaling factor. In a two-dimensional case, as it is the case with the cost function S here, the simplex would have three vertices S_0 , S_1 and S_2 (figure 4.14).

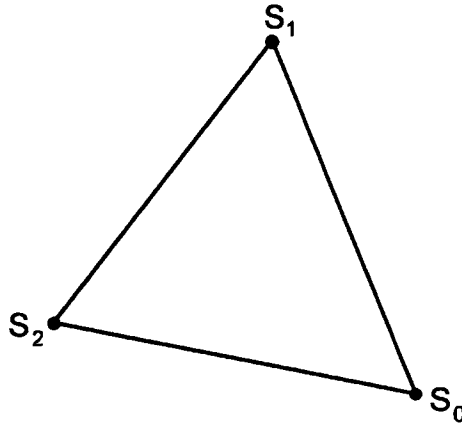


Figure 4. 14. Simplex for the cost function S as a 2-dimensional case

Then each iteration generates a new vertex for the simplex. If this new point is better than at least one of the existing vertices, it replaces the worst vertex in the simplex. In this way, the diameter of the simplex gets smaller the vertices moving downhill through an N -dimensional topography, until it encounters a (at least local) minimum. The algorithm stops when the diameter or the difference for the vertices reaches a specified tolerance.

The strategy for the generation of the new vertex is based on its relation to the other vertices in the simplex. First a search direction is established by connecting the highest vertex with the midpoint of the line between two other vertices (figure 4.15). To obtain a new vertex the simplex can be *reflected*, *expanded*, *contracted*, and *shrunk*. Reflecting vertex S_2 means to reflect S_2 along the search direction to give the new vertex S_r (figure 4.16). If the solution after reflection is better, i.e. the vertex is lowest of all, the algorithm tries an expansion. This means progressing in the same direction but doubling the step size to give S_e . (figure 4.16).

If the new vertex is not lowest of all then the second-highest point is taken for a next try. Similarly contraction of the vertex means decreasing the step size for finding new vertices either outside (S_{co}) or inside of the simplex (S_{ci}) (see figure 4.16).

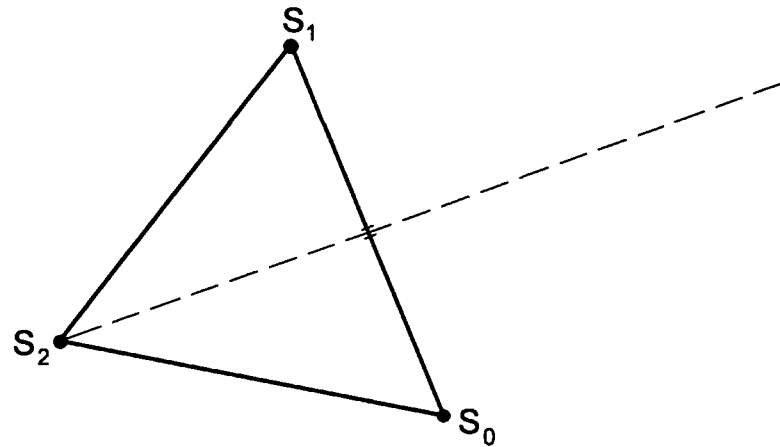


Figure 4.15. Definition of a search direction in the 2-dimensional case by the highest vertex S_2 and the midpoint of the line connecting the other two vertices.

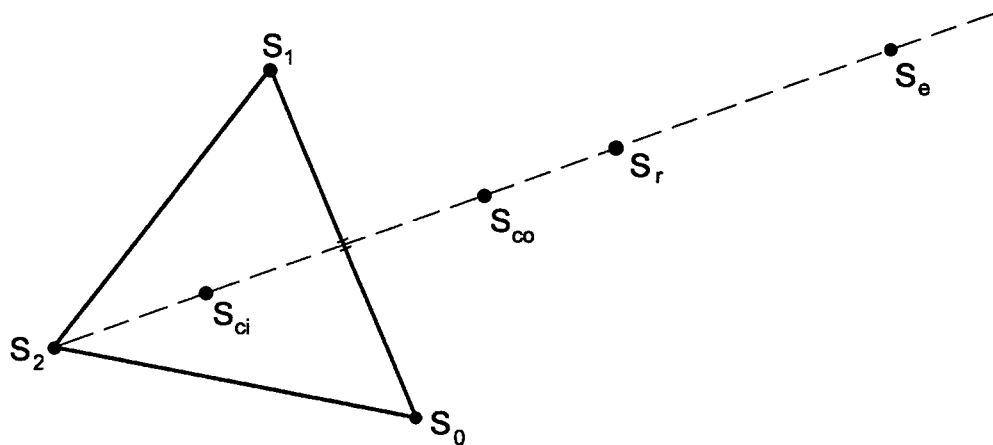


Figure 4.16. Finding a new vertex along the search direction: reflection, expansion, outside contraction and inside contraction yields the vertices S_r , S_e , S_{co} and S_{ci} .

If reflection, expansion, and contraction fail, the algorithm resorts to a shrinking operation. This operation retains the best point and shrinks the simplex, that is, for all vertices of the simplex except the best one (figure 4.17).

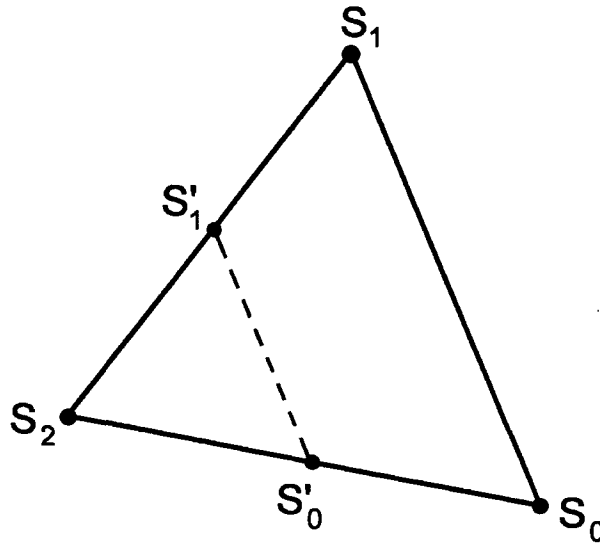


Figure 4. 17. If S_2 is the best vertex shrinking the simplex in this 2-dimensional case keeps S_2 and moves the other vertices S_0 and S_1 towards S_2 giving the new vertices S'_0 and S'_1 .

The process stops when a minimum in S is reached. A minimum can be either global (truly the lowest function value) or local (the lowest in a finite neighbourhood and not on the boundary of that neighbourhood). In general, using simplex methods gives no guarantee for finding global minima. What could be done is either finding minima starting from widely varying starting values of the fit parameters, and then pick the most extreme of these (if they are not all the same) or perturbing a local minimum by taking a finite amplitude step away from it, and then see if the routine returns to a better point, or always to the same one.

As a criterion for stopping the process the accuracy of the fit parameters and the cost function have been chosen here. The downhill move ends if all errors in the fit parameters, i.e. the difference of the parameters in all vertices to the average of all vertices, drops below a given limit. Consistency can be measured by the standard deviation of the errors resulting from repeated application of the algorithm. Small standard deviations show that repeated application of the algorithm gives comparable results.

4.3.3.2 Implementation of the Downhill Simplex method

There exist many implementations of the Simplex algorithm in all sorts of computing languages. A widely used algorithm called *AMOEBA* was given in a collection of numerical methods (Numerical recipes, [PR88]). Here, another version written in Pascal named *SIMP* [Ca84] was used as the basis for an implementation in fitting the calculated attenuation curves to the experimental data.

A code named *XATTFIT* written in Borland Delphi (Borland Software Corporation, Scotts Valley, USA) by R. Nowotny [No03] was composed of the procedure *SIMP* for the data fit including all the necessary routines for calculation and attenuation of x-ray spectra as used in XCOMPW [No97]. In each function evaluation an x-ray spectrum according to the parameter set supplied by the Simplex code for the current vertex is calculated, attenuated and finally the air kerma is obtained. The fitting process adjusts the calculated and the measured attenuation curves using two parameters: an additional tungsten or aluminium filter and a general normalisation factor.

A typical input for the program consists of:

- parameters of the x-ray unit under investigation and the measurement geometry, i.e. anode angle, nominal filtration given in the equivalent of mm Al and/or mm Cu, voltage ripple, and source to detector distance,
- measured normalized kerma yields for a selection of tubes voltages and aluminium absorbers,
- a selection of the filter material, either aluminium or tungsten,
- starting fit parameters, i.e. the initial thickness for the additional inherent filter (default values available here are 1 mm Al or 1 μ m W, respectively) and the normalisation factor (default value 1.0),
- the maximal number of iterations (default value 100), and
- a general maximum error (default value 10^{-4}).

Figure 4.18 shows an example for input screen of the code *XATTFIT*

Attenuation Curve Fit --- v. 1.1.2

Title: Exit

Anode angle, deg.: Inh. filtration, mmAl:

Voltage ripple: Inh. filtration, mmCu:

Distance, cm:

Kerma output, $\mu\text{Gy/mAs}$:

kVp, kV:		60	90	121	150
Added filtration, mm Al:	0	120,72	274,28	458,59	638,9
	2	65,96	177,26	324,76	476,2
	4	41,1	127,42	249,17	377,5
	8	19,01	74,59	162,17	259,9
	12	9,91	47,81	108,08	189,21

Open

Add. filter material: Add. filter start/final value:

Norm. factor start/final value:

Max number of iterations: General Maximum Error:

Figure 4. 18. Input screen of the XATTFIT showing the input parameters

Execution time of the code *XATTFIT* depends on the number of function evaluations performed given by the number of measurements supplied and the number of iterations required to find a minimum of the cost function. Typical execution time for the case shown in figure 4.18 using a PC (Intel Pentium IV, 1.60 GHz, 256 MB RAM) is 30 sec. The progress of the fitting process can be monitored as the current values for the filter thickness, the normalization factor and the value of the cost function are shown for each iteration in a window of the program. A typical output in this progress window is shown below for the data presented in figure 4.18:

Iteration Number	Add. Filt., fa	Norm. fact., c	Cost function, S
Iteration: 1	1,00000E+00	1,00000E+00	2,60386E-02
Iteration: 2	1,00000E+00	1,00000E+00	2,60386E-02
Iteration: 3	1,00000E+00	1,00000E+00	2,60386E-02
Iteration: 4	1,00000E+00	1,00000E+00	2,60386E-02
Iteration: 5	1,01396E+00	9,84128E-01	1,56342E-02
.....			
Iteration: 29	9,24895E-01	9,65661E-01	1,44180E-02
Iteration: 30	9,24653E-01	9,65624E-01	1,44180E-02
Iteration: 31	9,24653E-01	9,65624E-01	1,44180E-02
Iteration: 32	9,24653E-01	9,65624E-01	1,44180E-02
Iteration: 33	9,24653E-01	9,65624E-01	1,44180E-02

Number of parameters to fit :2

Number of variables (independent and dependent) per data point: 3

Number of data points :20

The program excited after 33 iterations.

Final simplex:

S ₀	9,245896E-01	9,656128E-01	1,441797E-02
S ₁	9,245332E-01	9,656012E-01	1,441797E-02
S ₂	9,245191E-01	9,656029E-01	1,441797E-02

Mean:	9,245473E-01	9,656057E-01	1,441797E-02
-------	--------------	--------------	--------------

Estimated fractional error:

7,630968E-05	1,202135E-05	2,357006E-08
--------------	--------------	--------------

When the variation for the parameters and the cost function is less than the error limit given in the input the program stops and presents the results including the calculated kerma data for the optimised fit parameters:

#	kVp,kV	filt.,mm Al	K _n meas.	K _n fit	K _n meas-K _n fit
1	6,000E+01	0,000E+00	1,207E+02	1,213E+02	-5,803E-01
2	6,000E+01	2,000E+00	6,596E+01	6,757E+01	-1,612E+00
3	6,000E+01	4,000E+00	4,110E+01	4,237E+01	-1,272E+00
4	6,000E+01	8,000E+00	1,901E+01	1,981E+01	-7,989E-01
5	6,000E+01	1,200E+01	9,910E+00	1,046E+01	-5,533E-01
6	9,000E+01	0,000E+00	2,743E+02	2,654E+02	8,885E+00
7	9,000E+01	2,000E+00	1,773E+02	1,737E+02	3,590E+00
8	9,000E+01	4,000E+00	1,274E+02	1,242E+02	3,203E+00
9	9,000E+01	8,000E+00	7,459E+01	7,247E+01	2,124E+00
10	9,000E+01	1,200E+01	4,781E+01	4,637E+01	1,444E+00
11	1,210E+02	0,000E+00	4,586E+02	4,426E+02	1,599E+01
12	1,210E+02	2,000E+00	3,248E+02	3,190E+02	5,806E+00
13	1,210E+02	4,000E+00	2,492E+02	2,452E+02	3,944E+00
14	1,210E+02	8,000E+00	1,622E+02	1,596E+02	2,567E+00
15	1,210E+02	1,200E+01	1,081E+02	1,112E+02	-3,103E+00
16	1,500E+02	0,000E+00	6,389E+02	6,233E+02	1,560E+01
17	1,500E+02	2,000E+00	4,762E+02	4,760E+02	2,326E-01
18	1,500E+02	4,000E+00	3,775E+02	3,817E+02	-4,156E+00
19	1,500E+02	8,000E+00	2,599E+02	2,640E+02	-4,144E+00
20	1,500E+02	1,200E+01	1,892E+02	1,925E+02	-3,327E+00

Standard deviation: 6,018E+00

Estimated error of the function: 1,418E+00

Figure 4.19 presents an example of measured and calculated attenuation data presented by the code *XATTFIT* for the fit result.

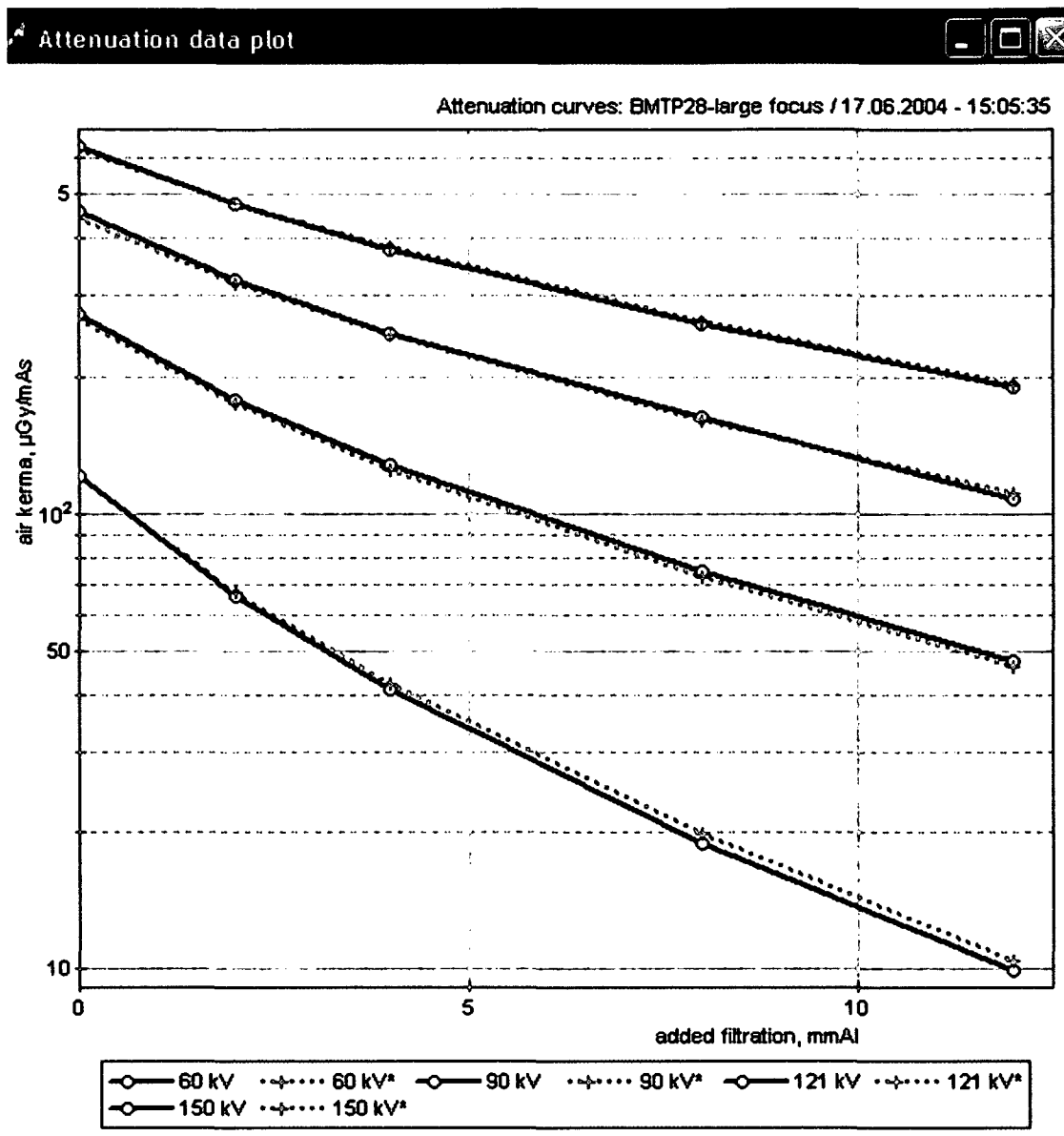


Figure 4. 19. Measured air kerma for a clinical x-ray unit (anode angle 16° , 2.5 mm Al nominal inherent filtration, voltage ripple 3.4%, distance 55 cm vs. additional filtration for various tube voltages. Dashed curves show the fit result (additional aluminium filter of 0.9245 mm, normalization factor 0.9656) using x-ray spectra calculated under the same presumptions.

The fit results have been tested for their robustness by varying the starting values of the parameters. In no case other minima were found. Variation of the error limit also did not give other positions of the minimum.

4.4. EXPERIMENTAL RESULTS

Attenuation curves have been determined for a total of nine clinical x-ray units with each of the x-ray tubes having a small and a large focal spot. For some units also some other built-in filter combinations were included in the measurements. A total of 23 sets of attenuation curves with a total of 350 single exposures were made. The age of the tubes and their total workload were not known. Hence it was not possible to give an estimate on the state of the anode surfaces. All units were equipped with converter generators. Voltage ripple was assumed to be equivalent to 12-pulse generators, i.e. 3.4%. The characteristic data of the x-ray units under investigation are given in table 4.4.

Table 4. 4. Type of x-ray units investigated in the present work with their main characteristics as focus size, anode angle and nominal filtration

Unit number	Name	Model/ Manufacturer	Nominal Focus sizes, mm	Anode angle	Nominal filtration, mm Al
1	BMTP28	BI150/12/59R-100 Siemens	1.0/0.3	16° and 10°	2.5
2	F6Gastro1	OPTITOP150/40/80 HC Siemens	1.0/0.6	12°	2.5
3	F6Skelett3	SRO 25/50 Philips	1.0/0.6	15°	2.5
4	F6Thorax1	OPTITOP150/30/50 HC Siemens	1.0/0.6	12°	2.5
5	F6Thorax2	SRO 33/100 Philips	1.3/0.6	13°	2.5
6	F7Skelett1	OPTITOP150/40/80 HC Siemens	1.0/0.6	12°	2.5
7	F7Skelett2	OPTITOP150/40/80 HC Siemens	1.0/0.6	12°	2.5
8	F6Gastro2	SMR 35/100 Philips	1.2/0.6	12°	2.5
9	F6Skelett2	SMR 35/100 Philips	1.2/0.6	12°	2.5

4.4.1 Determination of total filtration using the HVL method

Total filtrations for the above listed x-ray devices were determined using the HVL method according to ISO standards [ISO97]. Indeed, only the HVL method using the quality diagram recommended by the currently applicable standard [ISO97] has been applied in this work for comparison with the present fitting method. The other methods as described in paragraph 4.2 were not used any further but have been presented here just as an indication of other possible methods. Results for the total filtrations as a function of HVLs are given in table 4.5.

Table 4. 5. Experimental first HVLs measured at 60 kV for the clinical x-ray units. Total filtration (T.F.) as obtained using the HVL method (paragraph 4.2.7) is compared with the nominal filtration (N.F) given by the manufacturer.

Unit number/ Name	Focus	1st HVL at 60 kV	N.F.	T.F. mm Al	Rel. Diff. of N.F and T.F., %
1: BMTP28	large	2.28	2.5 mm Al	2.85	13
//	small	2.25	2.5 mm Al	2.78	11
2: F6Gastro1	large	2.42	2.5 mm Al	3.16	23
//	small	2.49	2.5 mm Al	3.23	25
3: F6Skelett3	large	2.31	2.5 mm Al	2.92	15
//	small	2.21	2.5 mm Al	2.69	39
4: F6Thorax1	large	2.18	2.5 mm Al	2.64	5.5
//	small	2.19	2.5 mm Al	2.65	6
5: F6Thorax2	large	2.20	2.5 mm Al	2.68	7
//	small	2.45	2.5 mm Al	2.78	11
6: F7Skelett1	large	2.18	2.5 mm Al	2.64	5.5
//	small	2.19	2.5 mm Al	2.65	6
7: F7Skelett2	large	2.52	2.5 mm Al	2.79	11
//	large	3.11	2.5 mm Al + 0.1mm Cu	5.09	*)
//	small	3.83	2.5 mm Al + 0.1mm Cu	6.15	*)
8: F6Gastro2	large	2.21	2.5 mm Al	2.69	7.3
//	small	2.27	2.5 mm Al	2.82	12
9: F6Skelett2	large	2.17	2.5 mm Al	2.62	4.7
//	small	2.21	2.5 mm Al	2.69	7.3

*) a comparison is not feasible as an additional copper filter is used here

Using the total filtration obtained by the HVL method the attenuation curves were then calculated, using the code XCOMPW [No97], with the same parameters (kVp, anode angle, source to detector distance, voltage ripple) as for the measurements.

The nominal filtration was replaced by the measured total filtration and then compared with experimentally determined attenuation curves. An example for such a comparison is given in figure 4.20.

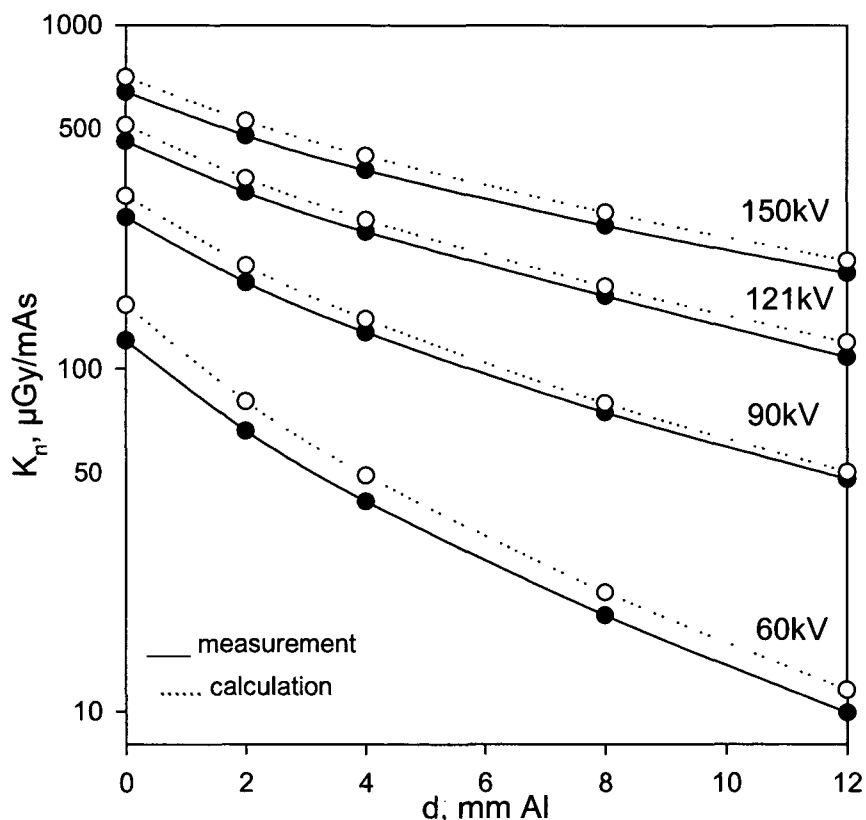


Figure 4. 20. Comparison of typical measured and calculated attenuation curves obtained for unit #1 (BMTP28). Normalized air kerma K_n ($\mu\text{Gy/mAs}$) is plotted versus added filter thickness d (mm Al). Data for calculated attenuation curves are obtained applying the total filtration as determined using the HVL method.

Nineteen such cases have been investigated here, each case being characterized by the focus, the anode angle, the source to detector distance, the voltage ripple and the nominal filtration. The results and a comparison for all data obtained are given in detail in Annex A (see figures A.1. (b) to A.23(b)).

The comparison of the measured attenuation curves with calculated data using the same parameter set and the total filtration as determined by the HVL method was made to get an indication on the accuracy on kerma data achieved using only that total filtration for an estimation of kerma output. It can be seen from these figures that unsatisfactory agreement is obtained between measured and calculated data in almost all

of the cases. These results could be expected, on one hand because it is essential that the tube assembly under investigation is almost identical to and operated under the same conditions as the reference tube from which the quality diagram is obtained, however no indication is given on the source of the published quality diagrams. On the other hand, as already mentioned in paragraph 4.2.7, Nagel [Na88] showed that the HVL method allows only for a rough estimation of the filtration and could typically give errors of up to $\pm 30\%$.

An improvement in the agreement could be achieved by an introduction of a common normalization factor, equal to 0.79 determined from the attenuation curve at 60 kV for x-ray unit #1, but still the agreement shows some deficiencies (figure 4.21). The normalization factor is determined from the attenuation curve at 60 kV as the HVL method uses this curve to deduce the total filtration.

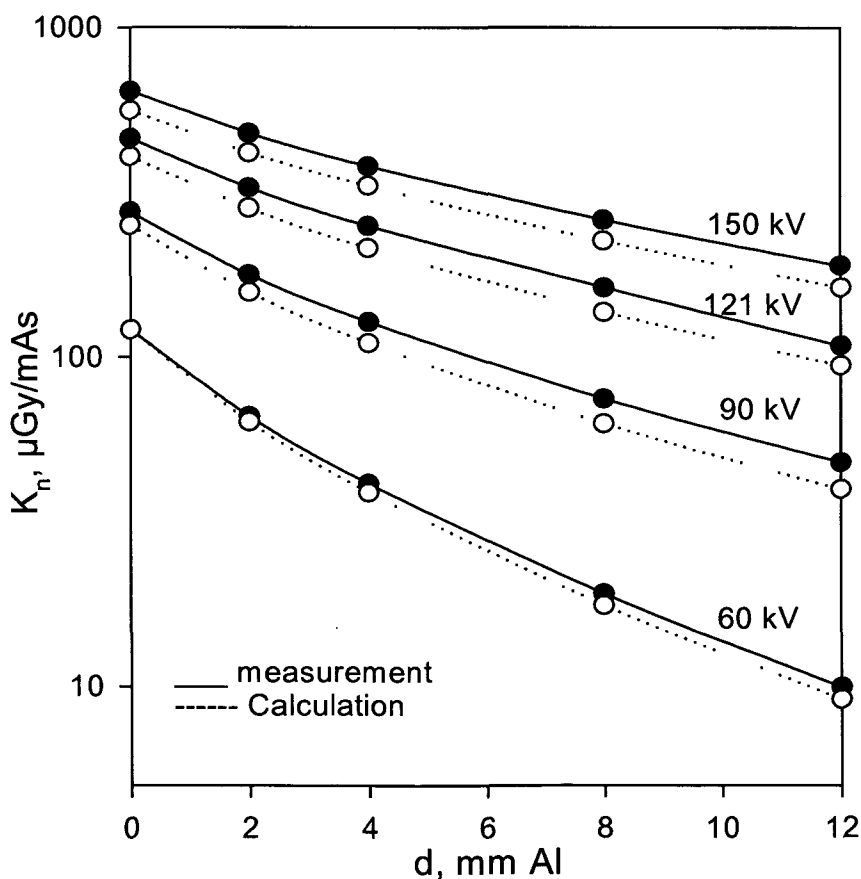


Figure 4. 21. Comparison of measured and calculated attenuation curves obtained for unit #1 (BMTP28). Data for calculated attenuation curves are obtained using the total filtration as determined using the HVL method but applying a normalisation factor to improve the agreement between measured and calculated data.

4.4.2 Determination of total filtration using the fit method

Total filtration for the above listed x-ray devices was determined using the fitting process described above. Data for the experimental attenuation curves i.e. air kerma output for a selection of added aluminium filters and tube voltages (see paragraph 4.3.1), are entered in the program together with the parameters of the x-ray unit, i.e. anode angle, voltage ripple and nominal filtration. Using these parameters, the algorithm as described in paragraph 4.3.3.2 obtained the values for the equivalent filter thickness additional to the nominal inherent filtration and the normalization factor optimised such as to give a best fit to the attenuation curves measured for that x-ray unit.

Two materials have been used for this additional filter, i.e. tungsten and aluminium. Tungsten is the material the anode is made of and according to the influence of anode surface roughness on kerma output (paragraph 3.9) a substantial amount of the additional filtration appearing with time for an x-ray tube will be due to absorption in an additional layer of tungsten. It is therefore interesting to get data on the thickness of such a tungsten layer. Aluminium is of interest not only because this is the material actually absorbing the x-rays but also all absorbing materials are expressed in terms of their equivalent in aluminium.

The results of the data fits have shown that using either tungsten or aluminium as the material for the additional filtration does not have a great impact on the accuracy of the data fits giving similar sets of calculated and measured attenuation curves. The explanation for this lies in the fact that kerma is a global parameter not reflecting to much the individual trends of the attenuation coefficient with photon energy.

The influence of the choice of the filter material on the spectral distributions, however, can be expected to exhibit larger differences. Indeed, the position of the K absorption edge must be considered when choosing a filter material. For aluminium ($Z = 13$, K-edge = 1.6 keV) the K-edge is not relevant, as only photons with an energy above approximately 15 keV will be exiting the tube housing. The effect of filtration on the spectra will be quite different when the filter is of the same material as the target

anode producing the x-rays, as attenuation for their own characteristic radiation is much less than for photon energies above the K-edge.

The most prominent effect for choosing tungsten instead of aluminium will be an increase in the drop of the Bremsstrahlung spectrum at the energy of the K-edge. To demonstrate the differences in the x-ray spectra obtained with aluminium and tungsten as materials for the additional filter, appropriate spectra were calculated with XCOMPW for the case with the largest filter thickness obtained with tungsten (11.89 μm) and the corresponding filter thickness of 1.72 mm aluminium (figure 4.22).

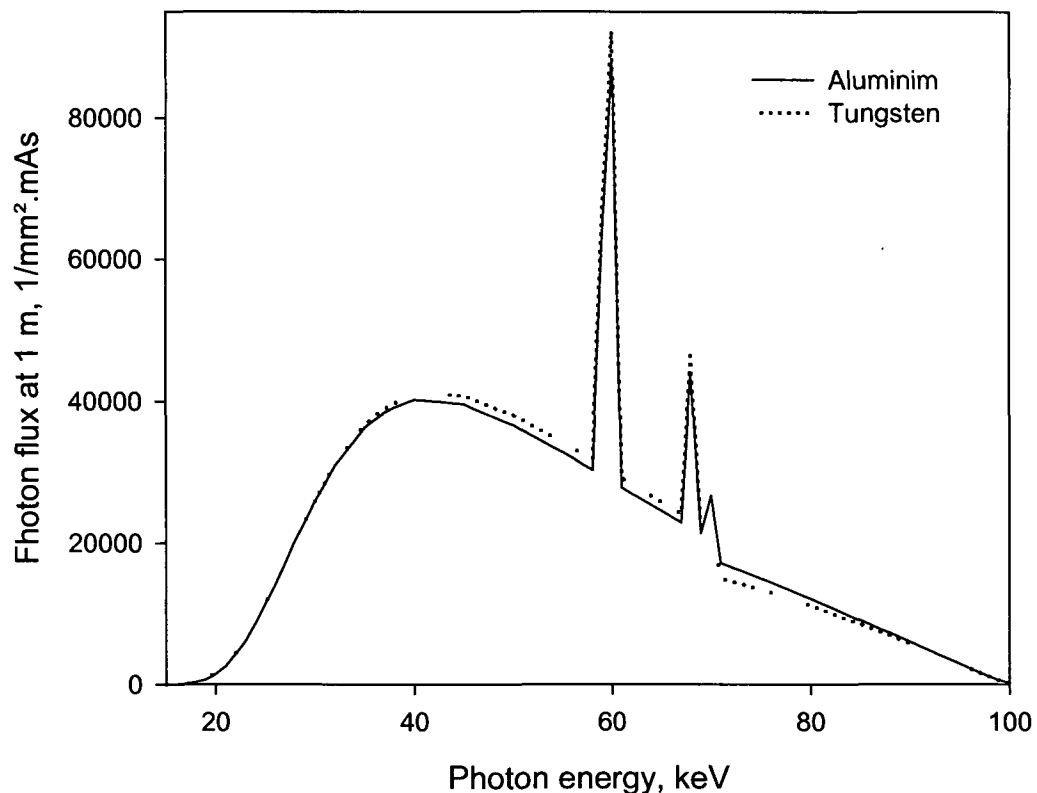


Figure 4. 22. Spectra obtained for unit #8 (small focus) for 100 kV tube voltage considering an additional filtration with tungsten or aluminium as obtained by the data fit.

Results for the additional tungsten and aluminium filtrations and for the total aluminium filtration (the sum of nominal and additional filtration) are summarized in table 4.6. An example for a comparison of experimental attenuation curves with

calculated data is shown in figure 4.23. Details and a comparison for all data fits obtained are given in annex A in figures A.1.(a) to A.23(a).

Table 4. 6. Results obtained for 19 settings showing additional inherent tungsten or aluminium filtration and the total filtration equivalent in aluminium obtained using the fitting method. Normalization factors are not shown here.

Unit number	Focus-Anode angle	Nominal filtration	Add. filtration, $\mu\text{m W}$	Add. filtration, mm Al	Total filtration, mm Al
1	large-16°	2.5 mm Al	6.57	0.92	3.42
1	small-10°	2.5 mm Al	3.83	0.54	3.04
2	large-12°	2.5 mm Al	6.42	0.90	3.40
2	small-12°	2.5 mm Al	7.62	1.07	3.57
3	large-15°	2.5 mm Al	7.48	1.04	3.54
3	small-15°	2.5 mm Al	7.89	1.10	3.60
4	large-12°	2.5 mm Al	2.43	0.34	2.84
4	small-12°	2.5 mm Al	2.80	0.40	2.90
5	large-13°	2.5 mm Al	5.44	0.77	3.27
5	small-13°	2.5 mm Al	6.20	0.87	3.37
6	large-12°	2.5 mm Al	2.80	0.40	2.90
6	small-12°	2.5 mm Al	3.30	0.47	2.97
7	large-12°	2.5 mm Al	2.84	0.41	2.91
7	large-12°	2.5 mm Al + 0.1mm Cu	2.90	0.42	2.92 mm Al + 0.1 mm Cu
7	small-12°	2.5 mm Al + 0.1mm Cu	5.01	0.67	3.17 mm Al +0.1 mm Cu
8	large-12°	2.5 mm Al	7.93	1.18	3.68
8	small-12°	2.5 mm Al	11.89	1.72	4.22
9	large-12°	2.5 mm Al	6.22	0.93	3.43
9	small-12°	2.5 mm Al	7.92	1.15	3.65

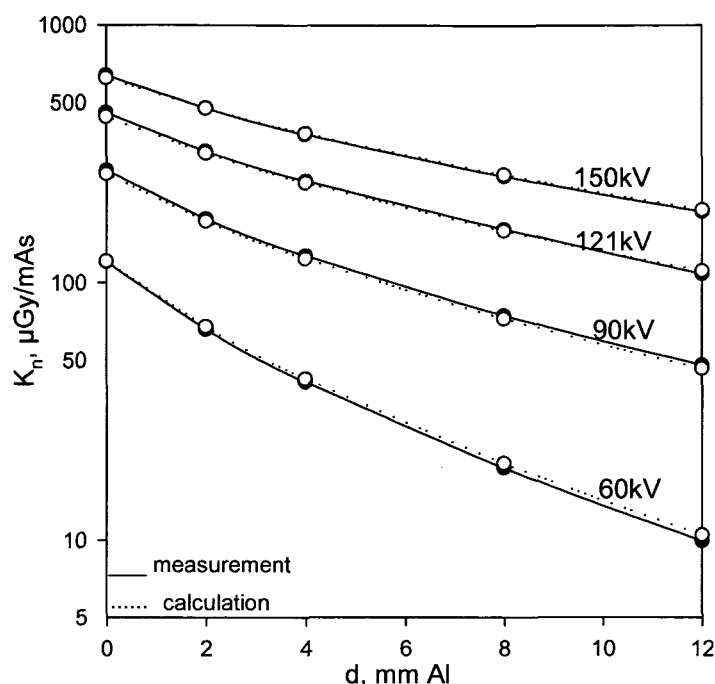


Figure 4. 23. Typical measured and calculated attenuation curves obtained for unit #1 (BMTP28). Normalized air kerma K_n (mGy/mAs) is plotted versus added filter thickness d (mm Al). Data for calculated attenuation curves are obtained using the fitting method and using 0.92 mm aluminium as the material for the added filtration. (6.57 μm also for tungsten)

Figures A.1(a) to A.23(a) in annex A were given only for aluminium as an additional absorbing material. The results obtained from the data fits with tungsten instead of aluminium as the absorbing material practically gave the same results. Therefore, it was not necessary to duplicate the figures. A summary of the results for the additional filtrations is however given for both materials in table 4.6.

4.4.2.1 Influence of tube voltage

From the figures A.1(a) to A.23(a) it can be observed that good agreement between calculated and measured attenuation curves results for most of the cases except for the attenuation curves in figures A.16(a) and A.18(a) corresponding to x-ray unit #8 and curves in figures A.20(a) and A.22(a) for x-ray unit #9. With these units (both incorporating the same model, Philips SMR 35/100) measured and calculated curves do not agree very well. Figure 4.24 illustrates such an example.

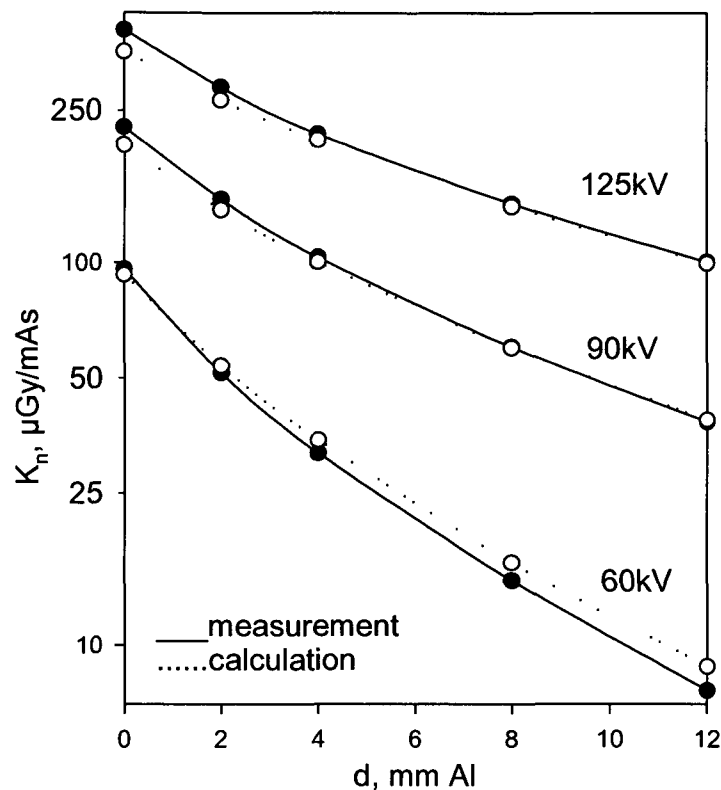


Figure 4. 24. Results of measured and calculated attenuation curves obtained for unit #8 (F6-GASTRO2). Normalized air kerma K_n (mGy/mAs) is plotted versus added filter thickness d (mm Al). Data for calculated attenuation curves are obtained using the fitting method and the nominal tube voltage as indicated on the generator console.

Since a method for the determination of total filtration using data fits to attenuation curves would be not very useful if it is only applicable in some selected cases these discrepancies were further investigated. The significant difference between measured and calculated attenuation curves for units #8 and #9 can be explained by a change in radiation beam quality. This change in the x-ray beam spectrum could occur due to (1) generator contributions, which are tube voltage and voltage waveform, (2) anode angle and (3) measurement geometry.

In our measurements, the anode angle is well known and need not be considered in this context. Consideration is also not given here to the measurement geometry, since this was adequately controlled by proper experimental techniques in order to obtain reliable output values. Uncertainties resulting from dosimetry have been considered and efforts were made to minimize them. Voltage ripple has some influence on radiation quality but the error arising from this factor is not large as it is illustrated later in paragraph 4.5.

If other tube operating conditions are kept constant, the kerma yield K increases approximately proportional to the square of the tube voltage ($K \propto kV^2$). Consideration has consequently been given to the agreement of actual tube voltage with the nominal voltage displayed on the control panel. All voltages used with these units were checked using a calibrated kVp meter (see paragraph 4.3.2). The results of the voltage measurements for units #8 and #9 are shown in table 4.7.

Table 4. 7. Results of measured tube voltages for x-ray units #8 and #9.

Nominal tube voltage, kV	Measured tube voltage, kVp _{avg}	
	Unit #8	Unit #9
60	57.4	55.6
90	86.9	86.4
125	122.9	120.6

The checks revealed some disagreement of nominal and measured kVp data. The measured kVp data were then used in data fits to obtain fit parameters consistent with the actual tube voltage. The same measurements as shown in figure 4.24 but using the measured tube voltages for a data fit are shown in figure 4.25. As can be seen there, agreement of measured and calculated attenuation curves is substantially improved when applying the correct kVp. The detailed results for all measurements are shown in the annex in figures A.17(a), A.19(a), A.21(a) and A.23(a). The corrected figures for added and total filtration obtained for the measured tube voltages are reported in table 4.8. Comparing the data for the total filtration obtained with both the nominal and the measured tube voltages in the last column give a clear indication of the discrepancies arising due to incorrect voltages. As a consequence, measurement of tube voltage of the x-ray beam should be part of a protocol for the determination of total filtration. For other units, the verification of the displayed kVp data showed an agreement within 0.5% (see paragraph 4.3.2).

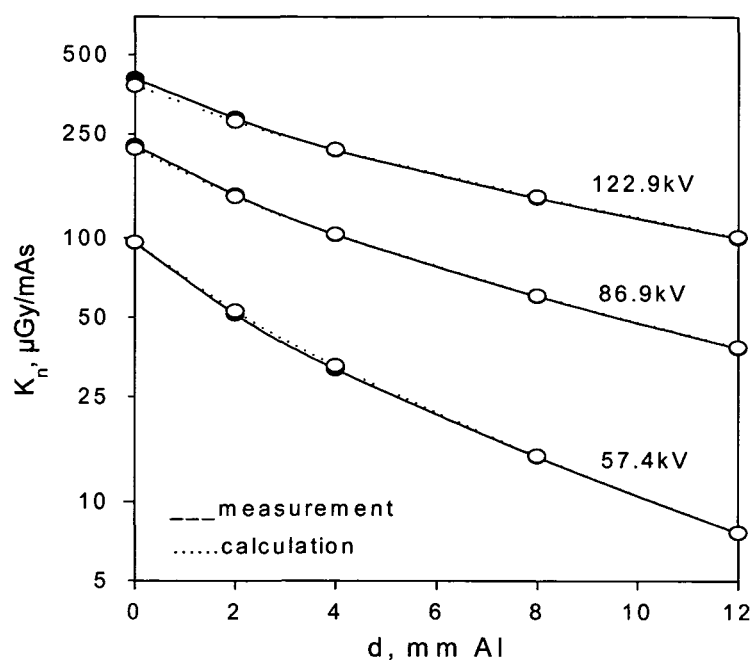


Figure 4. 25. Comparison of measured and calculated attenuation curves obtained for unit #8 (F6-GASTRO2). Data for calculated attenuation curves are obtained using the fitting method and considering the measured tube voltages as shown in the graph. Results for the same experimental data but using nominal tube voltages are shown in figure 4.24.

Table 4. 8. Results obtained for x-ray units #8 and #9 showing additional tungsten or aluminium filtration and the total aluminium filtration obtained using the fitting method after tube voltage corrections.

Unit number	Focus-Anode angle	Nominal filtration	Add. filtration, $\mu\text{m W}$	Add. filtration, mm Al	Total filtration, mm Al
8	large-12°	2.5 mm Al	5.64 7.93*	0.80 1.18*	3.30 3.68*
8	small-12°	2.5 mm Al	8.73 11.89*	1.23 1.72*	3.73 4.22*
9	large-12°	2.5 mm Al	4.76 6.22*	0.67 0.93*	3.17 3.43*
9	small-12°	2.5 mm Al	6.06 7.92*	0.85 1.15*	3.35 3.65*

* Results obtained using the nominal tube voltage as shown previously

4.5. SENSITIVITY OF FIT RESULTS WITH INPUT PARAMETERS

To gain experience on the variation of the fit results for added filtration and normalization factor with the various input parameters a simulation study was performed repeating the fit procedures with different input parameters. The parameters investigated were anode angle, tube voltage and tube voltage ripple.

4.5.1 Influence of anode angle

The anode angle is specified by the manufacturer and depends on the accuracy of the installation of the tube within the tube housing. Tilting the tube axis relative to the tube housing would change the effective anode angle given by the axis of the tube housing and the perpendicular to the anode surface. A deviation of 1° of the tube axis relative to the axis of the tube housing would result in a shift of the central beam axis in 1 m distance of 1.75 cm. It can be assumed that an interval for an effective tube angle of $\pm 1^\circ$ covers the variation encountered with most of the clinical x-ray units.

The influence of a variation in anode angle on additional filtration was determined by making data fits for the measurements obtained with the fixed parameters as ripple, distance and nominal filtration. The nominal anode angle was chosen and then varied in an interval of $\pm 2^\circ$. The experimental data for normalized kerma were used here for the data fit. Results for two examples are shown in table 4.9.

Table 4. 9. Variation of additional filtration f_a using different anode angles as input parameter. Results for two units are shown here.

Unit #1: BMTP28-LF

Anode angle, Degrees	f_a , mm Al	Difference, mm Al
14	0.941	0.016
15	0.931	0.006
16	0.925	-
17	0.921	0.004
18	0.919	0.006

Unit #2: F6Gastro1-LF

Anode angle, degrees	Additional filtration, mm Al	Difference, mm Al
10	0.898	0.025
11	0.910	0.013
12	0.923	-
13	0.888	0.035
14	0.880	0.043

From these simulations it can be concluded that a 1° error in anode angle will lead to less than 0.04 mm Al error in additional filtration in the data fit.

4.5.2 Influence of kVp

The significance of a variation in kVp was already demonstrated above (paragraph 4.4.2.1) but a systematic simulation on its influence was done here similar to the previous section. Here all input parameters to the data fit were kept constant except the tube voltage given for the measured normalized kerma. Standards accept an accuracy of 10% for the tube voltage [IEC98] but such a figure was introduced at times when transformer based generators were mostly in use. With converter generators a maximum variation of ± 5 kV for all the nominal tube voltages can be considered sufficient. Three examples for the results obtained in these simulations are shown in table 4.10 varying the tube voltage in an interval for the nominal tube voltage of ± 5 kV.

Table 4. 10. Three examples for the variation of additional filtration obtained by a data fit with tube voltages in an interval of ± 5 kV.

Unit #2: F6Gastro1-LF

Variation in tube voltage, kV	Additional filtration, mm Al	Difference, mm Al
0 (nominal tube voltage)	0.899	-
-5	0.592	0.307
+5	1.153	0.254

Unit #3: F6Skelett 3-LF

Variation in tube voltage, kV	Additional filtration, mm Al	Difference, mm Al
0 (nominal tube voltage)	1.040	-
-5	0.727	0.313
+5	1.303	0.263

Unit #4: F6Thorax 1-LF

Variation in tube voltage, kV	Additional filtration, mm Al	Difference, mm Al
0 (nominal tube voltage)	0.344	-
-5	0.152	0.192
+5	0.449	0.105

From the results of the simulations it can be concluded that a ± 5 kV variation in all nominal tube voltages can produce a variation in additional filtration of less than 0.35 mm Al. As already discussed (see paragraph 4.4.2.1) a check of the nominal tube voltages is therefore mandatory and should be a part of the protocol for the determination of total filtration. It should be kept in mind that the accuracy of the instruments available for a measurement of tube voltage usually amounts to ± 1 kV (see paragraph 4.3.2). Hence it is interesting to find out the variation in additional filtration obtained by the data fit with a deviation of tube voltages corresponding to this experimental accuracy. Results are shown in table 4.11 for the same units as in table 4.10 but for a ± 1 kV variation in tube voltage.

Table 4. 11. Three examples for the variation of additional filtration obtained by a data fit with tube voltages in an interval of ± 1 kV.

Unit #2: F6 Gastro1-LF

Variation in tube voltage, kV	Additional filtration, mm Al	Difference, mm Al
0 (nominal tube voltages)	0.899	-
-1	0.842	0.057
+1	0.954	0.055

Unit #3: F6 Skelett3-LF

Variation in tube voltage, kV	Additional filtration, mm Al	Difference, mm Al
0 (nominal tube voltage)	1.040	-
-1	0.984	0.056
+1	1.099	0.059

Unit #4: F6 Thorax1-LF

Variation in tube voltage, kV	Additional filtration, mm Al	Difference, mm Al
0 (nominal tube voltages)	0.344	-
-1	0.313	0.031
+1	0.373	0.029

From these simulations it can be concluded that a variation in tube voltage will lead to less than 0.06 mm Al error in additional filtration in the data fit.

4.5.3 Influence of voltage ripple

Voltage ripple for converter generators is typically the same as with 12-pulse transformer generators, i.e. 3.4%. There could be some variation in ripple particularly when tube current is varied. Then with higher electrical loading of the generator some increase in ripple might result if the generator shows some deficiencies in the voltage regulator feedback loop. Therefore simulations on the influence of a variation in voltage ripple on the additional filtration obtained by a data fit were performed. Parameter input was kept the same here except for the type of voltage ripple. As another type of voltage ripple a 6-pulse waveform trace with 13.4% ripple was chosen.

Table 4. 12. Examples for the variation of additional filtration obtained with a data fit using two kinds of voltage ripple.

Unit #1: BMTP28-LF.

Voltage ripple, %	Additional filtration, mm Al	Difference, mm Al
3.4	0.925	-
13.4	0.935	0.01

Unit #4: F6-Thorax2-SF

Voltage ripple, %	Additional filtration, mm Al	Difference, mm Al
3.4	0.400	-
13.4	0.408	0.008

It is evident that voltage ripple has rather little influence on the outcome of the data fit. From the results shown in table 4.12, it can be concluded that an increase in ripple from 3.4 to 13.4% results in a variation of less than 0.01 mm Al in additional filtration. This range of voltage ripples covers more than the variation of ripple anticipated with converter generators. The influence arising from this factor can then be neglected.

From the results of tables 4.10 to 4.12, we can consider that the most influencing parameter in the determination of total filtration is the tube voltage. As previously concluded a measurement of tube voltage is an essential prerequisite in the determination of total filtration.

4.6. CALCULATION OF ENTRANCE SURFACE DOSE FROM THE FIT PARAMETERS

Individual measurement of entrance surface dose (ESD) with patients is cumbersome and sometimes not feasible when a determination of patient dose is done in retrospective. An application of the fit parameters obtained for additional filtration f_a and normalization factor c could be a calculation of ESD for x-ray units where such measurements and the fit procedure have been performed. Indeed, using the code XCOMPW [No97] and applying the total filtration and the normalisation factor obtained from accurate air kerma and tube voltage measurements, would allow the assessment of patient doses in x-ray examinations, **for any conditions** (kVp, voltage ripple, anode angle, distance, other added filters).

ESD is a quantity used to describe the dose at the x-ray beam entrance side of the patient. The entrance dose is often helpful when determining other doses, e.g. organ doses, mean dose in the irradiated volume, energy imparted, and effective dose. The code XCOMPW calculates normalized entrance surface air kerma (ESAK), which has to be corrected by an appropriate backscatter factor to obtain ESD. Backscatter factors vary between about 1.3 and 1.4 (except for mammography), so a single average value of 1.35 can be used in most situations without appreciable error [ICRU85] and [ICRP87]. Normalized ESD is given in mGy/mAs at a certain distance and the tube voltage used.

In the following an example is given for a calculation of normalized ESAK for x-ray unit #1 using the fit parameters obtained from the attenuation curve measurements. As input all data for tube voltage, voltage ripple, anode angle and distance are entered in the program (see figure 4.26). Then in the filter section the nominal filtration (typically 2.5 mm Al equivalent) and the additional filter obtained from the data fit is entered. Any other combination of input parameters is possible for the selected x-ray unit for such a calculation. XCOMPW also provides for a calculation of up to 6 data sets to enable a comparison of the results.

The screenshot shows the XCOMPW software window with the following sections:

X-ray tube

Voltage, kVp: (20-150 kV)	Voltage Ripple:	Anode angle: (1-45 deg)	Distance, cm: (>8cm in air)	<input checked="" type="checkbox"/> incl. absorption in air
100	converter/3.4%	16,0	100	

Filtration

#	Filter Material	Thickness [mm]	Mass Th. [g/cm²]	
1:	ALUMINUM	2,5	0,66725	Add
2:	ALUMINUM	0,92	0,24831	Edit
3:				Delete

Absorber

#	Absorber Material	Thickness [mm]	Mass Th. [g/cm²]	
1:				Add
2:				Edit
3:				Delete

At the bottom, there are buttons for "Duplicate data" and "Calculate".

Figure 4. 26. Window of XCOMPW for the selection of the input parameters. Data set #1 (not shown here) is the same as #2 but without additional inherent filtration.

After finishing the calculation XCOMPW will give the results for the spectral parameters including among other parameters the normalized ESAK designated by air kerma, as shown in figure 4.27. The calculated ESAK data are then found to be:

- 123.9 $\mu\text{Gy/mAs}$ using only the nominal filtration of 2.5 mm Al, and without considering the change due to tube aging (the first column),
- 98.57 $\mu\text{Gy/mAs}$ considering the total filtration (2.5 + 0.92 mm Al) as determined using the semi empirical method (second column). This value has to be corrected with the normalization factor from the data fit to give finally $98.57 \mu\text{Gy/mAs} \times 0.97 = 95.6 \mu\text{Gy/mAs}$.

XCompW - Calculation of X-ray Spectra - [Results]						
File Options Window Help						
Parameter:	Spectrum #1:	Spectrum #2:	Spectrum #3:	Spectrum #4:	Spectrum #5:	Spectrum #6:
total [ph/(mm ² .mA.s)]	2,545E+06	2,194E+06				
K-X [ph/(mm ² .mA.s)]	1,447E+05	1,351E+05				
L-X [ph/(mm ² .mA.s)]	not calc.	not calc.				
<E>-spectrum[keV]	48,5	50,2				
<E>-kerma[keV]	40,9	43,5				
1.HVL-Al[mm]	3,28	3,87				
2.HVL-Al[mm]	5,22	5,83				
1.HVL-Cu[mm]	0,122	0,142				
2.HVL-Cu[mm]	0,229	0,278				
Air kerma [$\mu\text{Gy}/(\text{mA.s})$]	1,239E+02	9,857E+01				
E-tot[$\mu\text{J}/(\text{mm}^2.\text{mA.s})$]	1,977E-02	1,763E-02				
Absorber/estimates:						
E-tr [$\mu\text{J}/(\text{mm}^2.\text{mA.s})$]	0,000E+00	0,000E+00				
E-abs[$\mu\text{J}/(\text{mm}^2.\text{mA.s})$]	0,000E+00	0,000E+00				

Figure 4. 27. Window of XCOMPW showing the calculated x-ray spectral parameters.

The reduction in kerma output of about 25% conforms well to the pronounced effect of the reduction in the kerma output with tube ageing. XCOMPW further returns also spectral distributions for the x-ray spectra. In figure 4.28 the two spectra obtained for this case considering the nominal filtration only (curve A) and using the actual total filtration, obtained from our study (curve B), are shown. Spectrum B is not corrected by the normalization factor here. Spectrum B shows compared to spectrum A a reduced intensity and slight beam hardening due to the increased absorption caused by anode surface roughness.

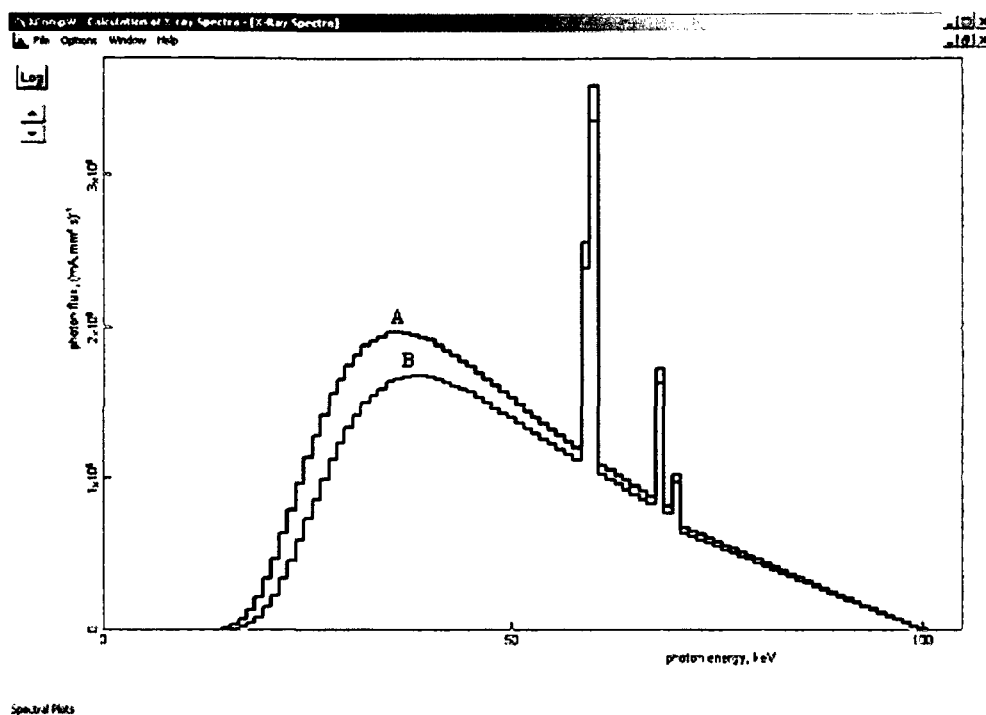


Figure 4. 28. Window of XCOMPW showing the x-ray spectra for the two data sets.

4.7. DISCUSSION

The determination of total filtration for clinical x-ray units is important as the inherent filtration is not constant but increases with tube usage. This increase is mostly due to the increasing roughness of the anode surface as was demonstrated in section 3. Hence, radiation quality is also not constant due to the increase in filtration. Radiation quality is an important parameter of the x-ray beam as it determines radiation dose to the patient and image quality. Therefore the measurement of total filtration is a long-standing matter of investigation in the surveillance of x-ray units.

Many methods for the determination of total filtration have been devised. An overview has been given in this section. All of the methods exhibit some deficiencies and it was therefore interesting to see if the concept of an additional absorbing layer due to the roughness of the anode surface can be used for a determination of total filtration also using a simple model for the generation of x-ray spectra, which was described in section 3.

The basic idea is to measure attenuation curves for the x-ray unit in question and adjust calculated attenuation curves by only varying the thickness of an additional filter and a general normalization factor. The filter material could be either tungsten as the additional filter layer due to roughness is made up of tungsten, or aluminium. The equivalent in aluminium is a common way of describing inherent filtration for an x-ray unit.

An algorithm for fitting calculated to measured data is used such as to obtain the best fit giving an optimised thickness of the additional filter. The programme for this data fit uses a modified Simplex-algorithm including all the necessary routines for calculation and attenuation of x-ray spectra as used in XCOMPW [No97]. This algorithm was implemented in a computer program (*XATTFIT*) [No03]. The program first calculates x-ray spectra according to the nominal values for the x-ray unit and then obtains the attenuation data using these spectra. The fitting process adjusts for two parameters, an additional tungsten or aluminium filter and a general normalisation factor, to obtain good agreement.

The fit results obtained with tungsten as the additional filter are shown in table 4.6. The thicknesses of the tungsten layers obtained from the attenuation data are in a range from 2.43 μm to 11.89 μm . Such a range of filter thicknesses corresponds very well to the thicknesses of the additional absorbing layers determined for rough anodes (see section 3). From figure 3.15 an associated surface roughness R_a can be derived ranging from 1.5 to 4.5 μm . These values are within the range of surface roughness found experimentally for the anode samples in section 3. As total filtration is usually given in terms of an equivalent aluminium filter, the same process was also done for aluminium as the additional filter material. Here, the thickness of the additional aluminium filter was in a range from 0.34 to 1.72 mm Al.

If one relates the added filtration to the anode surface roughness then a comparison of the added tungsten filter for large to small focal spots shows larger surface roughness for the small focal spots. Power density in the small focal spot in an x-ray tube is usually larger than for the large focus. This results in a larger anode loading and a larger roughness of the tracks for the small focal spots can be expected. This was found for all tubes except for the unit #1 (see table 4.6) which was mostly

operated using the large focus explaining this result. Indeed, this particular x-ray unit, dedicated to research and development work, is mainly used with its large focus. We then expect the anode surface roughness of this large focus to be more pronounced, compared to that one of the small focus.

The currently used method for the determination of total filtration that has been suggested in the respective standard [ISO97] is the HVL method. This is an indirect method relying on quality diagrams obtained for specific parameter settings. In contrast, the method for a determination of total filtration described in this work using attenuation curves for an analysis does not rely on any prerequisites as specific parameter settings but only requires the measurement of a set of kerma yields for some deliberately chosen tube voltages and filter thicknesses. Table 4.13 and figure 4.29 show a comparison for the total filtration determined by the HVL-method and by the data fit method developed in this work.

Table 4. 13. Difference and ratio for the total filtration (T.F.) determined by (a) the HVL-method and (b) the data fit method for the x-ray units investigated in this work.

Setup number	Unit number	Focus- Anode angle	T.F., mm Al HVL method (a)	T. F, mm Al Fit method (b)	Diff. (b) – (a) mm Al	Ratio (b) /(a) Rel. units
1	1	large-16°	2.85	3.42	0.57	1.20
2	1	small-10°	2.78	3.04	0.26	1.09
3	2	large-12°	3.16	3.40	0.24	1.08
4	2	small-12°	3.32	3.57	0.25	1.08
5	3	large-15°	2.92	3.54	0.62	1.20
6	3	small-15°	2.69	3.60	0.91	1.34
7	4	large-12°	2.64	2.84	0.20	1.08
8	4	small-12°	2.65	2.90	0.25	1.09
9	5	large-13°	2.68	3.27	0.59	1.20
10	5	small-13°	2.78	3.37	0.59	1.20
11	6	large-12°	2.64	2.90	0.26	1.10
12	6	small-12°	2.65	2.97	0.32	1.12
13	7	large-12°	2.79	2.91	0.12	1.04
14	8	large-12°	2.69	3.30	0.61	1.23
15	8	small-12°	2.82	3.73	0.91	1.32
16	9	large-12°	2.62	3.17	0.55	1.21
17	9	small-12°	2.69	3.35	0.66	1.25

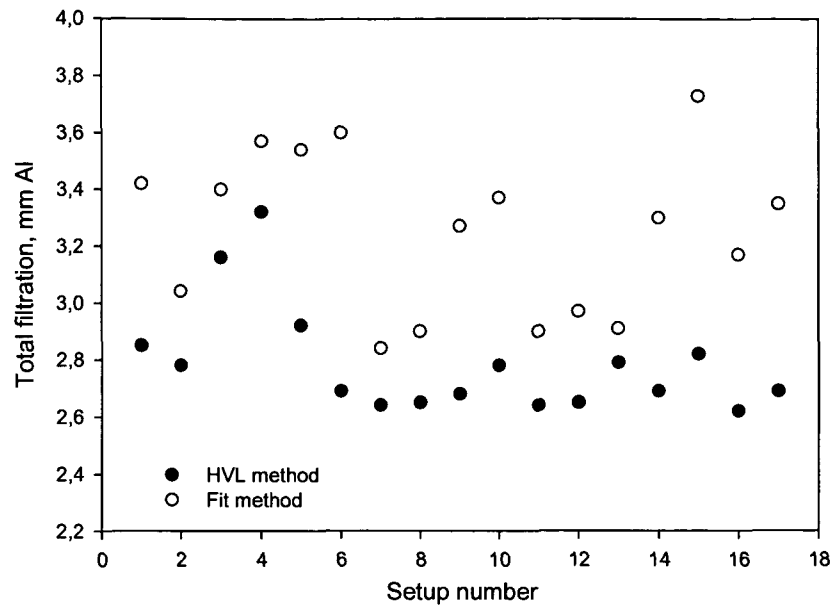


Figure 4. 29. Total filtration determined by the HVL-method and by the data fit method for different setups corresponding to the x-ray units investigated in this work (see table 4.13).

The total filtration determined by the fit method consistently gives larger filter thicknesses than with the HVL-method as shown in figure 4.29. From the simulation of the effect of surface roughness on beam quality it was concluded that the variation of HVL with tube voltage for varying roughness is not constant but has its maximum variation at 80 kV (see fig. 3.20b). The HVL-method uses an attenuation curve determined at a tube voltage of 60 kV while the fit method comprises measurements for a larger range of tube voltages. This could explain the larger values for the added filtration as determined by the fit method.

On the other hand one could explain this tendency by the code XCOMPW generating spectra, which are too hard. The higher penetrating power is then compensated by larger additional filtrations to adjust measured and calculated attenuation curves. To see if there is such a tendency in the results of the code XCOMPW for obtaining the specific radiation qualities, a comparison of HVL for the same radiation qualities given by some Primary Standards Dosimetry Laboratories (PSDL) such as the UK's National Physical Laboratory (NPL), the German Physikalisch Technische Bundesanstalt (PTB) and the Netherlands Meetintituut Van Swiden Laboratorium (NMI), together with the HVL specified in IEC 61267 [IEC04] and the results obtained from XCOMPW are shown in table 4.14.

Table 4. 14. HVL of radiation qualities used in diagnostic radiology developed by NPL, PTB and NMI, and recommended by IEC. The last column gives the HVL obtained with the code XCOMPW by [NO97].

Radiation quality	kVp, kV	HVL, mm Al				
		NPL	PTB	NMI	IEC	XCOMPW
RQR2	40	1.0	1.36	1.42	1.42	1.27
RQR3	50	1.5	1.72	1.77	1.78	1.60
RQR4	60	2.0	2.02	2.09	2.19	1.89
RQR5	70	2.5	2.29	2.37	2.58	2.16
RQR6	80	2.9	2.59	2.65	3.01	2.47
RQR7	90	3.3	2.91	3.00	3.48	2.79
RQR8	100	3.7	3.23	3.30	3.97	3.14
RQR9	120	4.5	3.88	4.00	5.00	3.87
RQR10	150	5.7	5.01	4.90	6.57	5.04
RQA2	40	2.4	2.13	2.20	2.2	2.04
RQA3	50	4.0	3.67	3.70	3.8	3.57
RQA4	60	5.7	5.24	5.20	5.4	5.11
RQA5	70	7.1	6.64	6.60	6.8	6.54
RQA6	80	8.4	7.96	8.00	8.2	7.95
RQA7	90	9.1	9.03	9.20	9.2	9.08
RQA8	100	9.9	9.93	-	10.1	10.03
RQA9	120	11.5	11.37	-	11.6	11.55
RQA10	150	12.8	12.97	-	13.3	13.24

From this table, it can be seen that some discrepancies are found for the radiation qualities (HVL) given by the different laboratories and specified in the draft of IEC [IEC04]; as an example we can see a variation of more than 25% for radiation quality RQR10 given by IEC and PTB. The radiation qualities have been determined under the specific conditions, which are different from one laboratory to another. For example, the required nominal filtration for the x-ray unit of 2.5 mm Al is not necessarily achieved using the same physical filter sets from one x-ray unit to the other. Standard laboratories and users have to adjust their filtration to meet the required radiation qualities but variations could still result giving different HVL values. IEC [IEC04] requires the user to reproduce the HVL within an uncertainty of 3%.

To find out if the x-ray spectra produced by XCOMPW are either too hard, too soft or adequate a set of data from table 4.14 has to be chosen. Facing the discrepancies in HVL it is a problem of choosing one standard as a reference to use in the comparison. As more details were available from PTB for the specific conditions in the generation of

the x-ray fields leading to the radiation qualities (e.g. the anode angle, ripple, nominal filtration, etc.) the parameters from PTB were used with XCOMPW to generate the corresponding x-ray spectra. The radiation qualities obtained with XCOMPW are also given in table 4.14. A comparison of the data from PTB and XCOMPW shows for the RQR series the calculated spectra are softer except for RQR9 and RQR10 having practically the same hardness. For the filtered spectra represented by series RQA the calculated spectra are softer compared to the PTB data up to tube voltages of 70 kV but equal within the limit or 3% for higher tube voltages (RQA6 to 10). Nevertheless, even when compared to all the other radiation qualities listed in table 4.14, the HVL from XCOMPW gives softer radiation qualities in most cases but a comparison is less stringent as the parameters for the production of these x-ray spectra are not available. These findings contradict a possible explanation made above that XCOMPW might be generating harder spectra compensated by an increased added filtration. Consequently, the tendency for obtaining higher added filtrations with the fit method compared to the HVL method most likely does not arise from this effect.

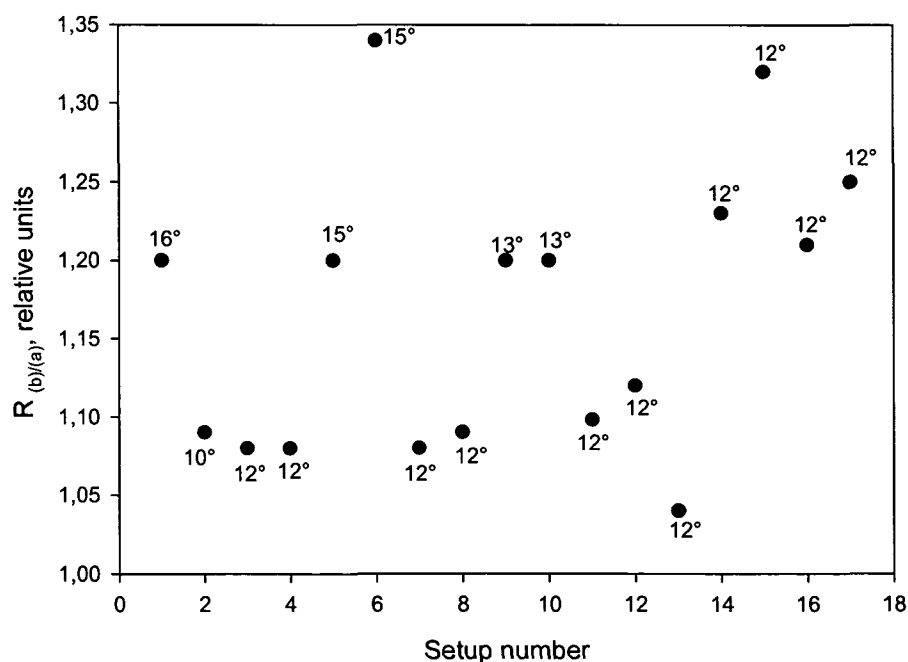


Figure 4. 30. Ratio $R_{(b)/(a)}$ of total filtrations (T.F.) determined by (a) the HVL-method and by (b) the data fit method for different setups corresponding to the x-ray units investigated in this work (see table 4.13). Anode angles are given for each measurement setup.

The same data as used in figure 4.29 but rather plotting the ratio of the total filtration obtained with data fit method and HVL-method are given in figure 4.30

together with the anode angle for each case. For most of the x-ray units having a smaller anode angle it appears that the discrepancies in added filtration obtained by the two methods are smaller than for the larger anode angles. The data for the setups 14 to 17 (units #8 and #9 with an anode angle of 12°) should not be included in this considerations as these two units revealed a disagreement in the values of nominal and measured tubes voltages (see paragraph 4.4.2.1). With the HVL method, the total filtration is derived from the first HVL measured at 60 kV [ISO97]. However, the measured tube voltage for these two units was about 10% less than the nominal 60 kV value. This difference yields lower HVL and consequently the total filtration deduced with the HVL method gives values, which are too low.

For other units with a greater anode angle, a larger ratio in total filtrations is obtained. It would be interesting to understand the reasons for this seemingly occurring trend but the problem here again is the usage of the quality diagrams in the HVL-method. The quality diagram [ISO97] used to derive the total filtration was obtained with units of an unknown anode angle. Strictly speaking, the quality diagram should be only applied for units operating in the same conditions as those used for the determination of this quality diagram. Using the quality diagrams for other parameters might introduce some systematic differences.

Many materials are contributing to the filtration of the primary x-ray beam. The filtration of all the technically required materials is summarized as the nominal filtration given in an equivalent of aluminium. All added filtration appearing during the use of the tube will be due to the increased absorption in the roughened anode surface usually made of tungsten. It is now somewhat a paradox that using either tungsten or aluminium as filter materials gives fairly similar results in terms of reproducing the attenuation curves. It is important to see if a filter material could be replaced by an equivalent of another material giving the same effect on beam quality.

To see the relationship of the added filtration obtained by the fit method for tungsten and aluminium as filtering material the data are plotted in figure 4.31. As can be seen the filter thicknesses for both materials have a nearly linear relationship. A polynomial regression of order 2 gives the equation $AF_{Al} = 0.0166 + 0.1339 \cdot AF_w + 8.2486e^{-4} \cdot AF_w^2$. While the equivalency of tungsten and

aluminium as materials for the added filtration is excellent it is clear that the calculated distributions of the x-ray photons for these two different absorber materials will be different. Mainly due to the K-edge and the steeper increase of the attenuation coefficient with decreasing photon energy (photoelectric effect) for tungsten a tungsten-filtered spectrum will look different to an aluminium-filtered spectrum. These differences in the x-ray spectra have been demonstrated in paragraph 4.4.2 (see figure 4.22) for the case with the largest filter thickness obtained with tungsten (11.89 μm) and a corresponding filter thickness of 1.72 mm with aluminium.

A calculation of the HVL for these two spectra with XCOMPW at a tube voltage of 100 kV gives $\text{HVL}_W = 4.30 \text{ mm Al}$ and $\text{HVL}_{Al} = 4.33 \text{ mm Al}$. The difference in HVL for the two spectra is less than 0.7%. This difference is small and well within the limits of 3% recommended by [IEC04]. The two spectra can then be considered as having the same radiation quality. This gives an indication on the fact that kerma and HVL measurements to some extent obscure the spectral distributions and enable the usage of equivalent filter thicknesses for the description of x-ray units and photon fields.

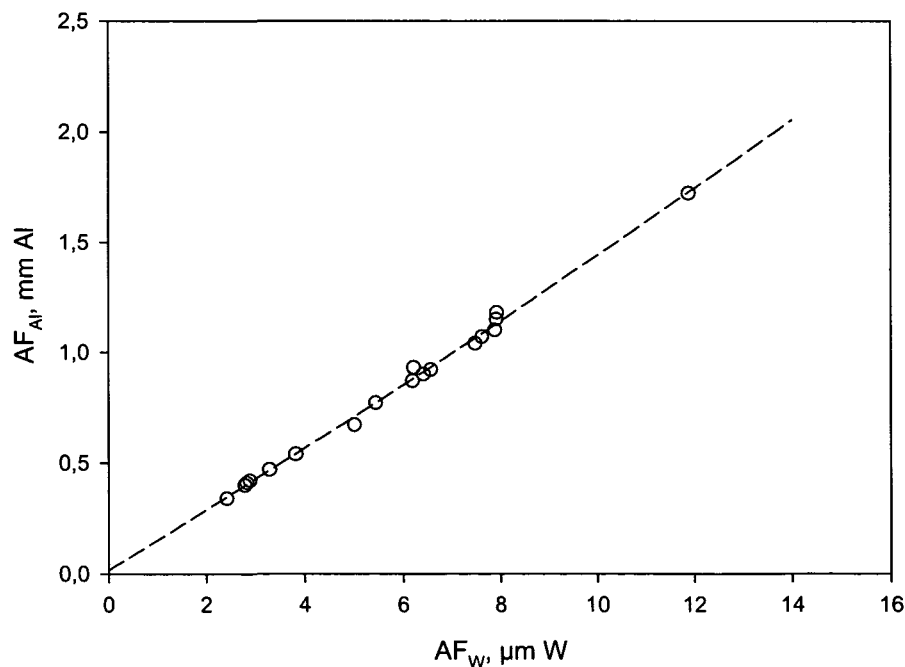


Figure 4.31. Relationship of the added filtration obtained by the fit method for tungsten (AF_W) and aluminium (AF_{Al}) as filtering material

An application of the data for the total filtration obtained is the calculation of kerma for an x-ray unit for any type of filter and any desired thickness. This capability can be assessed by calculating the kerma data of the attenuation curves using the thicknesses for total filtration obtained with both methods. Clearly a better agreement between measured and calculated attenuation curves is obtained using the fitting method comparing to the HVL method. A typical example is shown in figure 4.32, the diagrams for all measurements can be found in annex A. In contrast to indirect methods, no reference data are needed to determine the filter thickness with the fitting method and no specific parameters are required for the settings of the tube under investigation.

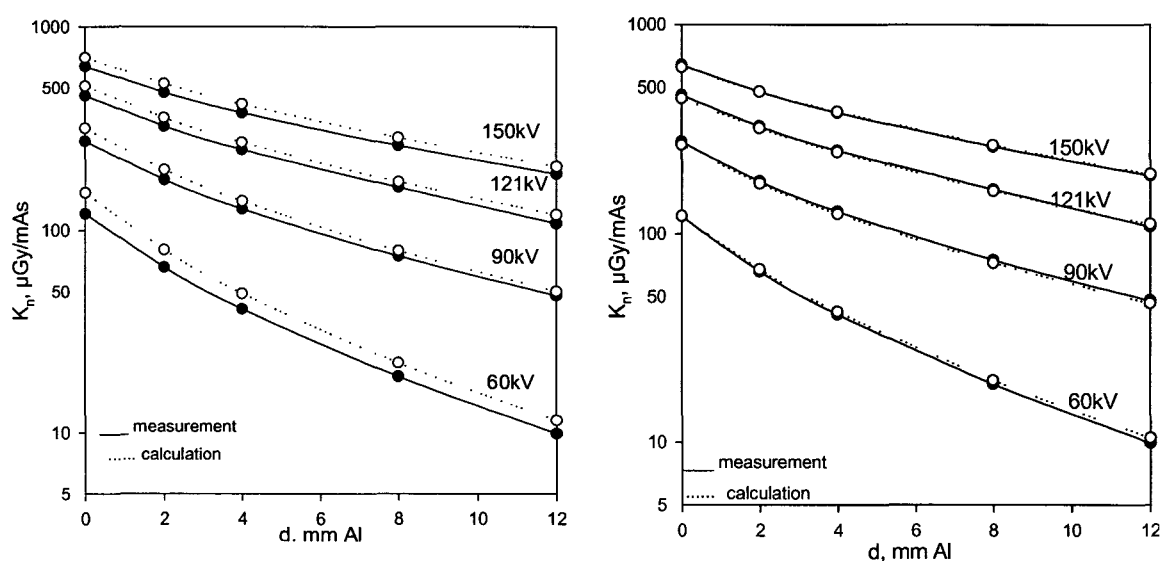


Figure 4. 32. Comparison of typical measured and calculated attenuation curves obtained for unit #1 (BMTP28). Normalised air kerma K_n (mGy/mAs) is plotted versus added filter thickness d (mm Al). Data for calculated attenuation curves are obtained applying the total filtration as determined using the HVL method (left) and the fit method (right).

Obviously the agreement of calculated attenuation curves using the total filtration obtained with the HVL-method is not as good as with the fit method. The fit method uses a normalization factor and it can be argued that a better agreement could be achieved if the data from the HVL-method could also be normalised. The tube voltage used in the HVL-method is 60 kV. If one uses the measured kerma at that voltage for normalisation the example given in figure 4.33 will show an improved agreement but still not as good as with the fit method.

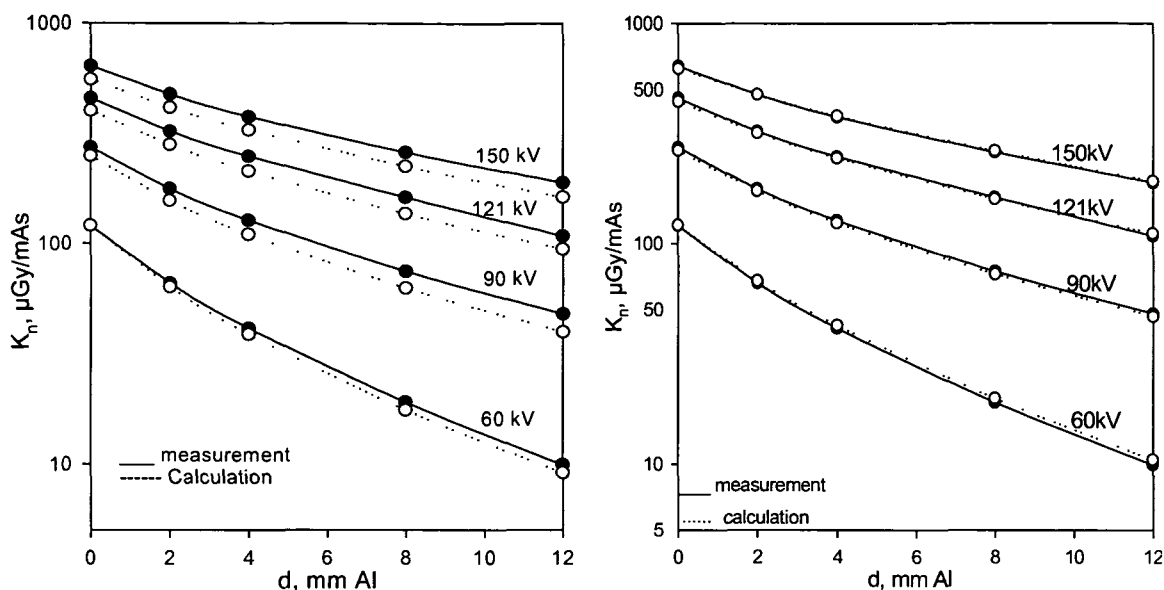


Figure 4.33. Comparison of typical measured and calculated attenuation curves obtained for unit #1 (BMTP28). Normalised air kerma K_n (mGy/mAs) is plotted versus added filter thickness d (mm Al). Data for calculated attenuation curves are obtained applying the total filtration as determined using the HVL method together with a normalisation factor (left) and the fit method (right).

Another similar application is the estimation of patient entrance surface air kerma for an x-ray unit for which the added filtration has been determined with the fit method. Indeed, using the code XCOMPW [No97] and applying the total filtration and the normalisation factor obtained from accurate air kerma and tube voltage measurements, would allow the assessment of patient entrance surface kerma in any x-ray projection and for any condition (kVp, voltage ripple, anode angle, distance, other added filters).

5. CONCLUSIONS

In diagnostic radiology a minimum filtration is needed with x-ray units to reduce radiation dose to the patient from the low energy x-rays in the spectrum. As the inherent filtration of tube and tube housing usually gives insufficient attenuation some additional filters are introduced to achieve the required filtration of an equivalent in aluminium of 2.5 mm [ICRP34]. The total inherent filtration also includes the attenuation of the x-rays in the anode material itself. The x-rays, produced by electrons slowed down in the anode, encounter some attenuation in the anode material, depending on the anode angle and the beam direction. The contribution of attenuation within the anode to inherent filtration is recognised in literature but not investigated thoroughly. This is easily explained since the state of the anode surface is usually not known and not considered in measurements of radiation output with x-ray units.

Investigating the effect of anode surface roughness on x-ray tube spectra with common clinical x-ray units without knowledge of the anode condition would be a difficult task. To study a possible contribution of surface roughness to total inherent filtration, actual surface profiles of anode samples were determined and the influence of these surface profiles on spectra and spectral parameters was investigated. To quantify the effect of anode surface roughness, geometrical irregularities of pitted surfaces have been assessed. For this purpose used rotating anodes were collected from decommissioned clinical x-ray tubes. The surface profiles and surface roughness of 8 focal tracks were determined and described using the arithmetic mean R_a of the deviation in the profile from the centre line ranging from 1.32 μm (sandblasted finish without surface degradation) to 5.32 μm (a track for a small focus).

The surface profiles were then used to calculate x-ray spectra using a computer code using the same model as in XCOMP32 [No97]. For each surface about 40000 spectra were calculated with the electrons entering the anode at random positions and spectral parameters were then determined. The simulation showed that for rough

surfaces, the x-rays have to penetrate an additional absorbing layer of tungsten increasing in thickness with anode roughness. The anode with the roughest focal track ($R_a=5.22\text{ }\mu\text{m}$) yields a mean additional absorber thickness in direction of the x-ray beam of about $18\text{ }\mu\text{m}$. The corresponding loss in output for this anode was about 30% at 70 kVp. The effect on mean photon energy is rather small but highest at 70 kVp (+1 keV at $R_a=5.22\text{ }\mu\text{m}$) and lowest at 140 kVp ($\sim 0\text{ keV}$). This is due to the K-edge in the attenuation coefficients of tungsten at 69.5 keV. Beam hardening is thus reduced for higher voltages as absorption at lower photon energies is balanced by higher absorption above the K-edge while at lower voltages beam hardening is fully effective. The pattern of changes in HVL is more complex but in essence also reflects voltage, roughness and tungsten K-edge. Finally, the results obtained showed that increased roughness due to tube ageing could result in an additional amount of filtration. As a consequence total filtration of the x-ray unit will increase with the tube age.

A further validation of these results on conventional x-ray units is not feasible and would require a unit allowing the dismantling of an x-ray anode to study the behaviour of anode surface with tube loading together with an x-ray spectrometry system and dosimetry. In this work, the roughening of the anode surface was determined quantitatively and the consequences were studied by simulation of the x-ray generation. Target pitting induced by tube usage affects the range distribution of the electrons as well as the attenuation of photons within the target.

The kind of variation in spectral output expected from target roughening may explain some differences between the experimental x-ray spectra data from Seelentag [Se79] and those calculated using the code XCOMP5R [No85]. Indeed, it was observed that only small amounts of additional absorption layers of tungsten would be sufficient to produce beam hardening that yields simulated x-ray spectra similar to those from [Se79].

The total filtration of a unit is an essential quantity but as a direct measurement of the total filtration of the x-ray tube assemblies is not feasible, various indirect methods for such a determination have been proposed [Ru49, Ar72, B 77, Th40, Su83, Po73]. All of these methods show some deficiencies mostly due to the unknown spectral distribution of x-rays and the variability of radiation quality with the continuing

use of the x-ray tubes. It was the incentive to develop a method for the determination of total filtration including the effects of anode surface deterioration. This method is based on the concept of an additional absorbing tungsten or aluminium layer to compensate for the effect of a rough anode surface from diagnostic x-ray units. The basic idea was to measure attenuation curves for the x-ray unit in question fitting calculated attenuation curves obtained by a model by only varying the thickness of an additional filter and a general normalization factor to the experimental data. The filter material could be either tungsten as the additional filter layer due to roughness is made up of tungsten, or aluminium. The equivalent in aluminium is a common way of describing inherent filtration for an x-ray unit. Using this concept, the fit method calculated first the spectral output using the code XCOMPW [No97]; the inherent filtration and a variable additional layer of tungsten attenuate then the output. The thickness of the additional filter was optimised, using the algorithm XATTFIT [No03] as to give the best fit to attenuation curves measured for that x-ray unit.

Attenuation curves have been determined for nine clinical x-ray units each having a small and a large focal spot plus one unit with a built-in filter combination, hence giving a total of 19 setups. The total filtrations for the x-ray devices were determined using the HVL method with the quality diagram recommended by the currently applicable standard [ISO97] and compared with the results given by the fit method.

A comparison of the measured attenuation curves with calculated attenuation data using the same parameter set and the total filtration, as determined by the HVL and the fit method, was made to assess the accuracy of kerma data using only the total filtration for a calculation. It can be seen from figures given in annex A that the fit method gives better results than the HVL method for almost all cases. Discrepancies arising from the HVL method could be expected, since it is essential that the tube assembly under investigation be almost identical to, and operated under the same conditions as the reference tube from which the quality diagram was obtained. On the other hand, Nagel [Na88] has shown that the HVL method allows only for a rough estimation of the filtration and could typically give errors of up to $\pm 30\%$. In contrast, the fit method does not rely on any prerequisites as specific parameter settings but only requires the measurement of a set of kerma yields for some tube voltages and filter

thicknesses. The total filtration determined by the fit method consistently gives larger filter thicknesses than with the HVL-method. From the simulation of the effect of surface roughness on beam quality, it was concluded that the variation of HVL with tube voltage for varying roughness is not constant but has its maximum variation at 80 kV (figure 3.20b). The HVL-method uses an attenuation curve determined at a tube voltage of 60 kV while the fit method comprises measurements for a larger range of tube voltages. This could explain the larger values for the added filtration as determined by the fit method.

The thicknesses of the tungsten layers obtained using the fit method vary from 2.43 μm to 11.89 μm , which corresponds very well to the thicknesses of the additional absorbing layers determined for rough anodes. A derived surface roughness R_a varying from 1.5 to 4.5 μm is within the range of surface roughness found experimentally for the anode samples in section 3. As a total filtration is usually given in terms of an equivalent aluminium filter, the same process was also done for aluminium as the additional filter material. Here, the thickness of the additional aluminium filter varies from 0.34 to 1.72 mm Al.

As could be expected, focal spots showed larger surface roughness for the small focus than for the large ones. Power density in the small focal spot in an x-ray tube is usually larger than for the large focus; this results in a larger anode loading and a larger roughness of the tracks for the focal spots. This was found for all tubes except for the unit # 1, which was mostly operated using the large focus, thereby explaining this result. Indeed, this particular x-ray unit, dedicated to research and development work, is mainly used with its large focus. The anode surface roughness of this large focus was, as expected, more pronounced compared to that of the small focus.

The results highlight the influence of the condition of the anode surface on the radiation output as a source of variability in spectral distribution and parameters (HVL, mean photon energy,...). This variability should always be kept in mind when comparing experimentally determined x-ray spectra. The variations encountered there very often are in range, which could be caused by surface roughening. The same is true when comparing the data for HVL from different dosimetry laboratories. Some of these discrepancies might be due to an imperfect model for the production of x-rays but anode

roughness should always be considered in this context despite of the difficulties in determining the amount of roughness.

A contribution of this work to the estimation of patient entrance surface doses in diagnostic radiology is highlighted. Indeed, using the code XCOMPW [No97] and applying the total filtration and the normalisation factor obtained from accurate air kerma and tube voltage measurements, would allow the assessment of patient entrance surface kerma in any x-ray projection and for any condition (kVp, voltage ripple, anode angle, distance, other added filters). This could help in the determination of patient doses for x-ray units without any means for an individual dose assessment, as dose-area-product meters or entrance-surface-dose (ESD) meters. If an evaluation of the inherent filtration is made for an x-ray unit using the fit method all ESD values could be deduced using the mAs-values obtained for an examination in diagnostic radiology with saving of time and expenses. An assessment of patient doses in diagnostic radiology using this method could contribute to the requirements stipulated by the *Council Directive 97/43/Euratom of 30 June 1997 on health protection of individuals against the dangers of ionising radiation in relation to medical exposure* [EU97].

References

- [Ac98] Acosta E., Llovet X., Coleoni E., Riveros J. A. and Salvat F. Monte Carlo simulation of x-ray emission by kilovolt electron bombardment. *Journal of Applied Physics*, volume **83**, number **11**, 6038 (1998)
- [Ar72] Ardran G. M. and Crooks H. E. The measurement of inherent filtration in diagnostic x-ray tubes and the effect of target angle on x-ray quality *Br. J. Radiol.* **45** 599-602 (1972)
- [At86] Attix F.H. Introduction to radiological physics and radiation dosimetry. A Wiley-Interscience Publication (1986)
- [Bä79] Bäuml A. Report STH 23/77 (Neuherberg, Institut für Strahlenhygiene des Bundesgesundheitsamtes) *Medizinische Physik*. Reich ed. (Heidelberg: Hüthig) 221-5 (1979)
- [Be99] Berger M. J., Hubbell J. H., Seltzer S. M., Coursey J. S. and Zucker D. S. *XCOM: Photon Cross Section Database* (version 1.2). [Online] Available: <http://physics.nist.gov/xcom>. National Institute of Standards and Technology, Gaithersburg, MD (1999)
- [Bi79] Birch R. and Marshall M. Computation of bremsstrahlung x-ray spectra and comparison with spectra measured with a Ge(Li)-detector *Phys. Med. Biol.* **24** 505-517 (1979)
- [Bi79a] Birch R., Marshall M. and Ardran G. M. Catalogue of spectral data for diagnostic x-rays. *Scientific Report Series – 30*. The Hospital Physicists' Association, London (1979)
- [Bi82] Birch R., Marshall L.H.J. Peaple: Theoretical and measured L x-rays from a solid Tungsten target. *Phys. Med. Bio.* **27** 1119 (1982)
- [Br97] Briesmeister J.F. MCNP - A General Monte Carlo N-Particle Transport Code - Version 4B, *Los Alamos National Laboratory report. LA-12625-M* (1997)
- [Br82] Bröndler Th., Eickelkamp E. and Jakschik J. Ein Meßgerät zur schnellen Bestimmung des Scheitelwertes der Röhrenspannung und Einschaltzeit von Röntgeneinrichtungen. *Fortsehr. Röntgenstr.* **137** 588 (1982)
- [Ca84] Caceci S. M. and Cacheris W. P. Fitting Curves to Data, The Simplex algorithm is an answer. *Byte*, 340-62 (1984)
- [Ca98a] Caon M., Bibbo G., Pattison J. and Bhat M. The effect on dose to computed tomography phantoms of varying the theoretical x-ray spectrum: A comparison of four diagnostic x-ray spectrum calculating codes *Med. Phys.* **25** (6) 1021-1027 (1998)

- [Cr97] Cranley K., Desponds L., Fogarty G.W.A. and Gilmore B.J. Catalogue of Diagnostic X-Ray Spectra & Other Data. Report **78**. Institute of Physics and Engineering in Medicine. (1997)
- [Cu90] Curry S., Dowdey J.E. and Murry R.C. Physics of diagnostic radiology. Lea & Febiger, Philadelphia, p.35, p. 50 (1990)
- [De02] DeWerd L.A., Micka J.A., Laird R.W. and Pearson D.W. The effect of spectra on calibration and measurement with mammographic ionization chambers. *Med. Phys.* **29** (11): 2649-54 (2002)
- [DIN01] Calibration Possibilities at PTW-FREIBURG, cert. DIN EN 46001. EN ISO 9001. Cert.Nr. 50040-60-00 (2001)
- [De99] Dendy P.P. and Heaton B. Physic for diagnostic radiology. Institute of physics publishing, Bristol, UK (1999)
- [El62] Elsas A. and Zimmer Th. Höhere Belastung von Drehanodenröhren durch Verwendung von legierten Anoden. *Fortschr. Röntgenstr.* **97** 511-514 (1962)
- [Ev55] Evans R. D. The atomic nucleus. McGraw-Hill, New York (1955)
- [Eu99] European Commission. Guidance on diagnostic reference levels (DRLs) for medical exposures: Radiation Protection **109** (1999)
- [Fa97] Farr R.F. and Allisy-Roberts P.J. Physics of medical imaging. SandersCompany Ltd, London, UK (1997)
- [Gr64] Green M. The angular distribution of characteristic x-radiation and its origin within a solid target. *Proc. Phys. Soc.* **83** 435 (1964)
- [Gr68] Green M. and Cosslett V.E. Measurements of K, L and M shell x-ray production efficiencies. *Brit. J. Appl. Phys.* **1** 425 (1968)
- [Ha84] Hajek P. and Nowomy R.: Reduktion der Strahlendosis durch Verwendung von Carbonfiber-Kassetten. *Fortschr. Röntgenstr.* **140** 334 (1984)
- [HPA77] Hospitals Physicists' Association: The physics of radiodiagnosis. Scientific Report Series 6, 2nd ed., HPA, London (1977)
- [Hu82] Hubbell J. H. Photon mass attenuation and energy-absorption coefficients from 1 keV to 20 MeV. *Int. J. Appl. Radiat. Isot.* **33** 1269 (1982)
- [IAEA96] International Atomic Energy Agency. International Basic Safety Standards for Protection against Ionising Radiation and for the Safety of Radiation Sources. Safety Series n° **115** (1996)
- [ICRP82] The International Commission on Radiological Protection. Protection of the Patient in Diagnostic Radiology ICRP **34** (Pergamon Press, Oxford) (1982)

- [ICRP87] The International Commission on Radiological Protection. ICRP Data for Use in Protection against External Radiation ICRP Publication 51. Ann. ICRP **17** (1987)
- [ICRU85] ICRU. Determination of Dose Equivalents resulting from External Radiation Sources. Report **39** (Bethesda, MD: ICRU Publications) (1985)
- [IEC73] International Electrotechnical Commission. Medical electrical equipment - Part 1: General requirements for safety - 3. Collateral standard: General requirements for radiation protection in diagnostic x-ray equipment. Standards publication n° **407** p 21(1973)
- [IEC76] International Electrotechnical Commission. Inherent filtration of an x-ray tube assembly. IEC Standards Publication n° **522** (IEC, Geneva) (1976)
- [IEC84] International Electrotechnical Commission. Determination of the maximum symmetrical radiation field from a rotating anode x-ray tube for medical diagnosis. Document 62B (sec. 91) (1984)
- [IEC98] International Electrotechnical Commission. Medical electrical equipment - Part 2-7: Particular requirements for the safety of high-voltage generators of diagnostic x-ray generators. Edition: 2.0, Document Number: IEC60601-2-7 (1998)
- [IEC04] International Electrotechnical Commission. Medical radiation x-ray equipment – Radiation conditions for use in the determination of characteristics. Report IEC 61267 (draft, to be published dec. 2004)
- [ISO81] Light metals and their alloys. Code of designation based on chemical symbols, ISO 2092. *Int. Organization for Standardization, Geneva* (1981)
- [ISO96] X and gamma reference radiation for calibrating dosimeters and dose rate meters and for determining their response as a function of photon energy - Part 1: Radiation characteristics and production methods ISO 4037-1. *Int. Organization for Standardization, Geneva* (1996)
- [Jo84] Johns H. E. and Cunningham J.R. “The physics of radiology”, Thomas, Springfield, Illinois, U.S.A.(1984).
- [Kr23] Kramers H. A. On the theory of x-ray absorption and of the continuous x-ray spectrum. *Philos. Mag.* **46** 836-871 (1923)
- [Kr02] Krmar M., Nikolic D. and Krstonosic P. A. Simple method for bremsstrahlung spectra reconstruction from transmission measurements. *Med.Phys.* **29**(6) (2002)
- [LI03] Llovet X. and Sorbier L. Monte Carlo simulation of x-ray spectra generated by kilo-electron-volt electrons. *Journal of Applied Physics*, volume **93**, number 7, 3844 (2003)

- [Mc69] McMaster W.H., DelGrande N.K., Mallett J.H. and Hubbell J.H. Compilation of x-ray cross-sections (sec. 2). Report UCRL-50174, Livermore (1969)
- [Me00] Mercier J.R., Kopp D.T., McDavid W.D., Dove S.B., Lancaster J.L. and Tucker D.M. Modification and benchmarking of MCNP for low-energy tungsten spectra *Med. Phys.* **27** 2680-2687 (2000)
- [Me00a] Mercier J.R., Kopp D.T., McDavid W.D., Dove S.B., Lancaster J.L. and Tucker D.M. Using measured 30-150 kVp polychromatic tungsten x-ray spectra to determine ion chamber factors, N_x (Gy C⁻¹). *Health Phys.* **79**(4) 402-406 (2000)
- [Na88] Nagel H.D. Limitations in the determination of total filtration of x-ray tube assemblies *Phys. Med. Biol.* **33** 271-9 (1988)
- [Ne65] Nedler J.A. and Mead R. A Simplex method for function minimisation. *Computer journal* **7** 308 (1965)
- [Ne85] Nelson W.R., Hirayama H. and Rogers D.W.O. EGS4 - Electron Gamma Shower version 4- SLAC-265 Institute for National Measurement Standards, National Research Council of Canada (1985)
- [No84] Nowotny R. Application of Simicrostrip detectors in medicine and structural analysis. *Nucl. Instr. Meth.* **34** 226 (1984)
- [No85] Nowotny R. and Höfer A. Ein Programm für die Berechnung von diagnostischen Röntgenspektren *Fortschr. Röntgenstr.* **142** 685-9 (1985)
- [No97] Nowotny R. Xcomp32, a Program for the Calculation of Diagnostic X-Ray Spectra. (abstract). *Med Bio Eng Comp* **35** Suppl. 2, 697 (1997)
- [No03] Nowotny R. A code *XATTFIT* composed of the procedure *SIMP* for the data fit. Private communication (2003)
- [Pa65] Pasternack B.S. and Blatz H. Radiation dosage to the population of New York City from medical diagnostic radiology. Progress report of the Institute of environmental medicine. (1965)
- [Pa74] Panossian L. and Krause R.A. Experimental K and L relative x-ray emission rates. *Atomic Data Nucl. Data Tables* **14** 91 (1974)
- [Pr88] Press W.H. and Flannery B.P. Numerical Recipes *Cambridge University Press* (1988)
- [Pr73] Procter N.M. A method of checking filtration and kilovoltage on diagnostic x-ray tubes. *Br. J. Radio.* **46** 525-8 (1973)
- [PTB00] Physikalisch Technische Bundesanstalt, Ulrike Ankerhold. Catalogue of x-ray spectra and their characteristic data-ISO and DIN radiation qualities, therapy and diagnostic radiations qualities, unfiltered x-ray spectra. (2000)

- [Re60] Reinsma K. The inherent filtration of x-ray tubes. *Radiology* **74** 971-2 (1960)
- [Ru49] Rump W. Über die Eingenfilterung von Röntgenrohren nebst deren Schutzbehältern und damit zusammenhängende Fragen. *Röntgenfortschr.* **71** 145-62 (1949)
- [Sa74] Salem S.I., Panossian S. L. and Krause R.A. Experimental K and L relative x-ray emission rates. *Atomic Data Nucl. Data tables* **14** 91 (1974)
- [Sa01] Salvat F., Fernandez-Varea J.M., Acosta E. and Sempau J. PENELOPE - A code for Monte Carlo simulation of Electron and photon transport. NEA, Nuclear Science Committee. (2001)
- [Sc58] Schorsch F. Gütebestimmung an Technischen Oberflächen. Wiss. Verl.-Ges. Stuttgart (1958)
- [Se82] Seelentag W.W., Panzer W., Drexler G., Platz L. and Saumer F. A catalogue of spectra for the calibration of dosimeters. GSF-Bericht 560, Ges. f. Strahlenforschung, Neuherberg (1979)
- [Se82] Seltzer S.M. and Berger M.J. Evaluation of the collision stopping power of elements and compounds for electrons and positrons. *Int.J. Appl. Radiat. Isot.* **33** 1189 (1982)
- [Se82a] Seltzer S.M. and Berger M.J. Procedure for calculating the radiation stopping power for electrons. *Int.J. Appl. Radiat. Isot.* **33** 1219 (1982)
- [So72] Soole B.W. The effect of target absorption on the attenuation characteristics of Bremsstrahlung generated at constant medium potentials. *J. Phys.* **B5** 1583 (1972)
- [Sp87] Sprawls P. Physical principles of medical imaging. Aspern Publishers, Inc, Maryland (1987)
- [St86] Stears J.G., Felmlee J. P. and Gray J. E. Half- value-layer increase owing to tungsten buildup in x-ray tube: fact or fiction. *Radiology* **160** 837-8 (1986)
- [St70] Storm E. and Israel H.I. Photon cross-sections from 1 keV to 100 MeV for elements $Z = 1$ to $Z = 100$. *Nucl. Data Tables* **A7** 565 (1970)
- [Su12] Sundararaman V., Prasad M.A. and Vota R.B. Computed spectra from diagnostic and therapeutic x-ray tubes. *Phys. Med. Bio.* **18** 208 (8) (1973)
- [Su83] Sutcliffe J.F. A simple method for measuring the quality of a diagnostic x-ray beam. *Phys. Med. Bio.* **28** 1459 (1983)
- [Ta59] Taylor L.S. Physical Foundations of Radiology, 2nd Edition, pp 227-57 (1959)

- [Te90] Teubner B. Dosimetrie ionisierender Strahlung. Reich ed. Stuttgart, P.199 (1990)
- [Th40] Thoreaus R. Standard curves of the absorption of roentgen rays in aluminium and their employment for estimating the equivalent of the initial filtration in roentgen tubes. *Acta Radiologica* **21** 603-14 (1940)
- [Tu91] Tucker M.D., Barnes G.T. and Chakraborty D.P. A semiempirical model for generating tungsten target x-ray spectra, *Phys. Med. Bio.* **18**, 211-218 (1991)
- [Ve99] Verhaegen F., Nahum A.E., Van de Putte S. and Namito Y. Monte Carlo Modelling for radiotherapy kV units. *Phys. Med. Bio.* **44** 1767 (1999)
- [Wh12] Whiddington R. The transmission of cathode rays through matter. Pro. Royal Soc. A86 360 (1912)

Annex A: Measured and calculated attenuation curves using the fit and the HVL method

The following figures show the attenuation curves, which have been obtained for 9 x-ray units with a total of 23 individual settings listed below. Each parameter set is characterised by focal spot size, anode angle, voltage ripple, nominal filtration and source-to-detector distance. With each parameter set a number of measurements were made using several tube voltages. Calculations were made with the nominal tube voltages as indicated on the console. Measurements of attenuation curves for some x-ray units (#8 and #9) have been redone taking into account a correction for the nominal tube voltages as explained in paragraph 4.4.2.1.

First, the total filtration determined from the HVL at 60kV tube voltage as given in [ISO97] (see paragraph 4.2.7) as the standard protocol used in metrology, is given for each data set.

Then, the results of the data fit process are shown using the attenuation curves under two presumptions: the additional filtration being either due to aluminium only, or due to tungsten only. Results are shown in figures A.1(a) to A.23(a).

In another comparison, the attenuation data were calculated, using the total filtration as determined with the HVL method instead of the nominal filtration. Results are shown in figures A.1(b) to A.23(b).

List of measurements:

<i>X-ray unit:</i> #1 - BMTP28- large focus.	A-3
<i>X-ray unit:</i> #1 - BMTP28- small focus.	A-4
<i>X-ray unit:</i> #2 - F6-GASTRO1- large focus.	A-5
<i>X-ray unit:</i> #2 - F6-GASTRO1- small focus.	A-6
<i>X-ray unit:</i> #3 - F6-SKELETT3- large focus.	A-7
<i>X-ray unit:</i> #3 - F6-SKELETT3- small focus.	A-8
<i>X-ray unit:</i> #4 - F6-THORAX1- large focus.	A-9
<i>X-ray unit:</i> #4 - F6-THORAX1- small focus.	A-10
<i>X-ray unit:</i> #5 - F6-THORAX2- large focus.	A-11
<i>X-ray unit:</i> #5 - F6-THORAX2- small focus.	A-12
<i>X-ray unit:</i> #6 - F7-SKELETT1- large focus.	A-13
<i>X-ray unit:</i> #6 - F7-SKELETT1- small focus.	A-14
<i>X-ray unit:</i> #7 - F7-SKELETT2- large focus.	A-15
<i>X-ray unit:</i> #7 - F7-SKELETT2- large focus - 0.1 mm Cu.	A-16
<i>X-ray unit:</i> #7 - F7-SKELETT2- small focus - 0.1 mm Cu.	A-17
<i>X-ray unit:</i> #8 - F6-GASTRO2- large focus.	A-18
<i>X-ray unit:</i> #8 - F6-GASTRO2- large focus; kVp correction.	A-19
<i>X-ray unit:</i> #8 - F6-GASTRO2- small focus.	A-20
<i>X-ray unit:</i> #8 - F6-GASTRO2- small focus, kVp correction.	A-21
<i>X-ray unit:</i> #9 - F6-SKELETT2- large focus.	A-22
<i>X-ray unit:</i> #9 - F6-SKELETT2- large focus - kVp correction.	A-23
<i>X-ray unit:</i> #9 - F6-SKELETT2- small focus.	A-24
<i>X-ray unit:</i> #9 - F6-SKELETT2- small focus - kVp correction.	A-25

X-ray unit: #1 - BMTP28-large focus

Anode angle: 16°

Voltage ripple: converter/3.4%

Distance: 55 cm

Nominal total filtration: 2.5 mm Al + 0 mm Cu

Total filtration by HVL method:

Measured HVL: 2.28 mm Al

Total filtration obtained from HVL: 2.847 mm Al

Data fit:

Final values (after 33 iterations):

Filter material	Added filter	Normalisation factor
Al	0.925 mm	0.9656
W	6.570 μ m	0.9644

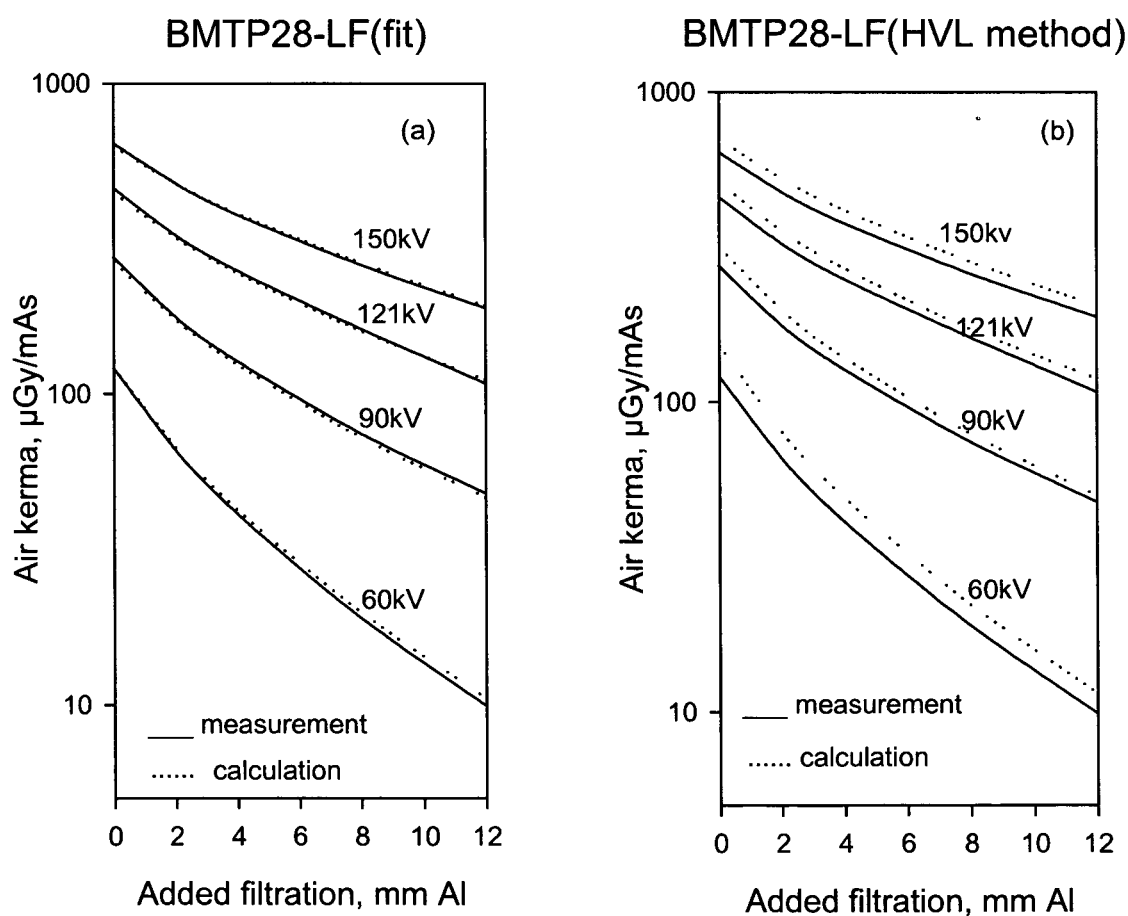


Figure A. 1. Measured attenuation curves obtained for various tube voltages compared with: (a) calculated data using 3.42 mm Al (= 2.5 mm Al nominal filtration + 0.92 mm Al additional filtration), (b) data calculated with the same parameters but using 2.85 mm Al determined with HVL method.

X-ray unit: #1 - BMTP28- small focus

Anode angle: 10°

Voltage ripple: converter/3.4%

Distance: 55 cm

Nominal total filtration: 2.5 mm Al + 0 mm Cu

Total filtration by HVL method:

Measured HVL: 2.47 mm Al

Total filtration obtained from HVL: 2.78 mm Al

Data fit:

Final values (after 43 iterations):

Filter material	Added filter	Normalisation factor
Al	0.5433 mm	0.8931
W	3.8301 μm	0.8918

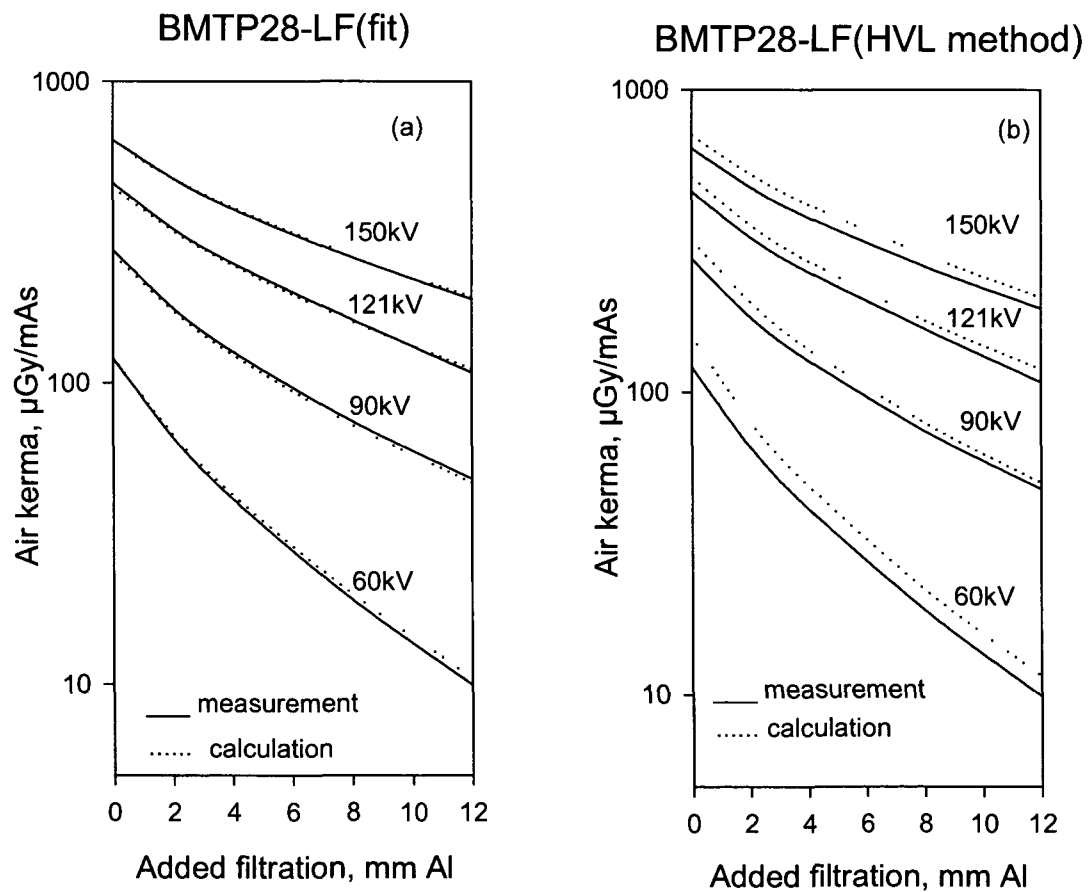


Figure A. 2. Measured attenuation curves obtained for various tube voltages compared with: (a) calculated data using 3.04 mm Al (= 2.5 mm Al nominal filtration + 0.54 mm Al additional filtration), (b) data calculated with the same parameters but using 2.78 mm Al determined with HVL method.

X-ray unit: #2 - F6-GASTRO1-large focus

Anode angle: 12°

Voltage ripple: converter/3.4%

Distance: 55 cm

Nominal total filtration: 2.5 mm Al + 0 mm Cu

Total filtration by HVL method:

Measured HVL: 2.42 mm Al

Total filtration obtained from HVL: 3.16 mm Al

Data fit:

Final values (after 36 iterations):

Filter material	Added filter	Normalisation factor
Al	0.8984 mm	0.9134
W	6.4207 μm	0.9125

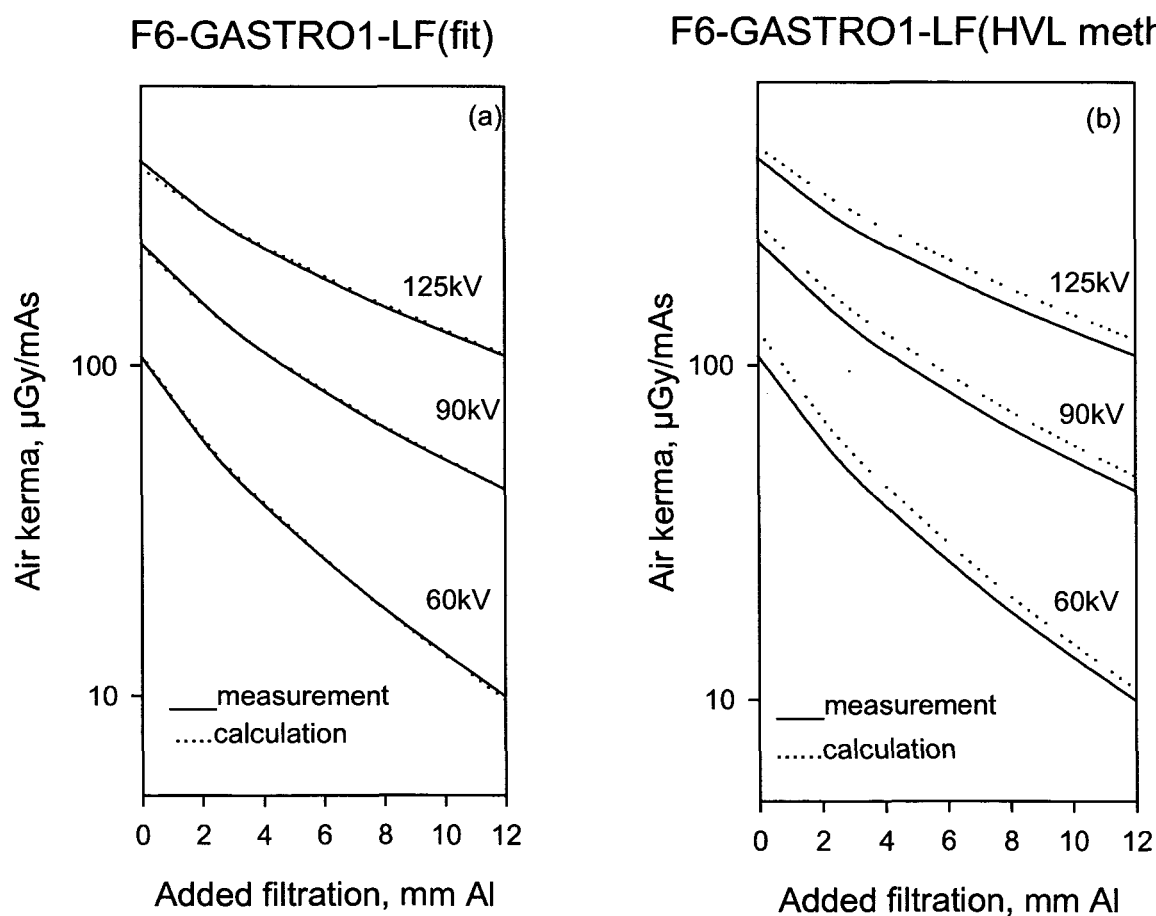


Figure A.3. Measured attenuation curves obtained for various tube voltages compared with: (a) calculated data using 3.4 mm Al (= 2.5 mm Al nominal filtration + 0.9 mm Al additional filtration), (b) data calculated with the same parameters but using 3.16 mm Al determined with HVL method.

X-ray unit: #2 - F6-GASTRO1-small focus

Anode angle: 16°

Voltage ripple: converter/3.4%

Distance: 55 cm

Nominal total filtration: 2.5 mm Al + 0 mm Cu

Total filtration by HVL method:

Measured HVL: 2.49 mm Al

Total filtration obtained from HVL: 3.32 mm Al

Data fit:

Final values (after 30 iterations):

Filter material	Added filter	Normalisation factor
Al	1.0699 mm	0,9303
W	7.6193 μm	0.9286

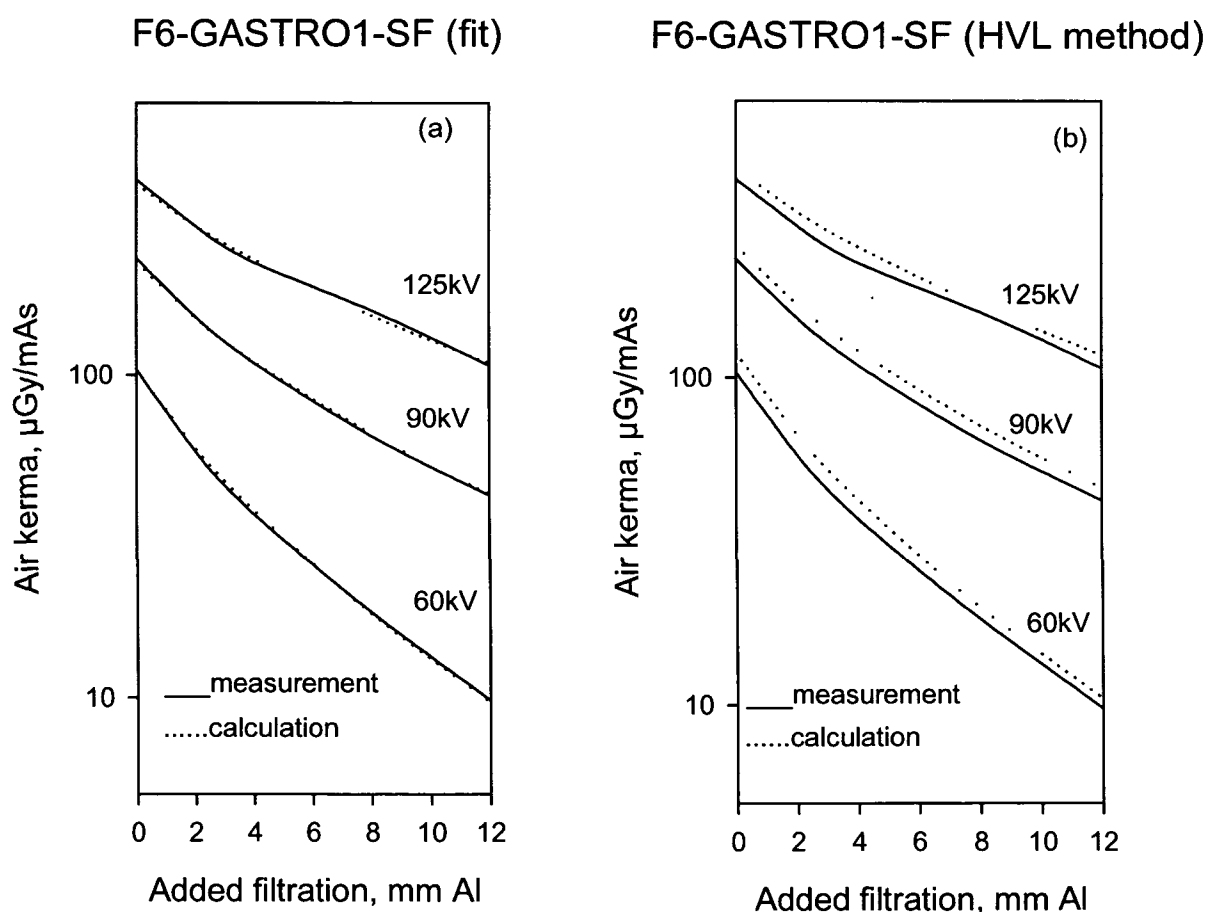


Figure A. 4. Measured attenuation curves obtained for various tube voltages compared with: (a) calculated data using 3.57 mm Al (= 2.5 mm Al nominal filtration + 1.07 mm Al additional filtration), (b) data calculated with the same parameters but using 3.32 mm Al determined with HVL method

X-ray unit: #3 - F6-SKELETT3-large focus

Anode angle: 15°

Voltage ripple: converter/3.4%

Distance: 55 cm

Nominal total filtration: 2.5 mm Al + 0 mm Cu

Total filtration by HVL method:

Measured HVL: 2.31 mm Al

Total filtration obtained from HVL: 2.92 mm Al

Data fit:

Final values (after 31 iterations):

Filter material	Added filter	Normalisation factor
Al	1.0424 mm	0.9743
W	7.4796 μ m	0.9742

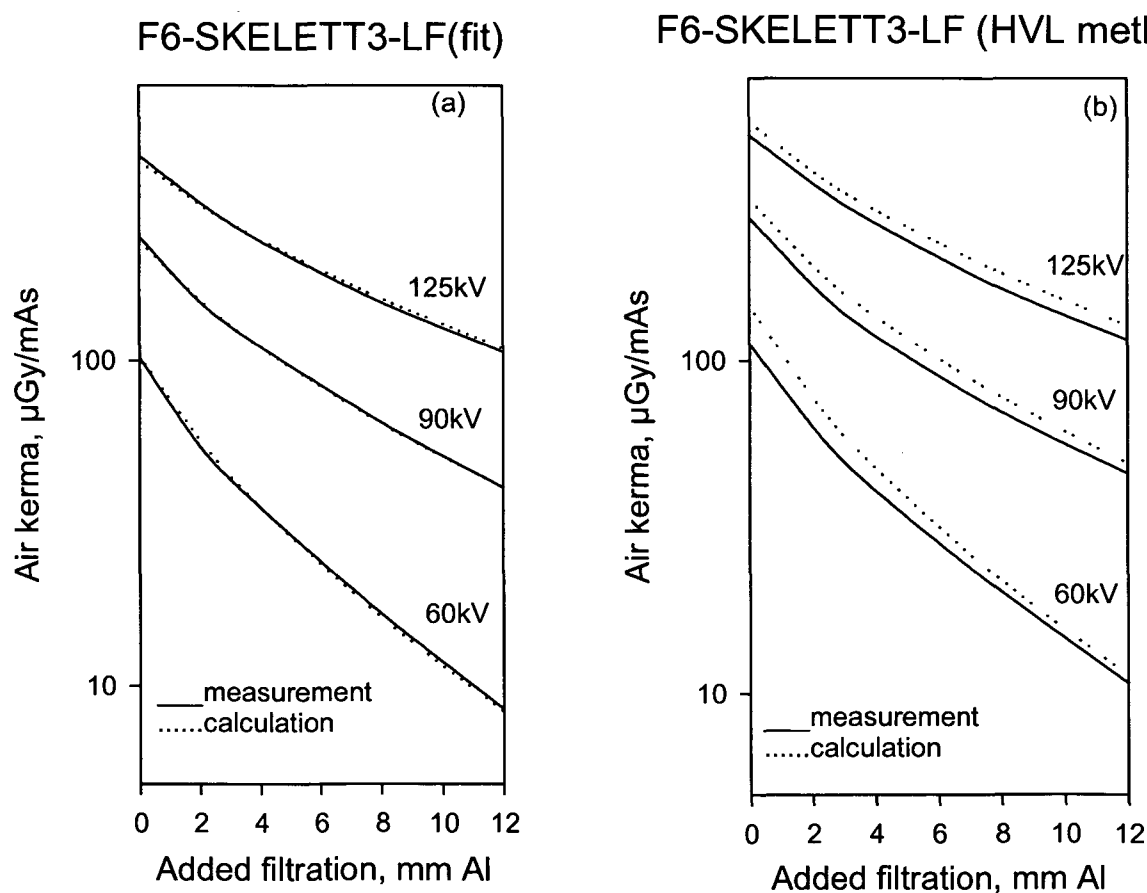


Figure A. 5. Measured attenuation curves obtained for various tube voltages compared with: (a) calculated data using 3.54 mm Al (= 2.5 mm Al nominal filtration + 1.04 mm Al additional filtration), (b) data calculated with the same parameters but using 2.9 mm Al determined with HVL method.

X-ray unit: #3 - F6-SKELETT3-small focus

Anode angle: 15°

Voltage ripple: converter/3.4%

Distance: 55 cm

Nominal total filtration: 2.5 mm Al + 0 mm Cu

Total filtration by HVL method:

Measured HVL: 2.63 mm Al

Total filtration obtained from HVL: 3.69 mm Al

Data fit:

Final values (after 36 iterations):

Filter material	Added filter	Normalisation factor
Al	1,1021 mm	0.948
W	7.8911 μm	0.9473

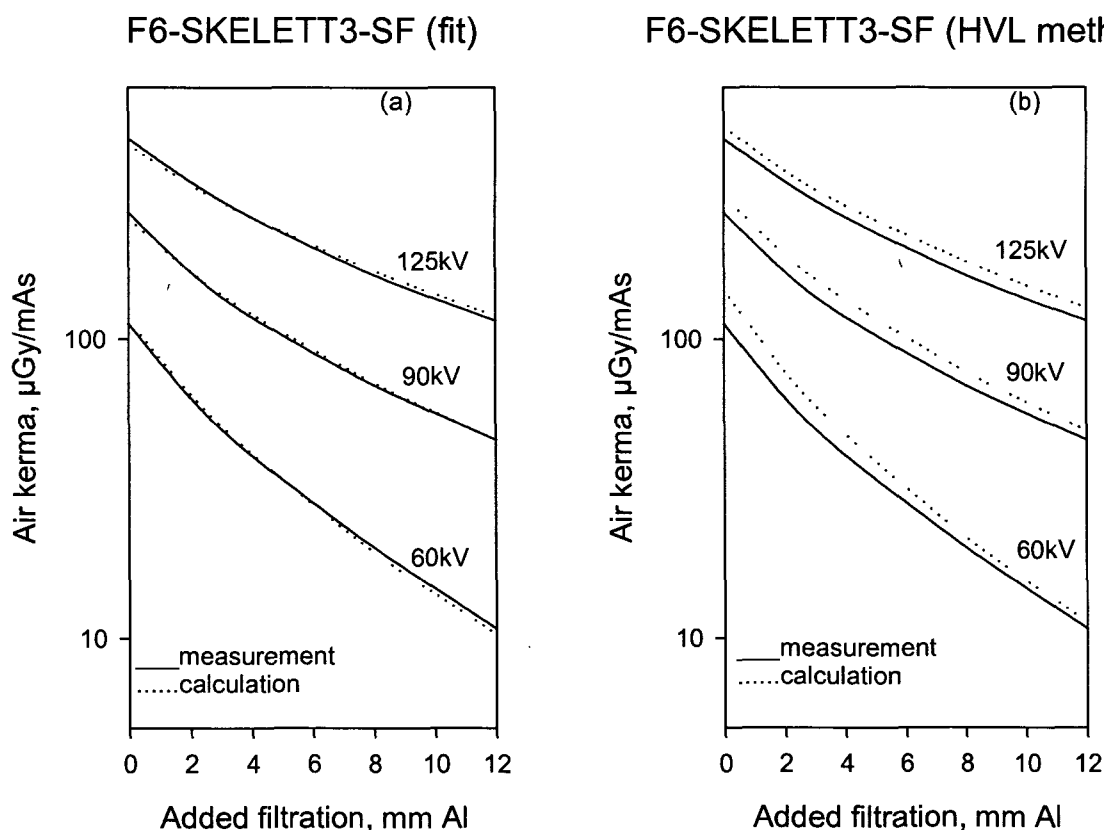


Figure A. 6. Measured attenuation curves obtained for various tube voltages compared with: (a) calculated data using 3.6 mm Al (= 2.5 mm Al nominal filtration + 1.01 mm Al additional filtration), (b) data calculated with the same parameters but using 3.7 mm Al determined with HVL method.

X-ray unit: #4 - F6-THORAX1-large focus

Anode angle: 12°

Voltage ripple: converter/3.4%

Distance: 55 cm

Nominal total filtration: 2.5 mm Al + 0 mm Cu

Total filtration by HVL method:

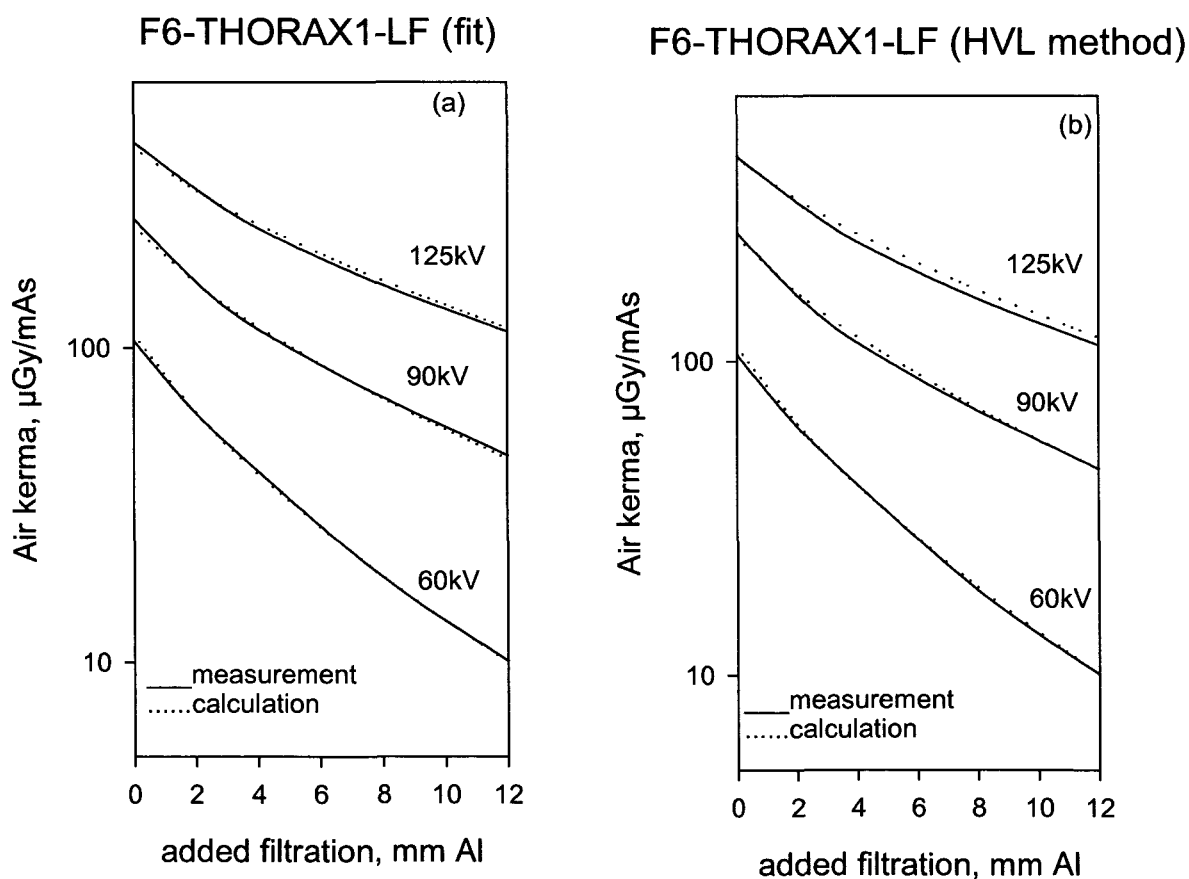
Measured HVL: 2.18 mm Al

Total filtration obtained from HVL: 2.64 mm Al

Data fit:

Final values (after 48 iterations):

Filter material	Added filter	Normalisation factor
Al	0.3444 mm	0.9367
W	2.4328 μm	0.9358



X-ray unit: #4 - F6-THORAX1-small focus

Anode angle: 12°

Voltage ripple: converter/3.4%

Distance: 55 cm

Nominal total filtration: 2.5 mm Al + 0 mm Cu

Total filtration by HVL method:

Measured HVL: 2.19 mm Al

Total filtration obtained from HVL: 2.65 mm Al

Data fit:

Final values (after 40 iterations):

Filter material	Added filter	Normalisation factor
Al	0.3965 mm	0.9358
W	2.8001 μ m	0.9347

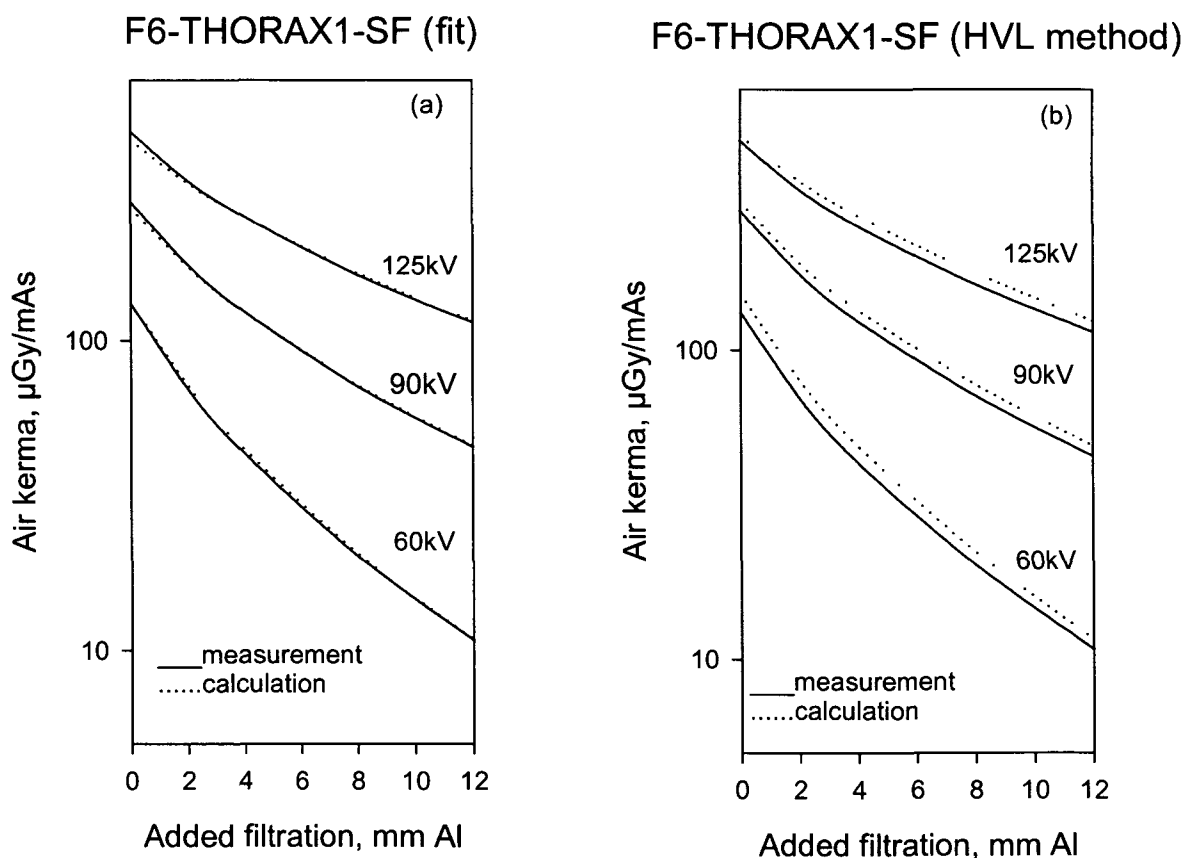


Figure A. 8. Measured attenuation curves obtained for various tube voltages compared with: (a) calculated data using 2.9 mm Al (= 2.5 mm Al nominal filtration + 0.4 mm Al additional filtration), (b) data calculated with the same parameters but using 2.65 mm Al determined with HVL method.

X-ray unit: #5 - F6-THORAX2-large focus

Anode angle: 13°

Voltage ripple: converter/3.4%

Distance: 55 cm

Nominal total filtration: 2.5 mm Al + 0 mm Cu

Total filtration by HVL method:

Measured HVL: 2.2 mm Al

Total filtration obtained from HVL: 2.68 mm Al

Data fit:

Final values (after 40 iterations):

Filter material	Added filter	Normalisation factor
Al	0.773 mm	0.9375
W	5.4441 μ m	0.935

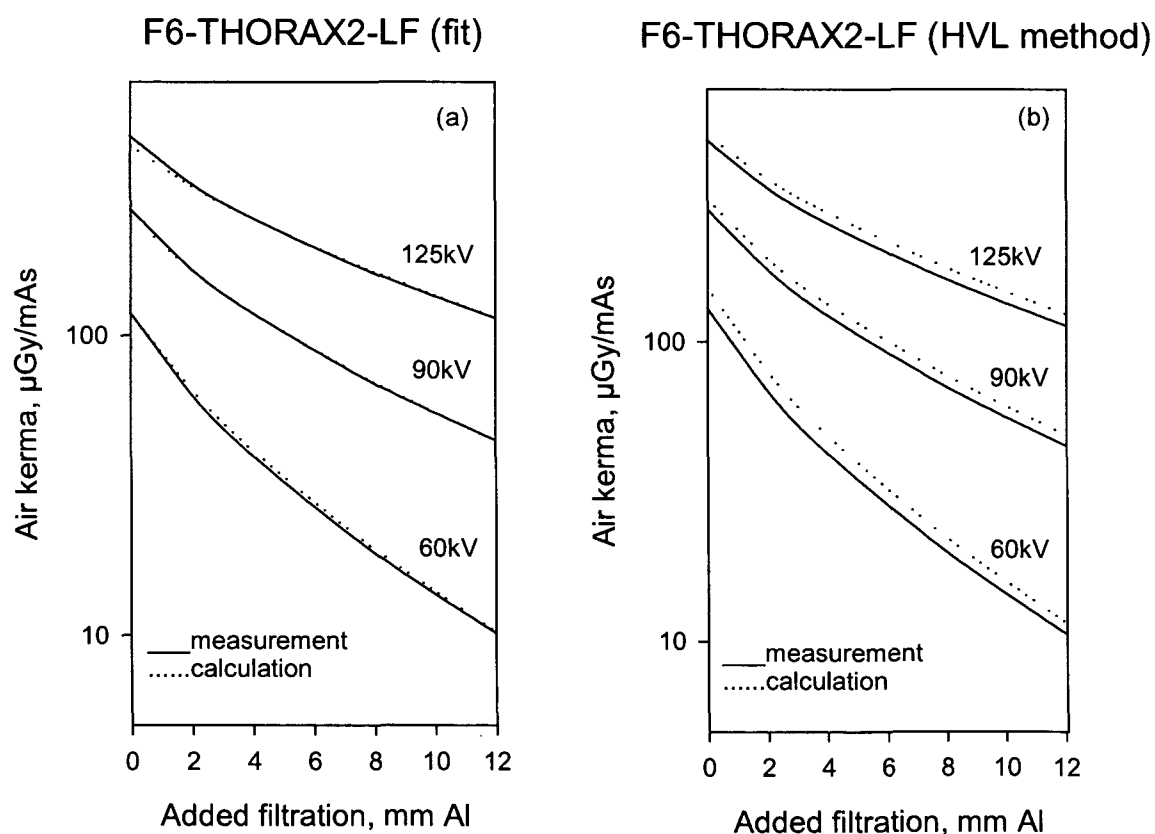


Figure A. 9. Measured attenuation curves obtained for various tube voltages compared with: (a) calculated data using 3.27 mm Al (= 2.5 mm Al nominal filtration + 0.77 mm Al additional filtration), (b) data calculated with the same parameters but using 2.68 mm Al determined with HVL method.

X-ray unit: #5 - F6-THORAX2-small focus

Anode angle: 16°

Voltage ripple: converter/3.4%

Distance: 55 cm

Nominal total filtration: 2.5 mm Al + 0 mm Cu

Total filtration by HVL method:

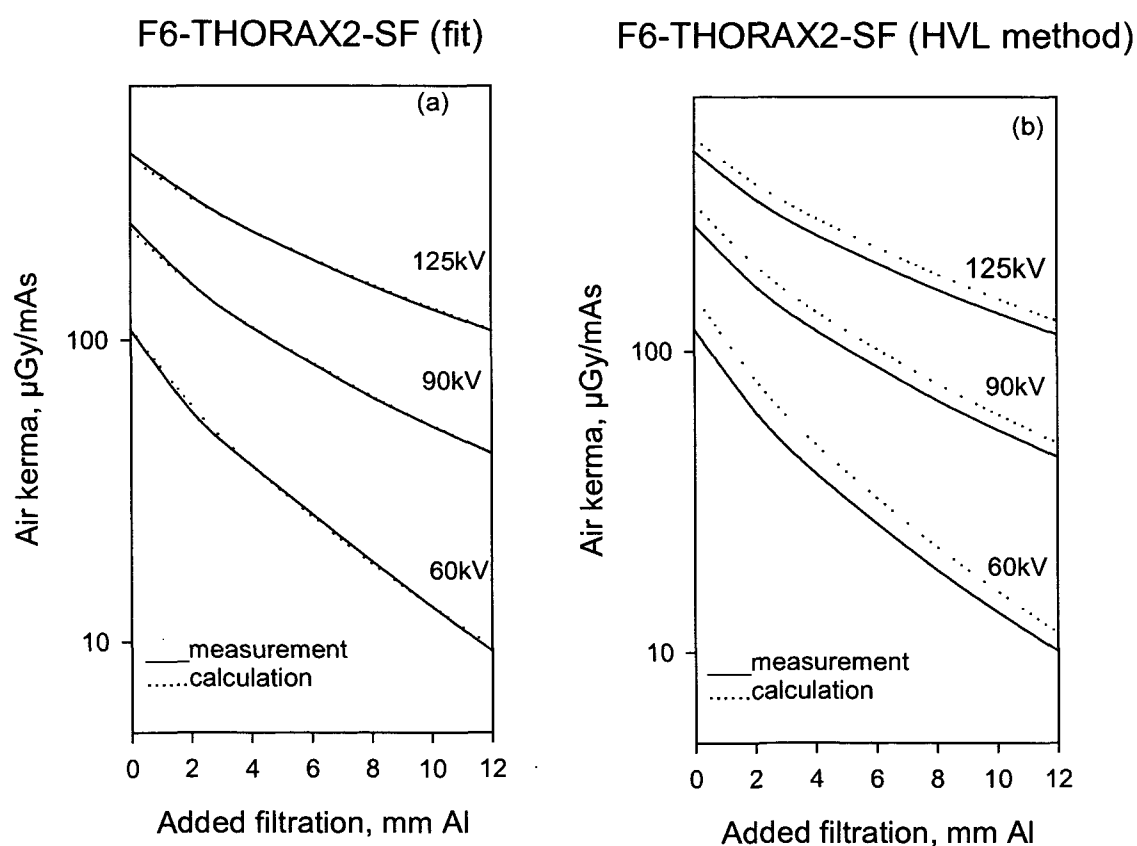
Measured HVL: 2.25 mm Al

Total filtration obtained from HVL: 2.78 mm Al

Data fit:

Final values (after 36 iterations):

Filter material	Added filter	Normalisation factor
Al	0.8745 mm	0.8957
W	6.1939 μm	0.8937



X-ray unit: #6 - F7-SKELETT1-large focus

Anode angle: 12°

Voltage ripple: converter/3.4%

Distance: 55 cm

Nominal total filtration: 2.5 mm Al + 0 mm Cu

Total filtration by HVL method:

Measured HVL: 2.18 mm Al

Total filtration obtained from HVL: 2.64 mm Al

Data fit:

Final values (after 41 iterations):

Filter material	Added filter	Normalisation factor
Al	0.4028 mm	0.9246
W	2.8003 μm	0.9239

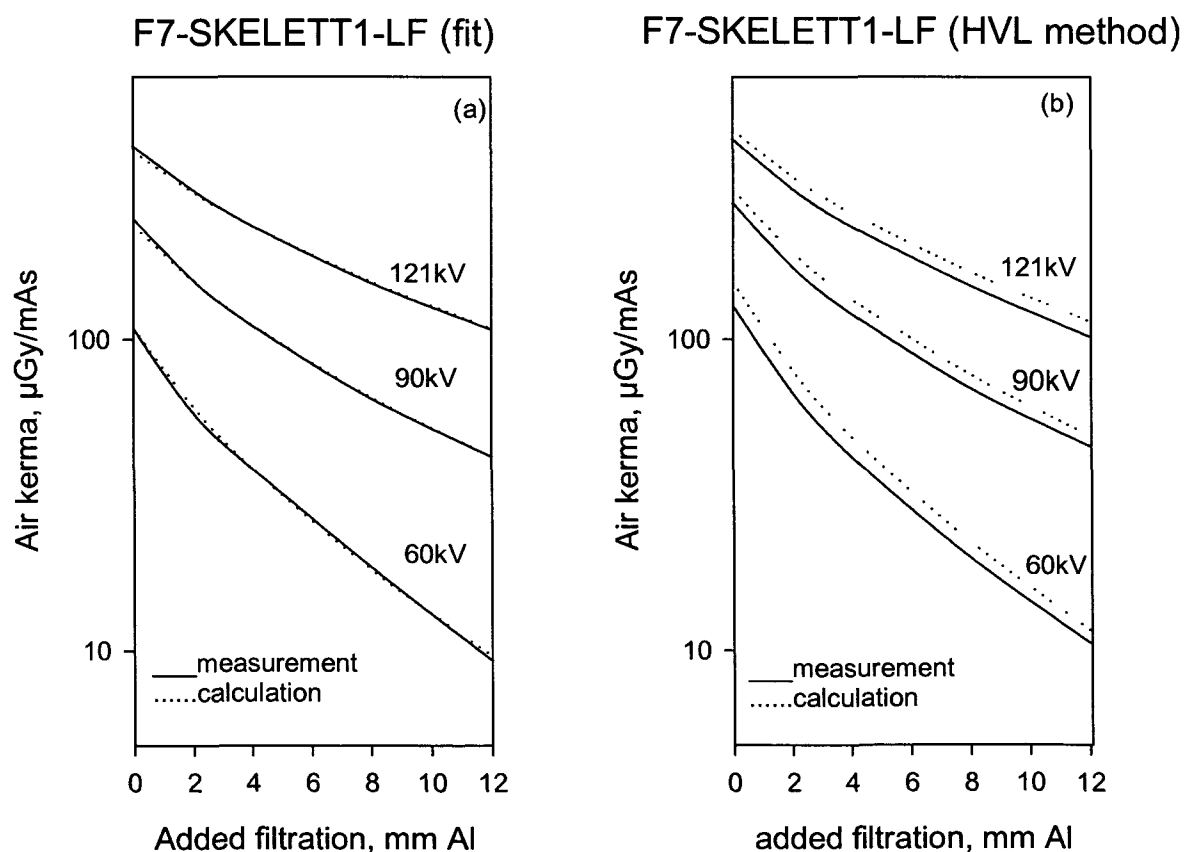


Figure A.11. Measured attenuation curves obtained for various tube voltages compared with: (a) calculated data using 3.42 mm Al (= 2.5 mm Al nominal filtration + 0.92 mm Al additional filtration), (b) data calculated with the same parameters but using 2.64 mm Al determined with HVL method.

X-ray unit: #6 - F7-SKELETT1-small focus

Anode angle: 12°

Voltage ripple: converter/3.4%

Distance: 55 cm

Nominal total filtration: 2.5 mm Al + 0 mm Cu

Total filtration by HVL method:

Measured HVL: 2.19 mm Al

Total filtration obtained from HVL: 2.65 mm Al

Data fit:

Final values (after 40 iterations):

Filter material	Added filter	Normalisation factor
Al	0.4699 mm	0.9264
W	3.3042 μm	0.9248

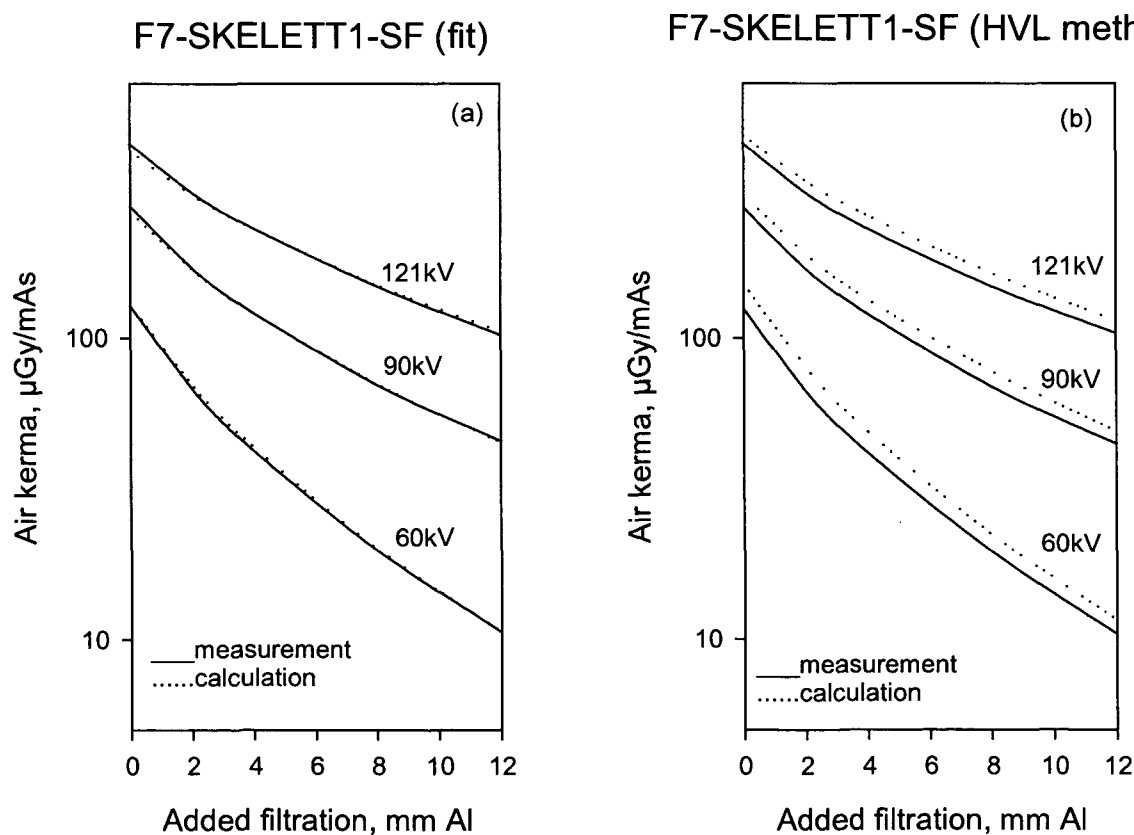


Figure A. 12. Measured attenuation curves obtained for various tube voltages compared with: (a) calculated data using 2.97 mm Al (= 2.5 mm Al nominal filtration + 0.47 mm Al additional filtration), (b) data calculated with the same parameters but using 2.65 mm Al determined with HVL method.

X-ray unit: #7 - F7-SKELETT2-large focus

Anode angle: 12°

Voltage ripple: converter/3.4%

Distance: 55 cm

Nominal total filtration: 2.5 mm Al + 0 mm Cu

Total filtration by HVL method:

Measured HVL: 2.25 mm Al

Total filtration obtained from HVL: 2.79 mm Al

Data fit:

Final values (after 43 iterations):

Filter material	Added filter	Normalisation factor
Al	0.4077 mm	0.8767
W	2.8425 μm	0.8749

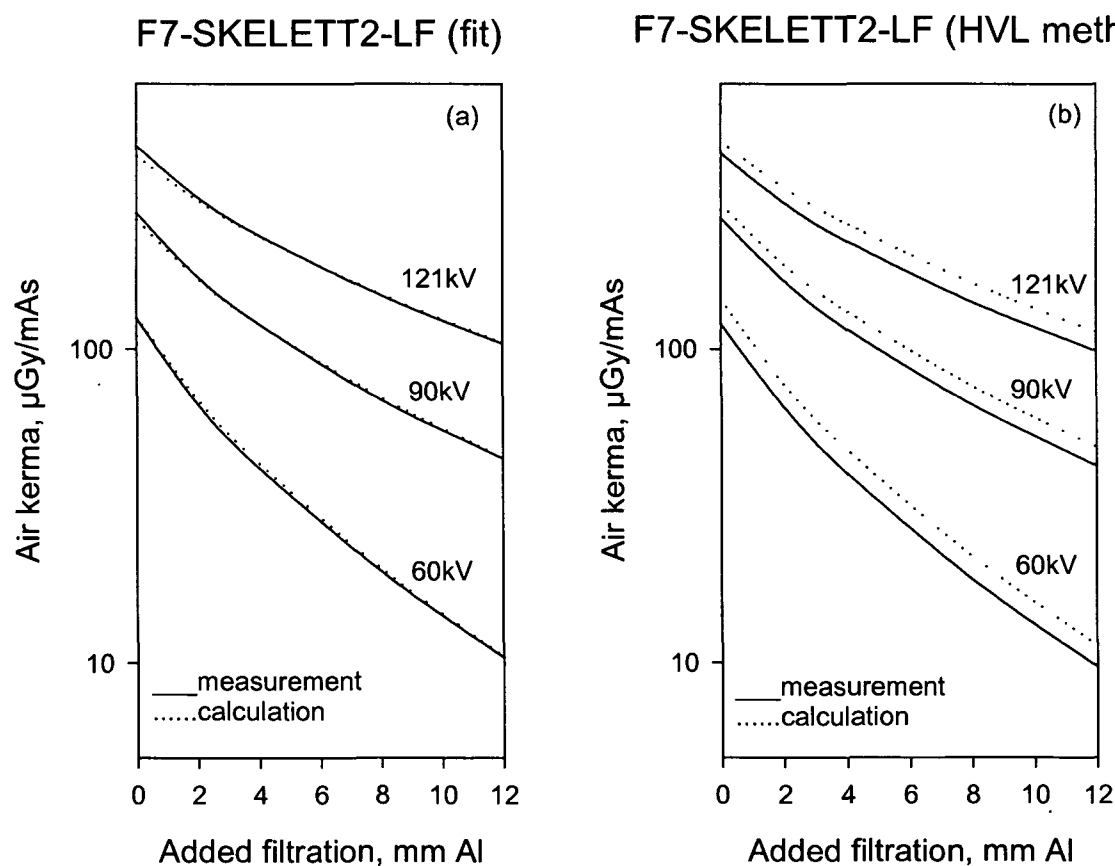


Figure A. 13. Measured attenuation curves obtained for various tube voltages compared with: (a) calculated data using 2.91 mm Al (= 2.5 mm Al nominal filtration + 0.41 mm Al additional filtration), (b) data calculated with the same parameters but using 2.79 mm Al determined with HVL method.

X-ray unit: #7 - F7-SKELETT2-large focus- 0.1mm Cu

Anode angle: 12°

Voltage ripple: converter/3.4%

Distance: 55 cm

Nominal total filtration: 2.5 mm Al + 0.1 mm Cu

Total filtration by HVL method:

Measured HVL: 3.11 mm Al

Total filtration obtained from HVL: 5.09 mm Al

Data fit:

Final values (after 44 iterations):

Filter material	Added filter	Normalisation factor
Al	0.4234 mm	0.8739
W	2.8951 μm	0.8711

F7-SKELETT2-LF-Cu (fit)

F7-SKELETT2-LF-Cu (HVL method)

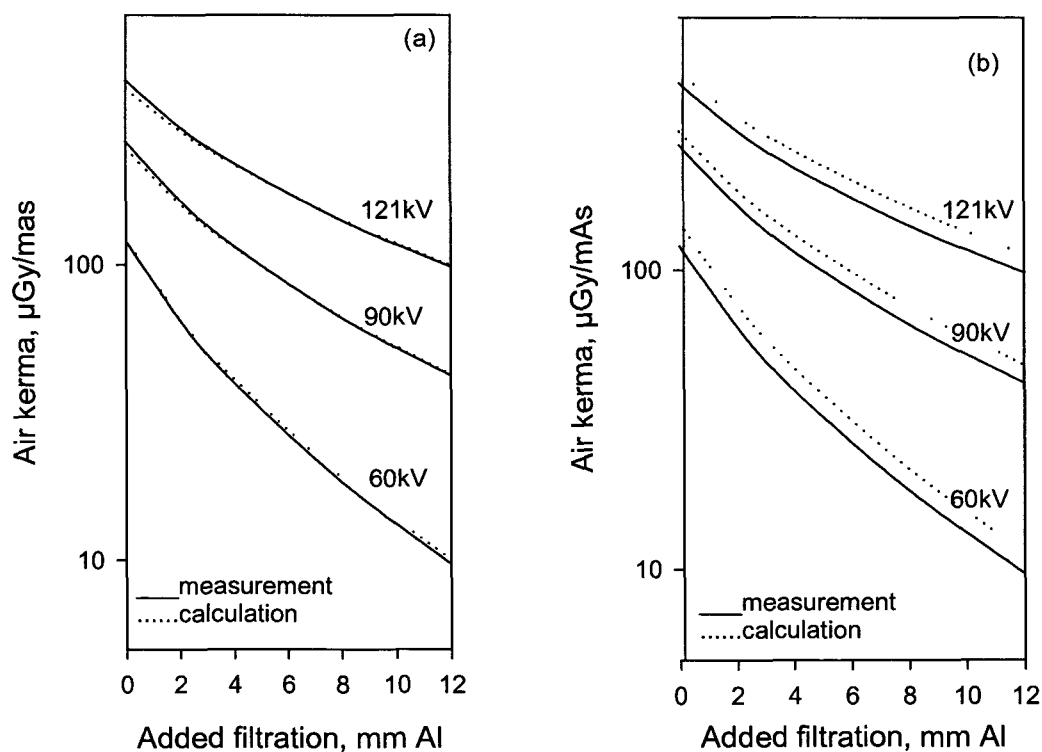


Figure A. 14. Measured attenuation curves obtained for various tube voltages compared with: (a) calculated data using 2.92 mm Al (= 2.5 mm Al + 0.1 mm Cu nominal filtration + 0.42 mm Al additional filtration), (b) data calculated with the same parameters but using 5.09 mm Al determined with HVL method.

X-ray unit: #7 - F7-SKELETT2-small focus-0.1mm Cu

Anode angle: 12°

Voltage ripple: converter/3.4%

Distance: 55 cm

Nominal total filtration: 2.5 mm Al + 0.1 mm Cu

Total filtration by HVL method:

Measured HVL: 3.38 mm Al

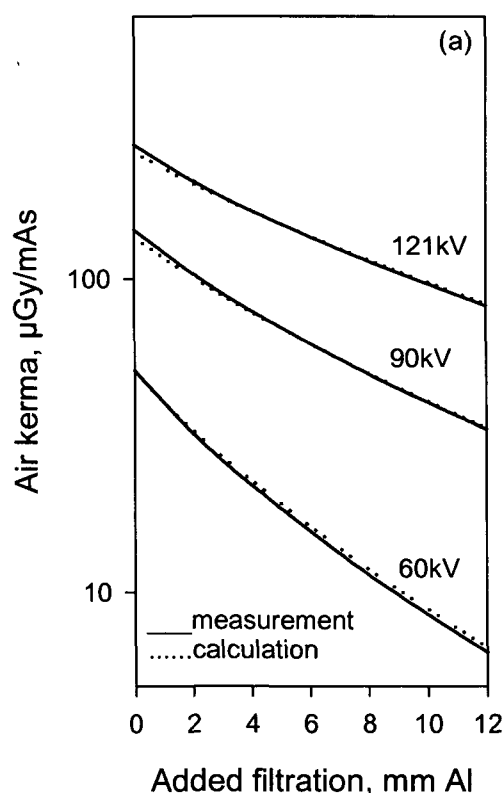
Total filtration obtained from HVL: 6.15 mm Al

Data fit:

Final values (after 52 iterations):

Filter material	Added filter	Normalisation factor
Al	0.6728 mm	0.851
W	5.0136 μ m	0.853

F7-SKELETT2-SF-Cu (fit)



F7-SKELETT2-SF-Cu (HVL method)

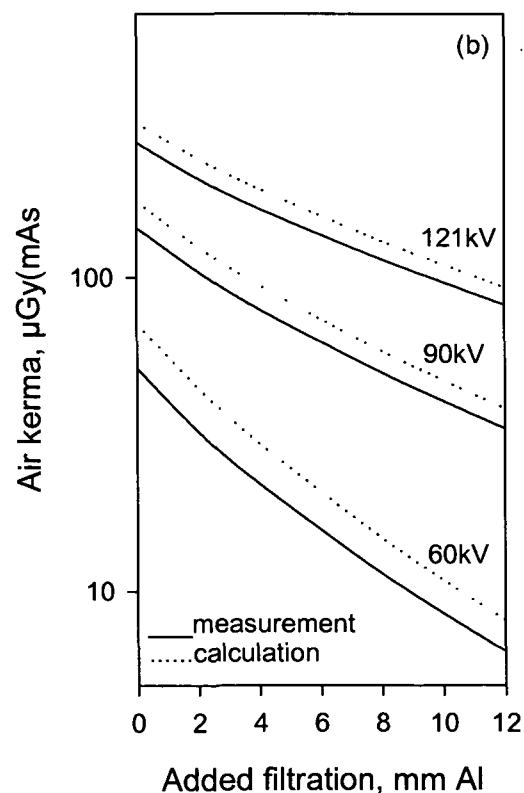


Figure A. 15. Measured attenuation curves obtained for various tube voltages compared with: (a) calculated data using 3.17 mm Al (= 2.5 mm Al + 0.1 mm Cu nominal filtration + 0.67 mm Al additional filtration), (b) data calculated with the same parameters but using 6.15 mm Al determined with HVL method.

X-ray unit: #8 - F6-GASTRO2-large focus

Anode angle: 12°

Voltage ripple: converter/3.4%

Distance: 55 cm

Nominal total filtration: 2.5 mm Al + 0 mm Cu

Total filtration by HVL method:

Measured HVL: 2.21 mm Al

Total filtration obtained from HVL: 2.69 mm Al

Data fit:

Final values (after 38 iterations):

Filter material	Added filter	Normalisation factor
Al	1.175 mm	0.8604
W	7.9256 μ m	0.8497

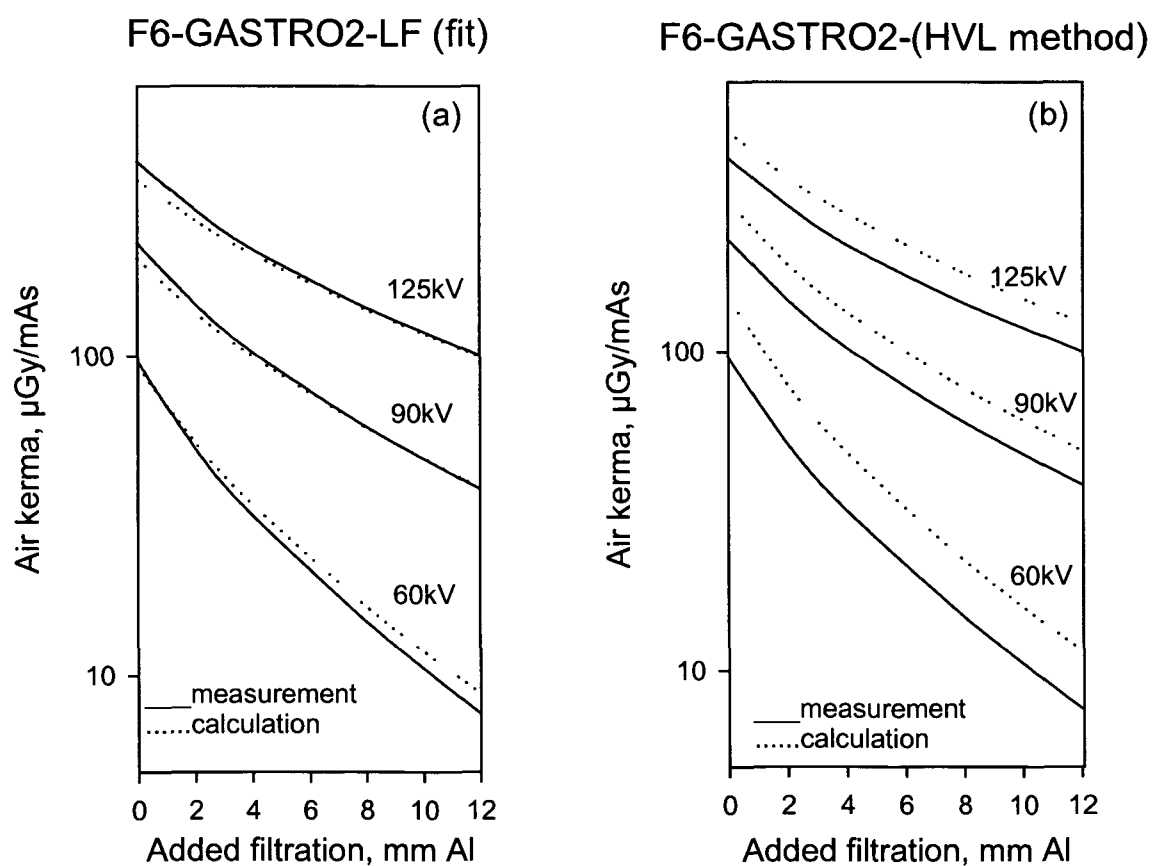


Figure A. 16. Measured attenuation curves obtained for various tube voltages compared with: (a) calculated data using 3.36 mm Al (= 2.5 mm Al nominal filtration + 0.86 mm Al additional filtration), (b) data calculated with the same parameters but using 2.69 mm Al determined with HVL method.

X-ray unit: #8 - F6-GASTRO2-large focus; *kVp correction*

Anode angle: 12°

Voltage ripple: converter/3.4%

Distance: 55 cm

Nominal total filtration: 2.5 mm Al + 0 mm Cu

Total filtration by HVL method:

Measured HVL: 2.21 mm Al

Total filtration obtained from HVL: 2.69 mm Al

Data fit:

Final values (after 38 iterations):

Filter material	Added filter	Normalisation factor
Al	0.7976 mm	0.8864
W	5.6408 μm	0.8846

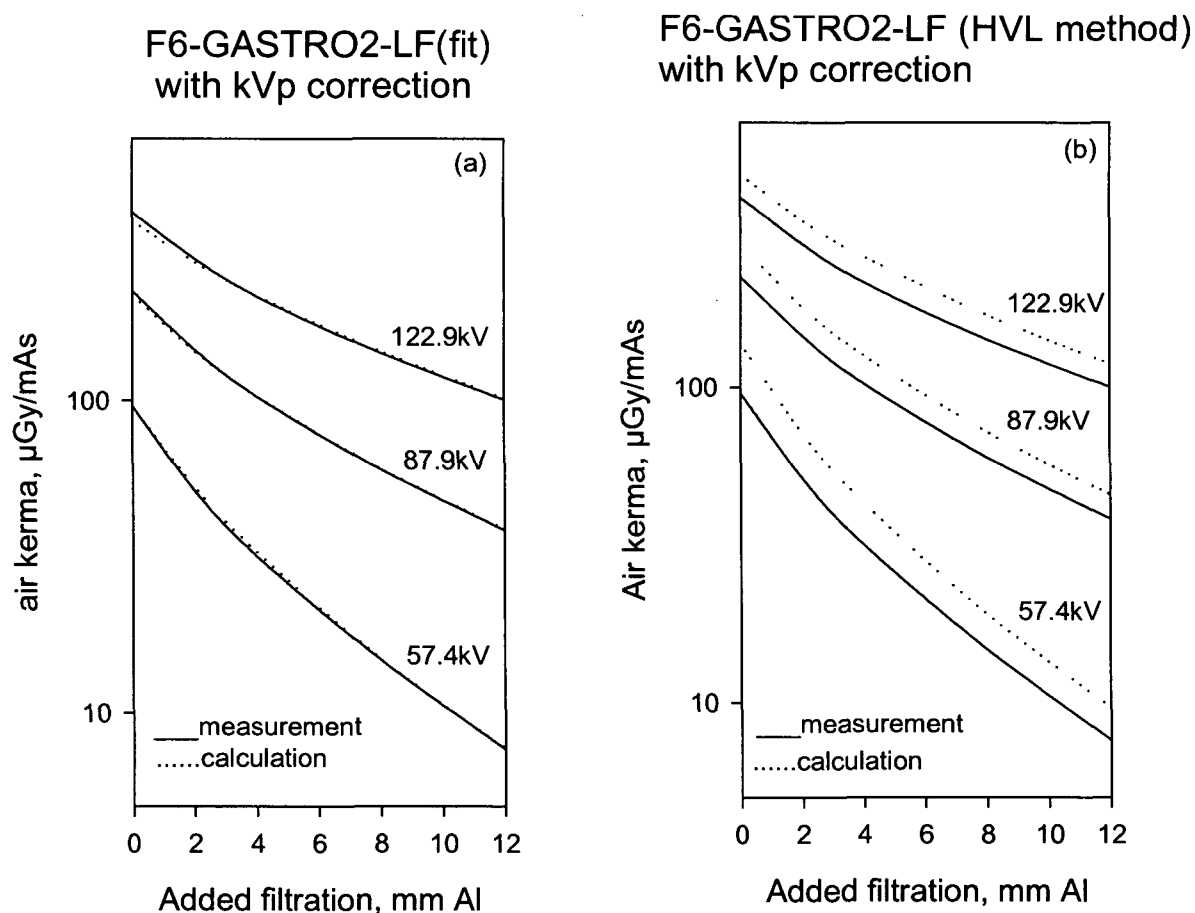


Figure A.17. Measured attenuation curves obtained for various tube voltages compared with: (a) calculated data using 3.3 mm Al (= 2.5 mm Al nominal filtration + 0.8 mm Al additional filtration), (b) data calculated with the same parameters but using 2.69 mm Al determined with HVL method.

X-ray unit: #8 - F6-GASTRO2-small focus

Anode angle: 12°

Voltage ripple: converter/3.4%

Distance: 55 cm

Nominal total filtration: 2.5 mm Al + 0 mm Cu

Total filtration by HVL method:

Measured HVL: 2.27 mm Al

Total filtration obtained from HVL: 2.82 mm Al

Data fit:

Final values (after 43 iterations):

Filter material	Added filter	Normalisation factor
Al	1.7208 mm	0.9388
W	11.8915 μ m	0.9276

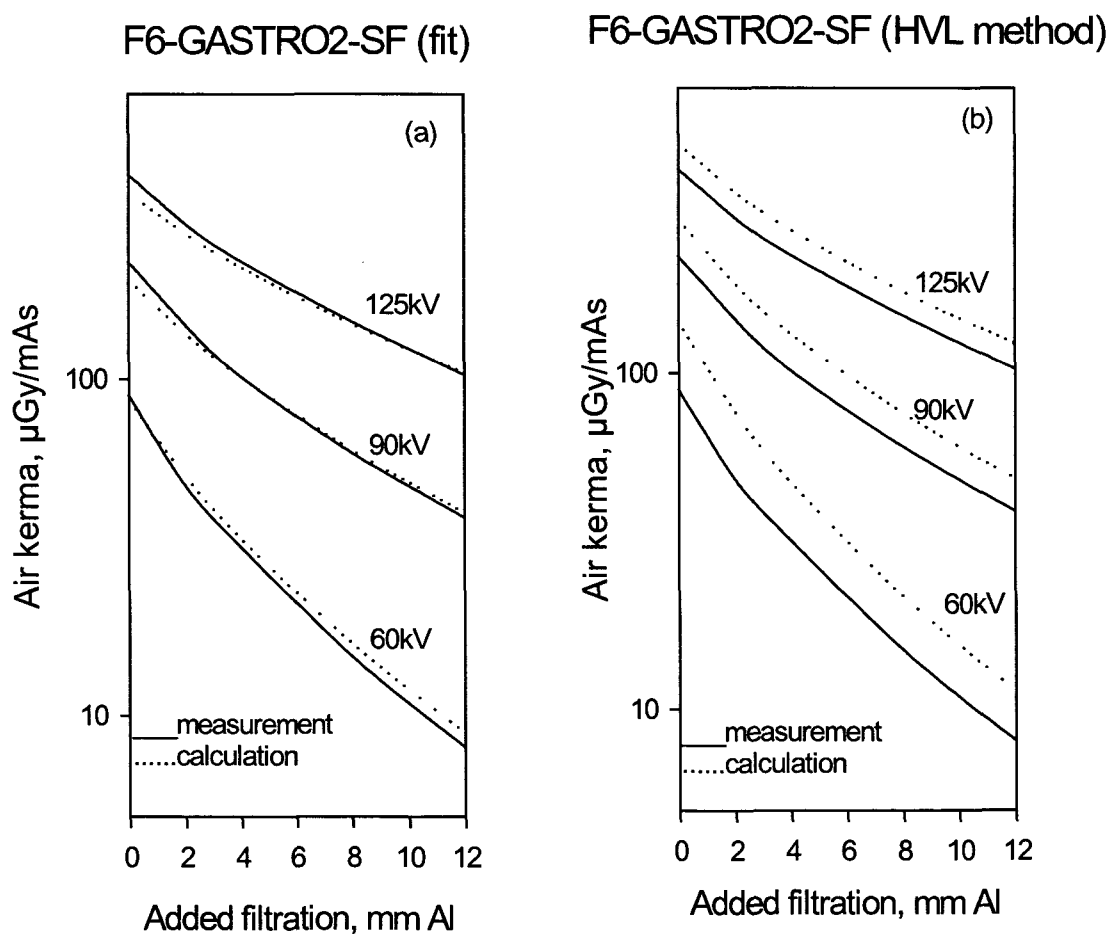


Figure A. 18. Measured attenuation curves obtained for various tube voltages compared with: (a) calculated data using 4.22 mm Al (= 2.5 mm Al nominal filtration + 1.72 mm Al additional filtration), (b) data calculated with the same parameters but using 2.82 mm Al determined with HVL method.

X-ray unit: #8 - F6-GASTRO2-small focus, kVp correction

Anode angle: 12°

Voltage ripple: converter/3.4%

Distance: 55 cm

Nominal total filtration: 2.5 mm Al + 0 mm Cu

Total filtration by HVL method:

Measured HVL: 2.27 mm Al

Total filtration obtained from HVL: 2.82mm Al

Data fit:

Final values (after 44 iterations):

Filter material	Added filter	Normalisation factor
Al	1.2287 mm	0.9522
W	8.731 μ m	0.95

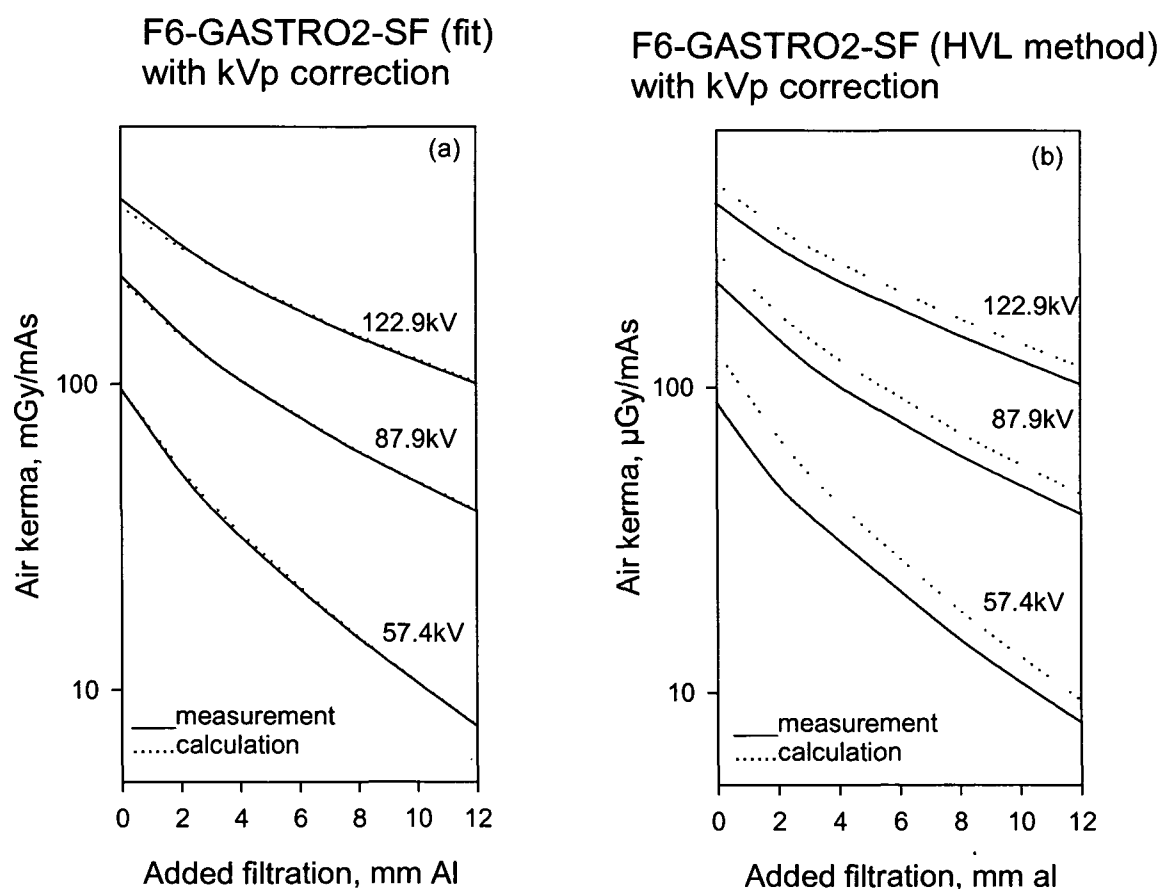


Figure A. 19. Measured attenuation curves obtained for various tube voltages compared with: (a) calculated data using 3.73 mm Al (= 2.5 mm Al nominal filtration + 1.23 mm Al additional filtration), (b) data calculated with the same parameters but using 2.82 mm Al determined with HVL method.

X-ray unit: #9 - F6-SKELETT2-large focus

Anode angle: 12°

Voltage ripple: converter/3.4%

Distance: 55 cm

Nominal total filtration: 2.5 mm Al + 0 mm Cu

Total filtration by HVL method:

Measured HVL: 2.17 mm Al

Total filtration obtained from HVL: 2.62 mm Al

Data fit:

Final values (after 44 iterations):

Filter material	Added filter	Normalisation factor
Al	0.9314 mm	0.9522
W	6.2172 μ m	0.9413

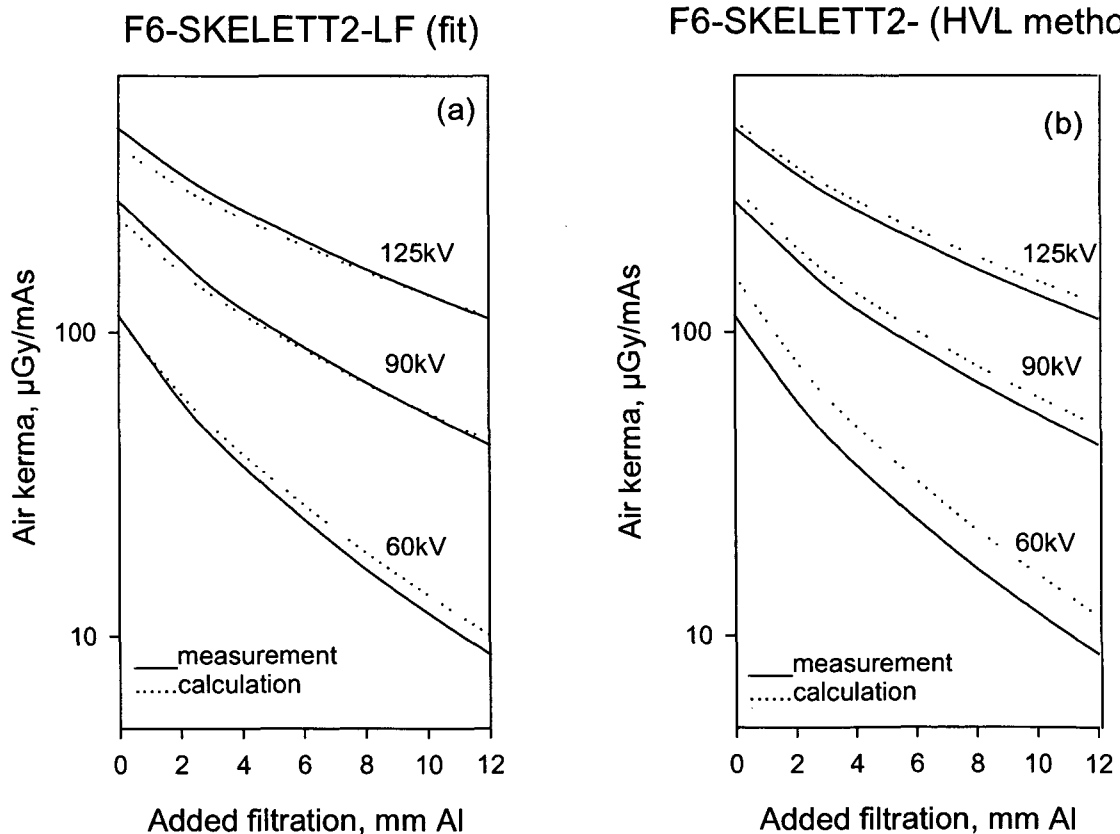


Figure A. 20. Measured attenuation curves obtained for various tube voltages compared with: (a) calculated data using 3.43 mm Al (= 2.5 mm Al nominal filtration + 0.93 mm Al additional filtration), (b) data calculated with the same parameters but using 2.62 mm Al determined with HVL method.

X-ray unit: #9 - F6-SKELETT2-large focus- kVp correction

Anode angle: 12°

Voltage ripple: converter/3.4%

Distance: 55 cm

Nominal total filtration: 2.5 mm Al + 0 mm Cu

Total filtration by HVL method:

Measured HVL: 2.17 mm Al

Total filtration obtained from HVL: 2.62mm Al

Data fit:

Final values (after 49 iterations):

Filter material	Added filter	Normalisation factor
Al	0.6711 mm	1.0339
W	4.7632 μ m	1.00326

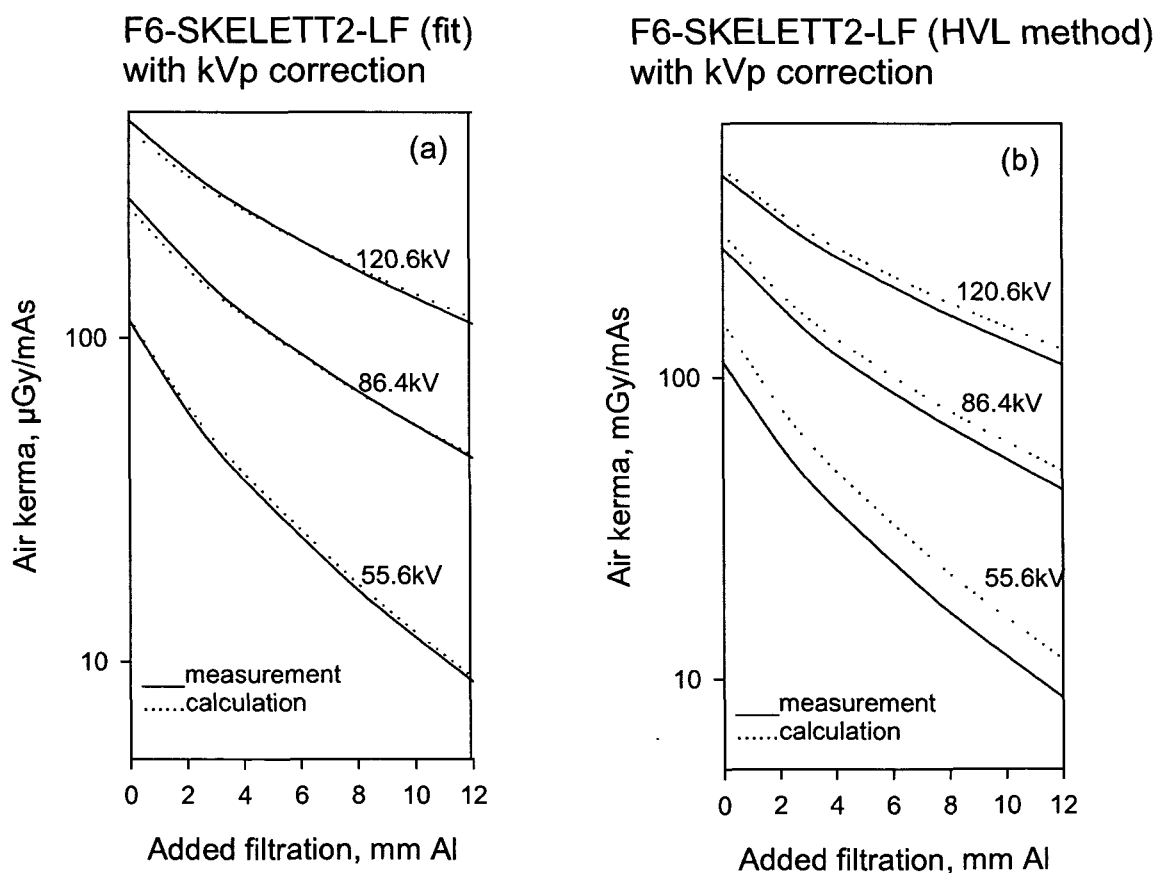


Figure A. 21. Measured attenuation curves obtained for various tube voltages compared with: (a) calculated data using 3.17 mm Al (= 2.5 mm Al nominal filtration + 0.67 mm Al additional filtration), (b) data calculated with the same parameters but using 2.62 mm Al determined with HVL method.

X-ray unit: #9 - F6-SKELETT2-small focus

Anode angle: 12°

Voltage ripple: converter/3.4%

Distance: 55 cm

Nominal total filtration: 2.5 mm Al + 0 mm Cu

Total filtration by HVL method:

Measured HVL: 2.21 mm Al

Total filtration obtained from HVL: 2.69 mm Al

Data fit:

Final values (after 41 iterations):

Filter material	Added filter	Normalisation factor
Al	1.1501 mm	0.9218
W	7.9222 μ m	0.9141

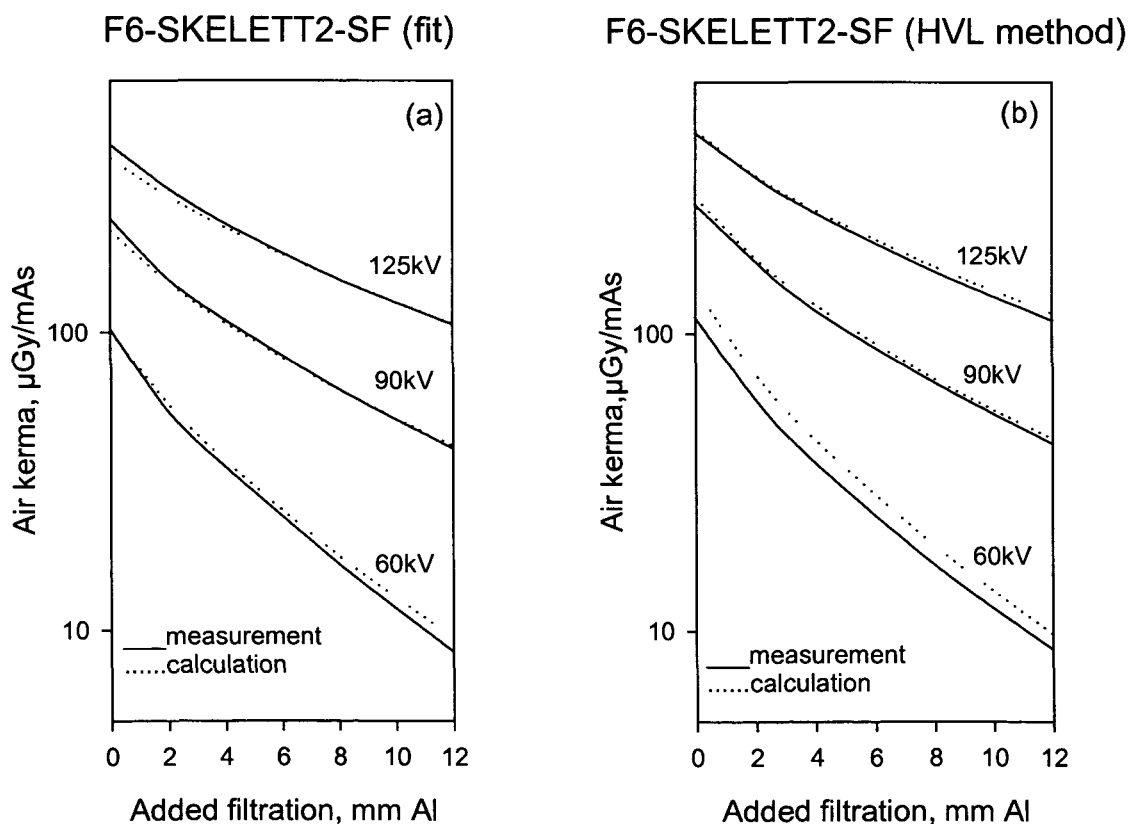


Figure A.22. Measured attenuation curves obtained for various tube voltages compared with: (a) calculated data using 3.65 mm Al (= 2.5 mm Al nominal filtration + 1.15 mm Al additional filtration), (b) data calculated with the same parameters but using 2.69 mm Al determined with HVL method.

X-ray unit: #9 - F6-SKELETT2-small focus – kVp correction

Anode angle: 12°

Voltage ripple: converter/3.4%

Distance: 55 cm

Nominal total filtration: 2.5 mm Al + 0 mm Cu

Total filtration by HVL method:

Measured HVL: 2.21 mm Al

Total filtration obtained from HVL: 2.69 mm Al

Data fit:

Final values (after 34 iterations):

Filter material	Added filter	Normalisation factor
Al	0.8471 mm	0.9894
W	6.0597 μm	0.9891

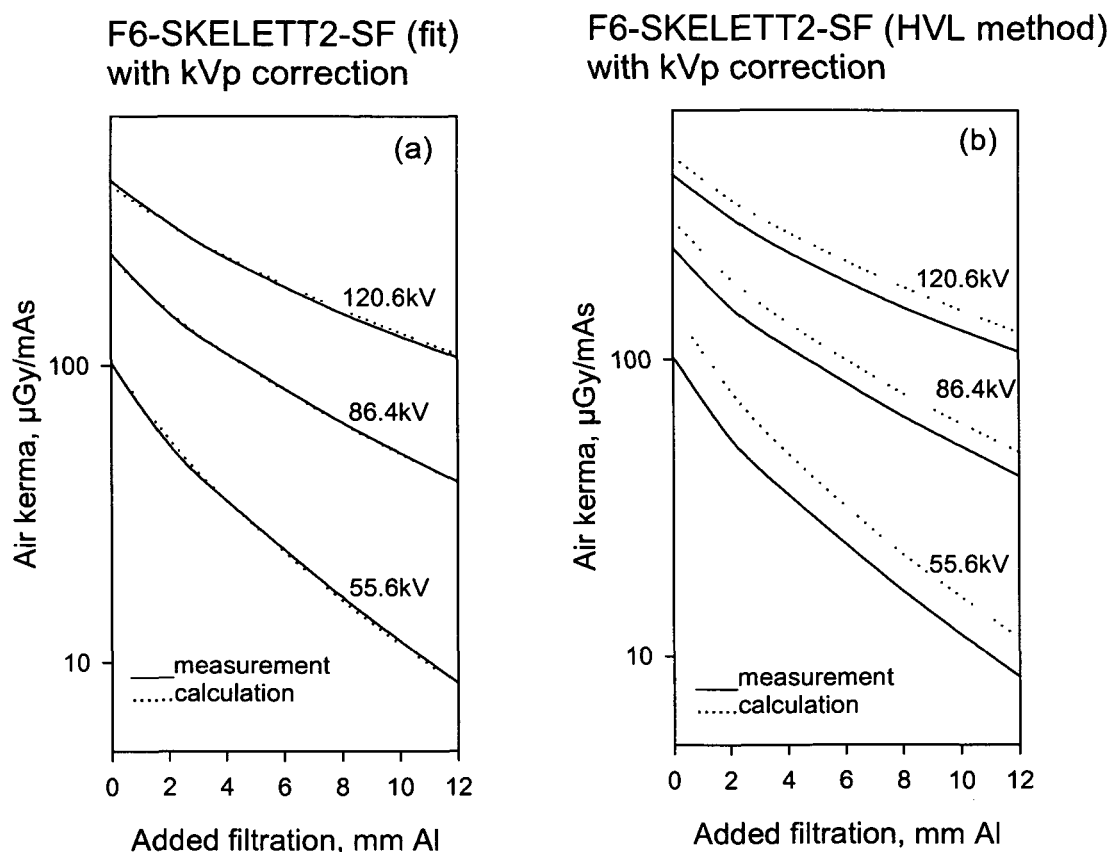


Figure A. 23. Measured attenuation curves obtained for various tube voltages compared with: (a) calculated data using 3.35 mm Al (= 2.5 mm Al nominal filtration + 0.85 mm Al additional filtration), (b) data calculated with the same parameters but using 2.69 mm Al determined with HVL method.

CURRICULUM VITAE

1. PERSONAL DATA

Name: MEGHZIFENE

Maiden name: BENNAB

Surname: Khadoudja

Date and place of birth: 1954-12-13, Paris, France

Nationality: Algerian

Marital status: married, two children

Adresse: 1190, Friedlgasse 52/4, Wien

Telephone: office 40 400 3979, home 925 37 76, mobile 06991 825 37 76

E-mail: Khadoudja.Meghzifene@meduniwien.ac.at

2. EDUCATION

- 2000-2004: Ph.D. student at the technical university, Vienna.
- 1981-1984: Commissariat aux Energies Nouvelles, Algiers, Algeria. This institution recently renamed Commissariat à l'Energie Atomique, was accredited by the university of Algiers for conducting post graduate studies in the field of nuclear applications
Master in Nuclear Physics, Health Physics option. Major fields of study: nuclear physics, physics of radiology and health physics. For partial fulfilment of the M.Sc. degree, I conducted my research work at the Université Catholique de Louvain, Brussels, Belgium from April 1983 to May 1984, under the supervision of Prof. A. Wambersie. The thesis "Thermoluminescent dosimetry in radiotherapy: application to linear accelerators" was defended in 1984
- 1975-1981: Ecole Nationale Polytechnique, Algiers, Algeria, Bachelor of Science, Engineer in Electronics. Major fields of study: electronics, physics and mathematics.
- 1971-1972: High School, Lycée Omar Racim, Algiers, Algeria, Baccalaureate. Major fields of study: mathematics, physics and natural sciences.

3. EMPLOYEMENT

- 1996-1998: senior radiation physicist in charge of quality assurance and dosimetry in diagnostic radiology. Department of Medical Physics, Centre de Radioprotection et de Sécurité, 2 Blvd Frantz Fanon, BP 399 Alger-Gare, Algiers and Centre d'Imagerie Médicale, Centre hospitalo-Universitaire Alger-Ouest, Algiers
Major achievements: Implementation of quality control procedures at a pilot hospital. Determination of doses to patients undergoing computed tomography examinations.

- 1986-1996: medical physicist, in charge of dosimetry and treatment planning in radiotherapy. Service de Radiothérapie, Hôpital Central de l'Armée, Kouba, Algiers
Major achievements: Dosimetry and treatment planning for radiotherapy patients. Quality control of irradiation units.
- 1984-1986: junior radiation physicist, in charge of calibration of dosimeters used in radiotherapy. Secondary Standard Dosimetry Laboratory, Centre de Radioprotection et de Sécurité, Algiers

4. GRANTS AND FELLOWSHIPS

- Fellowship grants by the European Community, Université catholique de Louvain, Brussels, April 83-May 1984 for completion of M.Sc. thesis in nuclear physics.
- Scientific visit to Secondary Standard Dosimetry Laboratories in Europe, under the IAEA fellowship; September-October 1985
- Practical training at the Agency's Dosimetry Laboratory at Seibersdorf in the field of calibration of dosimeters, under the IAEA fellowship; March-May 1986.
- Workshop on medical imaging, under the ICTP grant; September 1994

5. EXPERIENCE IN TEACHING

- Under graduate courses to health physicists at the Centre de Radioprotection et de Sécurité, Algiers in the field of quality control in diagnostic radiology, treatment planning and dosimetry.
- Supervision of training of medical physicists and health physicists at hospitals and at the Centre de Radioprotection et de Sécurité, for the partial fulfilment of their academic degree.

6. CONFERENCE ABSTRACTS

- Optimisation of breast cancer irradiation techniques, presented at the ASTRO meeting, Leuven, Belgium, 1991
- Quality assurance in diagnostic radiology, presented at the World Congress of Biophysics and Engineering, Rio de Janeiro, Brazil, 1994.
- The effect of anode surface roughness on radiation output for diagnostic x-ray sources, presented at the IAEI International Conference in Vienna, Austria, 25-28 November 2002